Measurement of the Spin Structure of the Neutron using Polarised Deep Inelastic Scattering

by

Ralf Bernd Kaiser

Diplom-Physiker, Universität Münster, 1992

A THESIS SUBMITTED IN PARTIAL FULFILLMENT
OF THE REQUIREMENTS FOR THE DEGREE OF
DOCTOR OF PHILOSOPHY
in the Department
of
Physics

SIMON FRASER UNIVERSITY
April 1997

Abstract

The measurement of the spin structure function g_1^p of the proton and its integral Γ_1^p by the EMC experiment at CERN in 1988 indicated that only $12\% \pm 17\%$ of the proton spin is carried by quarks. This unexpected result - the so called 'spin crisis' - lead to a series of new experimental proposals. One of these, the HERMES experiment, uses the polarised positron beam of the HERA accelerator together with a polarised internal gas target of hydrogen, deuterium or ^{3}He for the study of the spin structure of the nucleon. The scattered positrons and other products of the reaction are detected in a forward spectrometer with large acceptance.

This thesis focuses on three topics, after a review of the relevant theory and an overview of the HERMES experiment: The HERMES transition radiation detector (TRD), which is used to distinguish high energy positrons from hadrons, the HERMES particle identification (PID) system and the measurement of the spin structure function g_1^n of the neutron. The HERMES TRD is the main Canadian contribution to the apparatus of the experiment. The HERMES PID system allows the identification of positrons from deep inelastic scattering with an efficiency of 99% and a hadron contamination of less than 0.5%.

The first physics result from the 1995 HERMES data is the measurement of the spin structure function $g_1^n(x)$ of the neutron. The value of the resulting integral $\Gamma_1^n = \int_0^1 g_1^n(x)\ dx$ confirms previous measurements at SLAC and violates the Ellis-Jaffe sum rule by about one sigma. The contribution of the quarks to the spin of the neutron can be calculated in the framework of the quark parton model to be $37 \pm 16\%$, indicating that less than half of the spin of the neutron is carried by quarks.

Schüler
Ich wünschte recht gelehrt zu werden,
Und möchte gern, was auf der Erden,
Und in dem Himmel ist, erfassen,
Die Wissenschaft und die Natur.
Mephistopheles
Da seid Ihr auf der rechten Spur;
Doch müßt Ihr Euch nicht zerstreuen lassen.
Schüler
Ich bin dabei mit Seel und Leib;
Doch freilich würde mir behagen
Ein wenig Freiheit und Zeitvertreib
An schönen Sommerfeiertagen.

J.W.Goethe, Faust

Acknowledgments

Many people have supported me over the last four years, by answering my questions, by helping out with the intricacies of hardware and software, by discussions about HERMES physics or by simply being who they are. I would like to thank all of them.

My thesis advisor Mike Vetterli has given me the great opportunity to do my Ph.D. in Vancouver. Some of the most important things are not learned from books and being in Canada has changed and enriched my life more than I ever would have expected. I am also indebted to him for having given me the room to learn to work independently. I hope that now, by the time of my graduation, I meet the high expectations he has of a professional physicist. His energy, stamina and determination are qualities I hope to take with me.

I would like to thank Otto Häusser for being such a positive role model as a physicist who has been dedicated to physics all of his live. It is uplifting to see how much enthusiasm he still has for physics, after being involved in it for quite some time.

I would like to thank the two other members of my supervisory committee, Howard Trottier and Richard Woloshyn, for their interest in my work.

The Canadian HERMES group has been a great group to work with. Andy Miller, Anne Trudel, Robert Henderson, Peter Green, Eric Belz, Manuella Vincter, Gordon Greeniaus, Peter Kitching, Jinsong Ouyang, Paul Delheij, Martin Kückes, Robert Openshaw, Kalen Martens, Felix Menden and Doug Thiessen - they all have contributed to the work on the HERMES TRD and therefore also to this thesis. As this is the only Ph.D. thesis that is also concerned with the HERMES TRD, I would like them to also consider it 'theirs'.

During the work on the hardware part of this thesis I have more than once needed the support of the people in the various workshops at TRIUMF. The technicians in the TRIUMF detector facility and the scintillator shop in particular have been a great help and Rick, Steve and Chris are also great fun to play volleyball with.

The physics analysis in the NAPA group was instructive, stressful, intensive - and fun. This was of course due to the people in NAPA that are hard working but easy going individuals. Brad Filiponne, Bob McKeown, Bruce Bray, Paul Carter, Dirk De Schepper, Andrea Dvoredsky, Steve Pate, Greg Rakness, Ed Kinney, Richard Milner, Art Mateos, Laird Kramer, Hal Jackson and Ole Hansen have made the work in the North American Physics Analysis group within HERMES efficient as well as enjoyable. I would like to thank the EURO group as well, Wolfgang Lachnit, Johan Blouw, Manfred Ferstl, Philipp Geiger and Michael Düren were great to work with and extremely helpful by answering my frequent e-mails while I was writing my thesis.

Dirk De Schepper I would like to thank for working with me during all those analysis workshops, and for having the energy to still have a beer with me at the end of the day. His humour and his reliability make him ideal to work with. He has been a good friend, both in front of a computer in the middle of the night and rollerblading at the Santa Monica pier.

Kevin McIlhany I owe a great deal for all our discussions about particle identification at HERMES and for producing the datatrack ntuples that made my particle identification studies technically possible.

My fellow graduate students at SFU and TRIUMF, Alexander Gorelov, Doug Thiessen and Araz Hamian I would like to thank for working with me during our classes and for being my friends.

The German Academic Exchange Service (DAAD) generously financed the first three years of my Ph.D. with a fellowship. I am very thankful to them for saving me from Kraft dinners and for instead allowing me to develop a taste for some of the better local wines.

I also would like to thank Lufthansa for having something other than chicken and beef on the menu and for usually giving me an aisle seat; Jake's in Pasadena for serving food after midnight and having decently sized beers; and a certain Esso station in Hamburg-Bahrenfeld for being a source of food outside of the restrictive German opening hours.

Meinen Eltern danke ich für Ihre langjähringe Unterstützung. Die Sicherheit aus einer stabilen Familie zu kommen, hat mir die Energie gegeben, ohne die ich es nicht bis hierher geschafft hätte. Als Ihr mich vor 25 Jahren zum ersten Schultag gebracht habt, habt Ihr bestimmt nicht geglaubt, daß es ganz so lange dauern würde. Aber jetzt ist Euer Ältester ja endlich fertig mit der Schule.

Marianne, thank you for your patience, love and support, especially during the time of writing this thesis. First I was gone again and again and then I was here, but I really was not. I am also in your debt (and so is anybody who is reading this) for proof reading this thesis and for bringing my English into a better and much more readable form, sometimes against my will. It is not easy to correct my mistakes, especially when I like them.

I am very much looking forward to our life together. Wenn man einen Freund hat, der ein Floß bauen kann, dann braucht man sich vor nichts zu fürchten.

Contents

List of Tables

List of Figures

Chapter 1

Introduction

The fundamental structure of the world in which we live has always been the object of much scientific curiosity. Our understanding of the structure of atoms, atomic nuclei and nucleons has improved step by step over the course of this century. Most of the experimental evidence has been provided by scattering experiments, from the discovery of the atomic nucleus by Geiger, Marsden and Rutherford in 1909[1] up to the recent discovery of the top quark in 1995[2, 3]. This has led to the present understanding of the basic structure of matter as expressed in the Standard Model of particle physics, in which six quarks and six leptons are the fundamental building blocks of matter. In this model the nucleon (proton or neutron) is comprised of three quarks whose interactions are described by quantum chromodynamics (QCD).

The resolution in scattering experiments increases with higher momentum transfer Q^2. Together with the possibility to produce particles with higher mass the increased resolution has driven the trend in particle physics towards higher and higher energies. The energies of today's high energy colliders, such as HERA, are seven orders of magnitude higher (in the target rest frame) than in Rutherford's experiment. A complementary route to the increase in energy is the addition of spin degrees of freedom by using polarised beams and polarised targets. This approach offers insights into the complexity of the interactions between the constituents of the nucleon and provides possibilities to test the validity of QCD. The significance of the spin physics approach to nucleon structure is best expressed by citing R.Feynman's opinion about one of the most important theoretical predictions of high energy spin physics, the Bjorken sum rule: " It's verification, or failure, would have a most decisive effect on the direction of future high-energy theoretical physics"[4].

The first experiments on spin dependent deep inelastic scattering (DIS) were carried out at SLAC in the seventies[5] by the collaborations E80[6] and E130[7] with a polarised electron beam and a polarised butanol target. Further studies were done at CERN by the European Muon Collaboration (EMC) which utilised a polarised muon beam and a polarised ammonia target. The measurement of the spin dependent proton structure function g_1^p and its integral Γ_1^p by the EMC experiment in 1988 yielded the result that in the framework of the quark parton model only $12\% \pm 17\%$ of the proton spin is carried by its constituent quarks. This so called 'spin crisis' led to a wave of new experimental proposals, such as E142[8] and E143[9] at SLAC, the SMC experiment[11] at CERN, and the HERMES experiment[12] at DESY.

The HERMES experiment was approved in the fall of 1992 after high polarisation values had been achieved in the HERA electron storage ring[13]. It utilises the polarised HERA beam together with a polarised internal gas target of hydrogen, deuterium or ^{3}He and a forward spectrometer with large acceptance. HERMES is a collaboration of more than 200 physicists from 10 countries. The Canadian HERMES group (Simon Fraser University, TRIUMF, University of Alberta) is one of the original members of the collaboration and comprises almost 10% of the physicists in the experiment, one of the larger groups within HERMES.

The main contribution of the Canadian group to the apparatus of the experiment is the HERMES transition radiation detector (TRD) for positron/hadron separation. With an active area of 2×2.4 m^2 it is one of the largest transition radiation detectors in existence today and with a pion rejection factor of about 1400 it is also among the best performing TRDs. The TRD is part of the overall HERMES particle identification (PID) system which consists of the TRD, a Čerenkov counter, a preshower detector and a calorimeter. The combination of these four detectors allows the identification of positrons from deep inelastic scattering (DIS) reactions with an efficiency of 99% and a remaining hadron contamination of less than 0.5 %.

The first HERMES data were taken in 1995 with a polarised ^{3}He target which can be considered as an effective polarised neutron target, since 86% of the ^{3}He spin is carried by the neutron[14]. The two protons, predominantly in an S-state, have their spins anti-parallel due to the Pauli principle and there are only small admixtures from the D and S' states in the ground state. The beauty of the experiment lies in the fact that it uses the knowledge about one three body system (^{3}He) to investigate another, similar system (the nucleon). While the ^{3}He nucleus consists of two protons and one neutron, the neutron consists of two d quarks and one u quark. However, the neutron structure is significantly different from the ^{3}He structure and this is exactly the subject of the investigation.

The first physics analysis result from the 1995 HERMES data is the measurement of the spin structure function g_1 of the neutron. It has recently been submitted for publication[15] in Physics Letters. The value of the resulting integral Γ_1^n confirms previous experiments[8] at SLAC and can be compared to the theoretical value of the Ellis-Jaffe sum rule which it violates by about one sigma.

This thesis will, after a review of the relevant theory and an overview of the HERMES experiment, focus on three topics: The HERMES TRD, the HERMES particle identification (PID) and the measurement of the spin structure function g_1^n of the neutron.

Chapter 2 starts with a review of the theory of unpolarised and polarised deep inelastic scattering and then discusses several models of the nucleon spin. The quark parton model including QCD corrections is treated in some detail, as it will be used to interpret some of the results.

Chapter 3 describes the experimental apparatus of the HERMES experiment, from the polarised positron beam to the polarised internal target and the components of the spectrometer.

The HERMES TRD will be described in detail in chapter 4. This includes the theory of transition radiation, the details of the design and construction of the TRD and the TRD performance, also in comparison to similar TRDs in other experiments.

The HERMES particle identification is the subject of chapter 5. PID quantities that can be derived from a probability analysis of the detector responses are introduced. The calculation of efficiencies, contaminations and rejection factors from the experimental data is described using a simple model and first order corrections to these values are calculated. The interplay of the four PID detectors is examined in detail. The PID scheme used for the physics analysis is examined and positron efficiencies and hadron contaminations for the g_1^n measurement are derived.

The extraction of the spin structure function g_1^n is the topic of chapter 6, which starts with a description of the HERMES analysis software. The data quality, especially the quality of the TRD and the Čerenkov data is discussed next, followed by the extraction of the asymmetries $A_{||}^{^3\mathrm{He}}$ and A_1^n, and finally g_1^n. Systematic studies concerning the time dependence of $A_{||}^{^3\mathrm{He}}$ and the influence of the PID on the physics result follow. The first moment Γ_1^n of the spin structure function is evaluated and compared to the prediction of the Ellis-Jaffe sum rule. Finally the contribution of the quarks to the spin of the neutron is calculated in the framework of the quark parton model.

Chapter 2

Deep Inelastic Scattering and Nucleon Structure

2.1 Deep Inelastic Scattering

The term 'deep inelastic scattering' (DIS) refers to lepton-hadron scattering reactions that can be considered as elastic scattering off the pointlike constituents of the hadron, probing a small space-time region. Depending on the type of measurement, they are classified as inclusive reactions, where only the scattered lepton is detected or semi-inclusive reactions, where the hadron fragments are examined as well. Typically the probing lepton is an electron, positron, muon or neutrino and the target hadron is a nucleon.

2.1.1 Basic Formalism

The lowest order contribution to the deep inelastic scattering cross section is the exchange of a single virtual photon. While at higher energies contributions such as

Z^0 exchange become important, at HERMES energies (27.5 GeV positron beam) a description in the one photon approximation is sufficient. The Feynman diagram for one photon exchange is shown in figure 2.1.

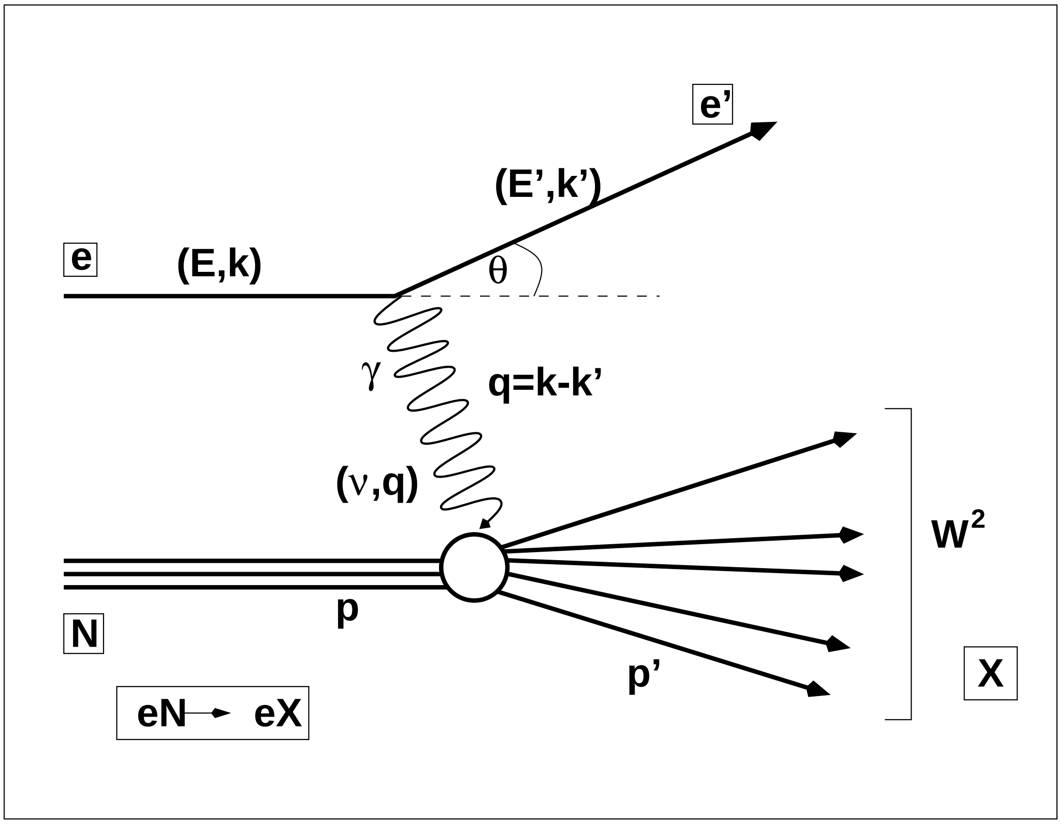

Figure 2.1: Feynman diagram for DIS in the one photon exchange approximation.

The kinematics of the scattering process are described by the 4-momenta of the incoming lepton (k), the scattered lepton (k'), the target nucleon (p) and the hadronic final state (p'). The set of kinematic variables conventionally used in the description of deep inelastic scattering is listed in table 2.1 below. The z-axis is assumed to be in the direction of the lepton beam. In the next few sections the basics of deep inelastic scattering and nucleon structure will be reviewed, following books by F.Halzen, A.D.Martin[16], W.Greiner, A.Schäfer[17] and R.G.Roberts[18] as well as review papers by M.Anselmino et al.[19], R.Jaffe[20] and A.V.Manohar[22].

Variable	**Definition**
M	The mass of the target hadron, usually the proton mass.
E	The energy of the incident lepton.
E'	The energy of the scattered lepton.
k	The 4-momentum of the incoming lepton. $k \overset{\text{lab}}{=} (E, 0, 0, E)$ in the laboratory frame if the lepton mass m is neglected.
k'	The 4-momentum of the scattered lepton. $k' \overset{\text{lab}}{=} (E', E' \sin\theta \cos\phi, E' \sin\theta \sin\phi, E' \cos\theta)$
p	The 4-momentum of the target. $p \overset{\text{lab}}{=} (M, 0, 0, 0)$ for a fixed target experiment.
q	The 4-momentum of the virtual photon. $q = k - k'$
ν	The energy of the virtual photon. $\nu = E - E'$
Q^2	The momentum transfer. $Q^2 = -q^2 \overset{\text{lab}}{=} 4EE' \sin^2 \frac{\theta}{2}$
W^2	The invariant mass of the final hadronic system. $W^2 = p'^2 = (p + q)^2 \overset{\text{lab}}{=} M^2 + 2M\nu - Q^2$

Table 2.1: Kinematic variables conventionally used in DIS

Assuming symmetry in the azimuthal scattering angle ϕ, only two variables are necessary to determine the kinematics of the scattering process: the scattering angle θ and the energy of the scattered lepton E'. Other possible sets of variables include ν and Q^2 and the dimensionless scaling variables x and y. An important combination is also Q^2 and x which are both Lorentz-invariant. The dimensionless variables x and y are defined as:

$$x = \frac{Q^2}{2p \cdot q} \overset{\text{lab}}{=} \frac{Q^2}{2M\nu} \qquad y = \frac{p \cdot q}{p \cdot k} \overset{\text{lab}}{=} \frac{\nu}{E} \tag{2.1}$$

The allowed range for these variables is $0 < x, y < 1$. The scaling variable x was first introduced by Bjorken and is for this reason also referred to as 'x-Bjorken' x_{Bj}. It is especially convenient in the description of DIS processes. In fact, deep inelastic scattering is often defined as scattering in the limit of $Q^2, \nu \to \infty$ for fixed x. The two variables x and Q^2 also have an intuitive interpretation. In the Breit (or infinite momentum) frame x represents the fraction of the nucleon momentum carried by the struck quark. The momentum transfer Q^2 can be related to the resolution that can be achieved via the wavelength of the virtual photon. This wavelength λ can be expressed in terms of x and Q^2 and is proportional to $1/Q$ for fixed x:

$$\lambda = \frac{\hbar}{|\vec{q}|} = \frac{\hbar}{\sqrt{\nu^2 + Q^2}} \propto \frac{1}{Q} \tag{2.2}$$

An increase in Q^2 therefore leads to an improved resolution for fixed x, which allows an investigation of the substructure of nucleons at a smaller scale.

The squared amplitude of deep inelastic scattering can be separated into a leptonic tensor $\mathcal{L}_{\mu\nu}$ and a hadronic tensor $\mathcal{W}^{\mu\nu}$ (see figure 2.2). The cross section σ then can be expressed as

$$\frac{d^2\sigma}{d\Omega\; dE'} = \frac{\alpha^2}{2MQ^4}\frac{E'}{E}\,\mathcal{L}_{\mu\nu}\mathcal{W}^{\mu\nu} \tag{2.3}$$

with α the fine structure constant and $d\Omega$ the solid angle.

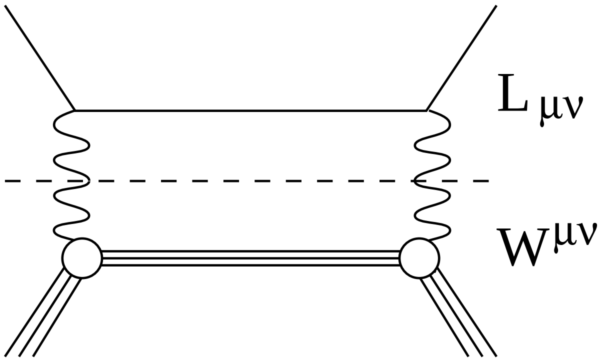

Figure 2.2: Separation of the cross section in $\mathcal{L}_{\mu\nu}$ and $\mathcal{W}^{\mu\nu}$

The leptonic tensor $\mathcal{L}_{\mu\nu}$ is given as

$$\mathcal{L}_{\mu\nu}(k, s_l; k', s_l') = [\bar{u}(k', s_l')\gamma_\mu u(k, s_l)]^*[\bar{u}(k', s_l')\gamma_\nu u(k, s_l)] \tag{2.4}$$

where $u, \bar{u}$ are the quark wave functions and s_l, s_l' are the covariant spin 4-vectors of the lepton.

The leptonic tensor can be split into symmetric (S) and antisymmetric (A) parts:

$$\begin{aligned}\mathcal{L}_{\mu\nu}(k,s_l;k',s_l') &= \mathcal{L}^S_{\mu\nu}(k;k') + i\mathcal{L}^A_{\mu\nu}(k,s_l;k') \\ &\quad + \mathcal{L'}^S_{\mu\nu}(k,s_l;k',s_l') + i\mathcal{L'}^A_{\mu\nu}(k;k',s_l')\end{aligned} \tag{2.5}$$

On summing over the final state spin s' and averaging over the initial spin s the unpolarised leptonic tensor is obtained

$$\begin{aligned}\mathcal{L}_{\mu\nu} &= 2\mathcal{L}^S_{\mu\nu} \\ &= 2[k_\mu k'_\nu + k'_\mu k_\nu - g_{\mu\nu}(k\cdot k' - m^2)],\end{aligned} \tag{2.6}$$

while on summing over s' alone the relevant expression for polarised DIS experiments is obtained

$$\begin{aligned}\mathcal{L}_{\mu\nu} &= 2\mathcal{L}^S_{\mu\nu} + 2i\mathcal{L}^A_{\mu\nu} \\ &= 2[k_\mu k'_\nu + k'_\mu k_\nu - g_{\mu\nu}(k\cdot k' - m^2) - i\varepsilon_{\mu\nu\alpha\beta}s_l^\alpha q^\beta] \\ &\approx 2[k_\mu k'_\nu + k'_\mu k_\nu - g_{\mu\nu}k\cdot k' - i\varepsilon_{\mu\nu\alpha\beta}s_l^\alpha q^\beta]\end{aligned} \tag{2.7}$$

if the lepton mass is neglected.

The hadronic tensor $\mathcal{W}^{\mu\nu}$ cannot be calculated rigorously like $\mathcal{L}^{\mu\nu}$, because the nucleon is not a pointlike particle. However, it can be parametrised by writing $\mathcal{W}^{\mu\nu}$ in terms of the hadron momentum p, the hadron spin s_h and the virtual photon momentum q. Upon imposing parity conservation, translation and time reversal invariance, hermiticity and current conservation just, four terms remain:

$$\begin{aligned}\mathcal{W}^{\mu\nu} = \mathbf{F}_1\left(-g_{\mu\nu} + \frac{q_\mu q_\nu}{p\cdot q}\right) + \frac{\mathbf{F}_2}{p\cdot q}\left(p_\mu - \frac{p\cdot q\; q_\mu}{q^2}\right)\left(p_\nu - \frac{p\cdot q\; q_\nu}{q^2}\right) \\ + \frac{i\mathbf{g}_1}{p\cdot q}\varepsilon_{\mu\nu\lambda\sigma}q^\lambda s_h^\sigma + \frac{i\mathbf{g}_2}{(p\cdot q)^2}\varepsilon_{\mu\nu\lambda\sigma}q^\lambda(p\cdot q s_h^\sigma - s_h\cdot q p^\sigma)\end{aligned} \tag{2.8}$$

The coefficients F_1, F_2, g_1, g_2 are known as structure functions and in general are a function of x and Q^2. Sometimes the structure functions W_1, W_2, G_1, G_2 are used instead, where

$$MW_1 = F_1 \qquad \nu W_2 = F_2 \tag{2.9}$$

$$M^2\nu G_1 = g_1 \qquad M\nu^2 G_2 = g_2. \tag{2.10}$$

While these have the advantage that the connection to elastic cross sections can be made more easily, F_1, F_2, g_1, g_2 have the advantage to 'scale' approximately in the DIS regime. In other words, they change only very slowly with Q^2 at fixed x since they are to leading order only functions of x:

$$F_{1,2}(x, Q^2) \approx F_{1,2}(x) \tag{2.11}$$

$$g_{1,2}(x, Q^2) \approx g_{1,2}(x) \tag{2.12}$$

$$\tag{2.13}$$

2.1.2 Unpolarised Structure Functions

The leptonic and hadronic tensors can be contracted explicitly to obtain the scattering cross section. For the case of unpolarised scattering the cross section may be obtained from equations (2.6) and (2.8) as follows:

$$\frac{d^2\sigma}{dx dQ^2} = \frac{4\pi\alpha^2}{Q^4}\left[\mathbf{F_1}(x, Q^2) \cdot y^2 + \frac{\mathbf{F_2}(x, Q^2)}{x}\left(1 - y - \frac{Mxy}{2E}\right)\right] \tag{2.14}$$

The structure functions F_1 and F_2 now contain all information about the (unpolarised) structure of the hadron that is revealed in deep inelastic scattering. An approximate relationship known as the Callan-Gross relation is observed between the two unpolarised structure functions as a result of the quarks having spin $\frac{1}{2}$:

$$F_2(x) \approx 2xF_1(x) \tag{2.15}$$

Alternately the cross section can be expressed in terms of the absorption cross sections for longitudinally (σ_L) and transversely (σ_T) polarised virtual photons[16].

$$\frac{d^2\sigma}{dx dQ^2} = \Gamma(\sigma_T + \varepsilon\sigma_L) \tag{2.16}$$

where Γ is the virtual photon flux and ε is the degree of longitudinal polarisation of the virtual photon:

$$\varepsilon = \frac{1 - y}{1 - y + \frac{y^2}{2}} \tag{2.17}$$

with y as defined in equation (2.1).

The ratio of the longitudinal and transverse cross sections R is related to the structure functions by

$$R(x,Q^2) = \frac{\sigma_L}{\sigma_T} = (1+\gamma^2)\frac{F_2(x,Q^2)}{2xF_1(x,Q^2)} - 1 \tag{2.18}$$

where γ^2 is the small kinematic factor:

$$\gamma^2 = \frac{4x^2M^2}{Q^2} \tag{2.19}$$

For the case of negligible γ^2 and R equation (2.18) reduces to the Callan-Gross relation (2.15).

2.1.3 Polarised Structure Functions

It follows from the structure of $\mathcal{L}^{\mu\nu}$ and $\mathcal{W}^{\mu\nu}$ that no spin dependent effects survive if the beam is unpolarised. The spin dependent cross section can best be defined as the difference between the cross sections for right- and left-handed incident leptons[20]:

$$\begin{aligned}\frac{d^3\Delta\sigma(\alpha)}{dx\ dy\ d\phi} &= \frac{d^3(\sigma(\alpha)-\sigma(\pi+\alpha))}{dx\ dy\ d\phi}\\ &= \frac{e^4}{4\pi^2Q^2}\left[\cos\alpha\left(\left[1-\frac{y}{2}-\frac{y^2}{4}\gamma^2\right]\mathbf{g_1}(x,Q^2)-\frac{y}{2}\gamma^2\mathbf{g_2}(x,Q^2)\right)\right.\\ &\qquad\left.-\sin\alpha\cos\phi\sqrt{\gamma^2\left[1-y-\frac{y^2}{4}\gamma^2\right]}\left(\frac{y}{2}\mathbf{g_1}(x,Q^2)+\mathbf{g_2}(x,Q^2)\right)\right]\end{aligned} \tag{2.20}$$

where γ^2 is defined in equation (2.19), α is the polar angle of the target polarisation with respect to the beam direction and ϕ is the azimuthal angle between the plane defined by k and s_h and the scattering plane defined by k and k' (see figure 2.3). It follows from equation (2.20) that all effects associated with the structure function $g_2(x,Q^2)$ are suppressed by a factor of at least $\gamma = 2Mx/\sqrt{Q^2}$. This means that g_2 effects are 'higher twist' effects, i.e. suppressed by a power of Q relative to the leading terms involving g_1. However, at $\alpha = 90°$ (for a transversely polarised target) the coefficient of the dominant term vanishes and the combination

$$\frac{y}{2}\mathbf{g_1} + \mathbf{g_2} \tag{2.21}$$

can be extracted.

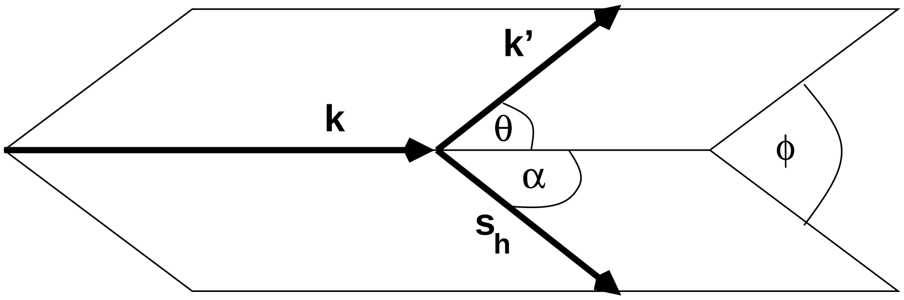

Figure 2.3: Schematics of the scattering planes and angles

Experimentally the spin structure functions $g_1(x)$ and $g_2(x)$ can be determined from asymmetry measurements on longitudinally ($\alpha = 0°, 180°$) and transversely ($\alpha = 90°, 270°$) polarised targets. The measured quantities are the asymmetries $A_{||}$ and $A_\perp$

$$A_{||} = \frac{\sigma^{\uparrow\downarrow} - \sigma^{\uparrow\uparrow}}{\sigma^{\uparrow\downarrow} + \sigma^{\uparrow\uparrow}} \qquad A_\perp = \frac{\sigma^{\uparrow\rightarrow} - \sigma^{\uparrow\leftarrow}}{\sigma^{\uparrow\rightarrow} + \sigma^{\uparrow\leftarrow}} \tag{2.22}$$

where $\sigma^{\uparrow\downarrow}, \sigma^{\uparrow\uparrow}$ are the cross sections for longitudinally polarised targets, while $\sigma^{\uparrow\rightarrow}, \sigma^{\uparrow\leftarrow}$ are the cross sections for transversely polarised targets.

These asymmetries can be related to the virtual photon asymmetries A_1 and A_2[19]:

$$\begin{aligned} A_{||} &= D(A_1 + \eta A_2) \\ A_\perp &= d(A_2 - \xi A_1) \end{aligned} \tag{2.23}$$

where

$$A_1 = \frac{\sigma_{\frac{1}{2}} - \sigma_{\frac{3}{2}}}{\sigma_{\frac{1}{2}} + \sigma_{\frac{3}{2}}} = \frac{g_1 - \gamma^2 g_2}{F_1} \tag{2.24}$$

$$A_2 = \frac{\sigma^{TL}}{\sigma^T} = \frac{\gamma(g_1 + g_2)}{F_1} \tag{2.25}$$

and the kinematic factors D, d, η, ξ are defined as:

$$\begin{aligned} D &= \frac{y(2-y)}{y^2 + 2(1-y)(1+R)} \\ \eta &= \frac{2y(1-y)}{2-y} \\ d &= D\,\sqrt{\frac{2\varepsilon}{1+\varepsilon}} \\ \xi &= \eta\,\frac{1+\varepsilon}{2\varepsilon} \end{aligned} \tag{2.26}$$

with ε defined by equation (2.17) and R by equation (2.18). D and d can be regarded as depolarisation factors of the virtual photon.

The virtual photon absorption cross sections $\sigma_{\frac{1}{2}}$ and $\sigma_{\frac{3}{2}}$ refer to the total angular momentum of the photon-nucleon system along the incident photon direction.

The extraction of g_1 from $A_{||}$ now proceeds through a series of approximations. There exists a positivity limit on A_2[23]:

$$|A_2| \leq \sqrt{R} \tag{2.27}$$

and A_2 has recently been measured to be consistent with zero[24]. The parameter η is small as well, which makes it reasonable to write

$$A_1 \approx \frac{A_{||}}{D} \tag{2.28}$$

The next approximation is to neglect the g_2 term in equation (2.24), where it is suppressed by a factor of γ^2:

$$g_1 \approx A_1 F_1. \tag{2.29}$$

$F_1(x)$ is then replaced by

$$F_1(x) \approx \frac{F_2(x)}{2x[1+R(x)]} \tag{2.30}$$

which is obtained from equation (2.18) for $4M^2x^2 \ll Q^2$. In combining these approximations the following is found:

$$g_1(x) \approx \frac{A_{||}}{D}\,\frac{F_2(x)}{2x[1+R(x)]} \tag{2.31}$$

This equation is a very good approximation for the case of a fully polarised target and a pure and perfectly polarised beam. In reality all these conditions are not strictly satisfied and this must be taken into account in the extraction of g_1^n. Additionally nuclear and radiative corrections have to be made as well. These are described in sections 6.4.1 and 6.4.2.

2.1.4 Sum Rules

Preceding the development of QCD J.Bjorken derived the 'Bjorken sum rule' as an application of $U(6)\otimes U(6)$ current algebra[25]. This a priori rather obscure relationship between spin dependent deep inelastic scattering and neutron beta decay has become the focal point of high energy spin physics. The Bjorken sum rule assumes only isospin symmetry and therefore tests QCD at a very fundamental level. In its elementary form the Bjorken sum rule reads:

$$\int_o^1 g_1^p(x)\ dx - \int_0^1 g_1^n(x)\ dx = \Gamma_1^p - \Gamma_1^n = \frac{1}{6}\,\frac{g_A}{g_V} = \frac{1}{6}(F+D) \tag{2.32}$$

where g_A, g_V are the axial and vector coupling constants measured in neutron beta decay[26] and F, D are the $\mathrm{SU(3)_F}$ weak coupling constants found in baryon decay[27]. QCD corrections to the Bjorken sum rule at finite Q^2 have been calculated[28], and on including these the sum rule becomes

$$\Gamma_1^p - \Gamma_1^n = \frac{1}{6}\,\frac{g_A}{g_V}\cdot C_1 \tag{2.33}$$

with the QCD correction C_1 for three quark flavours ($n_f = 3$):

$$C_1 = \left[1 - \frac{\alpha_s}{\pi} - \frac{43}{12}\frac{\alpha_s^2}{\pi^2} - 20.215\frac{\alpha_s^3}{\pi^3} - \mathcal{O}(130)\frac{\alpha_s^4}{\pi^4}\right] \tag{2.34}$$

It follows from equation (2.33) that the running coupling constant of QCD, α_s, can be extracted from a measurement of the Bjorken sum rule. Indeed this has been done[28] and it yields a result that is competitive with other measurements of α_s.

In time for the first polarised DIS experiments at SLAC, in 1974 J.Ellis and R.Jaffe derived separate sum rules for proton and neutron under the additional assumptions of exact SU(3) flavour symmetry and no polarisation of the sea quarks[33]. These assumptions implicitly mean that the contribution of the s-quarks in the sea (often referred to as the 'strange sea') is zero:

$$\Delta s \overset{!}{=} 0. \tag{2.35}$$

The Ellis-Jaffe sum rules under these assumptions read:

$$\Gamma_1^p = \int g_1^p(x)\ dx\ = \frac{1}{18}\ (9\mathrm{F} - \mathrm{D}) = 0.185 \tag{2.36}$$

$$\Gamma_1^n = \int g_1^n(x)\ dx = \frac{1}{18}\ (6\mathrm{F} - 4\mathrm{D}) = -0.024 \tag{2.37}$$

for F = 0.459, D = 0.789[27].

Ellis and Jaffe themselves never expected their sum rules to be more than a reasonable approximation ("We do not expect the sum rules...to be exact..."[33]). All experimental evidence so far in fact suggests that the Ellis-Jaffe sum rules are violated and that the strange sea is polarised.

2.1.5 Semi-Inclusive Deep Inelastic Scattering

In a semi-inclusive measurement at least one hadron $h^{\pm}$ is detected and explicitly reconstructed in addition to the scattered lepton:

$$\mathrm{e} + \mathrm{N} \rightarrow \mathrm{e}' + \mathrm{h}^{\pm} + \mathrm{X} \tag{2.38}$$

where X is the remaining undetected hadronic final state. In this case an additional variable $z \in [0, 1]$ is introduced which is defined as the ratio of the hadron energy to the total energy transfer:

$$z = \frac{p \cdot p_h}{p \cdot q} \overset{\mathrm{lab}}{=} \frac{E_h}{\nu} \tag{2.39}$$

The importance of semi-inclusive reactions lies in the fact that they allow the valence and sea quark contributions to the nucleon spin to be isolated. This is the strength of the HERMES experiment. In the framework of the quark parton model (see section 2.2.1) semi-inclusive scattering can be understood as a two step process: the absorption of a virtual photon by a quark and the subsequent fragmentation of the struck quark into hadrons. The latter process is described by fragmentation functions $D_q^h(z)$ which give the probability that a quark with flavour q will produce a hadron of type h. The fragmentation functions are assumed to be independent of the way the quark was produced. In analogy to the scaling of the structure functions they also obey scaling laws depending only on the momentum fraction z carried by the hadron. The fragmentation functions are subject to momentum and probability conservation:

$$\begin{aligned} \sum_h \int_0^1 z D_q^h(z)\ dz &= 1 \\ \sum_q \int_{z_{min}}^1 D_q^h(z)\ dz &= n_h \end{aligned} \tag{2.40}$$

where z_{min} is the threshold energy for producing a hadron of mass m_h and n_h is the average multiplicity of hadrons of type h.

The differential cross section $d\sigma_h$ for hadron production can be written in the quark parton model formalism as

$$\frac{1}{\sigma_{tot}(x,Q^2)} \frac{d\sigma_h(x,Q^2)}{dz} = \frac{\sum_i e_i^2 q_i(x,Q^2) D_i^h(z)}{\sum_i e_i^2 q_i(x,Q^2)} \tag{2.41}$$

where σ_{tot} is the total (inclusive) cross section, e_i is the charge of the quark i and $q_i(x,Q^2)$ is the distribution of quarks with flavour i in the nucleon.

The fragmentation functions are characterised as favoured or unfavoured fragmentation functions, depending on whether the struck quark is fragmenting into a hadron that contains the quark type as valence quark (favoured) or not (unfavoured). Due to its higher mass the strange quark is treated separately. In the case of charged pion production, all $D_q^{\pi\pm}$ can be related to only three fragmentation functions:

$$\begin{aligned} D_1(z) &= D_u^{\pi^+}(z) = D_d^{\pi^-}(z) = D_{\bar{d}}^{\pi^+}(z) = D_{\bar{u}}^{\pi^-}(z) \\ D_2(z) &= D_d^{\pi^+}(z) = D_u^{\pi^-}(z) = D_{\bar{u}}^{\pi^+}(z) = D_{\bar{d}}^{\pi^-}(z) \\ D_3(z) &= D_s^{\pi^+}(z) = D_s^{\pi^-}(z) = D_{\bar{s}}^{\pi^+}(z) = D_{\bar{s}}^{\pi^-}(z) \end{aligned} \tag{2.42}$$

In fact the unfavoured fragmentation function $D_2(z)$ can be described by the same parametrisation as $D_1(z)$ with a suppression factor η:

$$D_2(z) = \frac{1}{\eta} D_1(z) = \frac{1-z}{1+z}\, D_1(z) \tag{2.43}$$

An example for the interpretation of a semi-inclusive measurement in the framework of the quark parton model is given in section 2.2.1.

Due to the large acceptance of the HERMES spectrometer and its excellent particle identification, semi-inclusive measurements provide unique possibilities to the HERMES experiment. Many of the results in this thesis concerning the TRD, the particle identification and the 1995 data quality also apply to semi-inclusive measurements. However, the physics analysis in this thesis will focus on the (inclusive) measurement of g_1^n.

2.2 Models of the Nucleon Spin

Since the EMC measurement that caused the 'spin crisis' hundreds of theoretical papers about the spin structure of the nucleon have been published. While this has led to a much better understanding of the problem, reducing the 'crisis' to a mere 'puzzle', none of these models is entirely convincing yet. In the words of R.Jaffe[21]: "Theorists have not yet come up with a "gee whiz" solution, i.e. there is no simple and elegant explanation that leaves conventional quark model phenomenology intact and explains the small value of $\Delta\Sigma$ (the quark contribution to the nucleon spin)."

In general the spin of the nucleon can be separated into the contributions from valence quarks, sea quarks, gluons and orbital angular momenta from both gluons and quarks:

$$\langle S_z \rangle = \frac{1}{2} = \frac{1}{2}\, \Delta\Sigma + \Delta G + L_q + L_g \tag{2.44}$$

Here:

$$\begin{aligned}\Delta\Sigma &= \Delta V + \Delta S \\ &= \Delta u^v + \Delta d^v + \Delta u^s + \Delta d^s + \Delta s^s + \Delta\bar{u}^s + \Delta\bar{d}^s + \Delta\bar{s}^s\end{aligned} \tag{2.45}$$

is the quark contribution which in turn separates into the different flavours, as well as valence and sea contributions, ΔG is the gluon contribution and L_q, L_g are the contributions from quark and gluon orbital angular momenta respectively.

The experimental observation that $\Delta\Sigma$ is much smaller than 1 therefore means that gluons or orbital angular momenta have to account for part of the nucleon spin. In light of the knowledge that about half of the momentum of the nucleon is carried by gluons[29] this is not very surprising.

Due to the amount and complexity of the published work it is only possible in the framework of this thesis to give a short review of the main features of the quark parton model (QPM) and to point to some of the most important trends in nucleon spin models.

2.2.1 The Quark Parton Model

Structure Functions

The quark parton model (QPM) is a combination of the static quark model introduced by Gell-Mann and Zweig[30, 31] to explain the hadron mass spectrum and the parton model by Bjorken and Feynman[4, 32], introduced in conjunction with the electron scattering experiments at SLAC in the 1960s. The experimentally justified identification of partons with quarks leads to the quark parton model. In the infinite momentum frame the scaling variable x represents the fraction of the nucleon momentum carried by the struck quark. The quarks are for short times quasi-free and deep inelastic scattering off a nucleon can be treated as elastic scattering off a quark. The appeal of the QPM lies in the fact that it helps to visualise the mechanics of DIS processes and that it provides the possibility of quick approximate calculations. In the basic 'naive' quark parton model the interactions between the quarks are neglected, but it is possible to include these by means of QCD corrections, which leads to the QCD corrected QPM.

The meaning of the structure functions F_1, F_2, g_1, g_2 in the quark parton model is particularly transparent. With the notation that $q_i^{+(-)}(x)$ is the probability to find a quark with momentum fraction x and helicity parallel (anti-parallel) to the nucleon spin, the structure functions can be expressed as

$$\begin{aligned}\mathbf{F}_1(x) &= \tfrac{1}{2}\sum_i e_i^2\ (q_i^+(x) + q_i^-(x)) \\ \mathbf{F}_2(x) &= \sum_i e_i^2 x\ (q_i^+(x) + q_i^-(x)) \\ \mathbf{g}_1(x) &= \tfrac{1}{2}\sum_i e_i^2\ (q_i^+(x) - q_i^-(x)) \\ \mathbf{g}_2(x) &= 0 \end{aligned} \tag{2.46}$$

where the summation runs over all quark and anti-quark flavours i. The interpretation of the unpolarised structure functions in this picture is clear; they represent the sum of the x-distributions of the different quark flavours. For the assumption that the nucleon consists of two u quarks and one d quark that do not interact and hence each carry 1/3 of the nucleon momentum, F_2 is a δ-function at $x = \frac{1}{3}$. The introduction of interactions between the three quarks via gluons smears the momentum distribution into a broad peak with a maximum around $x = \frac{1}{3}$. The introduction of sea quarks leads to an additional contribution at small x and the resulting F_2 is a good qualitative description of the data (see figure 2.4).

The quark parton model also allows the visualisation of polarised deep inelastic scattering and the meaning of $g_1(x)$ (see figure 2.5). In analogy to $F_1(x)$, $g_1(x)$ describes the difference in the momentum distributions for quarks of helicity parallel or antiparallel to the nucleon spin. The virtual photon emitted by the lepton has spin 1 and can be absorbed only by a quark with opposite spin, due to helicity conservation. This means that the cross section $\sigma_{\frac{1}{2}}$ for nucleon spin opposite to the photon spin is a measure for the quark distribution with the same helicity as the nucleon $q^+(x)$ and the cross section $\sigma_{\frac{3}{2}}$ measures $q^-(x)$.

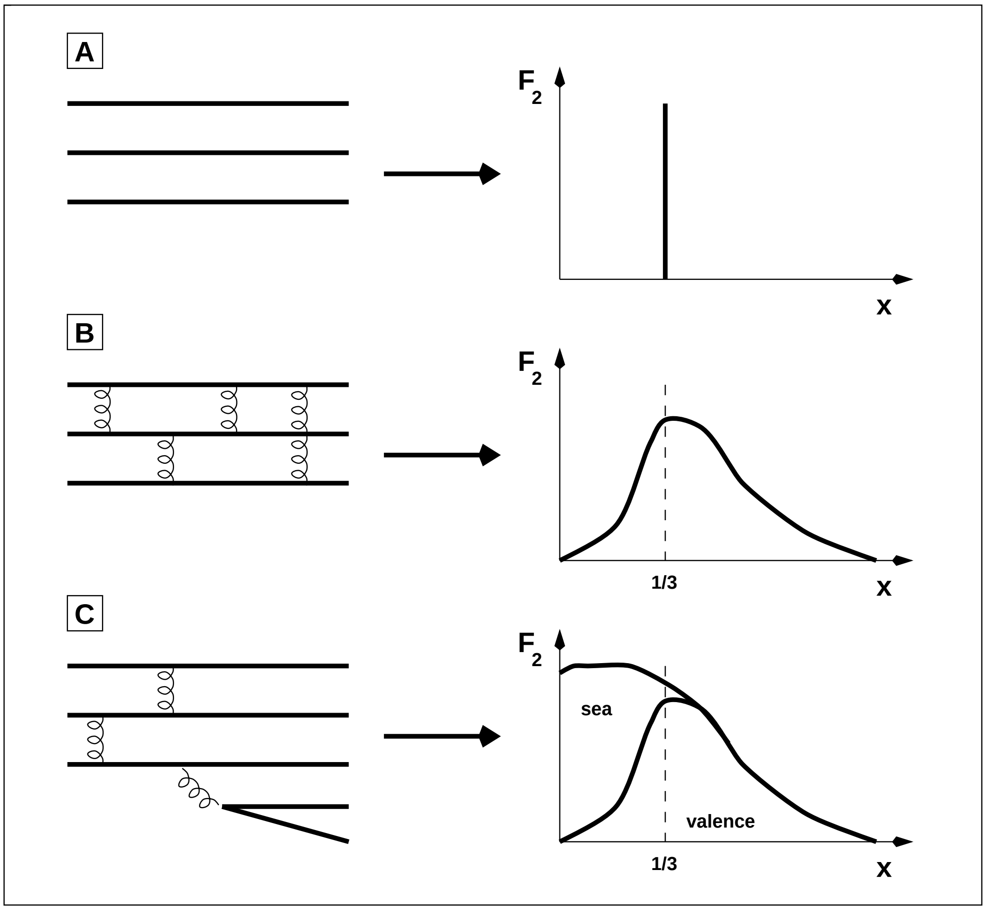

Figure 2.4: The structure function F_2 in the quark parton model for different assumptions: (A) the nucleon consists of three quarks without interactions, (B) interactions in the form of gluons are present, (C) small x contribution from sea quarks.

With A_1 as defined in equation (2.24), the structure functions as in equations (2.46) and the proportionalities

$$\begin{aligned} \sigma_{\frac{1}{2}} &\sim q^+(x) \\ \sigma_{\frac{3}{2}} &\sim q^-(x) \end{aligned} \tag{2.47}$$

A_1 may be written as

$$A_1(x) = \frac{g_1(x)}{F_1(x)} \tag{2.48}$$

which is just the approximation to equation (2.24) when g_2 is neglected. The structure function $g_2(x)$ is zero in the quark parton model and also has no straightforward interpretation.

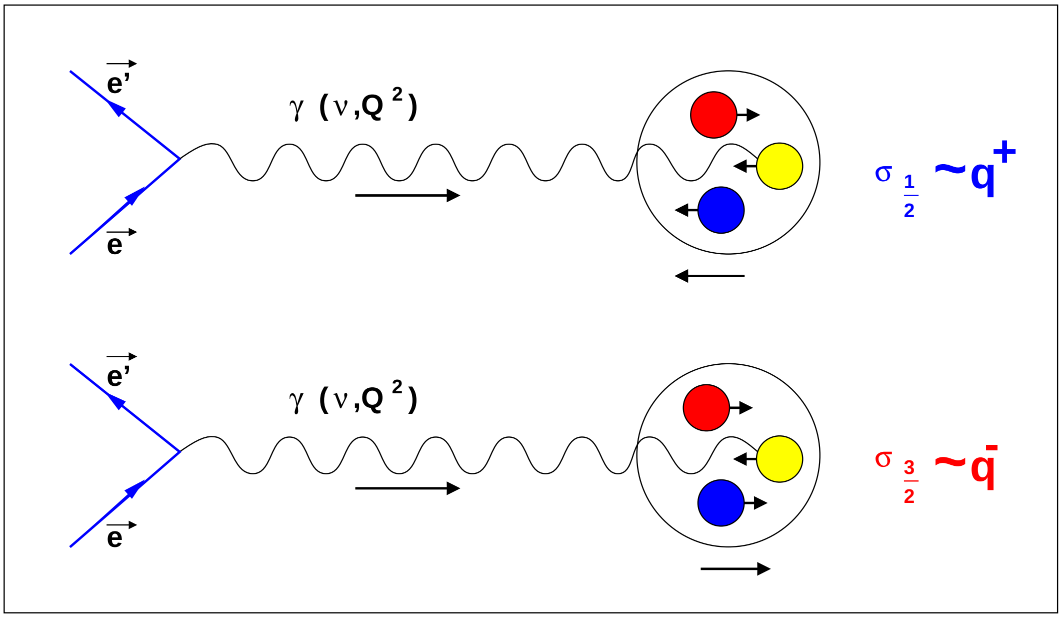

Figure 2.5: Polarised DIS in the quark parton model

Contribution of quarks to the nucleon spin

The quark contribution to the nucleon spin $\Delta\Sigma$ can be extracted in the context of the quark parton model either from a measurement of Γ_1^p or Γ_1^n, assuming that the Bjorken sum rule holds, or from a measurement of both of them. Four linear equations are necessary to derive the four unknown parameters $\Delta\Sigma$, Δu, Δd, Δs. Using the definition of Δq_i as

$$\Delta q_i = \int_0^1 \left(q_i^+(x) - q_i^-(x)\right)\, dx \tag{2.49}$$

and the form of $g_1(x)$ in the QPM (equation 2.46) the Ellis-Jaffe integrals can be written as

$$\begin{aligned}\Gamma_1^p &= \textstyle\int_0^1 g_1^p(x)\ dx = \frac{1}{18}(4\Delta u + \Delta d + \Delta s)\\ \Gamma_1^n &= \textstyle\int_0^1 g_1^n(x)\ dx = \frac{1}{18}(\Delta u + 4\Delta d + \Delta s)\end{aligned} \tag{2.50}$$

For example, a measurement of Γ_1^n yields the following four equations:

$$\begin{aligned} F + D &= \Delta u - \Delta d && \text{(Bjorken sum rule; neutron } \beta \text{ decay)}\\ 3F - D &= \Delta u + \Delta d - 2\Delta s && \text{(hyperon } \beta \text{ decay)}\\ 18\Gamma_1^n &= \Delta u + 4\Delta d + \Delta s && \text{(E-J integral for the neutron)}\\ \Delta\Sigma &= \Delta u + \Delta d + \Delta s && \text{(definition)}\end{aligned} \tag{2.51}$$

where F and D are $\mathrm{SU_F}(3)$ coupling constants measured in baryon decay. The first condition is obtained from the Bjorken sum rule, the second condition follows for SU(3) symmetry from Hyperon beta decay, the third one is just the Ellis-Jaffe integral and the last one the definition of $\Delta\Sigma$. These equations now allow in principle the extraction of the quark distributions Δq_i and the total quark spin $\Delta\Sigma$ from the measured values of F, D and Γ_1^n.

To include QCD corrections the Ellis-Jaffe integrals can be written as

$$\begin{aligned}\Gamma_1^p &= \left(\tfrac{1}{12}a_3 + \tfrac{1}{36}a_8\right) \cdot C_1 + \tfrac{1}{9}a_0 C_0\\ \Gamma_1^n &= \left(-\tfrac{1}{12}a_3 + \tfrac{1}{36}a_8\right) \cdot C_1 + \tfrac{1}{9}a_0 C_0\end{aligned} \tag{2.52}$$

where

$$\begin{aligned} a_3 &= F + D\\ a_8 &= 3F - D\\ a_0 &= \Delta\Sigma \end{aligned} \tag{2.53}$$

$$\tag{2.54}$$

$$\begin{aligned} C_1 &= \left[1 - \frac{\alpha_s}{\pi} - \frac{43}{12}\frac{\alpha_s^2}{\pi^2} - 20.215\frac{\alpha_s^3}{\pi^3} - \mathcal{O}(130)\frac{\alpha_s^4}{\pi^4}\right]\\ C_0 &= \left[1 - \frac{1}{3}\ \frac{\alpha_s}{\pi} - 0.549\ \frac{\alpha_s^2}{\pi^2} - \mathcal{O}(2)\ \frac{\alpha_s^3}{\pi^3}\right] \end{aligned} \tag{2.55}$$

The QCD correction factors are given in this case for three flavours ($n_f = 3$) which is appropriate for HERMES energies.

The QCD coupling constant α_s depends on Q^2 and can be parametrised as[34]:

$$\alpha_s(Q^2) = \frac{4\pi}{9\ln\left[\frac{Q^2}{\Lambda^2}\right]} \cdot \left[1 - \frac{64}{81}\,\frac{\ln\left[\ln\left[\frac{Q^2}{\Lambda^2}\right]\right]}{\ln\left[\frac{Q^2}{\Lambda^2}\right]} + \dots\right] \tag{2.56}$$

where Λ (~ 0.2 GeV) is the scale introduced by renormalisation. At the average Q^2 of HERMES (2.3 (GeV/c)^2) $\alpha_s(\langle Q^2\rangle) = 0.25$.

In combining equations (2.51) and (2.55) the QCD corrections can be included in the extraction of $\Delta\Sigma$ and Δq_i:

$$\begin{aligned}\Delta\Sigma(\Gamma_1^p) =& \frac{9}{C_0}\left[\Gamma_1^p - \left(\frac{F+D}{12} + \frac{3F-D}{36}\right)\cdot C_1\right]\\ \Delta\Sigma(\Gamma_1^n) =& \frac{9}{C_0}\left[\Gamma_1^n - \left(-\frac{F+D}{12} + \frac{3F-D}{36}\right)\cdot C_1\right]\end{aligned}$$

$$\begin{aligned}\Delta u =& \frac{\Delta\Sigma}{3} + \frac{3F-D}{6} + \frac{F+D}{2}\\ \Delta d =& \frac{\Delta\Sigma}{3} + \frac{3F-D}{6} - \frac{F+D}{2}\\ \Delta s =& \frac{\Delta\Sigma}{3} - \frac{3F-D}{3}\end{aligned} \tag{2.57}$$

Valence Quark Contribution

As an example of the interpretation in the framework of the quark parton model of a semi-inclusive measurement consider the pion asymmetry which is defined as

$$A^\pi(x) = \frac{N_{\uparrow\downarrow}^{\pi^+-\pi^-}(x) - N_{\uparrow\uparrow}^{\pi^+-\pi^-}(x)}{N_{\uparrow\downarrow}^{\pi^+-\pi^-}(x) + N_{\uparrow\uparrow}^{\pi^+-\pi^-}(x)} \tag{2.58}$$

where

$$\begin{aligned}N_{\uparrow\downarrow}^{\pi^+-\pi^-} &= N_{\uparrow\downarrow}^{\pi^+} - N_{\uparrow\downarrow}^{\pi^-}\\ N_{\uparrow\uparrow}^{\pi^+-\pi^-} &= N_{\uparrow\uparrow}^{\pi^+} - N_{\uparrow\uparrow}^{\pi^-}\end{aligned} \tag{2.59}$$

and $N^h_{\uparrow\uparrow}$, $N^h_{\uparrow\downarrow}$ are the numbers of hadrons produced in DIS in the case that the virtual photon spin and the target spin are parallel ($\uparrow\uparrow$) or antiparallel ($\uparrow\downarrow$). Writing the numerator and denominator of equation (2.58) explicitly in the QPM, it is evident that they depend on the polarised valence quark contributions $\Delta q^v = \Delta q - \Delta\bar{q}$, while all fragmentation functions cancel under certain assumptions. In the case of a hydrogen target $A^\pi_p(x)$ is given by

$$A^\pi_p(x) = \frac{4\Delta u^v(x) - \Delta d^v(x)}{4u^v(x) - d^v(x)} \tag{2.60}$$

If the results from two different targets (e.g. hydrogen $[A^\pi_p(x)]$ and deuterium $[A^\pi_d(x)]$), are combined, it is possible to obtain the polarised valence quark contributions $\Delta u^v(x)$ and $\Delta d^v(x)$

$$\begin{aligned}\Delta u^v(x) &= \frac{1}{5}\left[A^\pi_d(x)(u^v(x)+d^v(x)) + A^\pi_p(x)(4u^v(x)-d^v(x))\right]\\ \Delta d^v(x) &= \frac{1}{5}\left[4A^\pi_d(x)(u^v(x)+d^v(x)) - A^\pi_p(x)(4u^v(x)-d^v(x))\right]\end{aligned} \tag{2.61}$$

if the unpolarised valence quark contributions $u^v(x), d^v(x)$ are known.

A different combination of observables allows the sea quark contribution to be isolated. The determination of the valence and sea quark contributions to the nucleon spin from semi-inclusive processes is the next step in the investigation of the spin puzzle and is the strength of the HERMES experiment.

Conclusion

In the 'naive' quark parton model without QCD corrections the angular momentum sum (equation 2.44) becomes

$$\langle S_z\rangle = \frac{1}{2} = \frac{1}{2}\,\Delta\Sigma \tag{2.62}$$

whose measured violation[10] caused the 'spin crisis'. Despite all of its success the quark parton model does not explain the spin of the nucleon.

2.2.2 SU(6) Model

The magnetic moment of an elementary particle can be understood in the framework of quantum electrodynamics (QED) as resulting directly from its spin. In fact, the measurement and the theoretical prediction of the 'anomalous' magnetic moment of the electron is one of the most impressive agreements between QED and experimental data.

Without higher QED corrections the magnetic moment is

$$\mu = -\frac{e}{2m}\sigma = -g\frac{e}{2m}\mathbf{S} \tag{2.63}$$

where the gyromagnetic ratio is $g \approx 2$, and the spin operator is $\mathbf{S} = \frac{1}{2}\sigma$. In the simple quark model, where the nucleon consists of three valence quarks, SU(6) wave functions can be introduced as a product of flavour SU(3) and spin SU(2). These wave functions for the proton and the neutron can be written as[16]:

$$\begin{aligned} |p\uparrow\rangle = \sqrt{\frac{1}{18}}&[uud(2\uparrow\uparrow\downarrow - \uparrow\downarrow\uparrow - \downarrow\uparrow\uparrow) + udu(2\uparrow\downarrow\uparrow - \uparrow\uparrow\downarrow - \downarrow\uparrow\uparrow) \\ &+duu(2\downarrow\uparrow\uparrow - \uparrow\downarrow\uparrow - \uparrow\uparrow\downarrow)] \end{aligned} \tag{2.64}$$

$$\begin{aligned} |n\uparrow\rangle = \sqrt{\frac{1}{18}}&[ddu(2\uparrow\uparrow\downarrow - \uparrow\downarrow\uparrow - \downarrow\uparrow\uparrow) + dud(2\uparrow\downarrow\uparrow - \uparrow\uparrow\downarrow - \downarrow\uparrow\uparrow) \\ &+udd(2\downarrow\uparrow\uparrow - \uparrow\downarrow\uparrow - \uparrow\uparrow\downarrow)] \end{aligned} \tag{2.65}$$

From these wave functions the magnetic moments can be calculated using

$$\mu_p = \sum_{i=1}^{3}\langle p\uparrow|\mu_i(\sigma_3)_i|p\uparrow\rangle \tag{2.66}$$

with $\mu_i = e_i/2m_i$ and the nucleon magnetic moments are obtained in terms of the u- and d-quark magnetic moments:

$$\begin{aligned} \mu_p &= \frac{1}{3}(4\mu_u - \mu_d) \\ \mu_n &= \frac{1}{3}(4\mu_d - \mu_u) \end{aligned} \tag{2.67}$$

Since the magnetic moments of the quarks are not known experimentally, this model can only be tested by considering the ratio of the neutron and proton magnetic moments:

$$\frac{\mu_n}{\mu_p} = -\frac{2}{3}, \tag{2.68}$$

which is in good agreement with the measured value of $-0.68497945 \pm 0.00000058$[16].

The magnetic moments for other baryons can be calculated in the same manner. Using the measured magnetic moments of the proton, the neutron and the Λ as inputs to determine μ_u, μ_d and μ_s, numerical values can be extracted for all baryons that are in good agreement with the measured ones[35]. The comparison between the SU(6) quark model prediction and the measured values is shown in figure 2.6.

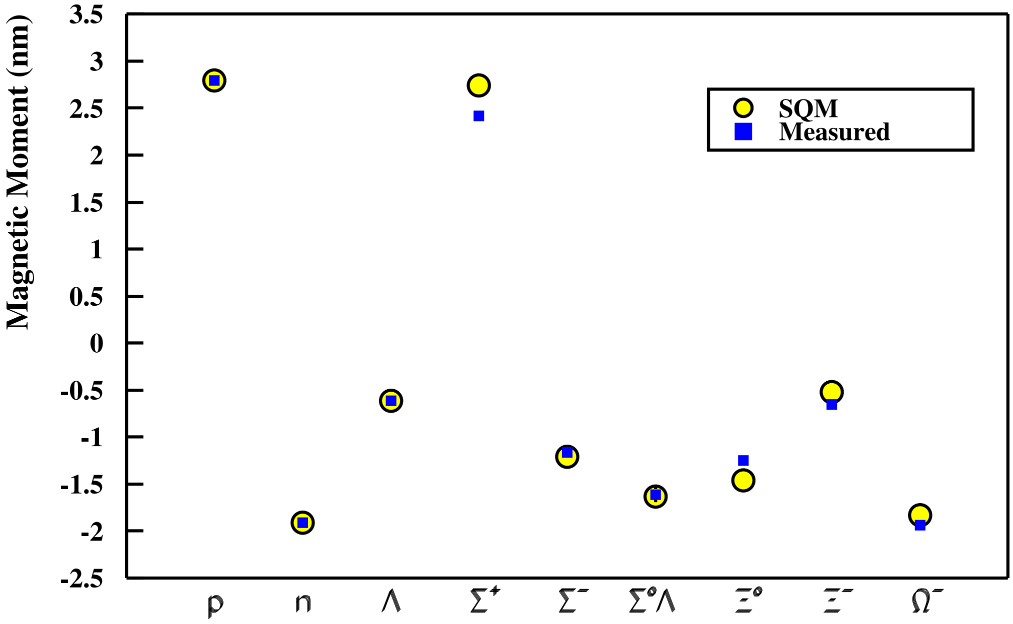

Figure 2.6: Comparison of the SU(6) prediction (circles) and the measured magnetic moments (squares)[35].

This implies that the spin structure of the nucleon at large distances, that is with lower resolution than in DIS experiments, is in fact largely given by the spin structure of the constituent quarks. The question 'Where does the spin of the nucleon come from ?' might be rephrased into 'Where does the spin of the constituent quarks come from?'. In this case the constituent quark has to be understood as a quasiparticle with nontrivial internal structure, i.e. consisting of a valence quark, many q$\bar{\text{q}}$ pairs and gluons[36].

2.2.3 The Axial Anomaly

An anomaly is said to occur in a quantum theory, when a symmetry of the classical Lagrangian is not a true symmetry of the full quantum theory. This is the case for the axial U(1) anomaly, also referred to as Adler-Bell-Jackiw anomaly[37, 38]. For massless quarks the QCD Lagrangian is invariant under the global U(1) axial transformations

$$\psi' \to \mathrm{e}^{-i\theta\gamma_5}\psi \tag{2.69}$$

which following Noether's theorem leads to the expectation that the axial current

$$J^f_{5\mu} = \bar{\psi}_f(x)\gamma_\mu\gamma_5\psi_f(x) \tag{2.70}$$

is conserved for quark operators of flavour f. However, explicit calculations show, that the current has an anomaly[19]:

$$\partial^\mu J^f_{5\mu} = \frac{\alpha_s}{4\pi} G^a_{\mu\nu}\widetilde{G}^{\mu\nu}_a \neq 0 \tag{2.71}$$

generated from coupling to the gluons.

The axial anomaly plays an important role in explaining the mass of the η' meson and in the $\pi^0 \to \gamma\gamma$ decay rate[39]. The Feynman diagram of the axial anomaly is shown in figure 2.7.

The axial anomaly links a possible polarised gluon contribution to the quark spin contribution measured in deep inelastic scattering. An alternative way to write Δq is

$$\widetilde{\Delta q} = \Delta q - \frac{\alpha_s}{2\pi}\Delta G \tag{2.72}$$

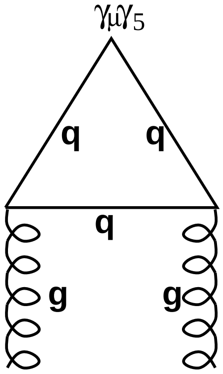

Figure 2.7: Feynman diagram of the U(1) axial anomaly

where the second term is derived from the gluon contribution ΔG to the nucleon spin. In this interpretation a_0 (see equation 2.54) becomes

$$a_0 = \widetilde{\Delta\Sigma} = \Delta\Sigma - 3\frac{\alpha_s}{2\pi}\Delta G \tag{2.73}$$

which implies that a small measured value of a_0 does not necessarily imply a small value of $\Delta\Sigma$ if ΔG is sufficiently large. The assumption that the strange sea is in fact unpolarised:

$$\widetilde{\Delta s} = \Delta s - \frac{\alpha_s}{2\pi}\Delta G \tag{2.74}$$

leads to a value of $\Delta G \approx 2$ for $\Delta s = 0$ at $Q^2 = 3$ $(\mathrm{GeV/c})^2$[40]. An equally large compensating term is found for the quark orbital angular momentum, so that the momentum sum rule (2.44) becomes[21]:

$$\langle S_z \rangle = \frac{1}{2} = \frac{1}{2}\left(\Delta\Sigma - 3\frac{\alpha_s}{2\pi}\Delta G\right) + \Delta G + \left(L_q + 3\frac{\alpha_s}{2\pi}\Delta G\right) + L_g \tag{2.75}$$

While this model offers an explanation for the small measured values of $\Delta\Sigma$ (actually, $\widetilde{\Delta\Sigma}$), a measurement of ΔG will be necessary to confirm this.

2.2.4 The Skyrme Model

While perturbative techniques usually expand QCD in powers of α_s, the theory can also be expanded in powers of $1/N_c$, where N_c is the number of colours. In the case of $N_c \to \infty$ a theory of non interacting mesons and glueballs is obtained and much of the simplicity of this theory seems to survive at $1/N_c = 1/3$[41].

Skyrme found that baryons can be incorporated into this scheme as nonperturbative static solutions, called solitons, that are characterised by a topological 'winding number' that can be identified with the baryon number B. The most famous such meson field configuration with non-vanishing topological quantum number is the Skyrme 'hedgehog', where the SU(2) isospin vector always has the same direction in isospin-space as $\overrightarrow{r}$ in coordinate space.

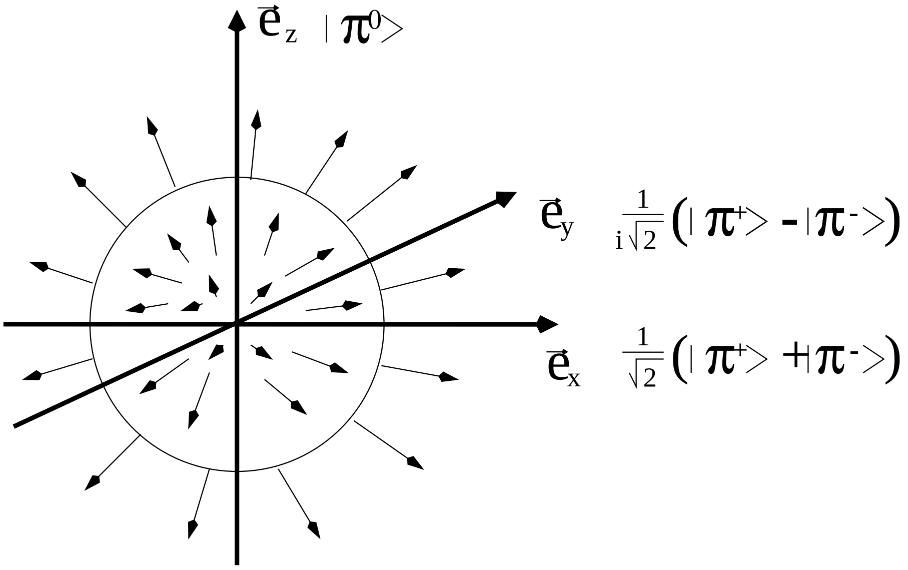

Figure 2.8: The Skyrme Hedgehog

The Lagrangian of the Skyrme model is given as[42]:

$$\mathcal{L} = -\frac{F_\pi^2}{16}\mathrm{Tr}\,[L_\mu, L^\mu] + \frac{1}{32e^2}\mathrm{Tr}\,([L_\mu, L_\nu]\,[L^\mu, L^\nu]) \tag{2.76}$$

where

$$\begin{aligned} U(t,\overrightarrow{r}) &= \exp\left[\frac{2i}{F_\pi}(\eta' + \sum_{a=1}^{8}\lambda_a\phi_a\right] \\ L_\mu &= U^\dagger\partial_\mu U \\ \phi &= \pi^\pm, \pi^0, K^\pm, K^0, \bar{K}^0, \eta \\ F_\pi &= 92\ \text{MeV} \end{aligned} \tag{2.77}$$

and e is a dimensionless, real valued parameter.

In the Skyrme model the nucleon is regarded as a 'lump' of light mesons and all the nucleon angular momentum is orbital in origin[40]. In other words,

$$\Delta\Sigma = 0 \qquad \Delta G = 0 \tag{2.78}$$

and the momentum sum becomes

$$\langle S_z \rangle = \frac{1}{2} = L_z \tag{2.79}$$

However, there are extensions of the simple Skyrme model that allow values of $\Delta\Sigma = 0.3$ in agreement with current data[42].

2.2.5 A Gauge Invariant Spin Sum Rule

The QCD angular momentum operator is usually given in the form[26]:

$$\vec{J} = \int d^3\vec{x}\left[\frac{1}{2}\bar{\psi}\vec{\gamma}\gamma_5\psi + \psi^\dagger\vec{x}\times(-i\vec{\nabla})\psi + \vec{E}\times\vec{A} + E_i(\vec{x}\times\vec{\nabla})A_i\right] \tag{2.80}$$

where the four terms can be identified with the quark spin, the quark orbital angular momentum, the gluon spin and the gluon angular momentum. This leads to the spin sum rule in its conventional form (see equation 2.44):

$$\langle S_z \rangle = \frac{1}{2}\Delta\Sigma + L_q + \Delta G + L_g \tag{2.81}$$

However, the contribution of gluon orbital angular momentum and gluon helicity are not gauge invariant and recently X.Ji has proposed an explicitly gauge invariant angular momentum operator[43]:

$$\vec{J} = \int d^3\vec{x} \left[\frac{1}{2}\bar{\psi}\vec{\gamma}\gamma_5\psi + \psi^\dagger(\vec{x} \times (-i\vec{D}))\psi + \vec{x} \times (\vec{E} \times \vec{B}) \right] \tag{2.82}$$

where $\vec{D} = \vec{\partial} + ig\vec{A}$ is the covariant derivative. This leads to the gauge invariant spin sum rule

$$\langle S_z \rangle = \frac{1}{2}\Delta\Sigma + L_q + J_g \tag{2.83}$$

The first two terms can be combined further to J_q, which then is not affected by the axial anomaly. The Q^2 evolution equation for the quark and gluon contributions is[43]:

$$\frac{\partial}{\partial \ln Q^2} \begin{pmatrix} J_q(Q^2) \\ J_g(Q^2) \end{pmatrix} = \frac{\alpha_s(Q^2)}{2\pi} \frac{1}{9} \begin{pmatrix} -16 & 3n_f \\ 16 & -3n_f \end{pmatrix} \begin{pmatrix} J_q(Q^2) \\ J_g(Q^2) \end{pmatrix} \tag{2.84}$$

where n_f is the number of quark flavours. This evolution equation has for $Q^2 \to \infty$ the fixed point solution

$$\begin{aligned} J_q(\infty) &= \frac{1}{2} \frac{3n_f}{16 + 3n_f} \\ J_g(\infty) &= \frac{1}{2} \frac{16}{16 + 3n_f} \end{aligned} \tag{2.85}$$

It follows from this result that about half of the nucleon spin is carried by gluons, much like the case of the nucleon momentum. In a recent paper X.Ji and I.Balitsky[44] starting from the gauge invariant angular momentum operator (2.82) calculate the values of the quark and gluon contributions at $Q^2 = 1$ (GeV/c)^2 to be

$$\begin{aligned} J_g &\sim 0.35 \pm 0.13 \\ J_q &\sim 0.15 \pm 0.13. \end{aligned} \tag{2.86}$$

They arrive at this result using the operator product expansion and QCD sum rule techniques. They suggest that the nucleon spin structure looks roughly as follows:

$$\langle S_z \rangle = \frac{1}{2} = 0.05 \text{ (from } \frac{1}{2}\Delta\Sigma) + 0.10 \text{ (from } L_q) + 0.35 \text{ (from } J_g) \tag{2.87}$$

However, even in this case it could be argued that using the experimental value of $\Delta\Sigma \approx 0.3$, a different result is reached that has no quark orbital angular momentum $L_q = 0$.

It is evident from these examples of important trends in nucleon spin models that despite the enormous progress that has been made in the last few years there are still many models with quite different predictions about the constitution of the nucleon spin. Eventually the experimental results will have to decide which theory is correct.

Chapter 3

The HERMES Experiment

The HERMES[45] experiment utilizes the longitudinally polarised positron (or electron) beam of the HERA accelerator in combination with a polarised internal gas target of hydrogen, deuterium or ^{3}He for the measurement of polarised deep inelastic scattering.

The experiment is located in the East Hall of the HERA accelerator at DESY in Hamburg, Germany. The HERA accelerator consists of positron and proton storage rings with 27.5 GeV and 820 GeV respectively. There are three other experiments at HERA, the two collider experiments ZEUS and H1, and HERA B which uses only the proton beam.

Figure 3.1 shows a schematic overview of the HERA positron ring indicating the direction of the beam polarisation by arrows. The three components of the HERMES experiment, the polarised beam, the polarised target and the spectrometer, are the subjects of the following sections.

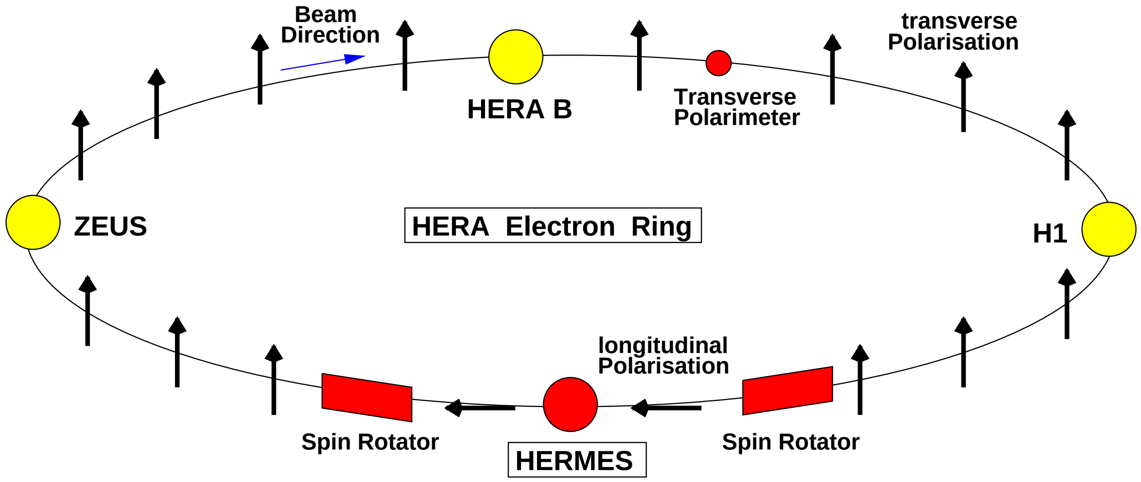

Figure 3.1: Schematic overview of Hera with the four experiments, the beam polarimeter and the spin rotators at the Hermes experiment.

3.1 The Polarised Positron Beam at Hera

3.1.1 Self Polarisation of Electrons

Positrons and electrons in a storage ring emit synchrotron radiation in the dipole and quadrupole fields of the bending and focusing magnets of the accelerator. A small fraction of the synchrotron radiation processes causes the positron spin to flip. The transition probabilities of one spin state into the other one are not symmetric and the state in which the positron spin is parallel to the magnetic field is favoured. (For electrons it is the spin state antiparallel to the magnetic field.) The resulting transverse spin polarisation $P(t)$ follows an exponential law and is known as Sokolov-Ternov effect[46]:

$$P(t) = \frac{8\sqrt{3}}{15}\left(1 - \mathrm{e}^{-\frac{t}{\tau_P}}\right) \qquad (3.1)$$

where the characteristic polarisation time τ_p depends strongly on the geometry of the ring and the beam energy:

$$\tau_P\ [s] = \frac{98.7\rho^2 R}{E_e^5} \tag{3.2}$$

R is the average radius of the ring in meters, ρ the bending radius of the dipole magnets in meters and E_e the beam energy in GeV. For a typical HERA positron energy of 27.5 GeV this leads to a polarisation time τ_p of 39 minutes.

The asymptotic limit for the beam polarisation under ideal conditions is the same for all ring geometries and energies:

$$P_{ST} = \frac{8\sqrt{3}}{15} \approx 92.4\% \tag{3.3}$$

In practical accelerators the maximum polarisation will be lower due to depolarising effects. Alignment errors in quadrupole magnets, spin diffusion, beam-beam interactions with the proton beam in the interaction zones of the collider experiments and depolarising resonances can all result in a reduction of the equlibrium beam polarisation[47]. The condition for depolarising resonances is given in terms of the beam tune ν_s which is defined as

$$\nu_s = \frac{g-2}{2}\gamma \tag{3.4}$$

where $(g-2)/2 = 1.16 \cdot 10^{-3}$ nm is the gyromagnetic anomaly and $\gamma = E/m$. The resonance condition is[48]:

$$\nu_s = n + n_x \cdot Q_x + n_y \cdot Q_y + n_s \cdot Q_s \tag{3.5}$$

where the n_i are integers, $Q_{x,y}$ denote the betatron tunes and Q_s is the synchrotron tune. The spin tune is the number of times the positron spin precesses per revolution in HERA. The beam energy is chosen in such a way that it is as far away as possible from any depolarising resonance. Therefore it is usually set to a value that is between two integers. In fact, the beam tune for the typical HERA energy (27.54 GeV) has been chosen to be 62.5 for this reason.

The depolarising effects can be modelled as a single competing process to the Sokolov-Ternov effect which also follows an exponential law with the characteristic depolarisation time τ_D. Expanding on equation (3.1) the rise of the beam polarisation can now be described by

$$P(t) = P_{max}\left(1 - \mathrm{e}^{\frac{t}{\tau_{eff}}}\right) \tag{3.6}$$

with

$$\tau_{eff} = \frac{\tau_D \tau_P}{\tau_D + \tau_P} \tag{3.7}$$

and

$$P_{max} = P_{ST}\frac{\tau_{eff}}{\tau_P}. \tag{3.8}$$

The influence of the depolarising effects leads to a smaller maximum polarisation and a shorter rise time. For a polarisation P_{max} of 50% the rise time τ_{eff} is 21 minutes.

The determination of τ_{eff} is a good procedure for the absolute calibration of the polarisation measurement as it directly determines the asymptotic polarisation value P_{max} (3.8).

The transverse polarisation is maximised by empirical optimisation using harmonic beam orbit correction bumps and minute beam energy adjustments[13]. Beam polarisation values up to 70% have been achieved at HERA.

3.1.2 Longitudinal Polarisation

The Sokolov-Ternov effect leads to a transverse polarisation of the positron beam, but the experiment requires longitudinal positron polarisation. A series of special dipole magnets on both sides of the experiment rotate the spin into the longitudinal direction and back. These so called 'spin rotators' have a length of 56 meters each[49].

In May 1994, after the installation of the spin rotators for the HERMES experiment a longitudinal polarisation of 56.6 % was measured in the first attempt without any fine tuning. This was the first time longitudinal beam polarisation had been achieved at a high energy storage ring[47]. The rise time curve of these data is shown in figure 3.2.

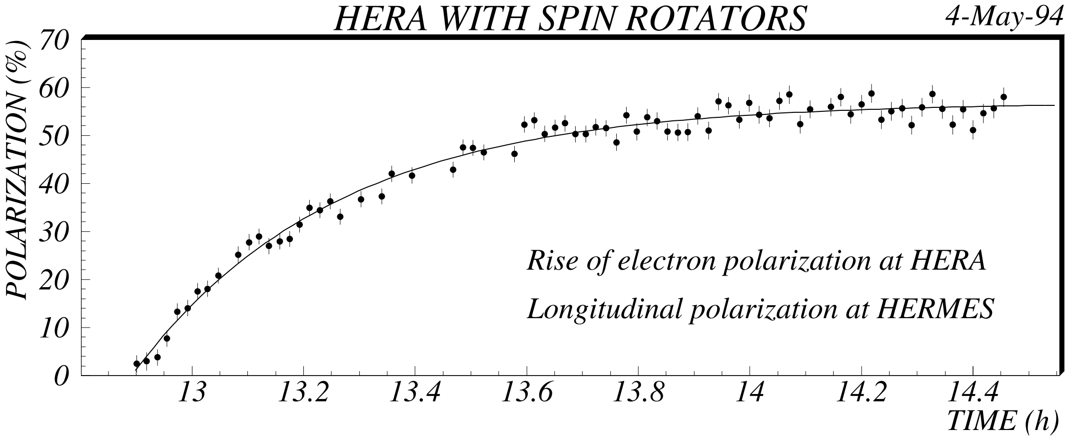

Figure 3.2: Rise of the longitudinal polarisation in HERA after the installation of the spin rotators. The points have been fitted with $P_{max} = 56.6 \pm 0.5$ % asymptotic polarisation and an effective rise time $\tau_{eff} = 20.8 \pm 0.7$ minutes.

The polarisation is measured by the transverse polarimeter in the HERA west area (see figure 3.1). However, the longitudinal polarisation in the HERMES region has the same magnitude, because the polarisation is uniform over the entire ring and even small errors in the spin rotators would lead to a strong depolarisation.

3.1.3 The HERA Beam Polarimeter

The transverse beam polarisation P_y in the HERA positron ring is measured by a Compton polarimeter using the single photon method. The polarimeter uses the asymmetry of the Compton cross section for the scattering of circularly polarised photons off vertically polarised positrons[51]. The beam polarisation P_y is obtained from the difference Δy in the mean value $\langle y \rangle$ of the spatial distribution of backscattered photons for left and right circularly polarised light:

$$\Delta y(E_\gamma) = \frac{\langle y \rangle_L - \langle y \rangle_R}{2} = P_y \Delta S_3 \Pi_\gamma(E_\gamma) \tag{3.9}$$

where ΔS_3 is the degree of circular polarisation and $\Pi_\gamma(E_\gamma)$ is the analysing power[50].

The HERA beam polarimeter uses an argon ion laser operating on the 514 nm line. The polarisation of the light is adjusted in a Pockels cell, transported into the HERA tunnel via several mirrors over a distance of about 200 m and finally scattered off the positron beam with a very small angle (3.1 mrad). Due to relativistic kinematics the backscattered Compton photons have energies of up to 13.88 GeV. A tungsten-scintillator calorimeter is used to detect these photons and measure their position as well as their energy[52].

This setup is operated in single photon mode which makes it possible to select the energy range of the backscattered photons with the largest asymmetry and therefore to optimise the analysing power of the polarimeter. The fact that the calorimeter also measures the energy of the photons opens the possibility of calibrating the polarimeter absolutely using the known energy dependence of the Compton asymmetry.

HERMES has built an additional beam polarimeter that measures the longitudinal beam polarisation in the HERMES region directly. It uses Compton scattering as well, but where the transverse polarimeter measures a position asymmetry, the longitudinal polarimeter measures an intensity asymmetry. This intensity asymmetry is based on the difference in the Compton cross section for photons with positive and negative helicity. The longitudinal polarimeter was commissioned in 1996 and will complement the transverse polarimeter in 1997. However, in 1995 it was not yet constructed and further references to the beam polarimeter in this thesis will always refer to the transverse polarimeter.

3.1.4 Beam Conditions in 1995

In 1995 the Hera electron ring was operated with positrons, due to the better performance that could be obtained with positrons compared to electrons. This is a result of a concentration of positively charged macroscopic particles trapped in the RF beam buckets that were observed in case of electron operation and which severely reduced the lifetime of the beam. As a result 'electron' and 'positron' may sometimes be used interchangeably in this thesis.

The beam current was typically 30 mA after injection and dropped to 10 mA with a lifetime of about 8 hours at which point the beam was dumped and the ring was refilled.

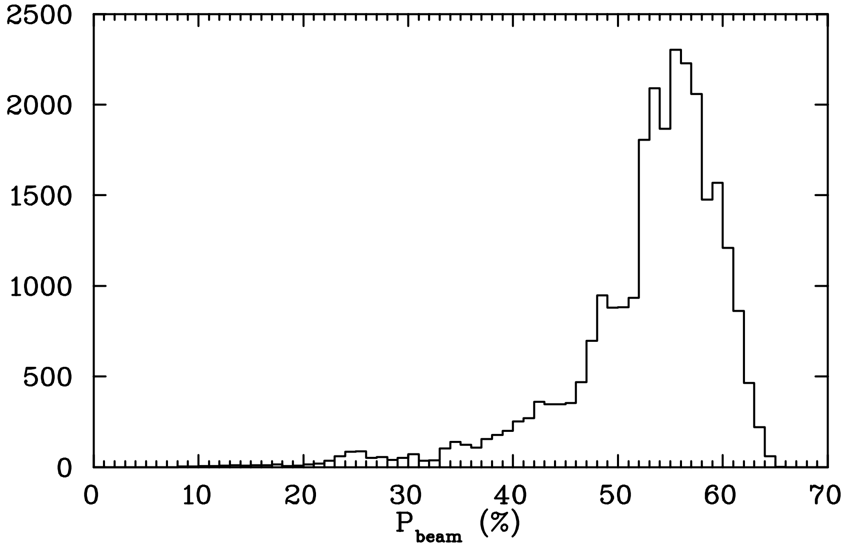

Figure 3.3: Beam Polarisation in 1995. The average value is 54.3 %.

A polarisation measurement is usually taken over the duration of one minute to obtain a statistical uncertainty of about 1% for the single measurement. To combine beam polarisation values with the other data on a burst level (10 s) and to bridge gaps in the polarimeter data during which good Hermes data were taken, a smoothing procedure for the 1995 polarisation data was applied. The smoothing procedure is based on cubic spline functions[53]. It excludes non-statistical fluctuations in the beam polarisation measurements that do not agree with the known facts about polarisation times as well as data points with poor statistics. Smoothed data points are provided for every burst. The resulting polarisation values for all of the 1995 data are collected into a histogram in figure 3.3[54]. The average beam polarisation for 1995 was 54.3 %. The total uncertainty of the polarisation measurement is dominated by the systematic error of 5.4% which is due to the uncertainty in the absolute calibration of the beam polarimeter using the rise time method.

3.2 The Polarised ^{3}He-Target

Hermes has chosen polarised internal gas targets of hydrogen, deuterium and ^{3}He, because they offer the best combination of high polarisation and purity of the target. In the case of hydrogen and deuterium the alternative would be the use of conventional solid polarised target materials like ammonia or butanol. However, the value of the dilution factor f, which is defined as the ratio of polarisable target nucleons to the total number of target nucleons, is much smaller for these targets. They have dilution factors f of 3/17 and 10/84, respectively, while H/D gas targets have a dilution factor of $f = 1$. It is not possible to produce a pure neutron target because a free neutron is not stable and decays with a mean lifetime of 14.7 minutes[55]. Hermes uses ^{3}He as an effective neutron target with the dilution factor (1/3). Although deuterium offers a more favourable dilution factor (1/2), ^{3}He represents the 'purer' polarised target. The helium spin is largely carried by the neutron[14], because the largest fraction of the ^{3}He wave function (89.3 %) is in the S-state in which the proton spins compensate one another. The rest of the wave function is either a D-state ($\sim$ 8%) or a mixed symmetry P-state. In both cases the protons contribute to the ^{3}He spin and a correction must be made for this in the analysis (see section 6.4.2). An additional advantage of gas targets is the possibility to flip the direction of the polarisation rapidly, which reduces systematic uncertainties in the experiment.

The polarised target consists of a source of polarised atoms, the target cell inside the HERA positron ring, a magnetic holding field and a target polarimeter. HERMES uses two targets that are based on different principles for H/D on the one hand and for ^{3}He on the other. The following sections will concentrate on the ^{3}He target only.

3.2.1 Polarisation by Optical Pumping

The ^{3}He atoms in the HERMES target are polarised by optical pumping. Atoms of ^{3}He are excited from the ground state (1^1S_0) into the metastable 2^3S_1 state by means of a radio frequency discharge. Atoms in this metastable state can be optically pumped into the 2^3P state using circularly polarised light of 1083 nm (see figure 3.4). Due to the circular polarisation of the laser light angular momentum is transferred and the ^{3}He system is polarised. Following metastability-exchange collisions a population of ^{3}He atoms in the electronic ground state with polarised nuclei is produced[56].

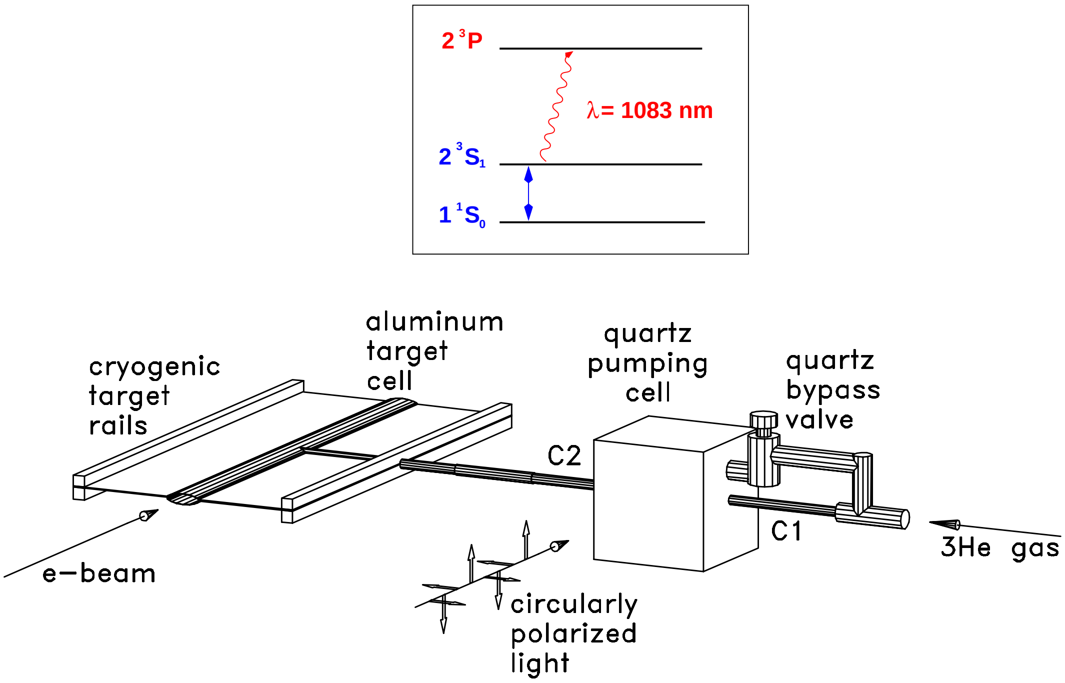

Figure 3.4: Schematics of the polarised ^{3}He target and of optical pumping

The laser used for this purpose is a 10 W CW Nd:LNA laser ($La_{0.85}Nd_{0.15}MgAl_{11}O_{19}$). The laser polarises the helium atoms inside a cubic pumping cell with an inner dimension of 85 mm. The gas flows through a capillary into the target cell. A schematic view of the target setup is shown in figure 3.4[58].

3.2.2 Design of the Target Region

The target cell itself is made from ultra pure aluminum, is 400 mm long and has a cross section of 2.9×9.8 mm^2. The wall thickness is only 51 μm.

Synchrotron radiation and wake fields from the positron beam heat up the target cell and can potentially destroy it. The target cell is shielded from most of the synchrotron radiation by a pair of movable collimators (C1) and one fixed collimator (C2) which is installed directly in front of the target cell. (see figure 3.5)

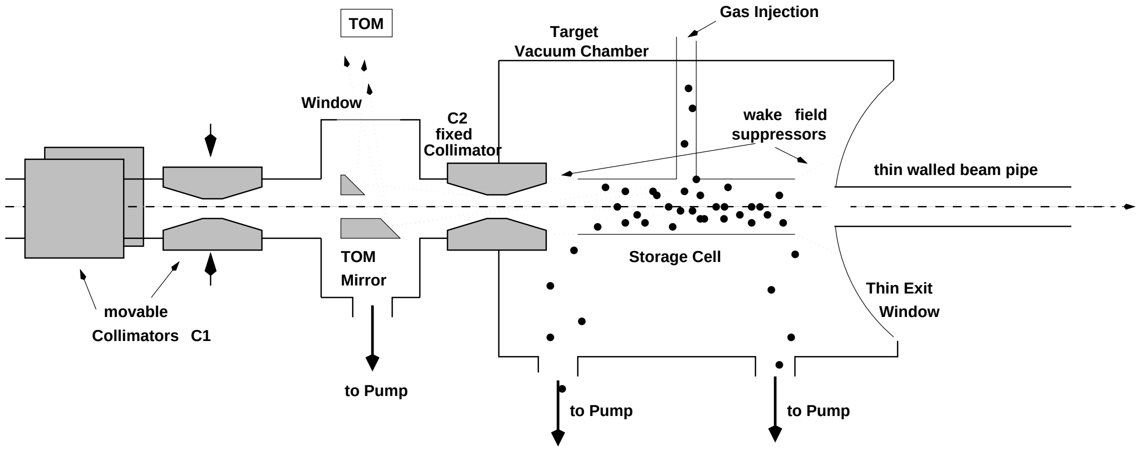

Figure 3.5: Schematic view of the HERMES target region.

The wake fields of short positron bunches can lead to RF losses in the target chamber. To avoid such losses, meshes made of 125 μm thin titanium are used to serve as a smooth transition from the beam pipe to the target cell. The target cell is cooled to about 25 K using liquid ^{4}He in cooling rails. It is open at both ends not to interfere with the stored beam. The target gas must be pumped out differentially on both sides. This design produces a triangular profile of the target density along the length of the cell (see figure 3.6).

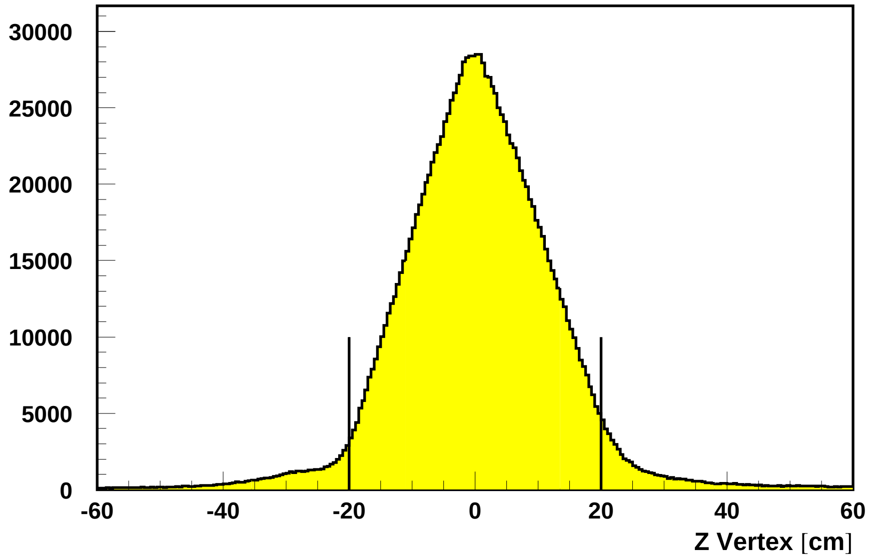

Figure 3.6: Longitudinal density profile of the target region as determined by the track reconstruction. The two lines indicate the extension of the target cell.

The target vacuum chamber has a specially designed thin exit window (0.3 mm stainless steel) followed by a beam pipe of the same thickness to allow the scattered particles to exit the target region with minimal interaction.

3.2.3 Measurement of the Target Polarisation

The polarisation of the ^{3}He target is monitored by two independent polarimeters that measure the polarisation inside the pumping cell as well as directly inside the target cell.

The pumping cell polarimeter uses the 667 nm transition induced by the RF discharge. The circular polarisation of the 667 nm light is related to the nuclear polarisation of the ^{3}He nuclei. This relation has been calibrated previously[57].

The second polarimeter is the target optical monitor (TOM) which measures the polarisation directly in the target cell[59] (see figure 3.5). The HERA positron beam excites atoms in the target gas. Among the excited levels is the 4^1D state with a lifetime of 37 ns, which is shorter than the spacing between HERA positron bunches of 96 ns. The nuclear polarisation of the excited ^{3}He atoms is transferred to the electronic system by hyperfine coupling within 1-2 ns. This results in the emission of circularly polarised light at 492.2 nm. By measuring this circular polarisation the ^{3}He polarisation can be determined[59].

Both polarisation measurements have been shown to agree well within their uncertainties. A comparison of both measurements is shown in figure 3.7. Target polarisation studies as a function of beam intensity have shown that no beam induced depolarisation of the target is observed.

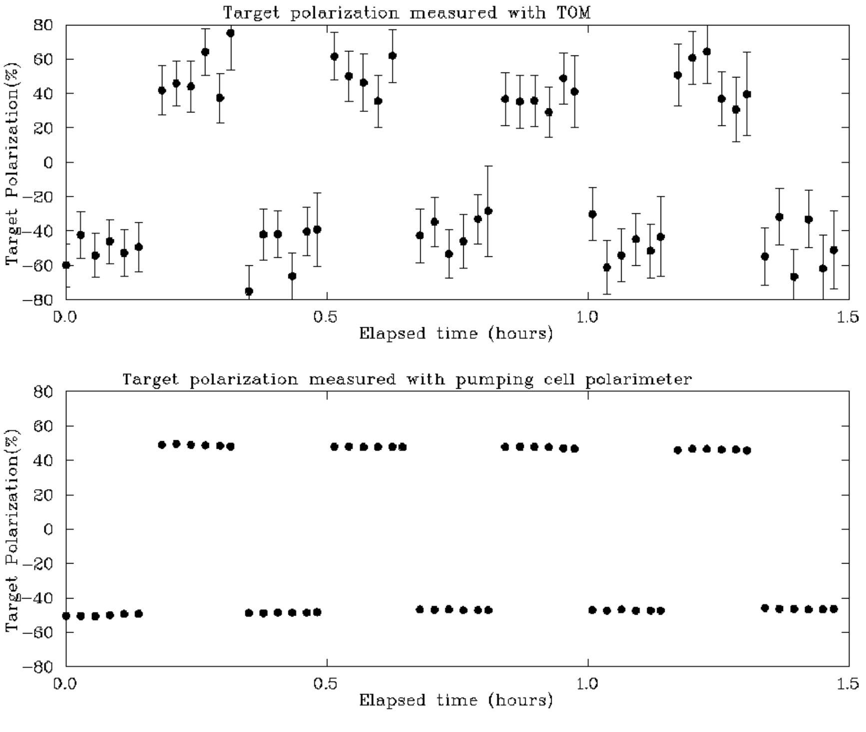

Figure 3.7: Target polarisation measured with pumping cell polarimeter and TOM.

3.2.4 Performance of the ^{3}He-Target in 1995

The sign of the target polarisation was reversed every 10 minutes by switching the polarisation of the pumping laser using a Pockels cell.

The typical value of the target density was 3.3×10^{14} atoms/cm^2. The average target polarisation in 1995 was 46% with an overall fractional systematic uncertainty of 5%.

3.3 The Spectrometer

3.3.1 Overview

The HERMES experiment is located in the East hall of the HERA accelerator at DESY. The spectrometer is constructed in the forward direction with a large acceptance. Both HERA beam pipes, the positron and the proton ring, pass through the mid-plane of the spectrometer. For this reason it is designed as a two part spectrometer with symmetric top and bottom halves. A septum plate inside the magnet protects the beams from the magnetic field. It limits the minimum of the acceptance in the vertical direction to ± 40 mrad. The maximum acceptance is 140 mrad in the vertical direction and $\pm$ 170 mrad in the horizontal direction. A 3D CAD drawing of the experiment is shown in figure 3.8.

The major components of the spectrometer are the spectrometer magnet, four sets of tracking chambers, four particle identification detectors and a luminosity monitor. The tracking system consists of gas microstrip chambers as vertex detector (VC), drift chambers in front of (FC) and behind the magnet (BC), as well as multi wire proportional chambers inside the magnet (MC). The vertex and front drift chambers determine the scattering angles (θ, ϕ) and the front part of the particle track trajectory. The back chambers (BC) determine the track trajectory behind the magnet. The particle momentum is deduced from the deflection of the particles in the magnetic field. The particle identification system consists of a threshold Čerenkov detector, a transition radiation detector (TRD) and a calorimeter, which is complemented by a preshower detector (H2). The calorimeter and the preshower detector form the standard physics trigger together with the other hodoscope (H1). The readout electronics and the gas systems for the wire chambers are located in the 'electronics trailer' (ET) which like the spectrometer itself sits on rails and allowed the assembly of the experiment inside the East hall next to the accelerator while the latter was operating. It also allows the experiment to be moved in and out if it is necessary to bring large equipment into or out of the accelerator tunnel. T-shaped iron enriched concrete shielding blocks form a removable shielding wall between the electronics trailer and the experiment.

3.3.2 The Spectrometer Magnet

The spectrometer magnet[61] is an H-frame type dipole magnet with a field integral of 1.3 Tm. Field clamps on both sides and a septum plate in the beam plane shield the tracking detectors and the HERA beams from the magnetic fields. Additionally a correction coil is used to compensate any remaining effects on the positron beam.

The magnet design was optimised using the 3D simulation codes MAFIA and TOSCA. The magnetic field has been mapped in three dimensions with a precision of $\Delta B_y/B < 0.3\%$ and a grid size of $1\times 9.8\times 4.9$ cm (longitudinal, horizontal, vertical)[62]. The measurements agree with the calculations within a few percent.

3.3.3 The Tracking Detectors

The tracking system has to fulfill several tasks. It has to find the vertex from which the track originates, which makes it possible to reject tracks that do not come from the target and also opens the possibility to identify secondary vertices from decaying particles. The tracking system also has to measure the scattering angles that define

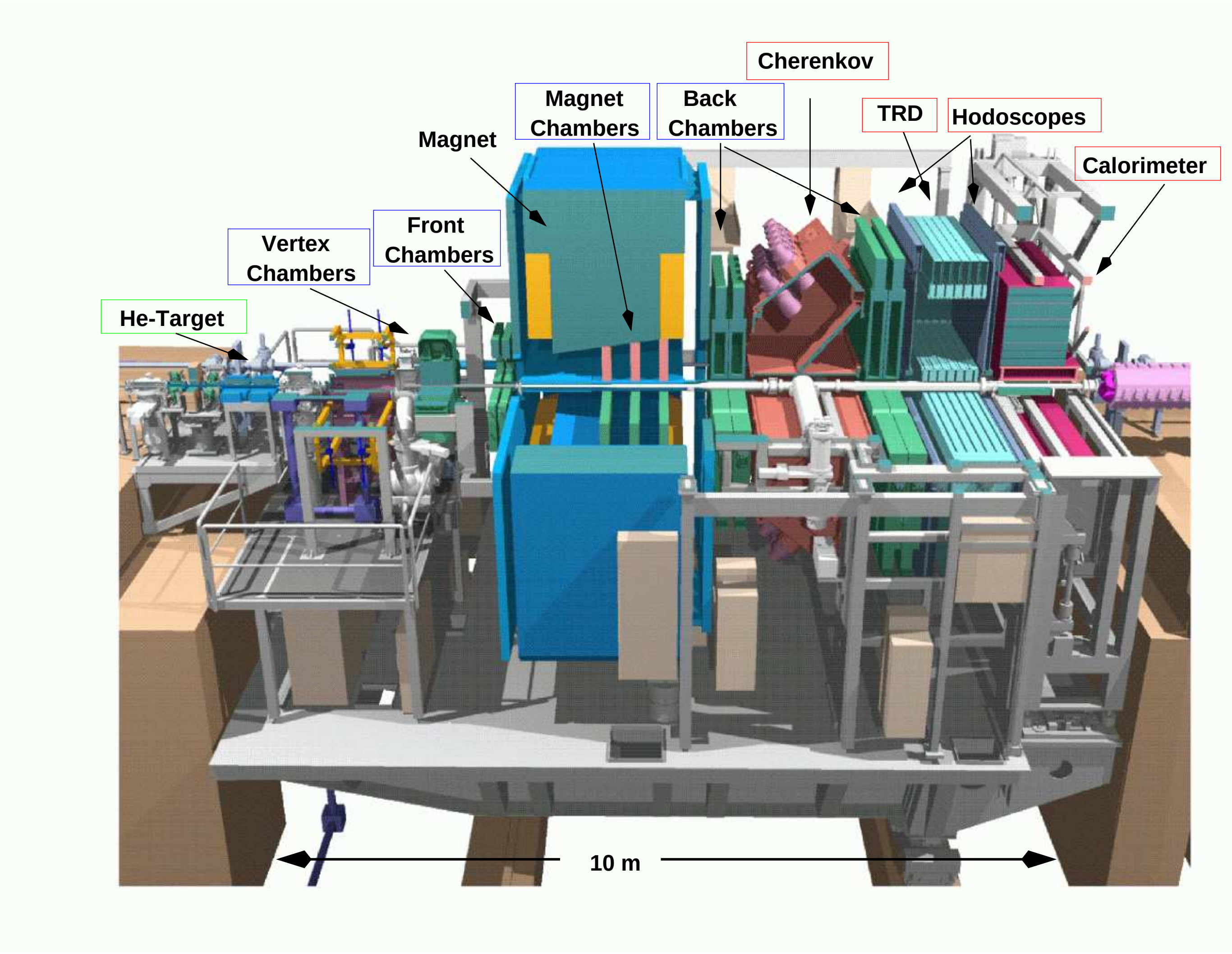

Figure 3.8: The HERMES Experiment

the kinematics of each event. The vertex chambers (VC) and the front chambers (FC) were designed for these tasks. The vertex chambers are microstrip gas chambers and their active area reaches close to the beam tube, up to a distance of only 20 mm from the positron beam. The front chambers are drift chambers with a single plane resolution of about 300 μm.

The two other tasks are the momentum measurement and the determination of the particle identification detector hits that are associated with a particular track. The back drift chambers (BC)[63] define partial backtracks which in combination with the partial front tracks allow the determination of the deflection in the magnetic field and hence of the momentum of the particle. The partial back tracks also allow the identification of the PID hits that belong to a certain particle.

The magnet chambers (MC) were originally designed to improve the matching of front and back tracks. It turned out that this was not necessary due to the low multiplicity of the events and the low background in the spectrometer. However, the MCs provide valuable information about low momentum tracks from particle decays that are so strongly deflected inside the magnet that they do not reach the back chambers.

Because of the large horizontal dimension of the tracking chambers it was not possible to have planes with horizontal wires in the detector. Therefore U and V planes with angles of ± 30 degrees were employed instead. In the front and back chambers two planes with the same wire orientation but a relative shift of half a cell size are used to resolve left-right ambiguities. The most important parameters of all tracking chambers are listed in table 3.1.

The Hermes reconstruction program (HRC)[64] utitilises two novel techniques, a tree search algorithm for track finding and look-up tables for the momentum determination, that lead to an extremely fast event reconstruction. The tree search algorithm is based on the idea that a track can be found with less resolution than is necessary for fitting it, and on a database of allowed patterns. The size of this data base has been strongly reduced by symmetry and self similarity considerations, from

	Vertex Chambers		Front Chambers		Magnet Chambers			Back Chambers	
Detector Name	VC1	VC2	FC1	FC2	MC1	MC2	MC3	BC1/2	BC3/4
mm from target	750	1000	1530	1650	2725	3047	3369	3950	5700
Active hor. (mm)	270	343	660	660	996	1210	1424	1880	2890
Active vert. (mm)	80	100	180	180	263	306	347	520	710
Chamber Type	microstrip gas		horizontal-drift		MWPC			horizontal-drift	
Cell Width (mm)	0.200		7		2			15	
Resolution/Plane (σ)	$65\,\mu$m		$300\,\mu$m		0.7 mm			$225\,\mu$m	
Wires in X plane	1350	1900	96	96	496	608	720	128	192
Wires in U,V plane	1350, 400	1900, 600	96	96	512	608	720	128	192
Module Config.	UXY		UU′XX′VV′		UXV			UU′XX′VV′	
Rad. Length/Module	1.2%		0.20%		0.29%			0.26%	
Readout	digital (APC)		TDC		digital (PCOS)			TDC	
Total Channels	24800		2304		11008			7680	

Table 3.1: Some tracking chamber properties.

the original 100,000,000 allowed patterns to only 50,000 that finally have to be stored. The fast momentum lookup technique also uses a predefined data base combined with interpolation and gives a momentum resolution of $\Delta P/P = 0.5\%$.

The vertex and front chambers were designed for the vertex reconstruction and the measurement of the scattering angles. However, for the 1995 running period the VC data are only usable for a fraction of the data set due to problems in the production of the VC readout chips. Therefore the front chambers alone have to define the front part of the track. The higher resolution back track information was used to optimise the front tracking resolution by providing an additional data point: The front tracks were forced to coincide with corresponding back tracks at the midpoint inside the magnet. Therefore the name 'forced bridging' is given to this procedure.

A fully reconstructed event with several hadron tracks and one positron track is depicted in figure 3.9. The positron is clearly identified by the particle identification detectors; the TRD shows no hits for the hadron tracks due to the value of the display threshold. This event also shows an identified secondary vertex from a K_s decay.

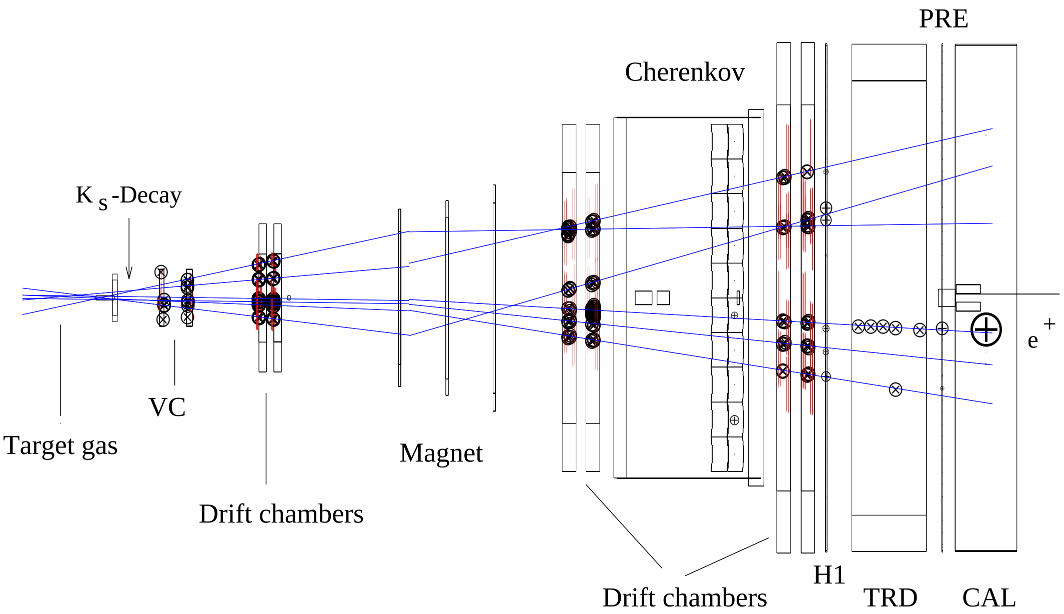

Figure 3.9: Example of a reconstructed HERMES event.

3.3.4 The Particle Identification Detectors

A clean identification of the scattered positrons is crucial for inclusive measurements in the HERMES experiment. Due to large hadronic backgrounds mainly from photoproduction, the ratio of pions to positrons can be as high as 400:1 at 4.5 GeV and angles of 7-8 degrees (see figure 3.10).

This means that a large hadron rejection must be achieved for inclusive measurements. Furthermore it is required for semi-inclusive studies that different types of hadrons are separated. The HERMES experiment includes four particle identification detectors: a lead glass calorimeter, a preshower detector, a Čerenkov and a transition radiation detector. These detectors make up the HERMES particle identification system together with the trigger and the charge discrimination by the spectrometer magnet. The first three detectors are described in the following sections. The TRD which is the main Canadian contribution to HERMES is the subject of a dedicated chapter.

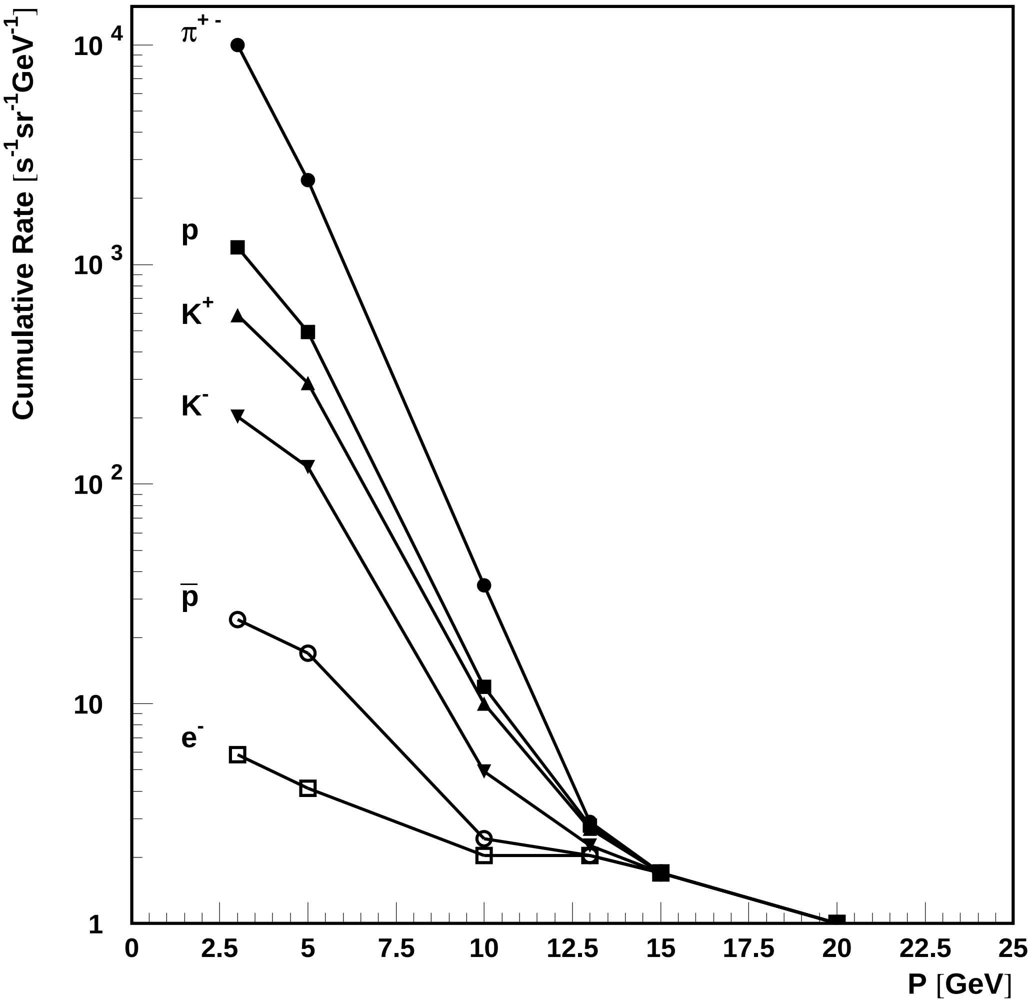

Figure 3.10: Cumulative charged particle rates for incident 35 GeV electrons with a luminosity of $3 \cdot 10^{32}\,\mathrm{cm}^{-2}\mathrm{s}^{-1}$ (^{3}He) and $7^\circ < \theta < 8^\circ$[45].

Calorimeter and Preshower Detector

The basic principle that the calorimeter and the preshower use for particle identification is the topological difference between electromagnetic and hadronic showers. Electromagnetic showers are produced by photons, electrons and positrons. They start practically immediately and almost all the energy can be contained in a detector of

20 radiation lengths thickness. A radiation length X_0 is defined as the mean distance over which a high energy electron loses all but $1/e$ of its energy by bremsstrahlung. Hadronic showers start further inside the material and have a larger lateral dimension. The inelastic nuclear interaction length λ plays a similar role as X_0 for the electromagnetic case. It is defined as the mean free path between inelastic interactions. The difference in the development of electromagnetic and hadronic showers is also expressed in the fact that the nuclear interaction length typically is an order of magnitude larger than the radiation length of a material. A hadron usually deposits only part of its energy in a detector designed to contain electromagnetic showers[67].

The HERMES calorimeter is designed to fulfill several tasks:

- Serve as part of the first level trigger by suppressing hadronic background.
- Provide a hadron rejection factor of ≥ 10 at the first level trigger and ≥ 100 in the offline analysis.
- Give a coarse position measurement.

Furthermore high radiation resistance is required to provide long term stability of the calorimeter response in the HERA environment.

The HERMES calorimeter consists of 840 radiation resistant F101 lead glass blocks arranged in two walls above and below the beam with photomultiplier readout from the back. Each lead glass block has the dimensions $9 \times 9 \times 50$ cm^3 (see also figure 3.11).

The HERMES spectrometer contains two hodoscopes, between the back chambers (BCs) and the TRD, and between the TRD and the calorimeter. They are both used for the physics trigger and they can both be used for time of flight measurements as well. The second hodoscope which is preceded by 1.1 cm of lead acts as a preshower detector. In fact the preshower detector and the calorimeter can be considered as a single electromagnetic calorimeter with a segmented longitudinal structure. The lead is two radiation lengths X_0 thick. Therefore the complete structure has 20 X_0

thickness and can contain electromagnetic showers completely. At the same time the lead only represents 6.4% of a nuclear interaction length λ, so that the addition of the preshower detector enhances the difference in shower topologies.

The hodoscopes consist of 42 plastic scintillator paddles which have a size of $9.3 \times 91 \times 1$ cm^3. Each paddle covers one vertical column of the lead glass blocks. To avoid acceptance gaps adjacent paddles overlap by 1.5 mm and paddles extend beyond the top and bottom ends of the lead glass wall. The paddles are read out by photomultipliers at the top or bottom end. The bottom part of the preshower detector and the calorimeter are shown schematically in figure 3.11.

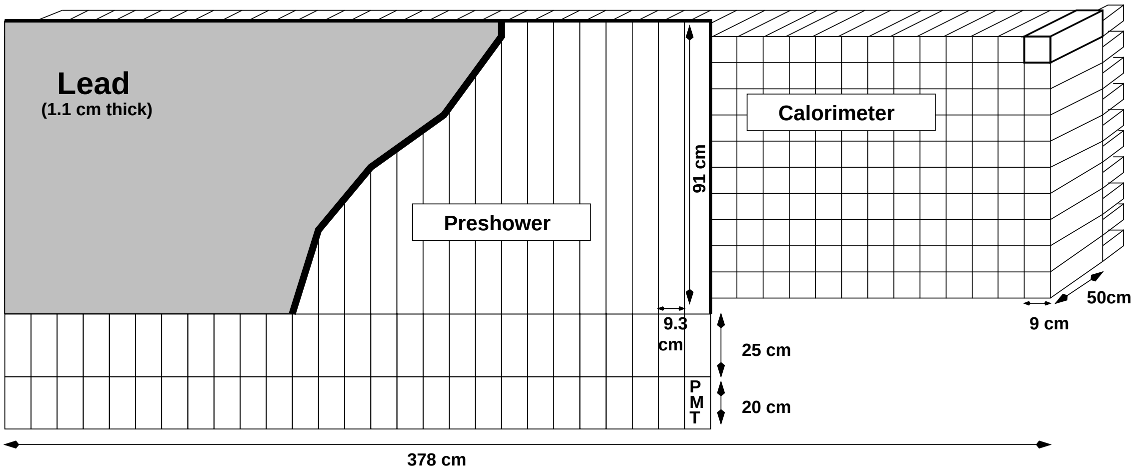

Figure 3.11: Schematic drawing of preshower and calorimeter (bottom part)

The response of the calorimeter for pions and electrons was determined in test beams. Additionally, a Monte Carlo study was performed[69]. Muons, being minimum ionising particles, give a rather narrow peak with a Landau tail at $E/p = 0.15$ in a spectrum of the ratio of calorimeter response $E = E_{cal}$ divided by particle momentum p. This corresponds to the deposition of about 750 MeV in the calorimeter for minimum ionising particles, which is in good agreement with the 780 MeV measured at the CERN test beam[70].

Regarding the calorimeter response derived from HERMES data, it has to be taken into account that the trigger disproportionately favours hadrons that deposit a lot of energy, so that the minimum ionising peak is strongly suppressed. Furthermore a high energy tail with values of $E/p > 1$ is observed (fig.3.12). This tail can be understood as an effect of pre-magnet bremsstrahlung and as an attenuation effect in the lead glass. In the case of energy loss of the particle before the magnet due to bremsstrahlung, the measured momentum will be smaller than the initial momentum. However, if the particle is only weakly deflected by the magnetic field the bremsstrahlung photon may be detected by the same cluster of calorimeter blocks as the particle itself, which leads to a value of $E/p > 1$. Most electromagnetic showers start already in the preshower detector and they dominate the peak at E/p=1. Showers that develop further inside a calorimeter block can still deposit most of their energy, but the light suffers less attenuation in the lead glass on its way to the photo multiplier[70]. This leads to a large value of E/p as well. The hadron/positron samples were defined by hard cuts on the Čerenkov and TRD responses (see section 5.3.1).

The energy dependence of E/p is of interest as well. To examine this dependence E/p vs E is plotted in figure 3.13. The band at $E/p = 1$ corresponds to the positrons, while the hadrons form two distributions in the lower left part of the plot. This separation is a trigger effect, caused by the 3.5 GeV threshold (indicated by a line in the plot). This trigger effect is a basic feature of the PID and will show up repeatedly in the description of the details of the PID.

The performance of the calorimeter has been measured in testbeams at CERN and DESY and it was found[71] that:

- the response to electrons is linear within 1% for energies between 1-30 GeV,
- the energy resolution is $\sigma/E[\%] = (5.1 \pm 1./1)\sqrt{E[GeV]} + (1.5 \pm 0.5)$, which is typical for lead glass calorimeters,
- the pion rejection of the calorimeter alone is about 100 for energies of 4-8 GeV (figure 3.16).

Hadrons typically leave a minimum ionising signal in the preshower detector. This peak is so pronounced that it is appropriate to use a logarithmic scale for the plot of the normalised preshower responses (figure 3.14). If the preshower threshold were raised to above the minimum ionising energy, the pion rejection would be increased significantly already at the first level trigger. However, the test beam results indicated that a high preshower threshold might create a time or position dependence of the positron rate due to gain shifts. Therefore the thresholds were set below the minimum ionising signal so as not to bias the data sample[70].

Positrons deposit an amount of energy that is roughly proportional to $\ln E$ while the preshower signal for hadrons is roughly constant, with a small positive slope (figure 3.15). The distribution of responses for positrons of a given energy is very broad.

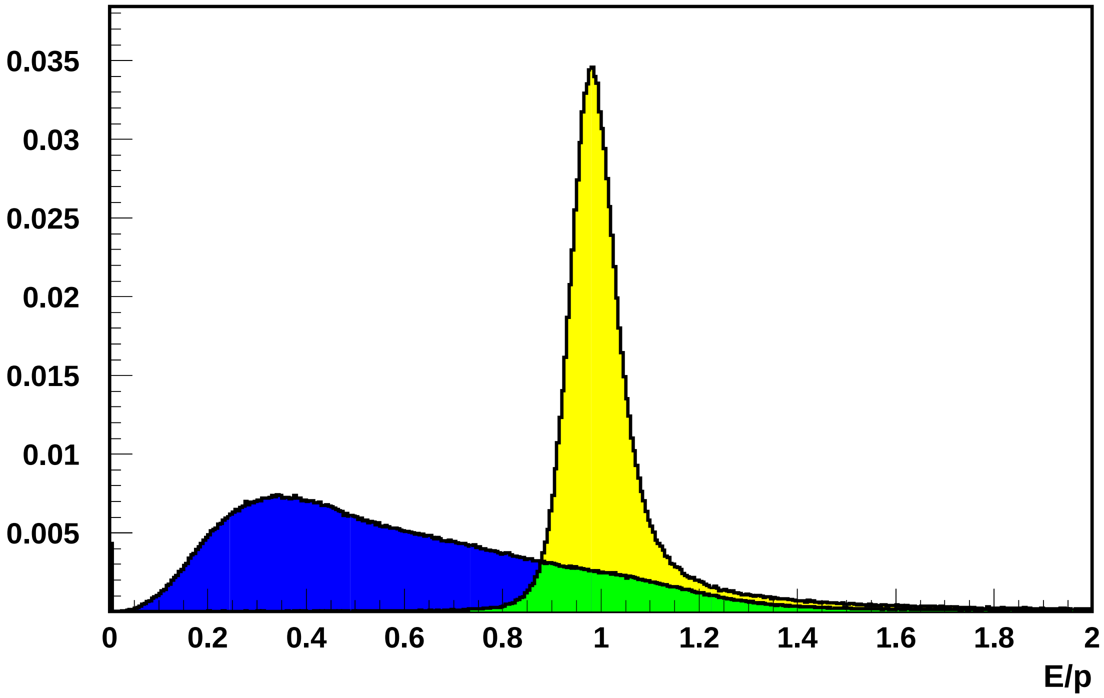

Figure 3.12: Normalised distributions of E/p from HERMES data for hadrons(dark) and positrons (light) integrated over all momenta.

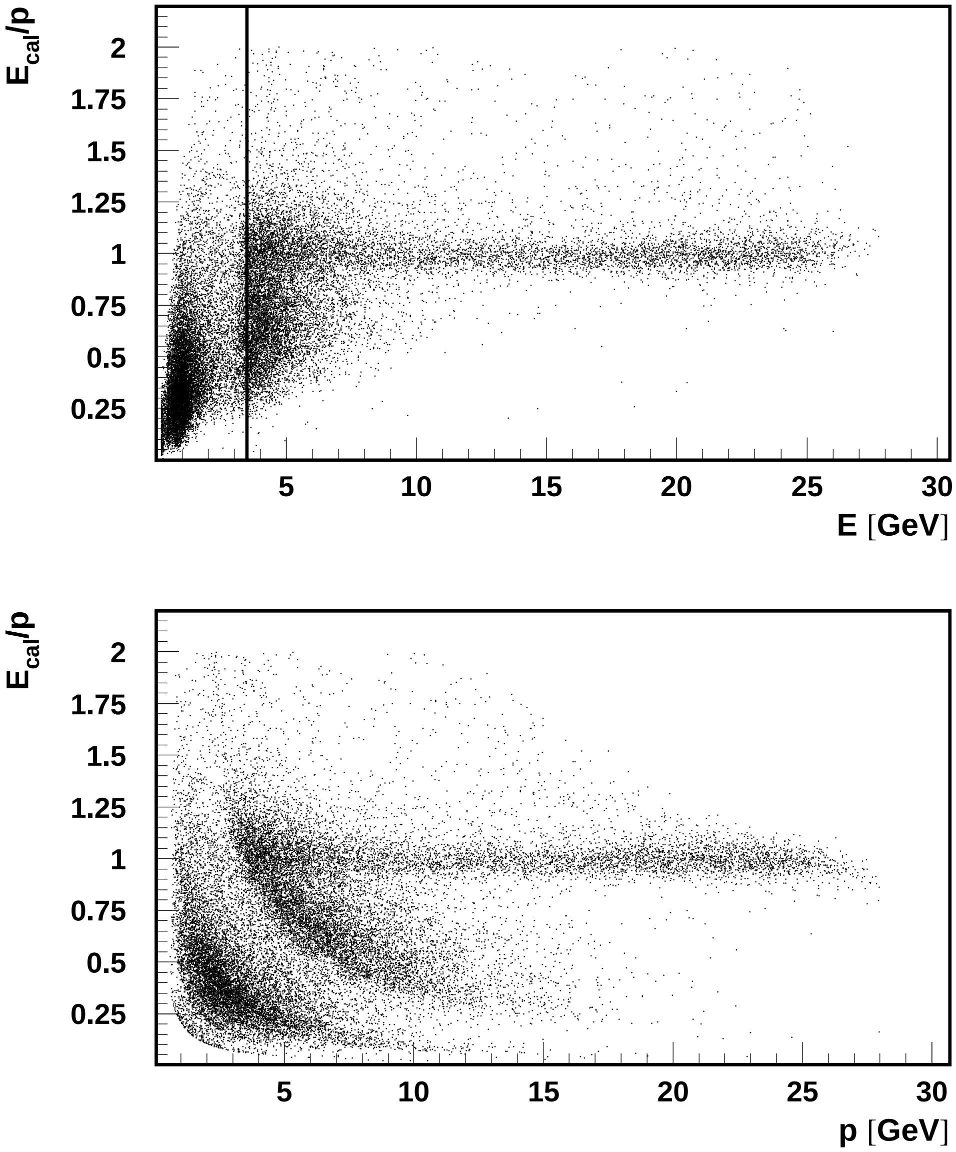

Figure 3.13: Ratio E/p vs calorimeter signal E and momentum p. The line indicates the trigger threshold at 3.5 GeV.

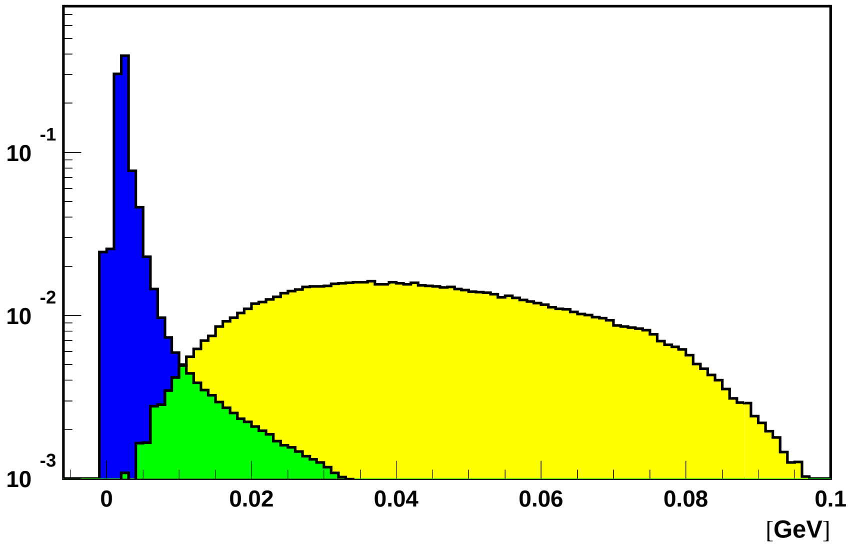

Figure 3.14: Normalised preshower signal for hadrons(dark) and positrons (light) integrated over all momenta.

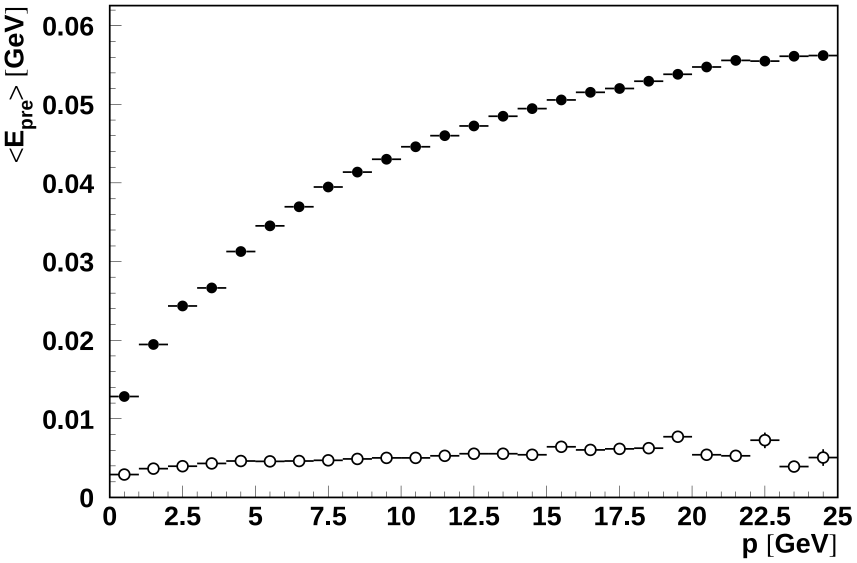

Figure 3.15: Energy dependence of the preshower response for positrons (dark) and hadrons (light)

The combination of the preshower and the calorimeter has been shown to yield a pion rejection of up to 5000:1 (resp. $2 \cdot 10^{-4}$) for an electron efficiency of 95%[71] for a single calorimeter block. The pion rejection factor is defined as the ratio of the total number of pions to the number of pions that were misidentified as electrons. In figure 3.16 the reciprocal ratio was plotted. Hence the pion rejection obtained from the calorimeter alone is improved by the preshower by a factor of 40 (see figure 3.16).

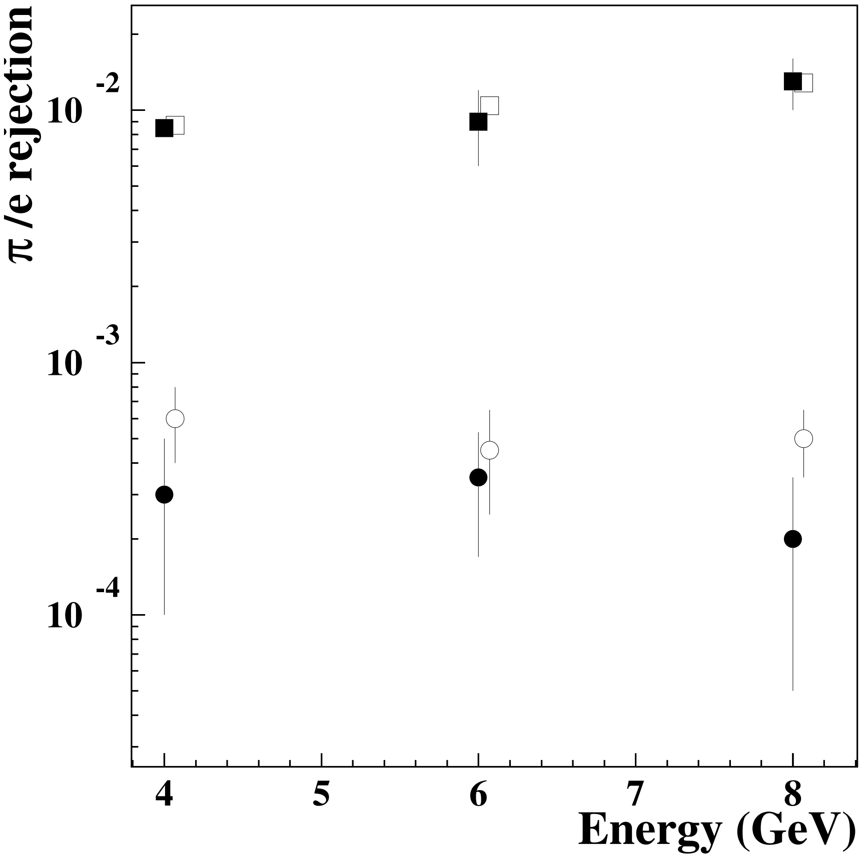

Figure 3.16: Pion/Electron rejection in a single block of calorimeter and preshower (95% efficiency). Filled and empty points are data and Monte Carlo simulation respectively. Squares refer to calorimeter only, circles to calorimeter plus preshower[68].

The Čerenkov Detector

The HERMES Čerenkov Detector consists of two identical threshold counters, above and below the beamline. The radiator in 1995 was nitrogen at atmospheric pressure. This was changed in 1996 to a mixture of C_4F_{10} and N_2 with a ratio of about 30:70 (by volume) to lower the pion threshold. The Čerenkov light is collected in the top and bottom detectors by a system of 20 mirrors and 20 photomultipliers each. The windows in the active area of the counters are made from Mylar (100μm) and Tedlar (50μm).The windows, mirrors and nitrogen together add up to a thickness of only 3.5% of a radiation length. Therefore the Čerenkov Detector can be located between the two sets of back tracking chambers without compromising the momentum measurement.

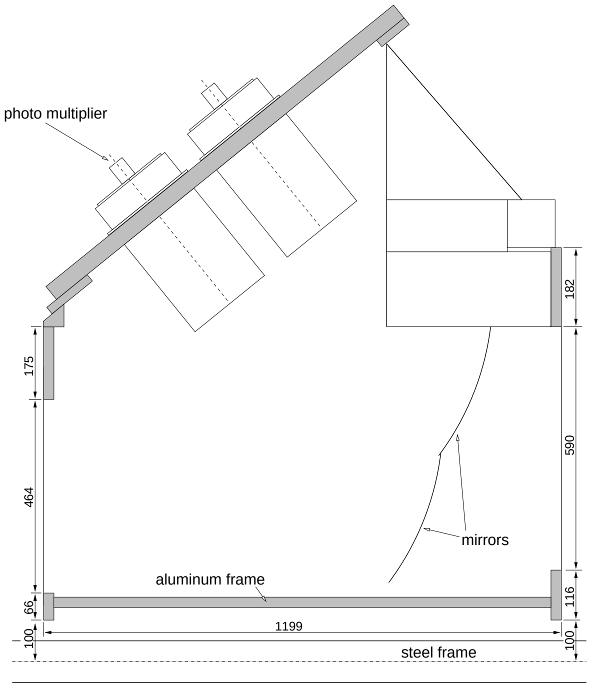

Figure 3.17: Schematic side view of the upper Čerenkov counter[64].

The threshold momenta for various particles in conjunction with other relevant parameters for the 1995 and 1996 running of the Čerenkov detector are given in table 3.2[55][72].

	1995	1996
radiator	N_2	C_4F_{10},N_2
n	1.000298	1.001223
$\beta_t\gamma_t$	40.96	28.6
$p_t(e)$	0.021 GeV	0.015 GeV
$p_t(\pi)$	5.72 GeV	3.99 GeV
$p_t(K)$	20.23 GeV	14.13 GeV
$p_t(p)$	38.42 GeV	26.83 GeV

Table 3.2: Parameters of the Čerenkov detector for 1995 and 1996

The response of the Čerenkov detector to positrons and pions can be determined by using the other PID detectors to define clean samples.

The typical measure for the intensity of a Čerenkov signal is the number of photoelectrons N_{pe} that are produced in the photomultipliers of the detector by the Čerenkov photons. The quantum efficiency is usually about 25%. About 3 photoelectrons are to be expected for a 10 GeV pion in the 1995 data. The pion threshold for 1995 data was at 5.72 GeV. Plotting $\langle N_{pe}\rangle$ versus momentum allows for a closer analysis of the detector response in the region around the pion threshold (figure 3.18).

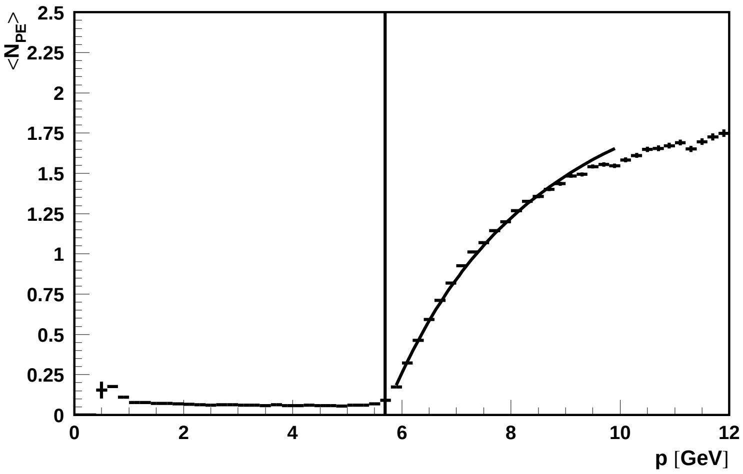

Figure 3.18: Mean number of photoelectrons versus momentum for pions (1995 data). The rise was fitted from 6-10 GeV; the vertical line indicates the theoretical threshold at 5.72 GeV

The fit to $\langle N_{pe} \rangle$ from 6 to 10 GeV gives $n = 1.0003 \pm 2 \cdot 10^{-6}$, which is in perfect agreement with the value of $n(N_2)$ from the literature (table 3.2). Also the theoretical value for the threshold at 5.72 GeV is in exact agreement with the observed value, while the mean number of photoelectrons is somewhat lower than expected. This can be due to lower quantum efficiencies of the photomultipliers and the contamination of the pion sample by heavier hadrons.

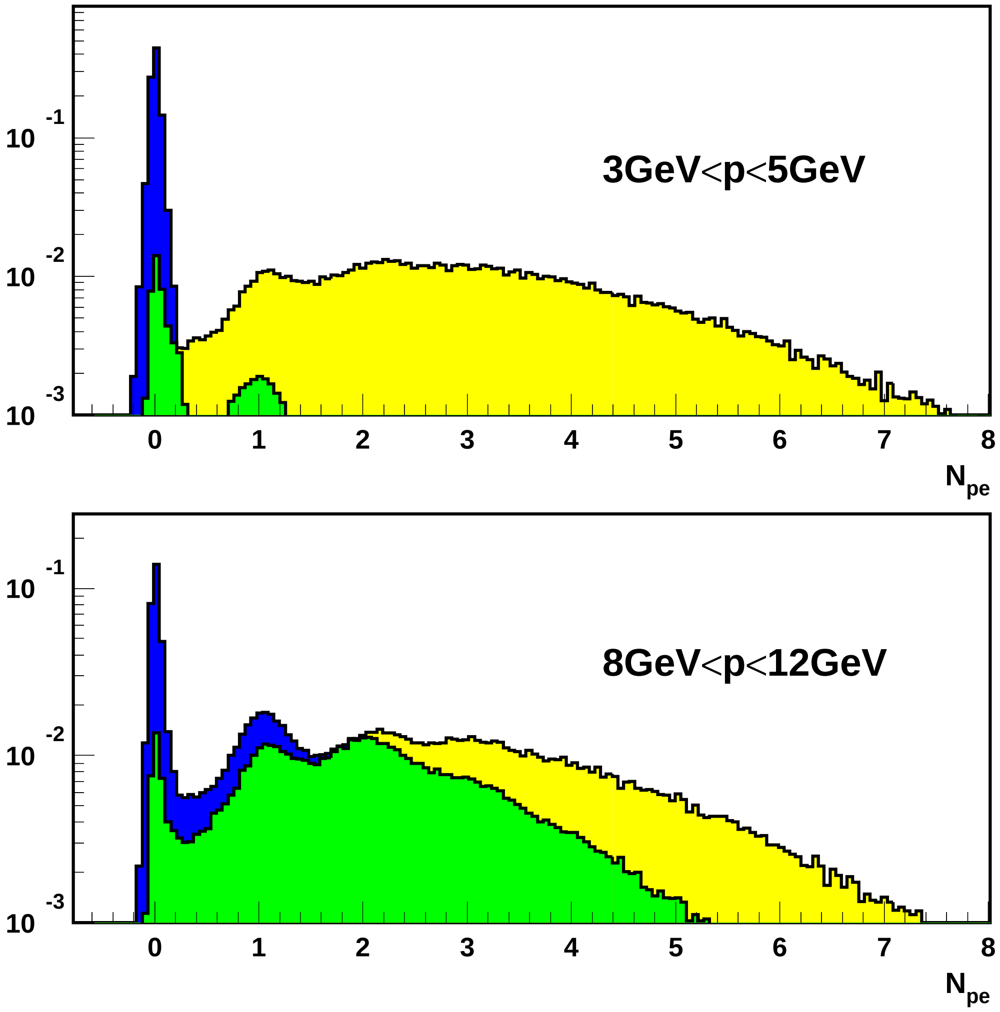

Figure 3.19: Normalised Čerenkov Signal for Hadrons (dark) and Positrons (light) below and above the Pion Threshold from 1995 Data

It is instructive to look at the pulse height spectra for hadrons and positrons both below and above the pion threshold, depicted in figure 3.19. As expected the hadron signal below the pion threshold is close zero with a few counts at one photoelectron, while the positrons show a smooth continuous distribution in N_{pe}, with an average around three. Above the pion threshold both distributions largely overlap, with a larger zero photoelectron peak in the hadron distribution, which is mostly due to kaons in the sample. The positron distributions above and below the threshold are almost identical. This illustrates that for the 1995 data the Čerenkov was an excellent tool for positron/hadron separation below 5.72 GeV and that it can be used for kaon/pion separation between 5.72 and 20.23 GeV. In the analysis of the 1996 data the detector will be used mainly for kaon/pion separation which is accomplished by lower pion and kaon momentum thresholds (table 3.2).

For 1998 a conversion of the current Čerenkov detector into an aerogel/gas ring imaging Čerenkov detector (RICH) has been proposed. This would allow the separation of pions, kaons and protons over the full kinematic acceptance of HERMES[73].

3.3.5 The Luminosity Monitor

The luminosity monitor consists of two sets of 12 $NaBi(WO_4)_2)$ crystals with a size of $22 \times 22 \times 200$ mm^3 located on the left and right side of the beam pipe 7.2 meters downstream from the target. The luminosity measurement is based on symmetric Bhabha scattering from the target electrons in the case of a positron beam and symmetric Møller scattering in the case of electrons. The horizontal acceptance of the luminosity monitor is 4.6-8.9 mrad. For a beam energy of 27.5 GeV the symmetric scattering angle is 6.1 mrad. The Bhabha events are separated from the background by requiring a minimum of 5 GeV deposited energy in each side of the luminosity monitor (see figure 3.20). The Bhabha coincidence rate is 132 Hz for a typical beam current of 20 mA and a target density of 1×10^{15} nucleons/cm^2[61]. It has been shown that the measured luminosity rate may depend on the horizontal position and slope of the positron beam[66].

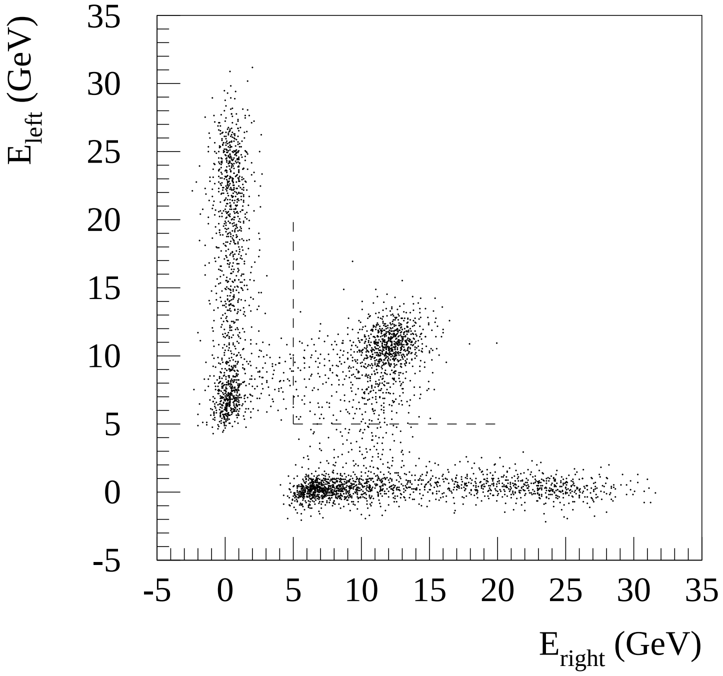

Figure 3.20: Deposited energy in either side of the luminosity monitor with the condition for a Bhabha event

3.3.6 The Trigger

The standard physics trigger for the 1995 data taking period required a coincidence of signals in both hodoscopes (H1, H2), the bunch crossing timing provided by the 'Hera-Clock' and a calorimeter signal with a minimum of 3.5 GeV deposited energy. With a typical target density and about 30 mA positron beam there were about 35 positron and 35 pion induced triggers per second, accompanied by a background rate of 20-100. This background is mostly due to the Hera proton ring which runs through the middle of the spectrometer. For this reason in 1996 an additional forward trigger scintillator was introduced in front of the magnet to improve the background rejection on the basis of time of flight.

3.3.7 The Gain Monitoring System

A gain monitoring system was installed for all detectors that use photomultiplier tubes for the readout (hodoscopes, calorimeter, luminosity monitor and Čerenkov detector). The light of a dye laser at 500 nm is attenuated by a rotating wheel with several attenuation plates and sent through glass fibres to the individual photomultipliers. The signals from the photomultipliers are then compared to the signal of a reference photodiode, thus providing a check of the relative gain of the photomultipliers.

3.4 Data Acquisition and Online Monitoring

3.4.1 Data Acquisition

The Hermes data acquisition system is based on a Fastbus backbone with Cern Host Interfaces (CHI) as Fastbus masters. The CHIs are equipped with digital signal processor (DSP) based Struck Fastbus Readout Engines (FRE) to improve their performance. The drift chamber readout uses LeCroy 1877 TDCs (time to digital converters), while the signals from the photomultiplier tubes and the TRD are digitized by LeCroy 1881 ADCs (analog to digital converters). The magnet chamber readout uses a LeCroy VME based PCOS4 system consisting of 2748 and 2749 modules. Incoming events are processed by the DSPs of the Struck Fastbus Readout Engines, resulting in a reduction of the eventsize by almost a factor of 2. During luminosity runs the data are written to staging disks on site in the East hall by an Alpha 3000X. Between fills of the accelerator these data are transferred via an FDDI link to the main DESY site where they are stored on tape. Additionally the data are also archived locally on exabyte tapes as a backup. The maximal throughput of data is on the order of 1.5 MB/s corresponding to an event rate of 150 Hz. The amount of raw data taken in 1995 was about 2 TeraByte[61].

3.4.2 Online Monitoring and Slow Control

There are many requirements that the online monitoring[74] of the Hermes experiment must meet. Not only must the status of the experiment be known in great detail at all times, but it also must be recorded for use in the offline analysis. At the same time information must be presented to the shift crew in a reliable way that allows for quick and efficient problem identification and that points to possible causes and solutions. To this end it is desirable to incorporate expert knowledge about the different components of the experiment into the monitoring software. It is equally desirable to make the online monitoring information readily available to the component experts in their home institutes.

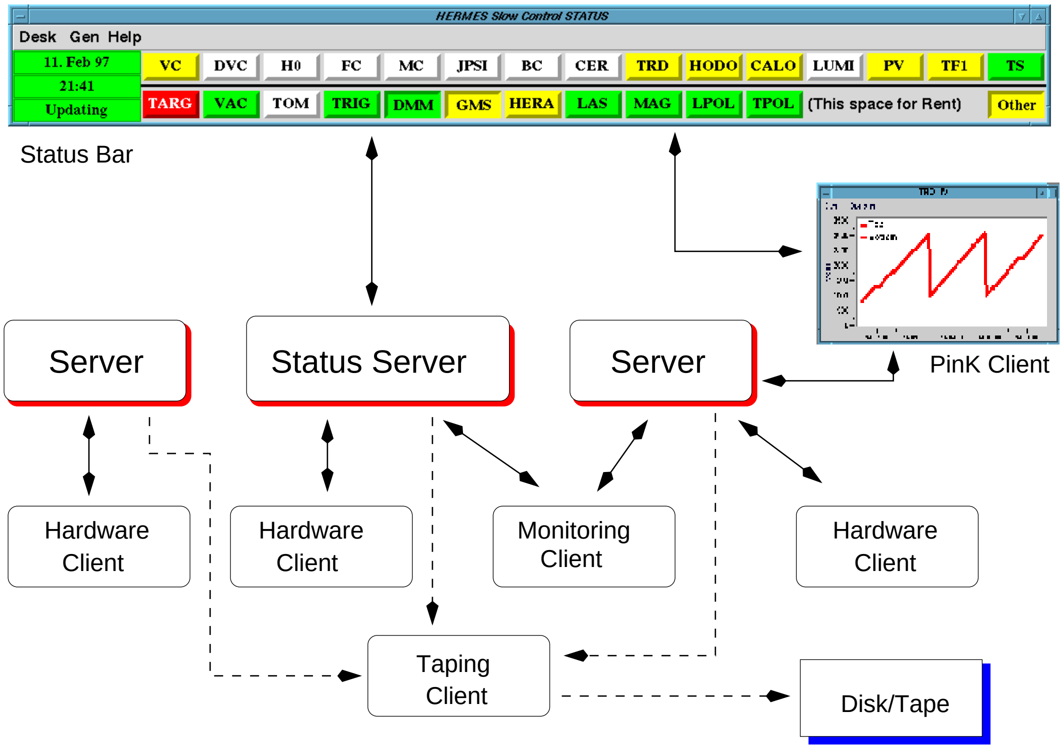

Figure 3.21: Schematic view of the Hermes online monitoring. Information is collected in servers and displayed by PinK clients. The status information is displayed by a particular GUI, the status bar.

The approach the Hermes collaboration has taken to provide a coherent online monitoring solution is based on three components: Adamo[75], Dad[78] and PinK[76]. Like the physics data structures the online monitoring data structures are also based on the Adamo entity relationship model. The Adamo model is complemented by the client-server based Distributed Adamo Database (Dad), which turns a collection of Adamo files into a cross platform accessible database with fast I/O. Dad is a distributed Adamo database providing the inter process communication for HERMES slow and experimental control. Finally there are the graphical user interfaces written in PinK - a Tcl/Tk[77] extension that allows easy access to Dad and Adamo objects. PinK graphical user interfaces (GUIs) form a particular kind of Dad client. The other two kinds of clients are hardware and monitoring clients. Hardware clients report the status of a detector component to a Dad server or communicate a command from the server to the hardware. Monitoring clients analyse the contents of a Dad server according to a set of rules and convert these into a status message (see figure 3.21). A special client is the taping client which collects the slow control information from all applicable servers and writes it to disk/tape for later use in the physics analysis. A particular advantage lies in the independence of the different clients from one another. Different experts can write the hardware, the monitoring and the PinK clients.

A multitude of PinK GUIs are used as permanent displays in the Hermes control room, and wherever a detector expert wants to access information. They monitor the different components of the experiment as well as the status of the Hera accelerator. The heart of the online monitoring system as far as the detector is concerned is the status server and the GUI that is connected to it, the status bar. (see figure 3.21). The status information for every detector component is collected in the status server and indicated in the status bar as the colour of the component button. This button gives access via mouseclick to a hierarchy of additional information and to every Hermes detector monitoring GUI, thus allowing the identification of the source of problems.

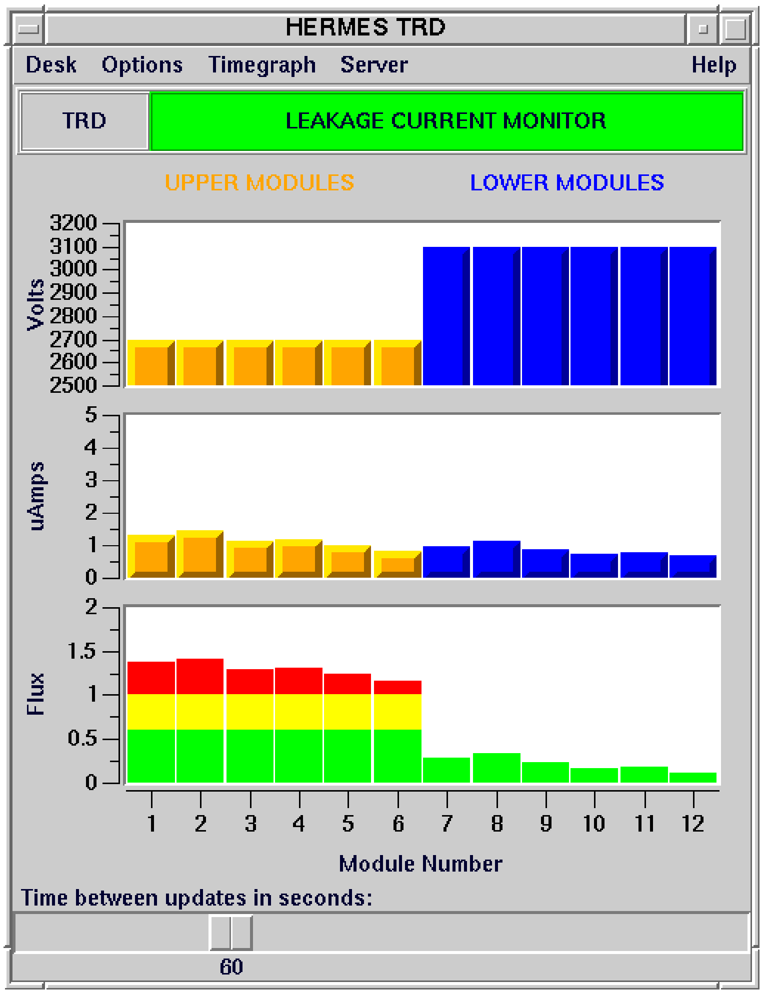

Figure 3.22: Picture of the TRD HV monitoring client

One can take the high voltage monitoring for the TRD as an example of a monitoring PinK GUI (figure 3.22). The obvious features are three barcharts for the high voltage, the leakage current and the 'flux' for each module. Besides these features a variety of time dependent graphs can be produced. The typical TRD operating voltage is 3100 V and the trip threshold is set to 10 μA. At the beginning of each fill when the detectors are switched on, the radiation background may be large which leads to large leakage currents and prohibits the TRD from reaching the full operational voltage. The flux value is a measure of this background and is defined as

$$\text{flux} = \log_{10}(2 \times 10^4 \cdot I/M) \tag{3.10}$$

where I is the leakage current and M is the gas gain calculated according to equation (4.52). This allows the prediction of the leakage current at 3100 V while the detector is still at a lower voltage and so avoids unnecessary trips. During 1995 the sensitivity of the TRD to synchrotron radiation background was used to help optimise the beam tune in the HERMES region by the HERA control room.

Chapter 4

The Transition Radiation Detector

The transition radiation detector (TRD) is the main contribution of the Canadian HERMES group to the apparatus of the HERMES experiment. It will be described in detail in this chapter, including a short review of the theory of transition radiation, details of the construction of the TRD and a comparison of the performance of the HERMES TRD to other transition radiation detectors.

The phenomenon of transition radiation (TR) was first predicted by Ginzburg and Frank for the optical region in 1946[79]. In the following decade it was shown by Garibian[80] that transition radiation is also emitted at x-ray energies. As opposed to the optical TR which is largely absorbed in the radiator itself, x-ray TR can be observed behind the radiator, which makes it potentially more valuable for applications. It took until the early 1970s before transition radiation was demonstrated to be useful for the identification of ultrarelativistic particles in high energy physics experiments[81]. During the last ten years transition radiation detectors have become part of the particle identification system of several major particle physics experiments. However, as a result of the long planning and installation phases of large experiments, the experience with TRDs is still limited and they still represent new technology.

The basic principle of transition radiation detectors lies in the proportionality between produced transition radiation and the Lorentz factor $\gamma = E/mc^2$ of a given particle. This makes it possible in principle to measure γ by detecting the emitted transition radiation, which in turn means that either the energy of a particle with known mass or the mass of a particle with known energy can be determined.

Transition radiation detectors are being used today for three different purposes:

- The separation of electrons and pions for energies below 100 GeV.
- The separation of pions and kaons for energies above 100 GeV.
- The measurement of the energy of cosmic muons with energies in the TeV region.

Most of them are used for electron/hadron separation, particularly in environments where the transition radiation detector offers an advantage to alternative possibilities such as Čerenkov detectors due to the smaller amount of space it requires.

4.1 Transition Radiation

A highly relativistic charged particle that crosses the boundary between two materials with different dielectric constants (ϵ_1, ϵ_2) emits transition radiation (figure 4.1). The cause for this effect can be found in the continuity conditions on electromagnetic fields at boundaries. The Lorentz-transformed electromagnetic fields in both media show a discontinuity in $\overrightarrow{D}$ that is proportional to ($\epsilon_1 - \epsilon_2$). The additional field that is introduced to remove the discontinuity is the transition radiation[82].

An intuitive analogy for the understanding of the character of transition radiation is Bremsstrahlung. In the case of Bremsstrahlung the particle emits radiation due to its rapidly changing velocity in a medium with constant ϵ, while transition radiation is emitted by a particle with constant velocity in a medium with rapidly changing dielectric constant[83]. In the case of a relativistic particle, transition radiation is, like Bremsstrahlung, emitted in the forward direction and the angle between the TR

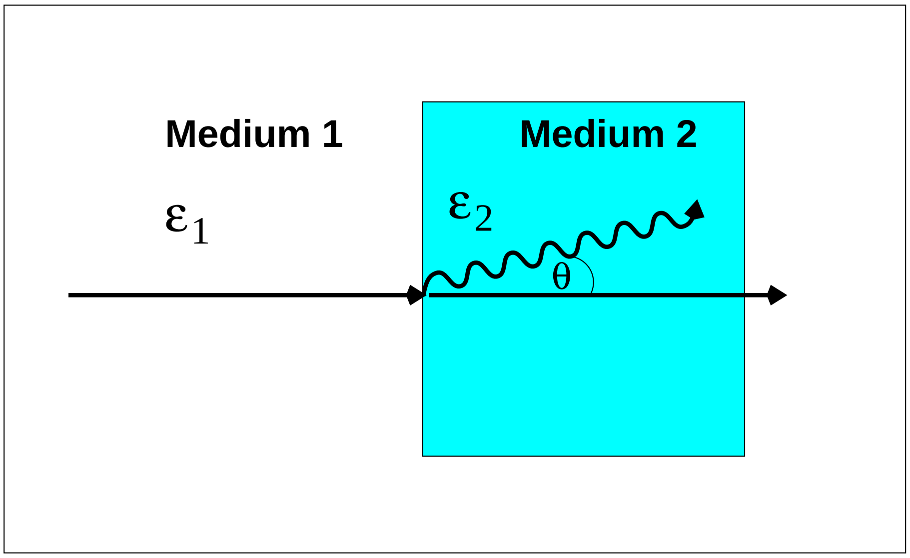

Figure 4.1: Emission of transition radiation at a dielectric boundary.

and the particle is proportional to $\frac{1}{\gamma}$. The transition radiation from ultrarelativistic particles ($\gamma > 1000$) is in the range of X-rays (several keV), which makes it useful for particle physics applications.

There are a number of comprehensive theoretical treatments of transition radiation. In the following sections the notation of Dolgoshein[83] and Artru[82] will be followed.

4.1.1 Single Boundary

First consider an ultrarelativistic particle crossing the boundary from one dielectric medium into another. In this case the transition radiation will be mostly comprised of X-rays and the medium can be considered an electron gas with dielectric 'constant'

$$\epsilon(\omega) = 1 - \frac{\omega_p^2}{\omega^2} = 1 - \xi^2 \tag{4.1}$$

where ω_p is the plasma frequency of the medium

$$\omega_p = \sqrt{\frac{4\pi\alpha n_e}{m_e}} = 28.8\sqrt{\rho\frac{Z}{A}} \quad [eV]. \tag{4.2}$$

Here n_e is the electron density, m_e the electron mass, ρ the density of the material, $\alpha = 1/137$, Z is the atomic number and A is the atomic weight. The transition radiation that is emitted per unit solid angle Ω and unit frequency ω can be approximated by

$$\begin{aligned}\left(\frac{d^2W}{d\omega d\Omega}\right)_{\text{SingleBoundary}} &= \frac{\alpha}{\pi}\left|\frac{\theta}{\gamma^{-2}+\theta^2+\xi_f^2} - \frac{\theta}{\gamma^{-2}+\theta^2+\xi_g^2}\right|^2 \\ &= \frac{\alpha}{\pi}\left|\frac{\theta}{\eta_f} - \frac{\theta}{\eta_g}\right|^2\end{aligned} \tag{4.3}$$

with

$$\eta_i = \gamma^{-2} + \theta^2 + \xi_i^2 \tag{4.4}$$

where θ is the angle of emission and the subscripts f and g stand for *foil* (or *fibre, foam*) and *gap* (or *gas*), the materials typically used for TRD radiators. This approximation is subject to the conditions

$$\gamma \gg 1; \quad \xi_g, \xi_f \ll 1; \quad \theta \ll 1 \tag{4.5}$$

The integration of equation (4.3) over Ω leads to the energy spectrum of transition radiation for a single boundary:

$$\frac{dW}{d\omega} = \frac{\alpha}{\pi}\left[\frac{\xi_f^2+\xi_g^2+2\gamma^{-2}}{\xi_f^2-\xi_g^2}\ln\frac{\gamma^{-2}+\xi_f^2}{\gamma^{-2}+\xi_g^2} - 2\right] \tag{4.6}$$

The spectrum from a single surface is a monotonically decreasing function that drops proportionally to w^{-4} at high frequencies. This behaviour introduces a frequency cutoff which leads to a condition for having a useful amount of TR yield:

$$\omega \lesssim \gamma\omega_{pf} \tag{4.7}$$

where ω_{pf} is the plasma frequency of the surface material. Figure 4.2 illustrates this with the energy spectrum from a polyethylene (CH_2) surface with plasma frequency $\omega_{pf} = 20.9$ eV.

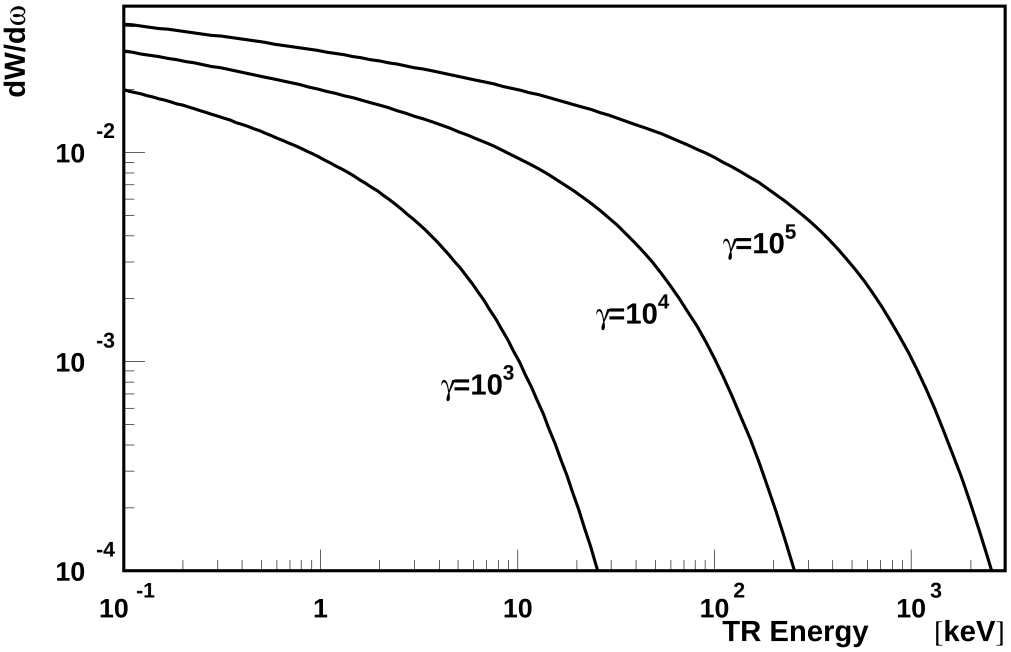

Figure 4.2: TR spectra from a polyethylene (CH_2) surface for for $\gamma = 10^3, 10^4, 10^5$, corresponding to electrons of 0.5, 5, and 50 GeV

Clearly for higher γ the TR spectrum is shifted towards higher energies. Therefore the probability for the emission of a photon above a certain energy grows with γ. The mean energy radiated in one medium/vacuum transition is obtained by integrating over (4.6) for $\xi_g = 0$:

$$W_{TR} = \frac{2}{3}\alpha\gamma\omega_{pf} \tag{4.8}$$

Equation (4.8) illustrates two main qualitative features of transition radiation:

The linear dependence on $\alpha = 1/137$ shows that many transitions are necessary for a practical detector. A useful formula for the mean number of photons above a certain energy per transition is

$$N(\omega > 0.15\gamma\omega_{pf}) \simeq 0.5\alpha \tag{4.9}$$

The direct proportionality to γ is the physical basis for the use of transition radiation detectors for electron/hadron separation. A 5 GeV pion has a γ of 36, while a 5 GeV electron has a γ of almost 10^4. This difference, of almost two orders of magnitude in radiated energy, can be used to distinguish electrons and hadrons.

However, equation (4.8) is only an ideal approximation that illustrates the qualitative behaviour of TR.

4.1.2 Single Foil - The Formation Zone

In moving from the case of a single boundary to a single foil a second boundary is introduced. Therefore an interference term is added to equation (4.3) and the resulting formula can be written as

$$\begin{aligned} \left(\frac{d^2W}{d\omega d\Omega}\right)_{\text{SingleFoil}} &= 4\sin^2\frac{\phi_f}{2}\cdot\left(\frac{d^2W}{d\omega d\Omega}\right)_{\text{SingleBoundary}} \\ &= 4\sin^2\frac{\phi_f}{2}\cdot\frac{\alpha}{\pi}\left|\frac{\theta}{\eta_f}-\frac{\theta}{\eta_g}\right|^2 \end{aligned} \tag{4.10}$$

with

$$\phi_f = \frac{1}{2}\eta_f d_f \omega \tag{4.11}$$

where d_f is the foil thickness. It is apparent that for values of d_f with

$$d_f < \frac{2}{\eta_f \omega} = z_f \tag{4.12}$$

the yield is smaller than the single surface yield due to destructive interference, and as it varies basically with ϕ_f^2 it is greatly reduced for $d_f \ll z_f$. The parameter z_f is referred to as the length of the 'formation zone'. The formation zone can also be understood as the minimum distance the particle needs to travel inside the new medium in order for the electromagnetic fields to reach a new equilibrium. The formation zones for air and polyethylene are illustrated in figure 4.3. The length of the formation zone is about 100 times larger in air than in polyethylene. The formation zone in polyethylene at 10 keV is about 10 μm for values of γ between 10^3 and 10^4.

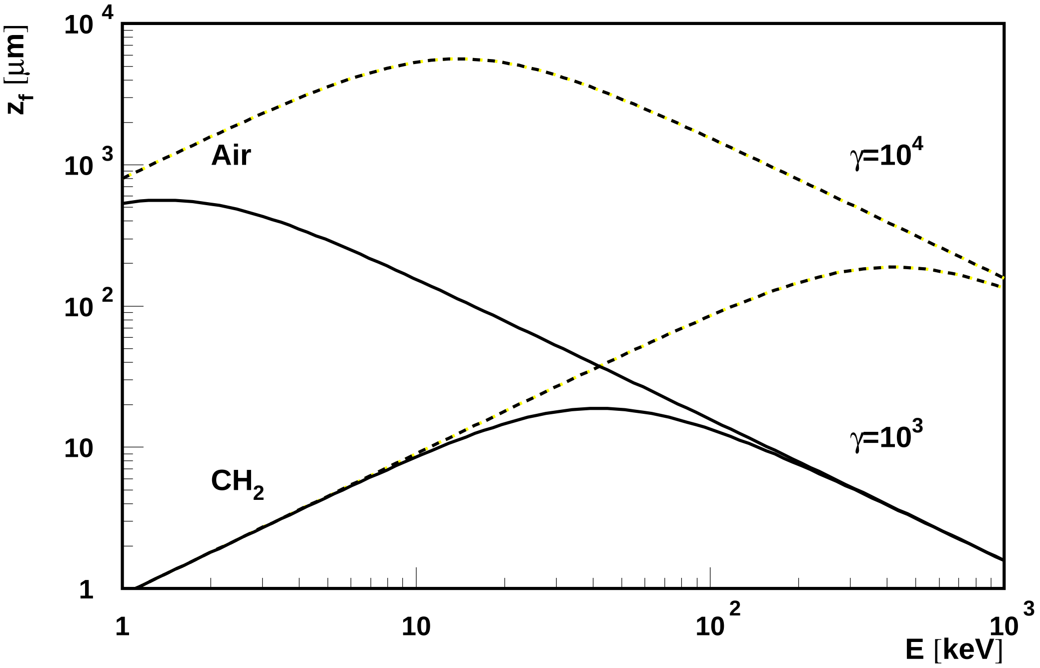

Figure 4.3: Formation Zones for Air and Polyethylene.

For values of γ with

$$\gamma > \gamma_f = \frac{d_f \omega_{pf}}{2} \tag{4.13}$$

the frequency cutoff is determined by the formation zone effect, because from

$$\phi_f \sim \frac{1}{2} \omega d_f \xi_f^2 = \frac{\gamma_f \omega_{pf}}{\omega} \sim 1 \tag{4.14}$$

the new cutoff condition follows

$$\omega < \min(\gamma \omega_{pf}, \gamma_f \omega_{pf}) \tag{4.15}$$

For practical calculations the following can be used, where ρ_f is the density of the foil material:

$$\begin{aligned} \gamma_f &\simeq 2.5(\omega_{pf}/\mathrm{eV})(d_f/\mu\mathrm{m}) \\ (\gamma_f \omega_{pf}/\mathrm{keV}) &\simeq 10^4(\rho_f d_f/\mathrm{gcm}^{-2}) \end{aligned} \tag{4.16}$$

4.1.3 Transition Radiation from a Foil Stack

As seen already in equation (4.8) the total TR yield is proportional to α. Hence, for the practical use of transition radiation several hundred foils must be used. Two additional phenomena are encountered in changing from a single foil to a stack of foils: Absorption of the emitted transition radiation within the foil stack and multiple foil interference. Now consider a stack of foils with thickness d_f and regular spacing where d_g is the thickness of the gaps. In this case an interference factor is added to the single foil yield[82]:

$$\left(\frac{d^2W}{d\omega d\Omega}\right)_{NFoils} = \left|\frac{1-C^N}{1-C}\right|^2 \left(\frac{d^2W}{d\omega d\Omega}\right)_{SingleFoil} \tag{4.17}$$

with

$$\begin{aligned} C &= \exp(i\phi_f + i\phi_g - \frac{1}{2}\sigma_f - \frac{1}{2}\sigma_g) \\ &= e^{i\phi - \frac{1}{2}\sigma} \end{aligned} \tag{4.18}$$

C depends on θ through ϕ_f and ϕ_g. The absorption factor σ_i is the product of the absorption coefficient μ, density ρ and thickness d of the radiator material:

$$\sigma_i = (\mu\rho d)_i \tag{4.19}$$

The average value of the interference factor can be expressed as the 'effective number of foils' N_{eff}:

$$N_{eff} = \frac{1-e^{-N\sigma}}{1-e^{-\sigma}} \tag{4.20}$$

which for $N \to \infty$ saturates at $\frac{1}{1-e^{-\sigma}}$. As previously shown the formation zones in air are about two orders of magnitude larger than in CH_2. An appreciable yield from the N foil stack can only be obtained if the gap between the foils is of the order of the air formation zone.

The radiators that are used in practice for transition radiation detectors are foil stacks, foams and fibres. While a regular foil stack is the optimal radiator, the mechanical design of large TRDs adds some other constraints that make the use of fibre or foam radiators more viable. In these cases the regular foil stack still provides a good guideline, because to the particle a foam or fibre radiator appears like an irregular stack of foils, where d_f and d_g follow more or less broad distributions.

4.1.4 Formalism in Dimensionless Variables

If the scaled variables

$$\Gamma = \frac{\gamma}{\gamma_f}$$
$$\nu = \frac{\omega}{\omega_f} \tag{4.21}$$

are introduced, with γ_f as in equation (4.13) and

$$\omega_f = \gamma_f \omega_{pf} \tag{4.22}$$

the single foil transition radiation yield can be expressed as

$$\left(\frac{d^2W}{d\omega d\Omega}\right)_{\text{SingleFoil}} = \frac{2\alpha}{\pi} G \tag{4.23}$$

with

$$G = \int_a^\infty (y-a)dy \cdot \left(\frac{1}{y} - \frac{1}{y+\nu}\right)^2 2\sin^2\frac{y+\nu}{2} \tag{4.24}$$

In the case of vacuum gaps the variables a and y are given as

$$a = \nu/\Gamma^2$$
$$y = \eta_g^2 \omega \frac{d_f}{2} \tag{4.25}$$

and ν and Γ are more convenient variables for G:

$$G = G(\nu, \Gamma). \tag{4.26}$$

This is the usual way to express G, since by transforming ω_{pf}, ω_{pg} and γ to

$$\begin{aligned} \omega'_{pf} &= \sqrt{\omega_{pf}^2 - \omega_{pg}^2} \\ \omega'_{pg} &= 0 \\ \gamma' &= \sqrt{\frac{1}{\gamma^2} + \frac{\omega_{pg}^2}{\omega^2}} \end{aligned} \tag{4.27}$$

the given choice of materials can always be reduced to the case of a vacuum gap and a material with an effective plasma frequency ω'_{pf}. Here γ' is the effective Lorentz factor.

$G(\nu, \Gamma)$ is shown in figure 4.4[82]; the function has peaks at values of $\nu^{-1} = \pi, 3\pi$ etc., and valleys at $\nu^{-1} = 2\pi, 4\pi$ etc. The peak at

$$\nu = \frac{1}{\pi} \tag{4.28}$$

can be used to optimise the transition radiation yield. The foil thickness and the X-ray detector can be chosen in such a way that the mean TR energy

$$\overline{\omega} \approx \frac{d_f \omega_{pf}^2}{2\pi} \tag{4.29}$$

corresponds to the condition (4.28). The height of the peak increases logarithmically with Γ:

$$G(\text{peak}) \approx \ln(\Gamma^4/\nu^3) - 2.4 \tag{4.30}$$

Using an extension of this formalism for the foil stack, Artru et al. find a steep increase for $\nu = \frac{1}{\pi}$ at

$$\Gamma = \frac{\sqrt{1 + d_g/d_f}}{\pi} \tag{4.31}$$

where d_g and d_f are the gap and foil thickness, respectively.

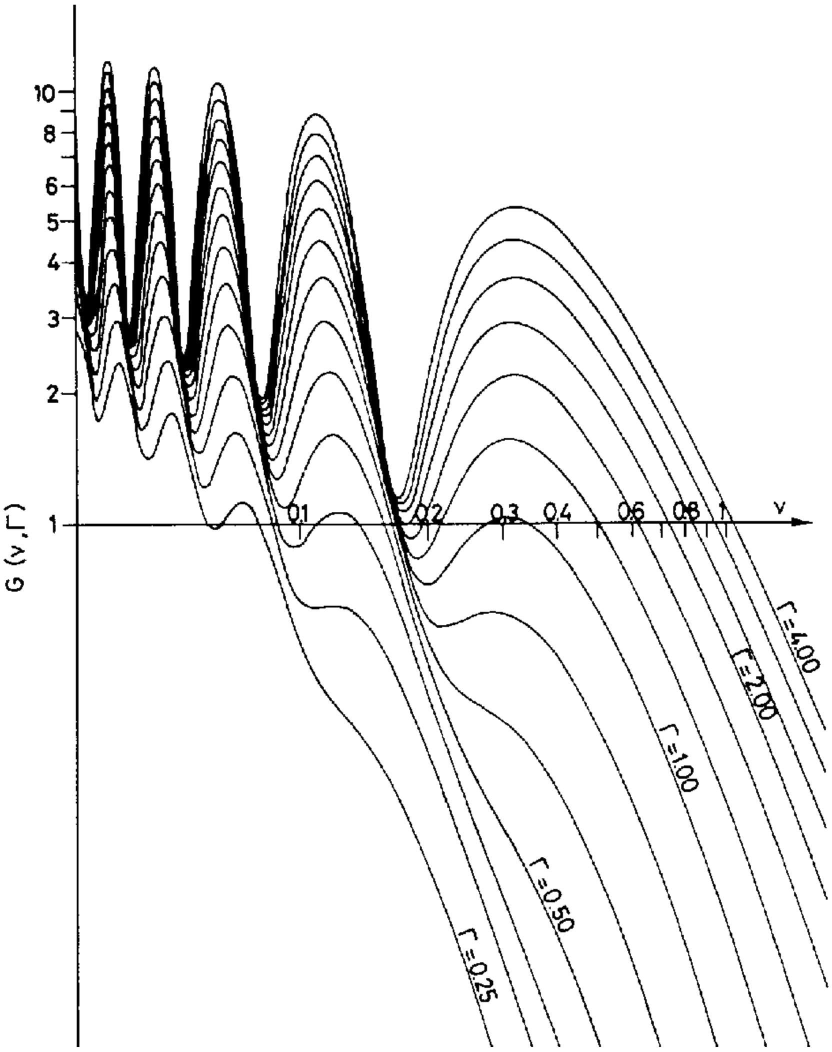

Figure 4.4: Transition radiation energy spectrum $G(\nu, \Gamma)$ for different values of Γ[82].

While transition radiation itself, unlike Čerenkov radiation, is not a threshold effect, effective thresholds can appear due to the geometry and the materials of the setup. The absorption of low energy X-rays in the radiator, the shift towards higher energies with γ and this pseudo-threshold effect lead to practically observed transition radiation only for particles with $\gamma \gtrsim 1000$.

4.2 Detection of Transition Radiation

In principle, transition radiation can be separated from the radiating charged particle by the use of a magnetic field. However, in most experiments this is not practical and due to the small emission angle θ the transition radiation photons will be detected together with the charged particle. Care must be taken not to disturb the charged particle more than necessary to minimise the effect on subsequent detectors, such as the calorimeter in HERMES. Both, the X-rays and the charged particles will deposit energy in any gaseous detector by ionisation of the gas. The response of the detector to the secondary electrons produced in this process will be the same for an X-ray or a charged particle. For this reason distinguishing particles with high and low γ is in practice reduced to determining the difference between a dE/dx and a $dE/dx + TR$ signal.

4.2.1 Charged Particles

A charged particle of moderate energy loses energy in a gas primarily by ionisation. The energy loss per unit length is given by the Bethe-Bloch equation[55]:

$$\frac{dE}{dx} = -Kz^2 \frac{Z}{A} \frac{1}{\beta^2} \left[\frac{1}{2} \ln \frac{2m_e c^2 \beta^2 \gamma^2 E_{max}}{I^2} - \beta^2 - \delta/2 \right] \tag{4.32}$$

with

$$K = 4\pi N_A r_e^2 m_e c^2 = 0.307 \quad MeVg^{-1}cm^2 \tag{4.33}$$

where ze is the charge of the incident particle, Z the atomic number and A the atomic mass of the gas, m_e and r_e the electron mass and classical radius, I the mean ionisation energy, δ a density effect correction, and E_{max} the maximum kinetic energy which can be transferred to a free electron in a single collision. For a particle with mass M and momentum $M\beta\gamma c$, E_{max} is given by

$$E_{max} = \frac{2m_e c^2 \beta^2 \gamma^2}{1 + 2\gamma m_e/M + (m_e/M)^2} \tag{4.34}$$

The basic features of the momentum dependence of the Bethe-Bloch equation are a fast drop at intermediate momentum which is proportional to β^{-2}, a minimum at

$$p \approx 3M/c \quad [GeV/c] \tag{4.35}$$

and a logarithmic rise for higher momenta. For the case of pions in the Hermes TRD this is illustrated in figure 4.5, showing the energy that was deposited in a single TRD module, normalised to ≈ 1 at the minimum.

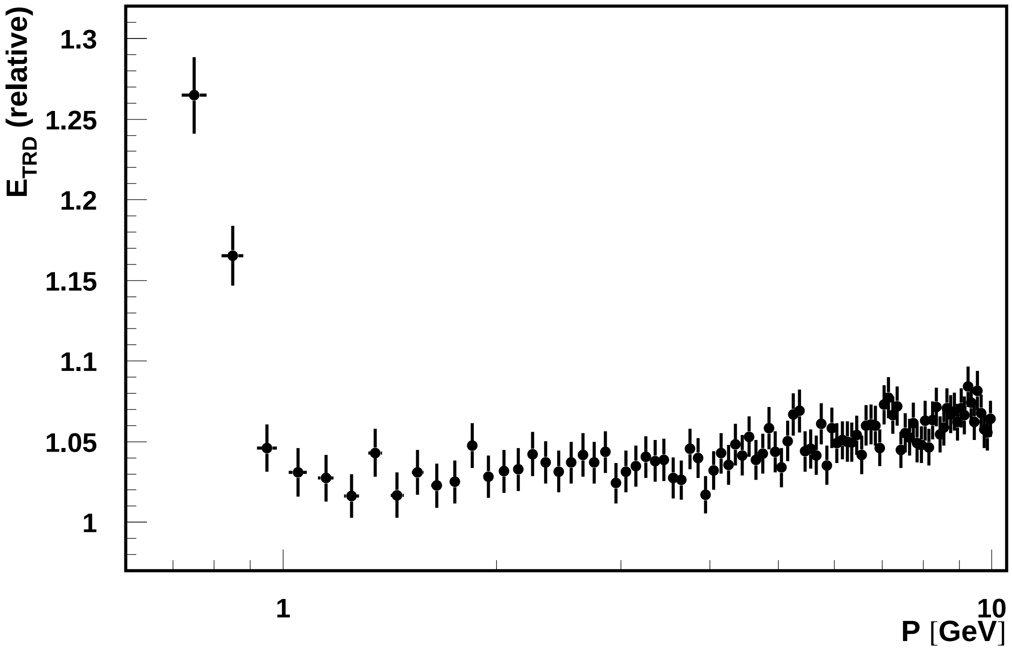

Figure 4.5: TRD signals of pions versus momentum, illustrating the drop, minimum and logarithmic rise of the Bethe-Bloch equation.

The position of the minimum of the distribution is at a slightly higher momentum than expected. This is likely due to kaon contamination of the pion sample and the longer paths through the detector for lower momentum particles as a result of their stronger deflection in the detector magnet. However, the qualitative features of equation (4.32) can be clearly seen.

In a number of collisions the energy that is transferred to the electron is large enough for this electron in turn to ionise another atom. These electrons are also referred to as *δ-rays.*

4.2.2 X-rays

The main process for energy loss in a gas for photons in the typical energy range of transition radiation (several keV) is photoelectric absorption. The photon flux absorbed in a layer of gas with thickness l is

$$F = 1 - e^{l/\lambda} \tag{4.36}$$

where λ is the mean absorption length, which is a function of the photon energy and the atomic number of the gas. A gas with higher atomic number Z will generally have a shorter absorption length, as the absorption increases as Z^4/ω^3. The mean absorption length for the noble gases Argon, Krypton and Xenon, that are frequently used in gaseous detectors, are shown in figure 4.6[83].

An X-ray photon with energy E_γ can be absorbed only in the j shell of an atom, if the binding energy E_j of the shell is smaller than the photon energy. Absorption of the photon results in the emission of a photoelectron with energy $E_e = E_\gamma - E_j$. The exited atom returns to the ground state by either the emission of a fluorescence photon or an Auger electron. The Auger electron results from the rearrangement of several electrons from higher shells and is emitted with an energy slightly smaller than E_j. A fluorescence photon is emitted if the exited electron drops from the i shell back into the j shell. The energy of this photon is $E_i - E_j$ and therefore smaller than E_j. This leads to a much longer absorption length and the 'escape peaks' that are shown in figure 4.6.

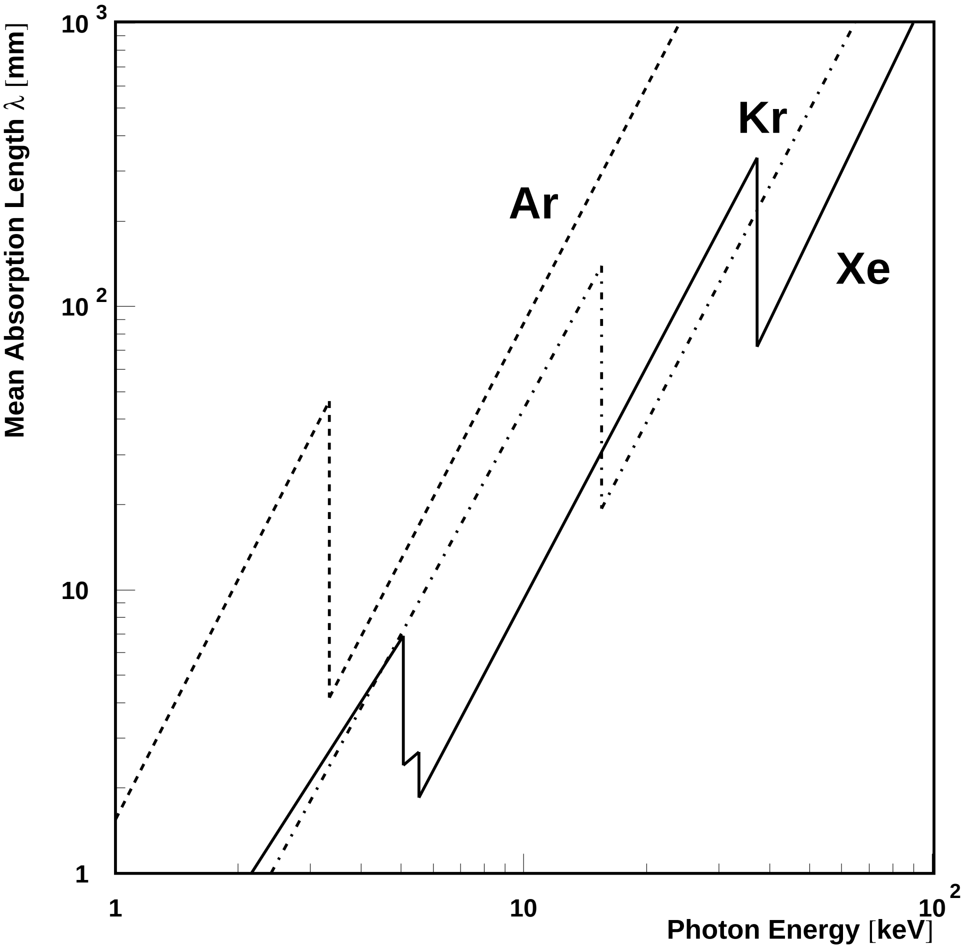

Figure 4.6: Mean absorption length λ in mm for argon, krypton and xenon[83].

4.2.3 Proportional Chambers

The simplest and most commonly used device to detect transition radiation is the multiwire proportional chamber (MWPC). The operation of a MWPC is based on the avalanche multiplication of photoelectrons in a strong electric field[85][86]. If the primary ionisation electrons gain sufficient energy from the accelerating electric field in the detector, they can also ionise gas atoms. These secondary electrons can, in turn, produce tertiary electrons and so on. The repetition of this process results in the formation of an avalanche.

If α is the mean free path of an electron in a gas, then $1/\alpha$ is the probability for an ionisation per unit path length, which is also known as the first *Townsend coefficient.* For n electrons that travel a path of length dx the number of secondary electrons is

$$dn = n\alpha \; dx \tag{4.37}$$

The integration over the total length of the path x yields the total number of secondary electrons

$$n = n_0 e^{\alpha x} \tag{4.38}$$

which shows the exponential growth typical of an avalanche. The multiplication factor M, often also referred to as the *gas gain*, is then defined as the increase in the number of electrons due to the avalanche:

$$M = \frac{n}{n_o} = e^{\alpha x} \tag{4.39}$$

For the case of a non-uniform field with $\alpha = \alpha(x)$ this becomes

$$M = exp\left[\int_{x1}^{x2} \alpha(x) dx\right] \tag{4.40}$$

In a simple proportional counter a wire used as the anode in the center of a cathode tube produces an electric field that is large at the wire and falls like $1/r$ to the walls. For thin wires very large fields can be achieved near the wire. The $1/r$ drop off of the electric field means that the primary electrons first drift towards the wire and produce an avalanche only when they are already close to the anode. The signal that is produced this way is proportional to the originally deposited energy and to the voltage of the chamber, hence the name *proportional chamber.* At a voltage V_T the field near the wire becomes large enough to start the avalanche spontaneously. The capacitance of the proportional counter can be written

$$C = \frac{2\pi\epsilon_0}{\ln(\frac{b}{a})} \tag{4.41}$$

with wire radius a and tube radius b. This also allows the definition of the critical energy E_c at which the avalanche starts in these terms:

$$E_c = \frac{CV_T}{2\pi\epsilon_0}\frac{1}{a} \tag{4.42}$$

In this case the integration runs from the wire radius to the critical radius r_c at which the field drops below E_c:

$$M = exp\left[\int_a^{r_c} \alpha(r)dr\right] \tag{4.43}$$

The frequently used ansatz

$$\frac{\alpha}{p} = Ae^{-B\frac{p}{E}} \tag{4.44}$$

with the pressure p and the material constants A and B, together with the assumption that the coefficient α depends linearly on the electron energy E_e

$$\alpha = kNE_e \tag{4.45}$$

where N is the number of molecules per unit volume and k is another material constant, leads in this case to a simple expression for the gas gain of a proportional counter with capacitance C for a voltage V[88]:

$$M(V) = e^{\frac{CV}{g_c}} \tag{4.46}$$

with

$$g_c = \pi\epsilon_0\sqrt{\frac{E_c}{kN}} \approx 1\ nCm^{-1} \tag{4.47}$$

The multiwire proportional chamber[87] is an extension of this principle, using thin wires strung between parallel cathode foils. This leads to a parallel electric field far away from the wires and to a field with $1/r$-dependence close to the wires, where the avalanche process takes place. The capacitance C per unit length is given by

$$C = \frac{2\pi\epsilon_0}{\pi\frac{l}{s} - \ln(\frac{2a}{s})} \tag{4.48}$$

where l is the anode-cathode distance, a the wire radius and s the wire spacing.

For the calculation of the voltage and pressure dependent gas gain for the Hermes TRD the following ansatz for α has been used, resulting in a much improved description of the data[88]:

$$\frac{\alpha}{p} = A(\frac{E}{p})^{\frac{1}{3}} e^{-B(\frac{p}{E})^{\frac{2}{3}}} \tag{4.49}$$

With the approximation

$$E(r) \approx \frac{CV}{2\pi\epsilon_0}\frac{1}{r} \tag{4.50}$$

this leads to

$$M(V) = e^{VCf(E,p)} \tag{4.51}$$

with

$$f(E,p) = \frac{3}{2}\frac{A}{B}\frac{1}{2\pi\epsilon_0}\left(e^{-B(\frac{p}{E(a)})^{\frac{2}{3}}} - e^{-B(\frac{p}{E(b)})^{\frac{2}{3}}}\right) - q_s \cdot q \tag{4.52}$$

where C is defined as in equation (4.48), p is the pressure and A, B are material constants.

In a pure noble gas secondary photons from the avalanche process ionise atoms in the cathode with the resulting electrons starting new avalanches. This leads to a continuous discharge. For this reason small amounts of a so called 'quench gas' are added to the gas in the proportional counter. This quench gas usually has polyatomic molecules which allow the absorption of photons over a wide energy range due to rotational and vibrational excited states. The quench gas absorbs the secondary photons and dissipates the energy through dissociation or elastic collisions. The additional term $q_s \cdot q$ in equation (4.52) takes into account the reduction of the gain due to the quench gas. Here q is the quench gas concentration in % and q_s is a material constant for the quench gas that was measured at TRIUMF[88].

4.2.4 Discrimination of dE/dx and TR

As already noted previously, in most practical transition radiation detectors the TR photons are detected together with the dE/dx signal of the charged particle. There are basically two different approaches to the discrimination of dE/dx and transition radiation. The two methods of discrimination are *cluster counting* and *charge integration*, also referred to as N- and Q-methods.

The N-method uses the difference in the time structure of the dE/dx and TR signals. The ionisation occurs along the entire path of the particle, which leads to a signal of smaller height and longer duration. The ionisation of the gas by a TR photon on the other hand is well defined in time, as the photon is usually absorbed within millimeters of the cathode (see figure 4.6). This yields a higher and shorter 'cluster' signal. By setting an appropriate threshold on the signal of the multiwire proportional chamber, these clusters can be counted. The distribution of the clusters is Poissonian, as is the background from δ-rays.

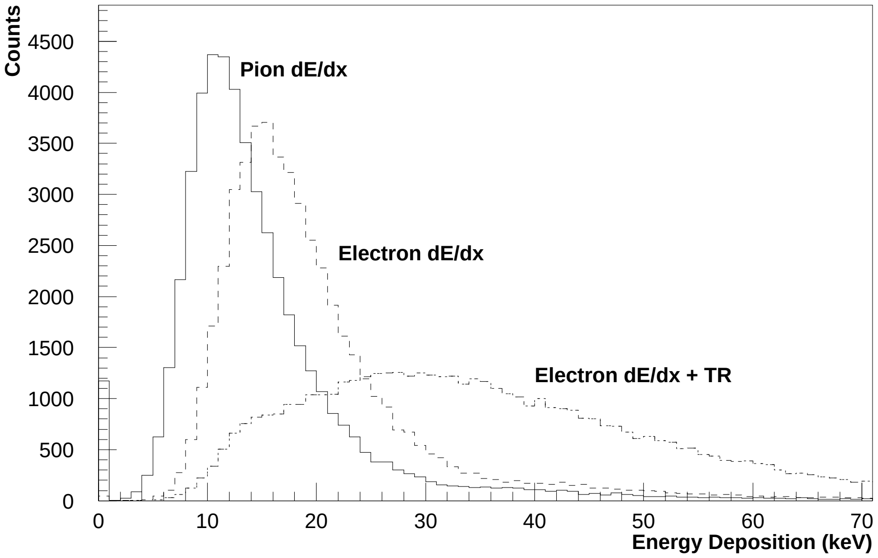

Figure 4.7: Single module TRD spectra for pions (dE/dx) and positrons dE/dx and dE/dx+TR. Monte Carlo simulation.

The Q-method uses the difference in total deposited energy. As illustrated in figure 4.7 the signal of a particle with high γ (e.g. an electron) is on average significantly larger than the signal of a low γ particle. As there are no data available from the HERMES TRD without the radiator, these distributions have been taken from a Monte Carlo simulation of the TRD[89] that was tuned to fit the CERN test beam data. In the case of the Q-method, the background from δ-rays manifests itself as a long high energy tail referred to as the Landau-tail.

Both methods have advantages and disadvantages. In principle, it might be expected that a better electron/hadron separation results from the cluster counting method, due to the fact that the Poissonian tail of the hadron spectrum is smaller than the Landau-tail of the hadron distribution for the charge integration method. Also a TRD using the N-method can be faster and therefore built into the trigger more easily. Alternately the Q-method may be economically more viable, due to the possibility of less expensive readout electronics.

An algorithm that is frequently used with the Q-method to improve the rejection of δ-rays is the truncated mean. The truncated mean E_{TM} is defined as

$$E_{TM} = \frac{\sum_{i=1}^{n} E_i - max(E_i)}{n-1} \tag{4.53}$$

The truncated mean is motivated by the fact that in the case of hadrons the module response that is 'truncated' usually belongs to the δ-ray tail of the distribution. This leads to a reduction of the overlap of the hadron and positron distributions, even if the truncated mean value for positrons is also smaller than the simple mean value. This improvement of the separation of both distributions translates directly into a better hadron rejection.

However, the optimal way to use the full available information in case of the Q-method is a Bayesian probability analysis (see equation 5.4). This leads in general to a pion rejection that is at least twice as good as for the truncated mean.

4.3 TRD Optimisation

Various parameters must be optimised in the design of a transition radiation detector. All components, the radiators, the X-ray detectors and the readout have to be adapted to the specific conditions under which the TRD will operate. It is apparent that a TRD which is used to measure the energy of cosmic muons[91] will look quite different from a TRD operating in a high rate environment which is used also as a tracking detector[92].

The ideal radiator would have a high plasma frequency ω_{pf} to maximize the TR yield (see equation 4.8) and an atomic number Z that is as low as possible to minimize the X-ray absorption in the radiator. The logical choices therefore are low Z metals, such as lithium. However, while transition radiation detectors using stacks of lithium foils have been built and successfully operated, their performance has remained consistently short of theoretical expectations. All experiments so far have shown that a CH_2 radiator basically performs just as well, while being a lot easier to handle.

The ideal structure for a radiator is the regular foil stack. For small TRDs this may be a feasible solution, but for larger experiments this becomes quickly irreconcilable with mechanical and structural considerations. Hence, for larger experiments foam and fibre radiators are favoured. Both of them appear as an irregular foil stack to the traversing particle. So far, fibre materials can be produced in a more regular matrix than foams and therefore typically perform better.

For particles in the several GeV energy range the ideal number of layers for CH_2 radiators in a transition radiation detector for electron/pion separation is about 300. The gaps between foils or fibres should be 200-300 μm and the optimal foil/fibre thickness is 10-25 μ[83]. For higher energies E the gap value has to be increased with E^2 which lengthens the TRD quadratically with the energy of the particle.

The two high Z noble gases krypton and xenon are the natural candidates for a TRD X-ray detector. At first krypton appears to be the better choice as it has a smaller absorption length for X-ray energies above 10 keV (see figure 4.6). However, almost all K-shell fluorescence X-rays of krypton escape detection, while 80 % of the xenon L-fluorescence X-rays are absorbed within 1 cm of xenon[83]. The superiority of xenon for TR X-ray detection has been experimentally verified[93, 94].

The most widely used quench gases are CH_4, CO_2 and CF_4. The choice between them depends on the particular requirements of the TRD, e.g. how fast the response should be.

The thickness of the X-ray detector should be of the order of one absorption length. This means about 10-30 mm per proportional chamber. The requirements are different for the charge integration method that requires a thicker detector to collect the entire deposited energy, than for the cluster counting method, where a thinner X-ray detector would be chosen.

Due to the absorption of TR X-rays within the radiator material (see equation 4.17) a TRD typically consists of a sequence of modules (radiator & detector). The single module radiators must contain at least 100 dielectric layers to allow for a sufficient yield of transition radiation (see equation 4.8). In most high energy physics experiments space is an issue and the total length of a TRD usually will be less than 80 cm. The number of modules therefore is in most cases limited to between 4 and 8.

4.4 Design and Construction of the HERMES TRD

There are twelve TRD modules in total, six above and six below the beampipe. The outer dimensions of the two TRD halves are $401 \times 112 \times 61$ cm^3. Each module consists of a radiator and a multiwire proportional chamber. The radiator has a thickness of 6.35 cm, followed by a flush gap of 0.635 cm (see section 4.4.2), the proportional chamber of 2.54 cm thickness and another flush gap, making the total thickness of each module 10.16 cm. (The original measures were in inches.)

The active area of the TRD is 325×72.4 cm^2, which is 4.7 m^2 of active surface for the top and bottom combined. This makes the HERMES TRD one of the three largest transition radiation detectors in existence. All foils, the window foils of the gap and the cathode foils of the proportional chamber, are made of 50 μm aluminized mylar which is glued to the aluminum frames with a two component epoxy (Araldite). Figure 4.8 shows a schematic view of the TRD.

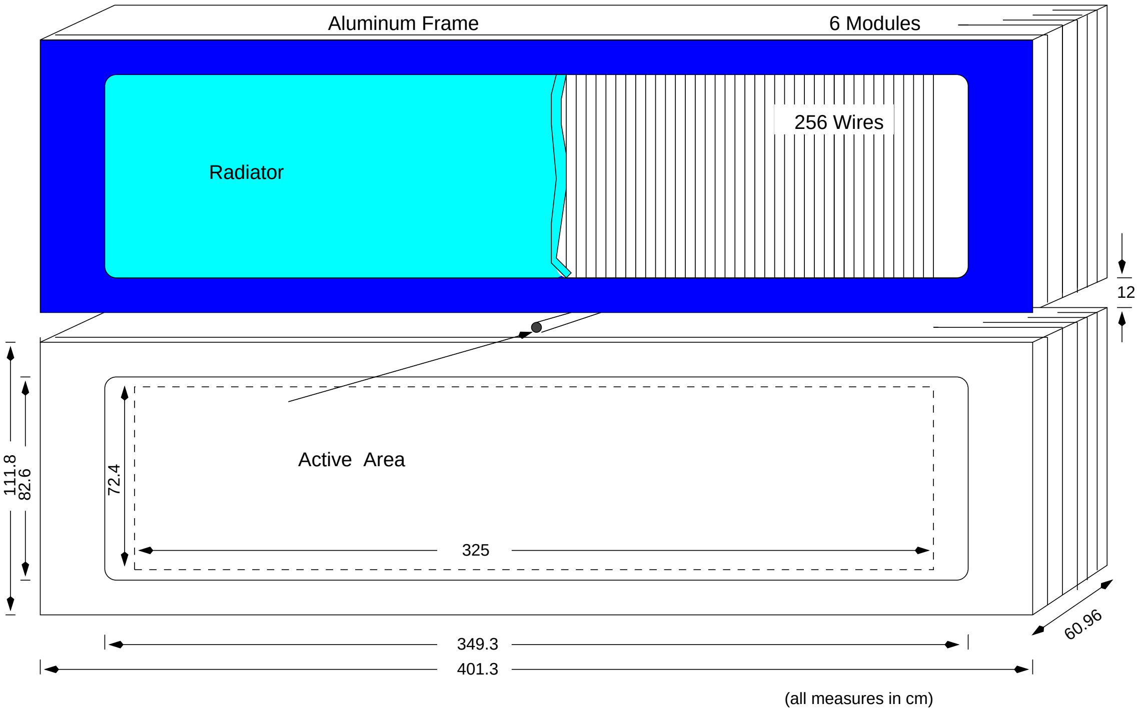

Figure 4.8: Schematic view of the TRD.

4.4.1 The TRD Radiator

A series of foil, foam and fibre radiators was evaluated in a test beam at CERN. As expected the foils performed the best, with the fibres producing about 85% of the TR of the foils. Due to the size of the HERMES TRD, the mechanical advantages of a fibre radiator made this the technology of choice.

The TRD radiator is a loosely packed array of cylindrical polyethylene/polypropylene fibres, that are arranged in two-dimensional layers. The fibres have typical

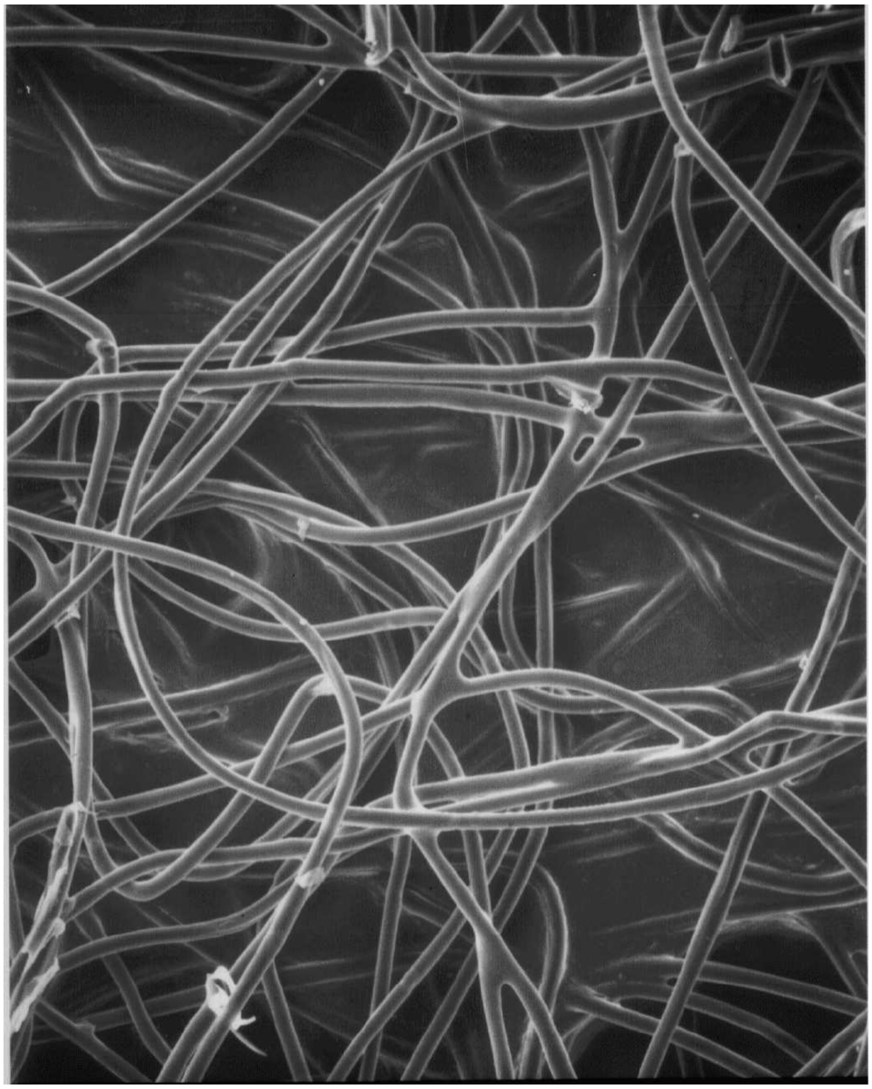

Figure 4.9: Scanning electron microscope picture of the TRD radiator. The diameter of the fibres is about 17-20 μm.

diameters of 17-20 μm, the radiator density is 0.059 g/cm^3 and the thickness of each radiator is 6.35 mm. The cylindrical shape of the fibres leads to an average effective fibre thickness of about 14 μm, which in combination with the bulk density of about 0.9 g/cm^3 for polyethylene leads to an average gap size of about 200 μm. There are about 300 layers per radiator. A scanning electron microscope picture of the radiator is shown in figure 4.9.

This radiator produces a transition radiation spectrum with a mean energy $\overline{\omega}$ of 4.9 keV for the single photon according to equation (4.29). The transition radiation energy for the case $\nu = 1$ is 15.5 keV. The pseudo-threshold below which practically no TR can be observed may be calculated with equation (4.31) to be at $\gamma \approx 920$, which for the energy range of HERMES is equivalent to all positrons being above and all hadrons being below the threshold.

4.4.2 The Multi Wire Proportional Chambers

The geometry of a single proportional chamber is shown in figure 4.10. There are 256 sense wires, spaced 12.7 mm (1/2 inch) apart; the thickness of the chamber is 2.54 cm (1 inch). The wires are made of gold plated beryllium-copper and have a diameter of 75 μm. At both ends five field shaping wires with larger diameters are used to limit the gas gain. The thickness of 2.54 cm corresponds to about one absorption length for the TR photons around 15.5 GeV (see figure 4.6).

Flush gaps of 6.35 mm width protect the MWPCs on either side from the ambient atmosphere. Carbon dioxide is circulated through these flush gaps to avoid the diffusion of oxygen and nitrogen into the wire chamber. An oxygen impurity would severely reduce the signal by absorbing the electrons as they drift towards the anode.

The multiwire proportional chambers are filled with a mixture of 90% xenon and 10% methane. Methane is a very effective quench gas in the energy region between 7.9 and 14.5 eV. CO_2 was considered as well, but turned out to produce a detector response that is too slow.

An additional factor which served to determine the high voltage was the drift velocity from regions of low field in the wire chambers. The event rate dictates that the signal charge collection occurs within 1 μs. Between the requirements of adequate gain and prompt charge collection the two parameters of wire diameter and high voltage were uniquely specified for a given gas mixture. For the chosen gas mixture and a wire diameter of 75 μm the optimal operating voltage of the MWPCs was determined to be 3100 volts[93, 98].

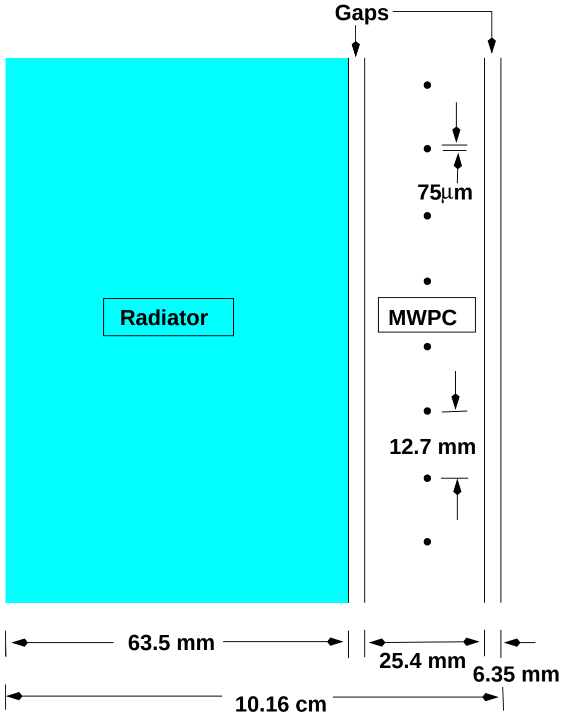

Figure 4.10: Schematic top view of one TRD module

4.4.3 Construction of the TRD

The HERMES TRD was entirely constructed in the detector facility of the TRIUMF laboratory. For this purpose a new clean room was installed in the 'meson hall' side of the TRIUMF cyclotron building.

A single TRD module consists of five aluminum frames in total. The middle frame carries the wires of the proportional chamber, the adjacent frames hold the cathode foils and the first and last frames hold both the window foils and one half of a radiator. Figure 4.11 shows a schematic side view, albeit not to scale, of the structure of a single TRD module. The back window frame of one module and the front window frame of the following module each carry one half of a radiator. The last window frame of the last top and bottom modules does not hold a radiator, while there is an additional half-radiator mounted in front of the very first top and bottom modules.

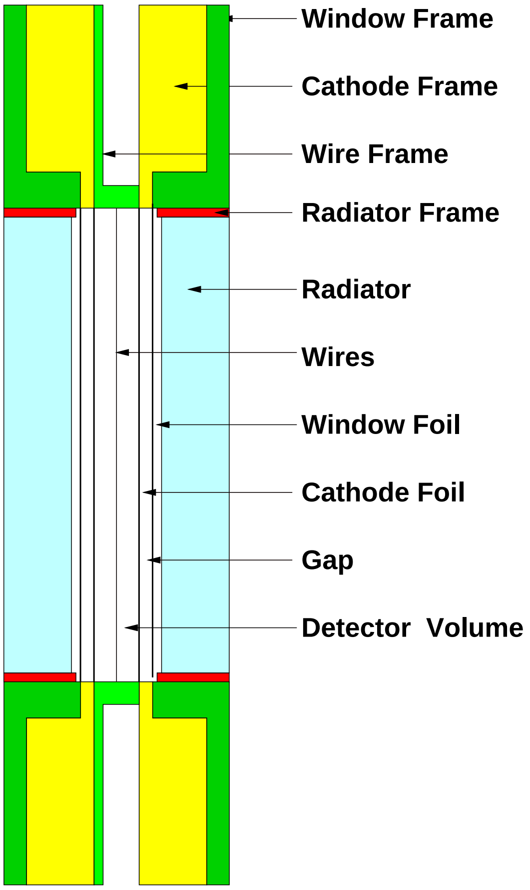

Figure 4.11: Schematic side view of one TRD module (dimensions not to size).

The foils for both cathodes and windows are made from 50 μm aluminized mylar. Using a tensioning device that was specifically designed for the purpose all foils were stretched to a high and isotropic tension. First internal stresses in the foils were relaxed by pre-stretching them to a high tension of about 3.03 kN/m (17.3 lb/in). After 10 minutes the tension was lowered to 1.75 kN/m (10 lb/in). The foils were stretched out over a massive granite slab with a polished surface.

The frame itself was pre-stressed on a neighbouring table to the same tension using a system of ropes and pulleys. A consistent glue bead was laid down by a semi-automatic cart. This cart used a static mixer tube to blend the two components of the epoxy glue (Araldite) without trapped air bubbles. These bubbles might otherwise lead to problems with non-consistent glue connections causing the foil to peel off of the frame or to problems with the gas tight sealing of the chamber.

The pre-stressed frame with the glue bead was lifted over to the granite slab with the stretched foil, lowered onto the foil and glued using a hydraulic system to apply pressure during the curing process.

The foil tension was measured to relax over the period of two months and to stabilise at about 1.26 kN/m (7.2 lb/in). This unusually high tension for a wire chamber cathode foil helps to keep the anode-cathode distance as constant as possible. The gas gain depends on the capacitance of the chamber (see equation 4.51), and a constant anode-cathode distance keeps the capacitance constant. Hence, the high foil tension helps to keep the gas gain constant.

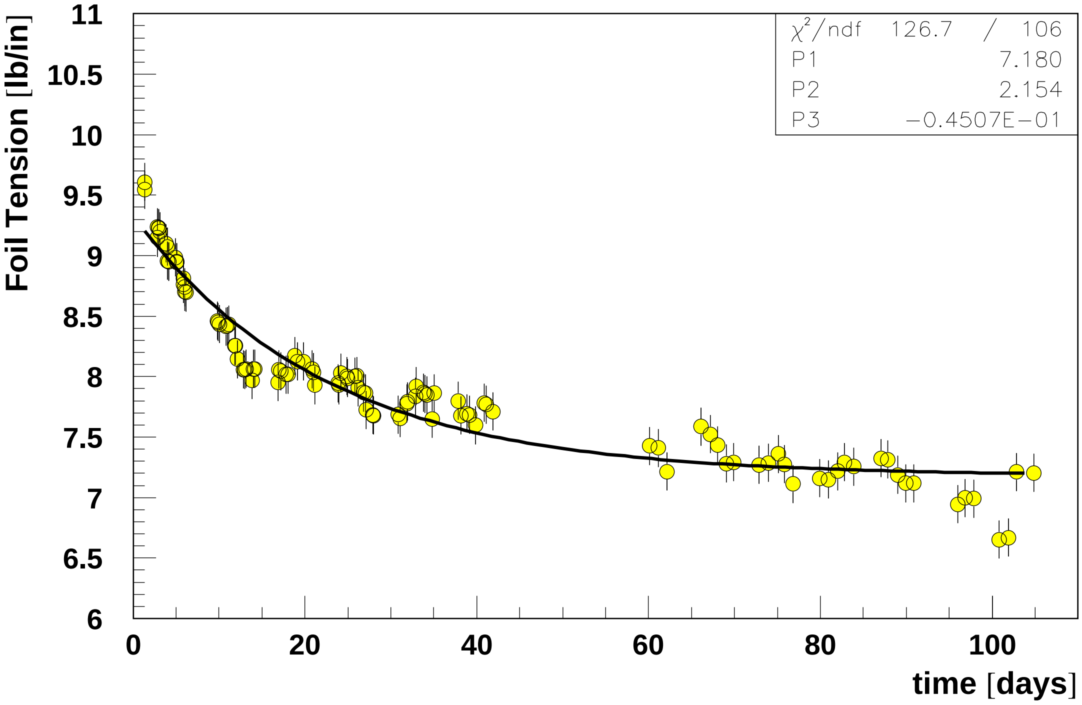

Figure 4.12: Foil tension for a TRD cathode foil monitored over 3 months.

The relaxing foil tension is shown figure 4.12. The fit with a function of the form

$$F(t) = p_1 + p_2 \cdot \mathrm{e}^{p_3 \cdot t} \tag{4.54}$$

describes the observed behaviour well. The tension stayed constant within the uncertainty of the measurement after about 60 days. The relatively large error bars on the single measurements reflect the corrections for changing temperatures that had to be made.

The gold plated beryllium-copper wires were strung on horizontally mounted frames which were also pre-stressed. Precision holes drilled into rails of ULTEM determine the position of the crimp pins which hold the wires. The use of crimp pins instead of soldering pads allows the replacement of broken wires in the narrow spaces of the HERMES experiment. The tension of the individual wires was tested after stringing, and wires with incorrect tensions were replaced.

The frames were assembled into modules and the single modules were subjected to a series of gas and high voltage tests. The responses of the single modules were scanned using a radioactive source on a specifically designed test stand and wires with sub-standard performance were replaced.

The radiators are held by thin aluminum frames which are mounted to the window frames. There are two such radiators per module, each one consisting of ten layers of polypropylene fibre material. The radiator layers were sewn together with surgical needles and thread and glued into their aluminum holding frames with RTV 715 electric glue.

A total of 13 modules and 28 half radiators were constructed and shipped to DESY in special crates in the fall of 1994.

4.4.4 The Gas System

Numerical simulations of the TRD wire chambers show that a change of 10 μm in the anode-cathode distance produces a 1% change in the gain and that the relative pressure in the chamber has to be controlled to one part in 10^5 to maintain the cathode separation to within 10 μm[98]. This was one of the important design specifications for a sophisticated gas system which was built for the TRD[96].

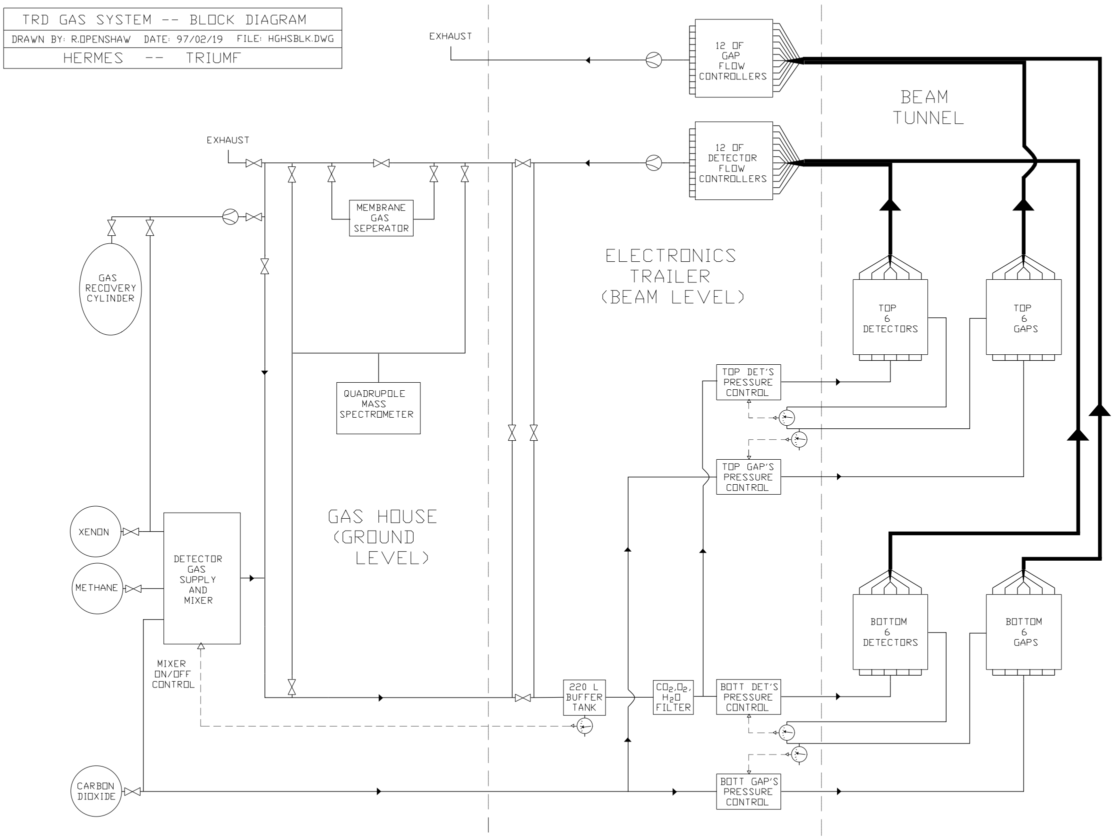

Figure 4.13: Block diagram of the TRD gas system

Sections of the TRD gas system are distributed over the whole HERMES hall. It can be divided into three parts. The first part of the system is inside the beam tunnel, situated at the detector. It consists of the gas volumes of the detectors and the flush gaps as well as the gas distribution manifold. All control units are located outside the tunnel, where they are accessible during the running period. The second part, consisting of the pressure control and the filters for CO_2, O_2 and H_2O is located on the top floor of the electronics trailer, outside the beam tunnel at the same altitude as the chambers. The gas mixing as well as the mass spectrometer which is used to monitor the composition of the chamber gas is in the 'gas house', eight floors above on ground level next to the Hermes Hall. The gas supplies, and the membrane gas separator for the purification and possible recovery of the xenon are also located here. The slow control for the gas system is provided by an industrial programmable logic control (PLC) system that was purchased from the Allen Bradley company. It is located in the electronics trailer as well, but may be controlled from a terminal in the gas house. A block diagram with the main components of the TRD gas system is shown in figure 4.13[95].

The TRD gas system fulfills three main functions:

- Maintain differential pressure stability between detector and gaps to better than 10 μbar.
- Keep the Xe/CH_4 ratio to within 0.1-0.2 % on a short time scale.
- Control impurities of the gas to 0.1-0.2 % on a short time scale.

The gas system uses proportional-integral-differential pressure controllers to keep the differential pressure stable. The gas composition is monitored by a quadrupole mass spectrometer and the gas is cleaned during recycling by molecular sieves and during filling using a membrane gas separator.

The excellent performance of the gas system is illustrated in figure 4.14. During a week of high atmospheric activity with atmospheric pressures between 996 and 1014 mbar, the differential pressures between the gaps and the detectors were kept constant within 10 μbar[96].

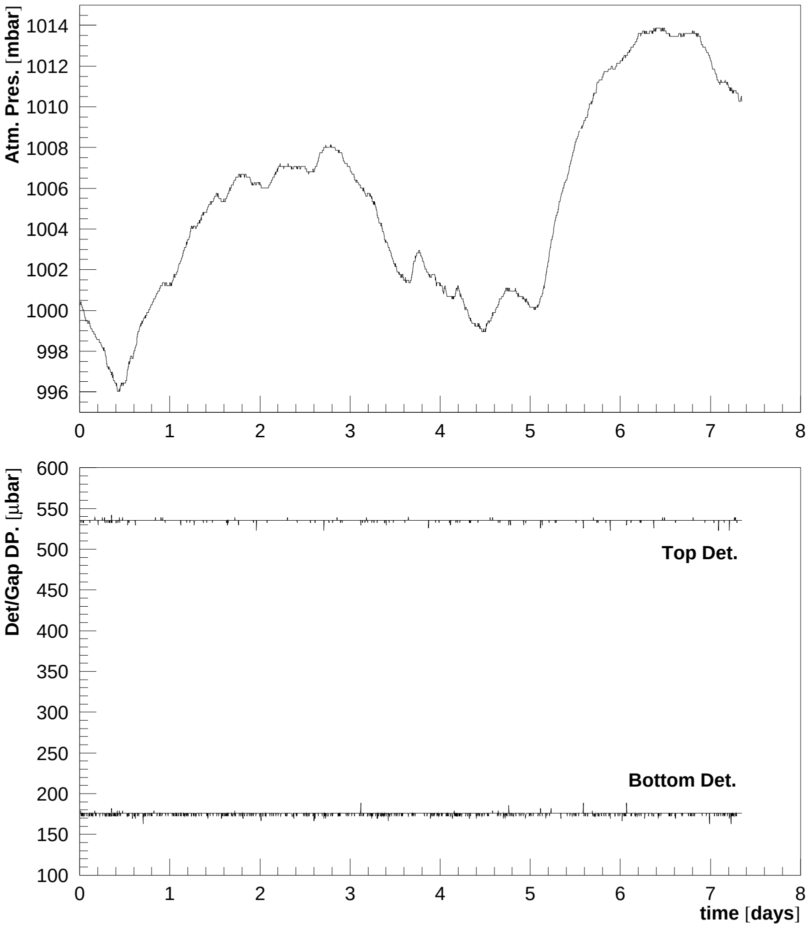

Figure 4.14: Atmospheric pressure (top) and differential pressure between gap and wire chambers (bottom).

4.4.5 TRD Readout

The TRD and the electronics trailer are not far apart, but the specific geometry requires cable lengths of about 35 m. This, together with the attempt to have access to as much of the readout equipment during the running period as possible, leads to a two step amplification process for the TRD signal. This involves pre-amplifiers and receivers that are connected by twisted pair cables. The layout of one channel each is shown schematically in figure 4.15[97].

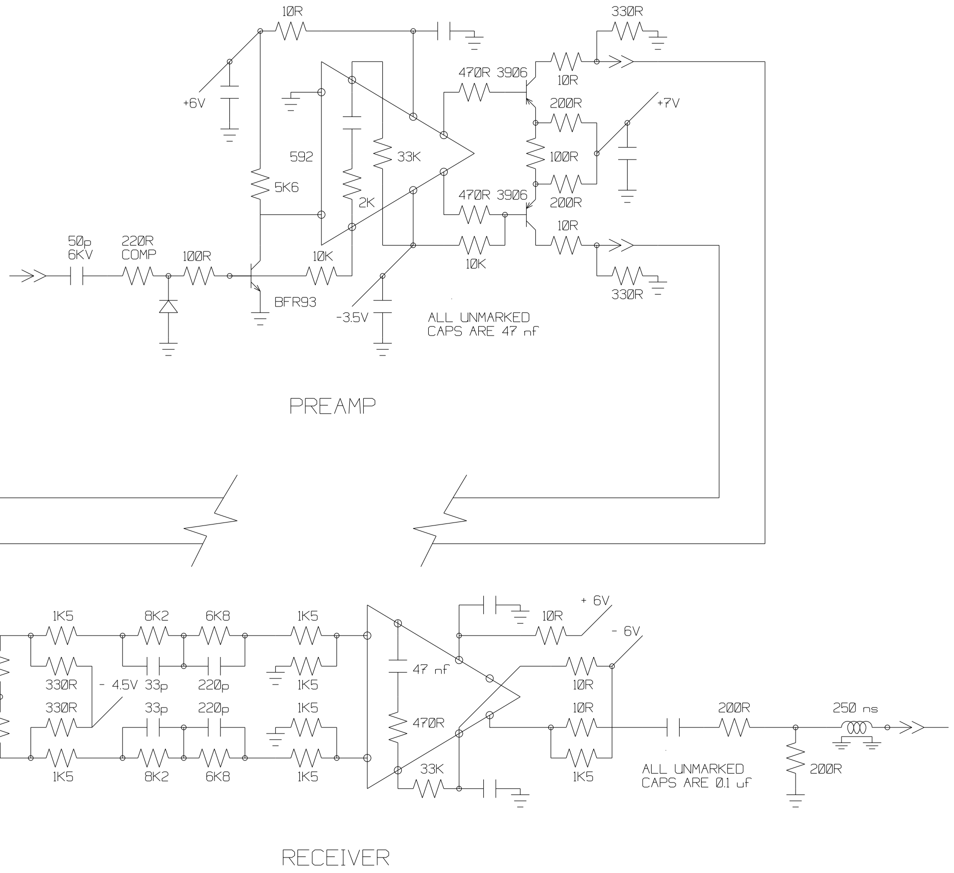

Figure 4.15: Schematics of one TRD readout channel. Pre-amplifier (top) and receiver (bottom) are connected by 35 m long twisted pair cables.

The pre-amplifiers are located directly on the chambers, with eight channels combined on one pre-amp card and a total number of readout channels of 3072. The aluminum frame of the TRD chambers is water cooled to keep the operating temperature constant (∼ 30°C). The current signal on the wires is differentiated by the pre-amps, converted into a voltage signal and amplified with a maximum peak signal of 500 mV. The use of differential signals allows for the elimination of common mode noise picked up by the cables. The receiver boards are located in the electronics trailer. They shape the signal while keeping the total size of the signal constant and then attenuate it appropriately for the Fastbus ADCs. Finally a delay line of 250 ns allows enough time for the trigger logic to make its decision.

A channel multiplexing scheme was implemented to minimize the number of ADCs. Two receiver channels (i.e. two wires) use the same ADC channel. One channel with a high rate (close to the beampipe) is paired with a channel with only a low hit rate. The signals are digitized in LeCroy 1881 ADCs which are read out by the HERMES data acquisition system (see chapter 3.4).

4.5 Calibration of the TRD

4.5.1 Influences on the TRD Gain

The TRD response must be kept as constant as possible to obtain an optimal TRD pion rejection. Every gain fluctuation will smear out the distributions of pions and positrons and so degrade their separation. Although much care was taken in the design of the hardware to minimise gain excursions, an offline calibration of the TRD response is required.

Many outside influences on the TRD gain can lead to fluctuations. First consider the gas gain in the chamber. Impurities in the gas mixture as well as changes in the differential pressure can influence the gas gain. Impurities in the gas may for example work as an additional quench gas and thus lower the gas gain. A change in differential pressure influences the foil shape and so the capacitance of the chamber, which changes the gas gain as well. The gas gain can also vary with the temperature and the pressure of the gas. Even if the differential pressure is kept constant, the absolute pressure in the chambers will change as the atmospheric pressure changes since the chambers track the ambient pressure. While equation (4.51) suggests the dependence of the gain on pressure to be an exponential of an exponential it turns out that the pressure dependence of the relative gain in the observed pressure region is well described by a linear approximation. Figure 4.16 shows this dependence for both the top and bottom detectors together with a linear fit to the bottom data. The average pion response of the TRD has been used to determine the gain, the values have been normalised to a gain of 1 at 1013 mbar.

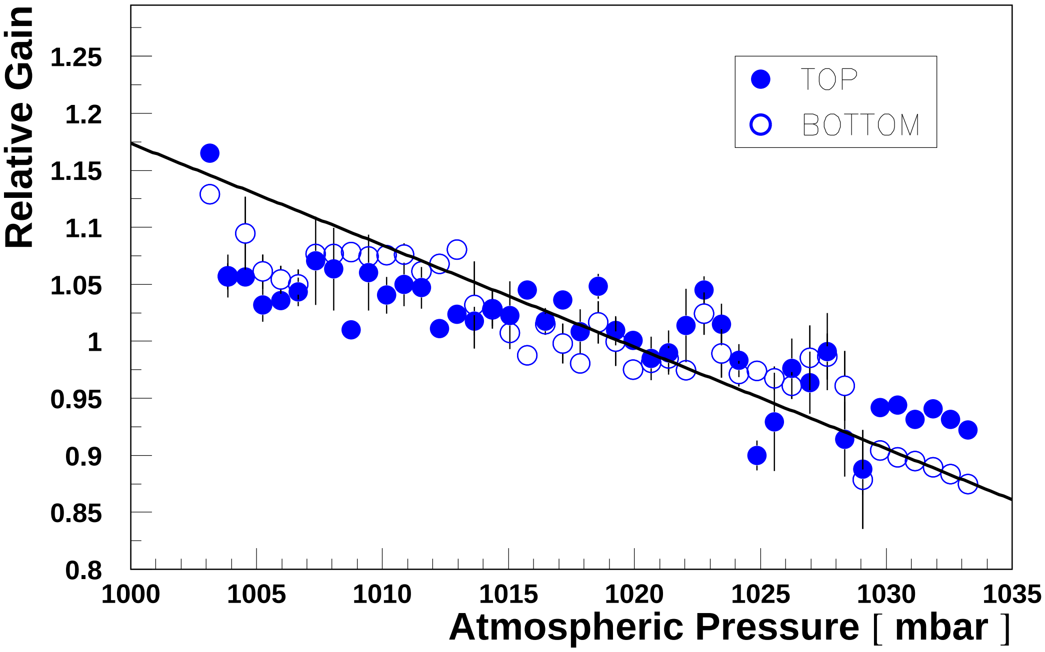

Figure 4.16: Atmospheric pressure dependence of the relative TRD gain.

The other possible source of gain fluctuations is electronic: the pre-amplifiers and receivers. The electronic gain can vary for different readout channels and the ambient temperature can influence the electronic gain. The temperature for the chambers as well as for the electronics is kept constant by a water cooling system. Although temperature drifts of several degrees were observed under certain conditions, they were usually small and only a minor source of gain fluctuations.

While the control of the differential pressure works well, its value will usually not be zero. Due to the high density of the xenon in the chambers compared to the carbon dioxide in the flush gaps, the hydrostatic pressure deflects the cathode foils, leading to an s-shaped vertical profile of the cathode-anode distance. Larger distances will decrease the electric field for a given voltage, which in turn will lower the gain. Therefore the differential pressure must be adjusted in such a way as to minimize the overall deflection of the foils. A computer model of the foils showed that the deflection rises linearly with differential pressure from 0-2 mbar, where a 1 mbar pressure difference produces a 4.75 mm shift. This means that a differential pressure of 10 μbar gives a foil shift of 50 μm. The relative gain change can be approximated by[88]

$$\frac{\Delta M}{M} = 0.4 \, \frac{\Delta l}{1 \text{ mm}} \tag{4.55}$$

where Δl is the change in thickness of the wire chamber (i.e. twice the foil deflection). With this approximation the 10 μbar foil shift leads to 1% gain change.

The vertical profile of the chamber is determined by a combination of the differential pressure and the hydrostatic pressure. Therefore it should be in principle the combination of a hyperbolic cosine and a linear function. For practical purposes this can be represented well by a 3rd or 5th order polynomial. Figure 4.17 shows the variation of the relative gain with the vertical position for top and bottom detector. The vertical position of a pion and therefore its scattering angle from the target is correlated to its momentum. Furthermore, the TRD response is momentum dependent (see below in figure 4.23). Hence, for this study the momentum of the pions was restricted to the narrow range of 2-2.5 GeV to decouple the y and the momentum dependence of the TRD gain. The top detector shows a clear s-shape with deviations in the relative gain on the order of ±10%, while the bottom detector has been compensated better with a profile that is almost flat. Both distributions have been fitted with 5th order polynomials which describe the data well.

Remembering that a low relative gain corresponds to a 'bulge' in the detector foil and using the approximation of equation (4.55), the horizontal and vertical position dependence of the relative TRD gain can be used to map a 'foil profile' of the top and bottom TRD. This profile is shown in figure 4.18; the maximum foil deflection is 250 μm. The differential pressure in the top detector has not yet been optimised and it clearly shows the bulge structure that one would expect. The bottom detector has already been optimised and displays a flatter profile. Of course these distributions cannot be taken at face value, as other outside influences e.g. the proton beam background may also locally influence the TRD gain. However, they give a qualitative description of the shape of the TRD foils.

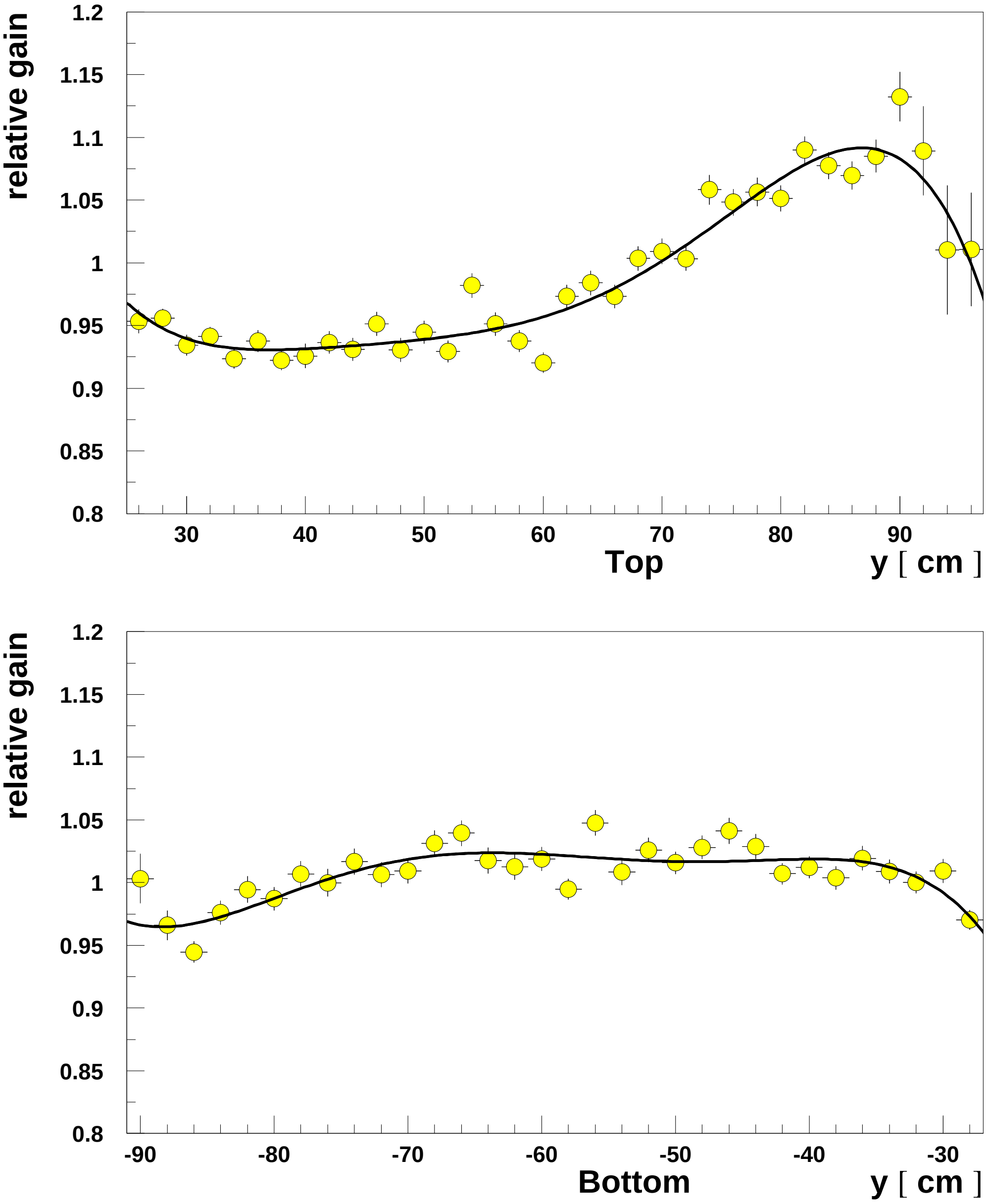

Figure 4.17: Vertical profile of the relative TRD gain for top and bottom detector. Data from the first modules for Runs 2700-2900.

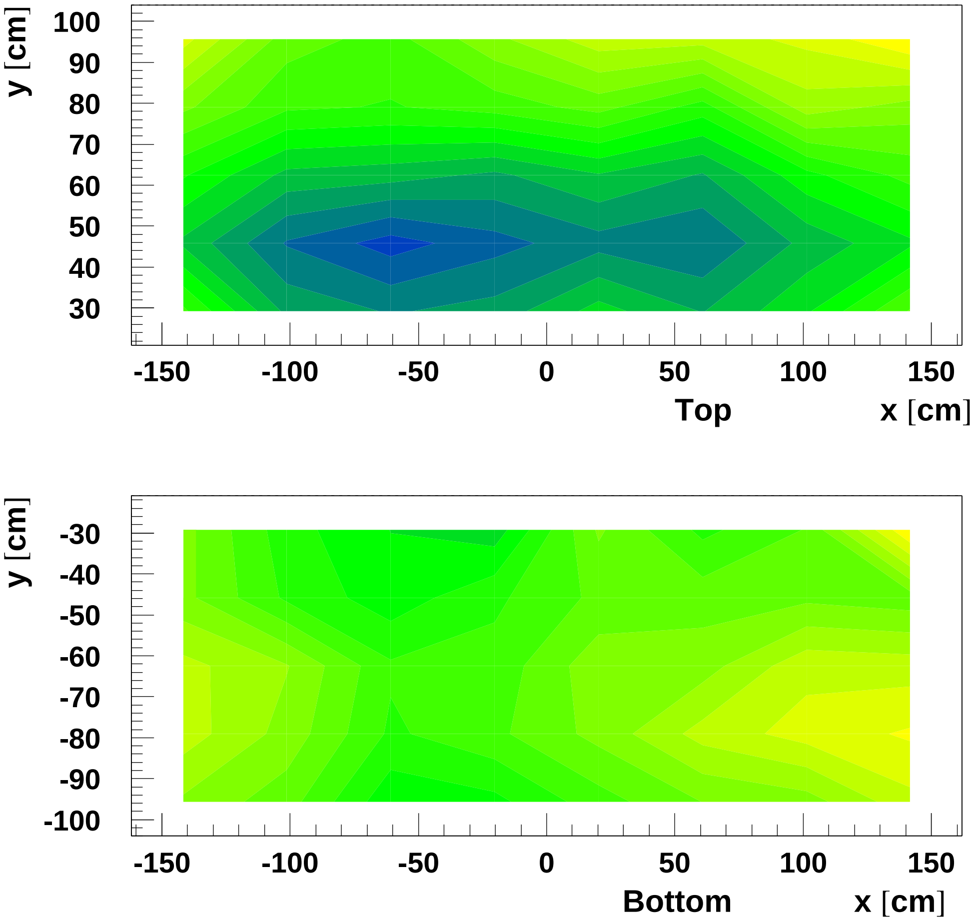

Figure 4.18: TRD chamber 'profile' from the truncated mean response of 2-2.5 GeV Pions from Runs 2700-2800. Maximum deflection is 250 μm.

The y-dependence of the TRD gain is not yet included in the TRD calibration, but will be in the near future. The chosen method is to fit the momentum dependence of the TRD response to increase the usable statistics and to fit the distributions with 5th order polynomials[100].

4.5.2 Run-by-Run Calibration

An extensive Monte Carlo study modeling the TRD and matching the resulting distributions to the results of the CERN TRD tests has been carried out[89]. The run-by-run calibration scheme that was introduced for the TRD is based on the excellent agreement between Monte Carlo distributions and data. Distributions of Monte Carlo simulations and HERMES data for 5 GeV pions and positrons from the first module of the TRD are shown in figure 4.19 below.

The distributions are in very good agreement. However, the MC distribution for the positrons had to be shifted (and appropriately compressed) by a factor of 0.9. As the Monte Carlo had been optimized to match the CERN test results, the likely reason is a difference in the test and the final radiator. The density of the radiator and therefore the number of layers is about 10% lower in the HERMES TRD than it was for the CERN test.

The 5 GeV pion MC distribution was used for the run-by-run calibration. For each run pions were selected (identified by $PID3 < -5$, see chapter 5) and their responses collected in a histogram with 1 keV bins from 0 to 25 keV. A three step fitting procedure using Gaussian fits of decreasing range, ending with a range of $\pm 1\sigma$, was used to determine the peak position of the pion distribution. The corresponding peak value for the Monte Carlo distribution is 11.25 keV.

The multiplicative calibration factors for the data were chosen to put the pion peak of the experimental data at this value. There is one calibration factor per TRD module for each run of the 1995 data with good TRD run quality.

The calibration procedure takes place in the framework of the HERMES data decoder HDC. First the pedestal values for each channel are subtracted from the raw ADC value. In the first reconstruction run of the data (i.e. version A) a constant value of 0.015 is used for the conversion from ADC channels to keV; this gives the right order of magnitude. The multiplicative calibration factors for each run are then determined from these data and used in any following reconstruction run.

The quality of the TRD calibration for the 1995 data is illustrated for the top first TRD module in figure 4.20. The spread of the pion peak positions per run is reduced from ±30% to ±2% and the distribution of the pion peak values after the calibration becomes essentially Gaussian (see figure 4.21).

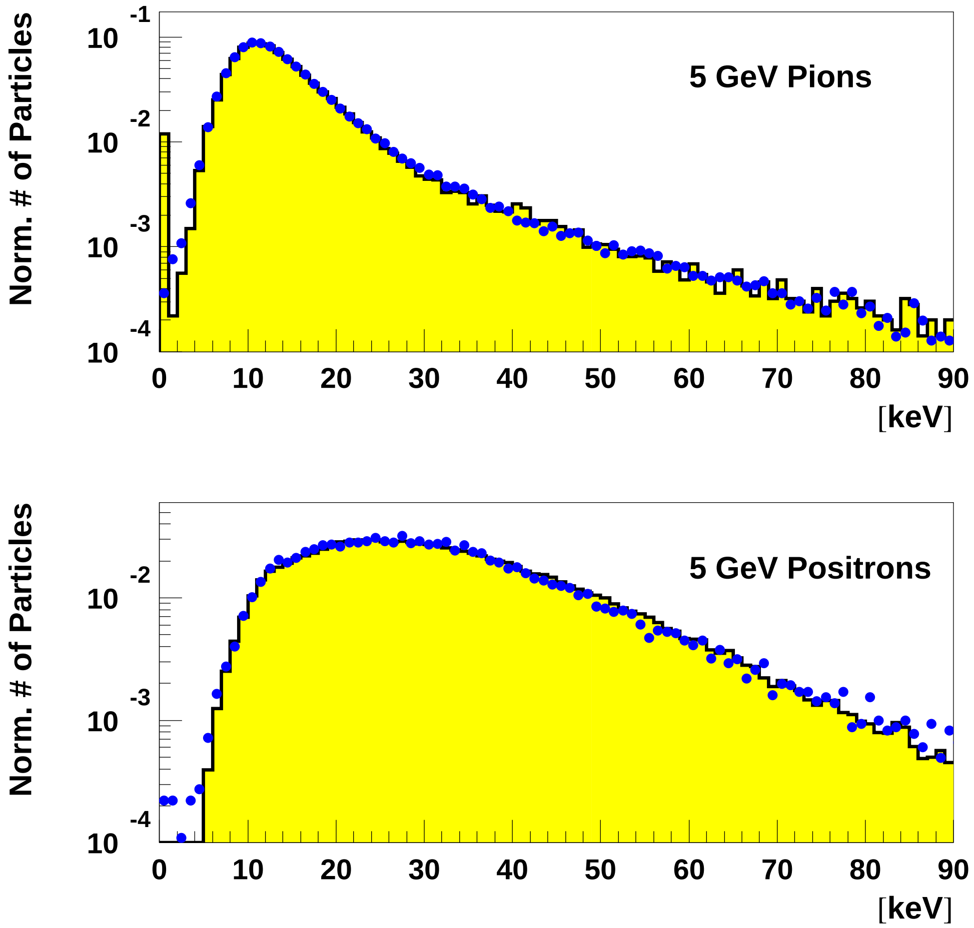

Figure 4.19: Comparison of TRD Monte Carlo (histogram) and HERMES data (full circles) for 5 GeV pions and positrons. The positron MC distribution was shifted and compressed by a factor of 0.9; both distributions were normalised to 1.

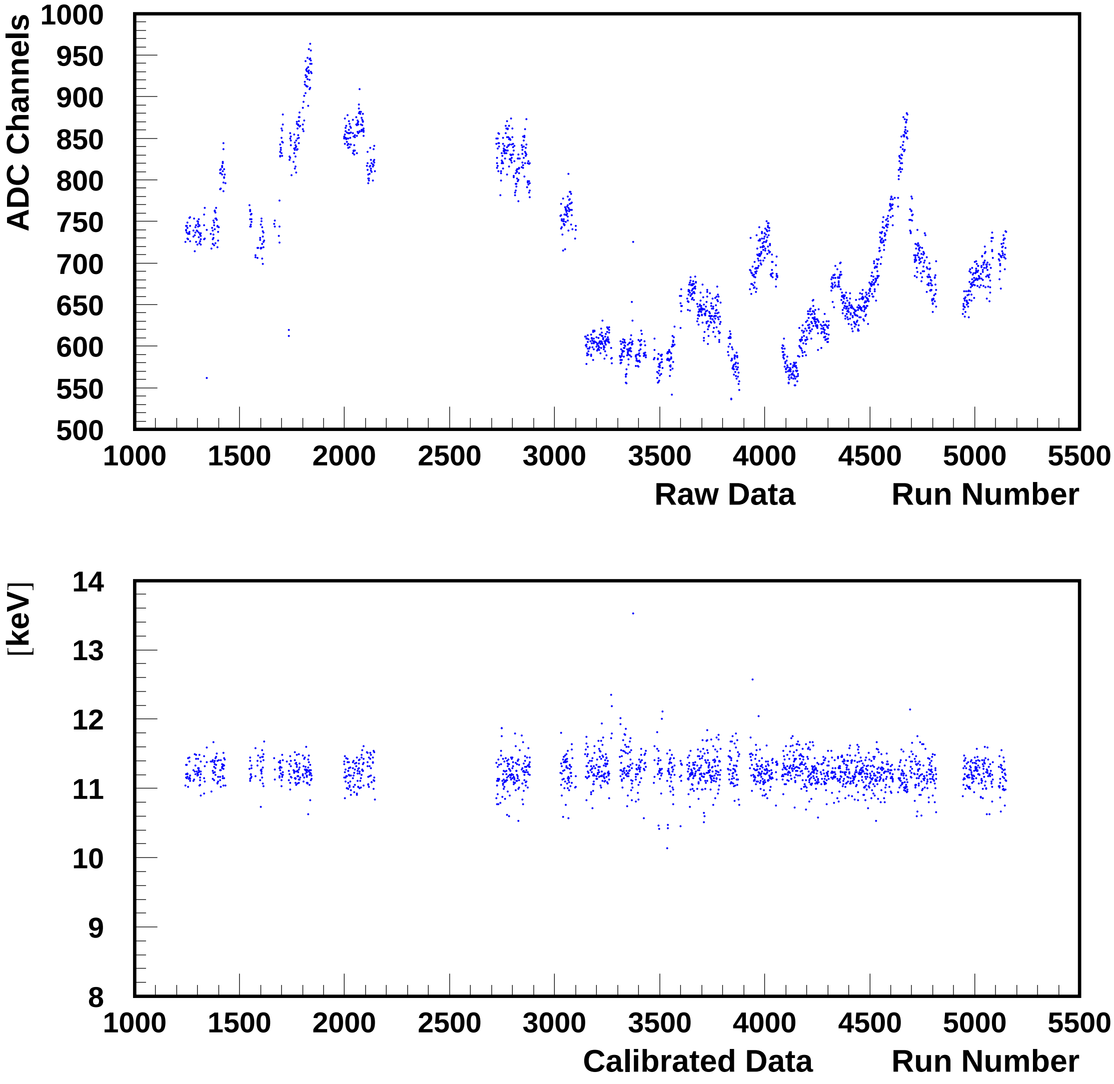

Figure 4.20: Pion peak position per Run before (top) and after the calibration (bottom)

The bin width of the original pion histograms (1 keV) used for the fitting procedure, leads to an expected uncertainty on the peak position on the order of $1/\sqrt{12} \cdot\ 1 = 0.28$ keV which is in good agreement with the observed rms of the distribution.

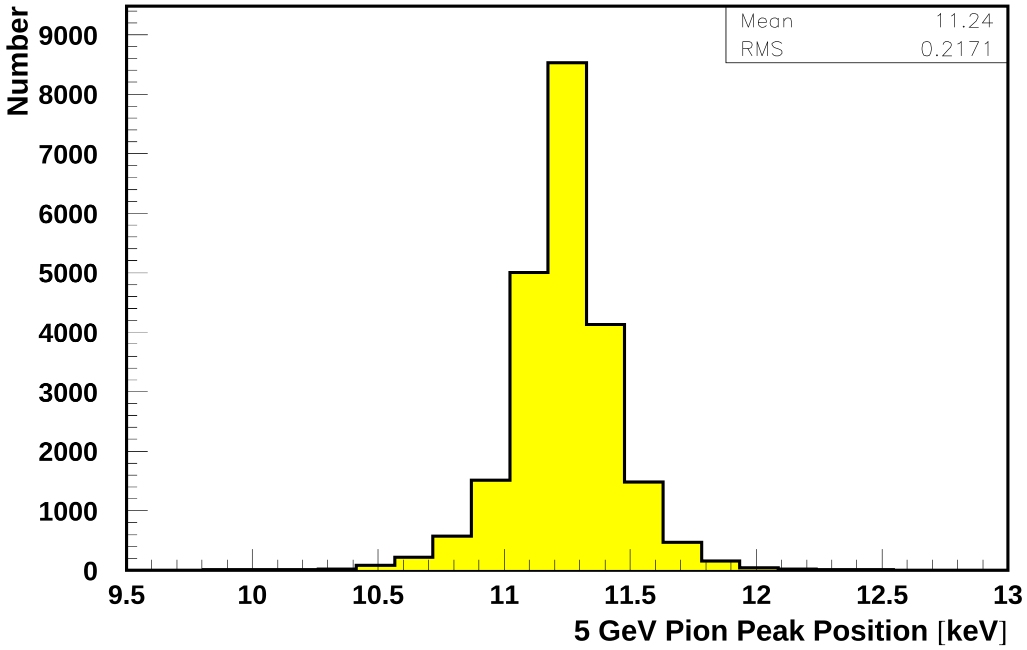

Figure 4.21: Pion peak position after the calibration for all runs and modules

In figure 4.21 all pion peak values for all modules and runs have been combined. The average value is 11.24 keV in excellent agreement with the intended 11.25 keV from the MC distribution.

4.6 Performance of the TRD

In each module of the TRD the hadrons leave only a dE/dx signal, while the positrons will produce on average 1-2 TR photons. The single module response has an average value of about 15 keV for hadrons and 35 keV for positrons. The hadrons are mostly pions, with some kaons mixed in and protons from target fragments at lower momenta. The hadron distribution of the single module TRD response has a peak around 12 keV and a long Landau-tail as a result of δ-rays, fast secondary electrons. The positron distribution is a convolution of the positron dE/dx and the transition radiation spectrum (see figure 4.7). The peak of the positron dE/dx distribution is still visible as a 'shoulder' at about 13 keV in the single module response. This shoulder corresponds to positrons which did not radiate TR.

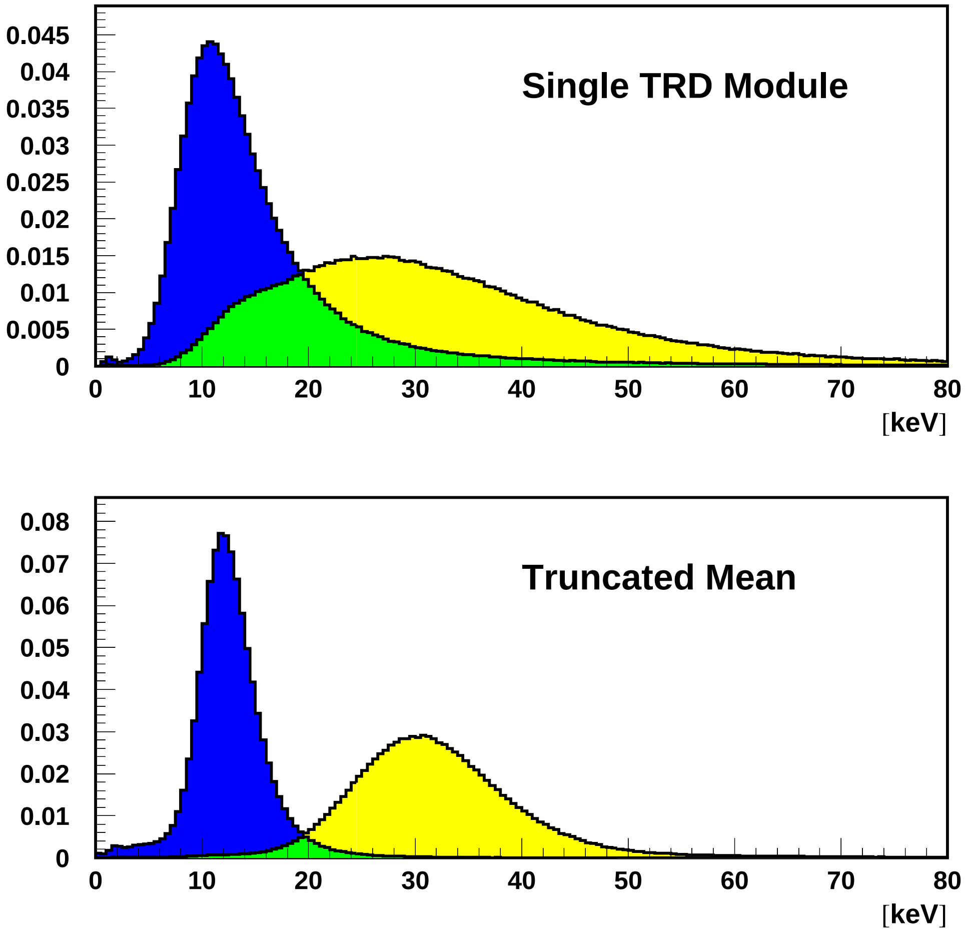

Figure 4.22: Normalised TRD response for hadrons (dark) and positrons (light) for a single module and for the truncated mean (integrated over all momenta).

For each track the responses of the six modules are combined using the truncated mean method (equation 4.53) to form one value that can be used for the physics analysis. The truncated mean results in a significant reduction of the Landau-tail and therefore in a better separation of the hadron and positron distributions. The TRD truncated mean value is also referred to as 'pulsTRD'. Both, the single module response and the truncated mean are shown in figure 4.22. The distributions have been normalised.

The performance of a TRD is usually measured by its pion rejection factor (PRF). The pion rejection factor is defined as

$$\mathrm{PRF} = \frac{\#\ \text{pions total}}{\#\ \text{pions above the cut}} \tag{4.56}$$

for a cut on the energy deposited in the TRD corresponding to a given positron (electron) efficiency. A more systematic treatment of the pion rejection factor can be found in section 5.2. The overall pion rejection factor (integrated over all momenta) of the HERMES TRD is 149 ± 4 for a positron efficiency of 90 %. This value was generated from 80 runs between runs 4200 and 4368 and is representative of the 1995 data set.

As the momentum, and therefore γ increases, the TR yield for positrons also increases, before it saturates as the result of absorption and interference effects. Figure 4.23 illustrates the momentum dependence of the average TRD response for pions and positrons, for both a single module and the truncated mean. The transition radiation saturates at about 2.5 GeV for the first and 4 GeV for the sixth module. The pion signal is basically constant; it shows the slow logarithmic rise expected from the Bethe-Bloch formula (see also figure 4.5).

The momentum dependence of the TRD response results in a momentum dependence of the pion rejection factor. The pion rejection factor for 90% positron efficiency is about 50 at low momenta and rises to values of 200 for high momenta. For 5 GeV a pion rejection factor of about 130 is found, clearly exceeding the design goal of 100 (figure 4.24). More detailed numerical values are given in table 4.1 below.

The pion rejection factor can be determined separately for the top and bottom TRD (figure 4.25). The bottom detector appears to perform better in general than the top detector. A possible reason for this may be found in the better optimisation of the vertical profile in the bottom detector (see figure 4.18). Detailed numerical values are given in table 4.2.

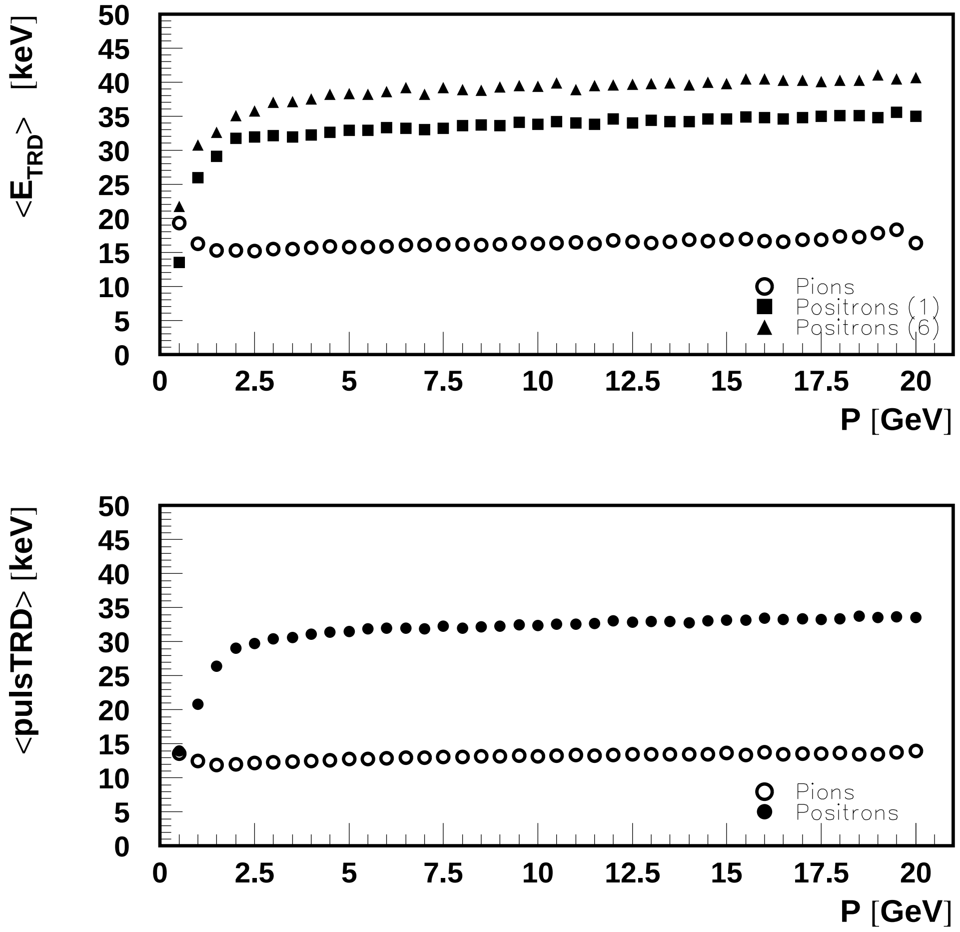

Figure 4.23: Momentum dependence of the average TRD response for pions and positrons. The upper plot shows the single module response (for positrons module 1 and 6), the lower plot shows the truncated mean.

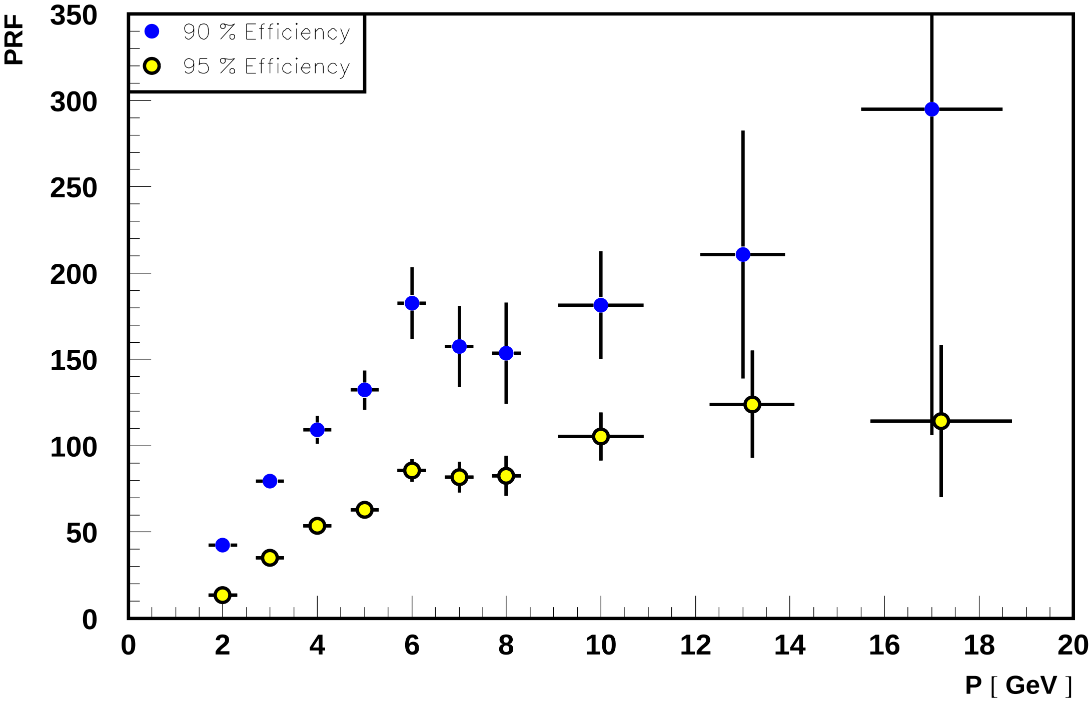

Figure 4.24: Momentum dependence of TRD pion rejection factor for 90% and 95% positron efficiency.

p [GeV]	PRF for 90% Efficiency	PRF for 95% Efficiency
2	42.3±1.8	13.4 ± 0.3
3	79.3±4.3	35.2 ± 1.2
4	109±8	53.5 ± 2.8
5	132±11	62.9 ± 3.7
6	183±21	85.8 ± 6.7
7	158±24	81.8 ± 8.9
8	154±29	82.5 ± 12
10	182±31	105 ± 14
14	211±72	124 ± 31
17	199±140	114 ± 44

Table 4.1: Pion rejection factors for 90 and 95 % positron efficiency.

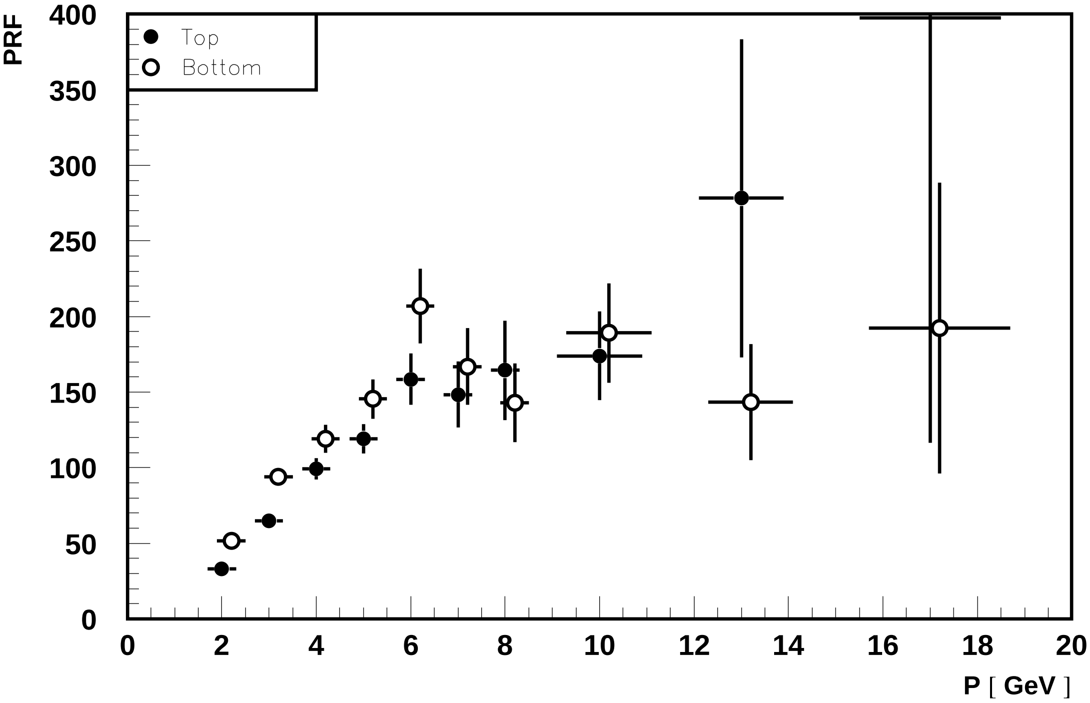

Figure 4.25: Momentum dependence of TRD pion rejection factor for top and bottom detector for 90% positron efficiency.

p [GeV]	Top PRF for 90% Efficiency	Bottom PRF for 90% Efficiency
2	33.2 ±1.5	51.4 ± 2.0
3	64.8 ±3.1	93.9 ± 5.4
4	99.3 ±7.0	119 ± 9
5	119 ±10	145 ± 13
6	158 ±17	207 ± 25
7	148 ±22	167 ± 25
8	164 ±33	143 ± 26
10	174 ±29	189 ± 32
14	278 ±105	143 ± 38
17	398 ±281	192 ± 96

Table 4.2: Pion rejection factors for top and bottom detector for 90 % positron efficiency.

The average positron signal is higher in module six than in module one which is seen in figure 4.23. This is the result of X-rays that are not absorbed by a previous module 'punching through' to the next module. This effect is shown for all six modules in figure 4.26.

The entire TRD may be viewed as a 'foil stack', in which the wire chambers provide a measurement of the saturation of transition radiation described by equation (4.20). A function representing the effective foil number N_{eff} and an additive term C due to the dE/dx signal

$$F(x) = C + \frac{1 - e^{-NSx}}{1 - e^{-S}} \tag{4.57}$$

with fitting parameters C, N, S describes the data well (see figure 4.26). The constant value of C=14 keV agrees with the Monte Carlo result for the dE/dx signal of a positron (see figure 4.7).

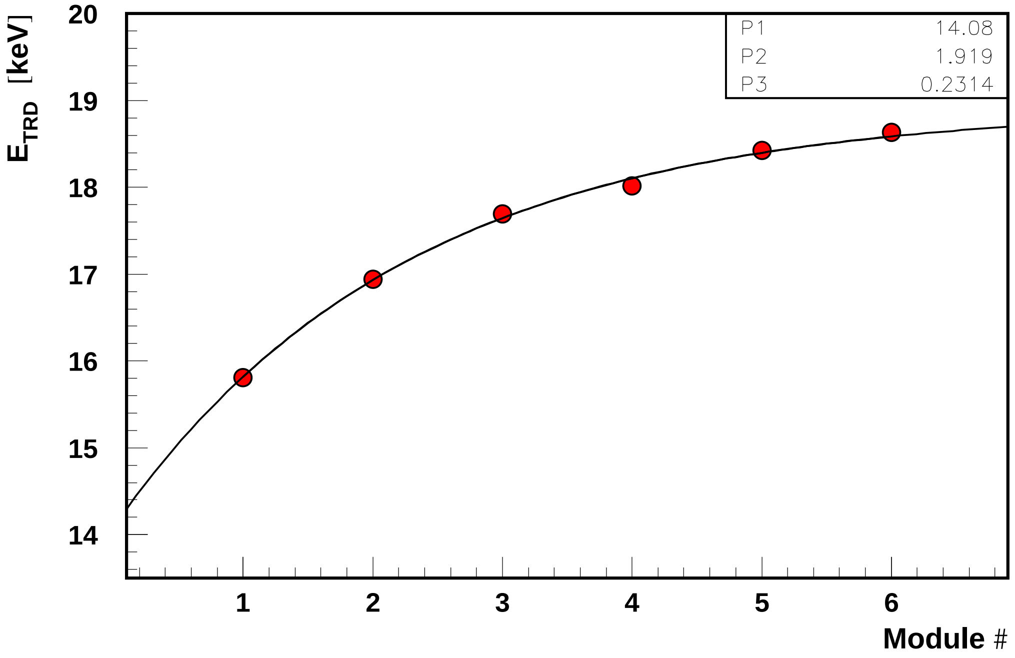

Figure 4.26: Average TRD response for positrons for all six TRD modules.

Recently a probability based analysis of the TRD response was implemented. Using a Bayesian probability analysis which also takes into account the hadron and positron fluxes, a pion rejection factor in excess of 1400 was obtained[99]. The parameter PID_{TRD} is generated in the way described in section 5.1. The PID_{TRD} distributions for hadrons and positrons are shown in figure 4.27.

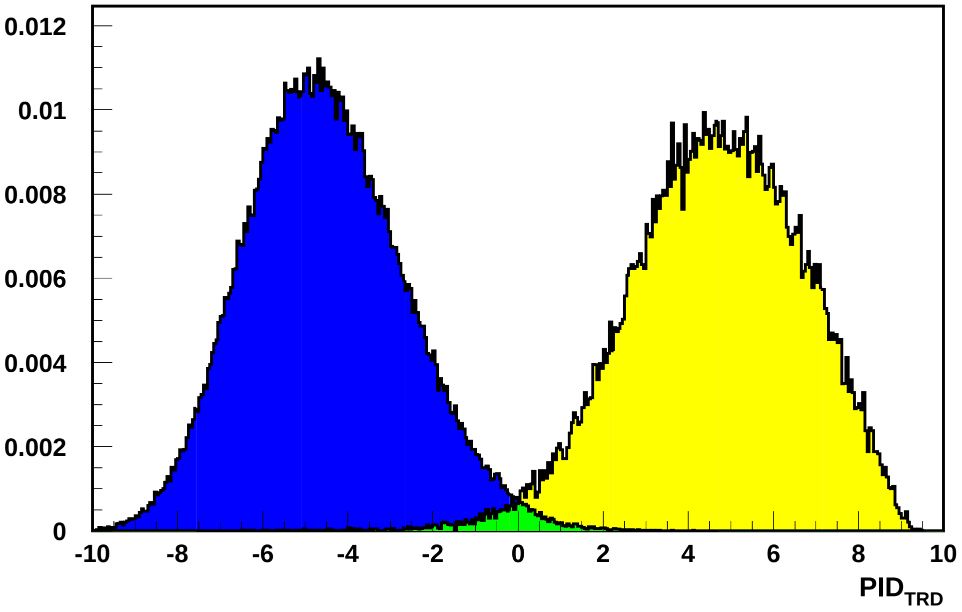

Figure 4.27: Distributions of PID_{TRD} for hadrons (dark) and positrons (light)

An important parameter for the performance of a TRD is its overall length. It has been shown that the dependence on the total length of the TRD of the pion rejection is essentially exponential[84, 90]. One study was carried out by Fabjan et al. using both Lithium and CH_2 radiators with the cluster counting algorithm in a small 10×10 cm^2 test setup. A comparison of data for the HERMES TRD confirms the assumed behaviour (figure 4.28). The pion rejection factor of about 5500 for the 72 cm long TRD with lithium radiator is the largest PRF that has been published. The fact that the performance of the HERMES TRD is comparable to this much smaller detector is evidence for the excellent performance of the HERMES TRD.

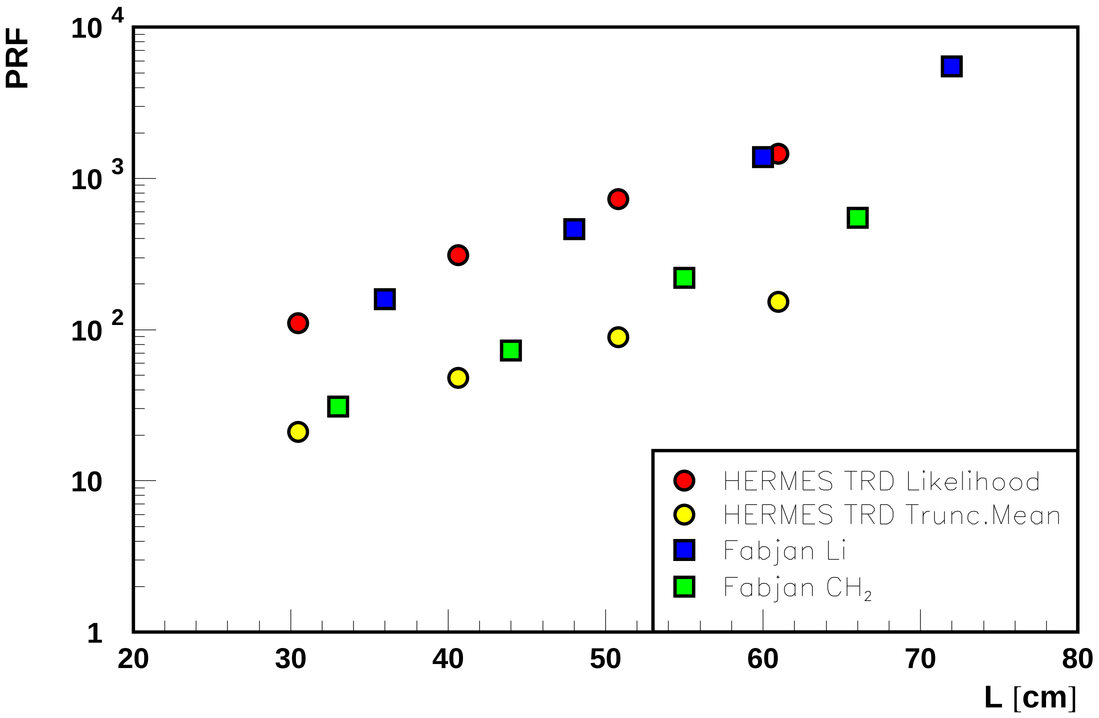

Figure 4.28: Comparison of the performance of the HERMES TRD with the measurements of Fabjan et al.

It is tempting of course, to compare the pion rejection factor of the HERMES TRD to that of other, similar detectors. It is not always possible to compare directly published values for the performance of transition radiation detectors. This is because three different parameters are used in the literature to measure TRD performance: The pion rejection factor for a given electron efficiency; the efficiency ratio R; and the pion contamination for a given electron efficiency. The pion rejection factor has been introduced previously (equation 4.56). The efficiency ratio is defined as

$$R = \frac{\varepsilon_\pi}{\varepsilon_e} \tag{4.58}$$

where $\varepsilon_\pi, \varepsilon_e$ are the pion and electron efficiencies respectively. The electron efficiency is usually set to 0.9 to quote TRD performance. The pion rejection factor and R are equivalent for the same electron efficiency, and they can be converted easily into one another using

$$\mathrm{PRF} = \frac{1}{\varepsilon_e \cdot R}. \tag{4.59}$$

The use of the pion contamination as a parameter to quantify the performance of a TRD is questionable, because the contamination value depends strongly on the relative fluxes of pions and positrons in a given experiment, under given experimental conditions (see chapter 5.2).

A compilation of pion rejection factors from various experiments is shown in figure 4.29 and table 4.3. The TRDs that are selected for the comparison are all either working components of current or past particle physics experiments or are prototypes for future experiments. Pure detectors physics experiments have not been considered. Furthermore, only TRDs with similar materials, that is CH_2 radiators and readout with xenon filled wire chambers have been selected. All quoted pion rejection factors are for an electron efficiency of 0.9. For those TRDs which quote their performance in terms of pion contamination a flux ratio of 1 was assumed.

Experiment	Length [cm]	Pion Rejection Factor	Reference
UA2	21	11	[101]
D0	31.5	71	[102]
VENUS	32	15	[103]
ZEUS	40	100	[106]
H1	50	20	[104]
PHENIX	50	330	[105]
HERMES	61	1460	[99]
HELIOS	70	2200	[83]
NA31	100	70	[107]
ATLAS	115	300	[92]

Table 4.3: Pion rejection factors for various experiments for 90 % electron/positron efficiency.

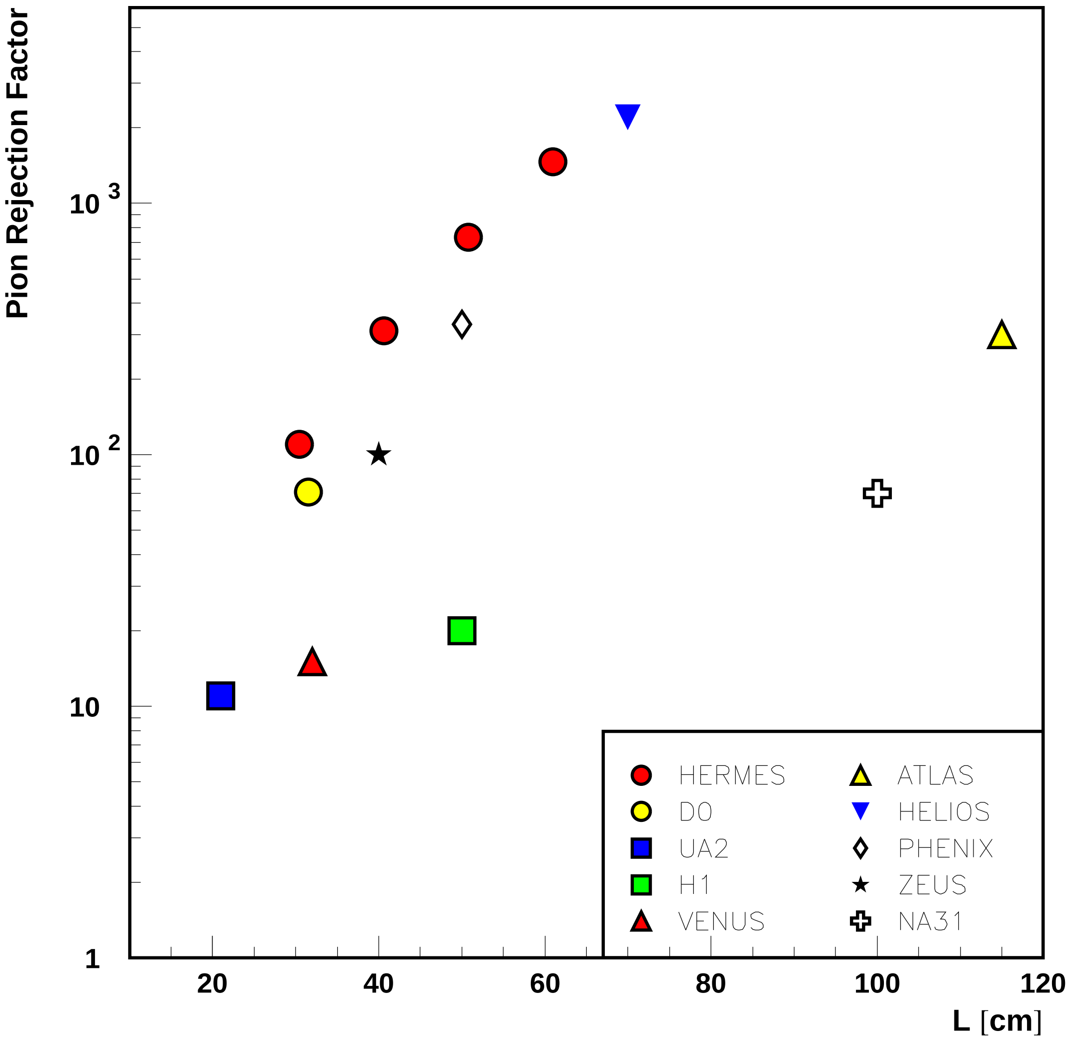

Figure 4.29: Comparison of the performance of the HERMES TRD with the performances of other TRDs

The four points shown for the HERMES TRD in figure 4.29 are for the use of 3,4,5 or 6 modules, starting from the front of the TRD. This allows a comparison of the performance of the HERMES TRD to detectors of different length. It is apparent that the HERMES TRD outperforms practically all other TRDs. The D0 TRD, the PHENIX prototype, the ZEUS test chamber and the HELIOS TRD show a similar performance, while the others form a second, lower line in the diagram.

There is a certain amount of bias in this comparison, as some of the other TRDs have a double function, e.g. the ATLAS prototype is a combination of a particle identification and a tracking detector. The prototypes in this comparison also usually use only one module and then combine several events to simulate the performance of a multi-module TRD. Due to the 'punch through' effect this necessarily will give a lower value than the same number of modules ordered in a row (see figure 4.26). Nevertheless, the comparison to other detectors shows that the HERMES TRD was successfully optimised and there is not very much room left for improvement.

Chapter 5

Particle Identification at HERMES

5.1 PID Quantities

5.1.1 Definition of PID Quantities

Particle identification (PID) uses the fact that different types of particles cause different detector responses. These responses can be used directly in the data analysis or they can be first converted into probabilities. The first case will be referred to as 'hard cuts'. A cut is a condition that is imposed on a measured quantity to select a specific data sample. If probability based analysis is used, the response of each detector must first be converted into a conditional probability $\mathcal{L}_D^i$ that the response of the detector D was caused by a particle of the type i. This can be done by using distributions generated from test beam data or from clean particle samples obtained with restrictive hard cuts on the other PID detectors in the experiment. These distributions are normalised and either used directly or by fitting with an analytical function. In both cases the conditional probability distributions are referred to as 'parent distributions' $\mathcal{L}_D^i$. The term 'conditional probability' refers to the fact that the parent distributions are normalised to 1.

The conditional probabilities from several detectors D can be combined into an overall conditional probability

$$\mathcal{L}^i = \prod_D \mathcal{L}^i_D \tag{5.1}$$

The conditional probabilities can be transformed into true probabilities $\mathcal{P}^i$ that a particular particle is of type i, if all particle fluxes, represented by the flux factors ϕ^i, are known. This is a nontrivial problem, since these flux factors are in general functions of momentum and scattering angle

$$\phi^i = \phi^i(p, \theta) \tag{5.2}$$

or two similar variables. Usually this problem can only be solved by a Monte Carlo simulation of the detectors or by an iterative procedure. In the case that all flux factors are known the probability $\mathcal{P}^i$ is given by Bayes' theorem:

$$\mathcal{P}^i = \frac{\phi^i \mathcal{L}^i}{\sum_j \phi^j \mathcal{L}^j} \tag{5.3}$$

For the simple case of only two particle types, positron and hadron, the positron probability is therefore given as

$$\mathcal{P}^e = \frac{\mathcal{L}^e}{\Phi \mathcal{L}^h + \mathcal{L}^e} \tag{5.4}$$

where only the conditional probabilities and the flux ratio $\Phi = \phi^h/\phi^e$ have to be known. In this case it is equivalent to create a PID parameter from the ratio of the positron and hadron probabilities by taking the logarithm:

$$PID = \log_{10}\left(\frac{\mathcal{P}^e}{\mathcal{P}^h}\right) = \log_{10}\left(\frac{\mathcal{L}^e}{\Phi \mathcal{L}^h}\right) = \log_{10}\left(\frac{\mathcal{L}^e}{\mathcal{L}^h}\right) - \log_{10}\Phi \tag{5.5}$$

The advantage of this quantity is that it produces a distribution that intuitively resembles the response of a detector. Furthermore, it is practical that $PID = 0$ is simply the value where a particle is equally likely to be a positron or a hadron and therefore the natural value for a cut. If the flux ratio Φ is neglected, the PID

distribution is shifted by $\log_{10}\Phi$. Therefore Φ can be neglected if it is not a strong function of (p, θ). Otherwise a momentum dependent cut can in principle replace the knowledge of Φ. Another way to express PID is by introducing a PID parameter for each detector

$$PID_D = \log_{10}\left(\frac{\mathcal{L}^e_D}{\mathcal{L}^h_D}\right) \tag{5.6}$$

which results in

$$PID = \sum_D PID_D - \log_{10}\Phi \tag{5.7}$$

5.1.2 PID2, PID3, PID4

The PID quantity that is typically used for the analysis of 1995 HERMES data is PID3 which combines the calorimeter, preshower and Čerenkov responses and is defined as

$$\begin{aligned} PID3 &= PID_{cal} + PID_{pre} + PID_{cer} && (5.8) \\ &= \log_{10}\left(\frac{\mathcal{L}^e_{cal}\mathcal{L}^e_{pre}\mathcal{L}^e_{cer}}{\mathcal{L}^h_{cal}\mathcal{L}^h_{pre}\mathcal{L}^h_{cer}}\right) && (5.9) \end{aligned}$$

PID3 is not equivalent to the probability $\mathcal{P}^e$, because it does not include the flux ratio. This was done so as to not bias the PID3 parameter with respect to different kinematic cuts, e.g. for DIS and photo production events. It has to be pointed out that a cut on PID3 in this case is not in any way clearly defined. However, PID3 can be used as if it were the response of a single particle identification detector with excellent positron-hadron separation.

The standard particle identification cut for the 1995 inclusive analysis follows the valley between the positron and hadron distributions in the PID3-pulsTRD plane, where pulsTRD is the truncated mean signal of the TRD. A more detailed description can be found in the section 'HERMES PID Cuts' (5.3).

The PID parameters PID2 and PID4 are sometimes used as well. They are defined in an analogous way to PID3. While PID2 uses only the calorimeter and the preshower, PID4 also includes the TRD. For 1995 PID4 is constructed using parent distributions for positrons and hadrons generated from pulsTRD spectra. They include no momentum dependence. A full probability analysis of the TRD is in progress[99] and it is to be expected that in the future PID4 will be defined according to equation (5.5), that is includes the flux ratio and PID_{TRD}. Figure 5.1 shows PID2, PID3 and PID4 for comparison. The large impact of the TRD is apparent in the difference between PID3 and PID4.

The probability analysis is always only as good as the parent distributions that it uses. If they do not resemble the data closely, the produced probability or PID quantity is not correct. Also it should be remembered that the PID quantity as defined in equation (5.5) is only useful for the case of two particle types. For a larger number of particle types the full probability analysis must be used. As an alternative, the number of parent distributions could be increased. For example for three types of particles (i=positron, pion, kaon) six parent distributions could be used (positron, not-positrons, etc.) for each detector to define three PID parameters.

$$PID_D^i = \log_{10}\left(\frac{\mathcal{L}_D^i}{\mathcal{L}_D^{\neq i}}\right) \tag{5.10}$$

The disadvantage of this method is the increase in the number of necessary parent distributions, while the distributions may be somewhat easier to interpret.

5.1.3 Parent Distributions

The parent distributions $\mathcal{L}_{det}^i$ for the calorimeter, the preshower and the Čerenkov detector are given as analytical expressions that were fitted to test beam or HERMES data. The TRD parent distributions were originally obtained from a Monte Carlo simulation that was tuned to CERN test beam results. They were later replaced by distributions generated from the 1995 HERMES data, mostly due to an observed difference in the positron distributions with respect to the test beam data related to the use of different radiators.

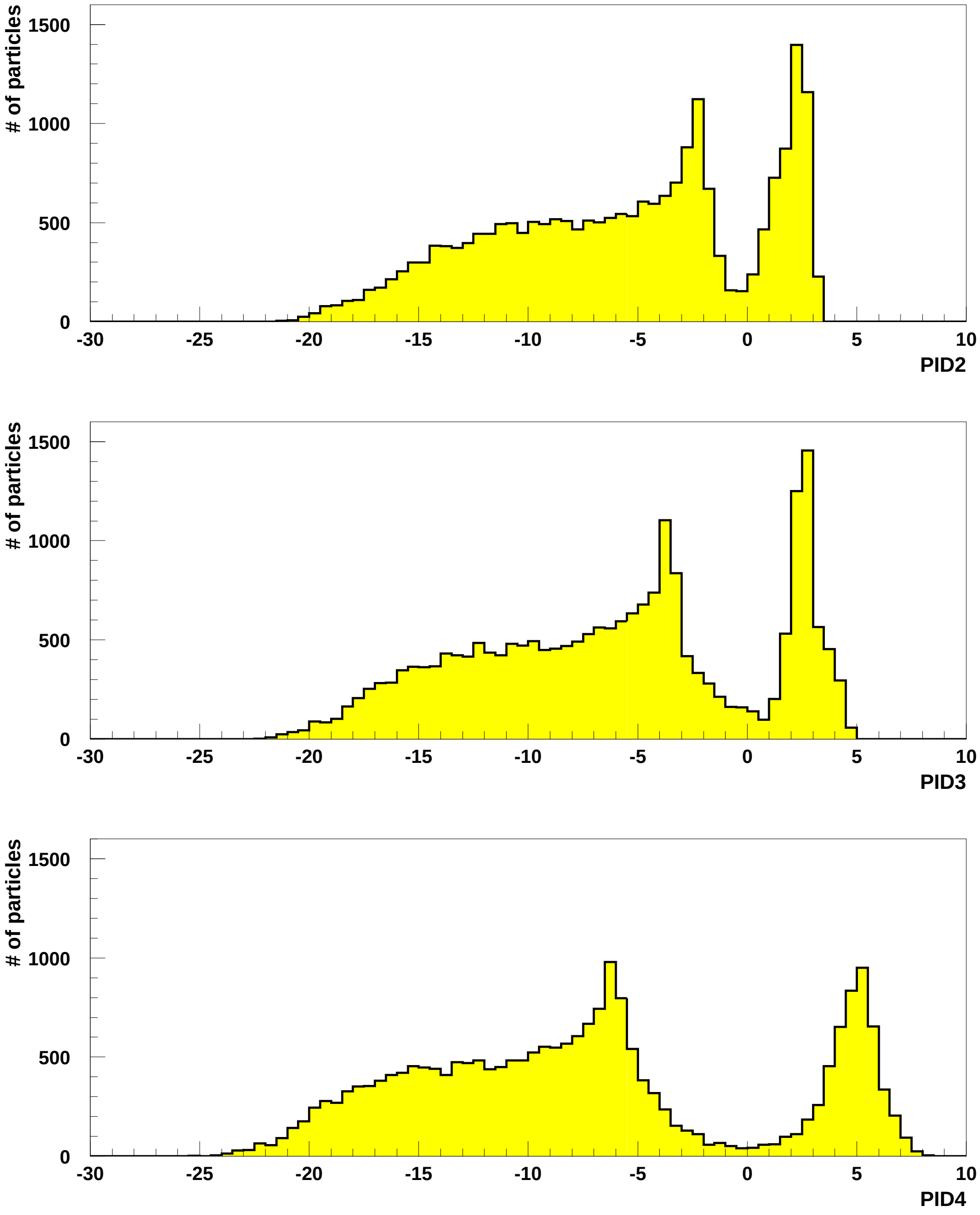

Figure 5.1: Comparison between the PID parameters PID2, PID3 and PID4. Data from one run (4220). The separation of the hadron (< 0) and positron peaks (> 0) clearly improves from PID2 to PID4.

Calorimeter

The measured calorimeter energy E_{cal} and the ratio $R_{cal} = E_{cal}/p$ of calorimeter energy to momentum measured by the tracking system are the parameters used for the calorimeter parent distributions. The calorimeter is calibrated so that

$$\langle R_{cal} \rangle = 1 \qquad \text{for positrons.} \tag{5.11}$$

The positron spectrum is modelled as a Gaussian distribution with an additional high energy tail:

$$\mathcal{L}^e_{cal} = \begin{cases} \frac{1}{\sqrt{2\pi}\sigma} \cdot e^{-\frac{(R_{cal}-1)^2}{2\sigma^2}} & \text{for } R_{cal} \leq 1 \\ \frac{1}{\sqrt{2\pi}\sigma} \left[e^{-\frac{(R_{cal}-1)^2}{2\sigma^2}} + C_{e1}(R_{cal}-1)e^{-C_{e2}(R_{cal}-1)} \right] & \text{for } R_{cal} > 1 \end{cases} \tag{5.12}$$

with constants C_{e1}, C_{e2}. The energy resolution of the calorimeter ΔE_{cal} as well as the spectrometer resolution Δp determine σ:

$$\sigma = \sqrt{\Delta E_{cal}^2 + \Delta p^2} \qquad \text{with} \qquad \Delta E_{cal} = a + \frac{b}{\sqrt{p}} \tag{5.13}$$

where a and b are fit parameters. The hadron parent distribution is set to a constant (C_π) for hadron energies below the trigger threshold E_{thr}. Above the threshold it is described by an exponential decline:

$$\mathcal{L}^h_{cal} = \begin{cases} C_\pi & \text{for } E_{cal} \leq E_{thr} \\ C_\pi e^{-C_\pi (R_{cal} - \frac{E_{thr}}{p})} & \text{for } E_{cal} > E_{thr} \end{cases} \tag{5.14}$$

Preshower Detector

The modeling of the parent distributions for the preshower detector is similar to the calorimeter, but slightly more complicated. Again the deposited energy E_{pre}, the momentum p and a ratio R_{pre} are used as parameters. In this case R_{pre} is the ratio of measured preshower energy and the expected energy deposition by a positron of the same momentum :

$$R_{pre}(p) = \frac{E_{pre}}{\langle E^e_{pre}(p)\rangle} \tag{5.15}$$

where $\langle E^e_{pre}(p)\rangle$ is a quadratic polynomial in p that was fit to the CERN test beam data.

An asymmetric Gaussian is used for both electrons/positrons and hadrons:

$$\mathcal{A}(x,\bar{x},\sigma_1,\sigma_2) = \begin{cases} \frac{1}{\sqrt{2\pi}\sigma_1} e^{-\frac{(x-\bar{x})^2}{2\sigma_1^2}} & \text{for } x < \overline{x} \\ \frac{1}{\sqrt{2\pi}\sigma_1} e^{-\frac{(x-\overline{x})^2}{2\sigma_2^2}} & \text{for } x \geq \bar{x} \end{cases} \tag{5.16}$$

The positron distribution is a function of R_{pre} with parameters C_e, σ_{e1} and σ_{e2}:

$$\mathcal{L}^e_{pre} = C_e \mathcal{A}(R_{pre}, \overline{R_{pre}}, \sigma_{e1}, \sigma_{e2}) \tag{5.17}$$

The hadron parent distribution is described as a function of E_{pre} with an additional high energy tail

$$\mathcal{L}^h_{pre} = C_{h1} \mathcal{A}(E_{pre}, \overline{E_{pre}}, \sigma_{h1}, \sigma_{h2}) + C_{h2} e^{-C_{h3} R_{pre}} \tag{5.18}$$

with parameters $C_{h1,h2,h3}, \sigma_{h1}$ and σ_{h2}.

Čerenkov Detector

The normalised spectrum of photoelectrons N_{pe} can be described by convoluting a Poisson distribution for the number of photoelectrons with Gaussian distributions for each photoelectron peak[72].

$$\mathfrak{L}_{cer}^{i} = P_{pe}(h, u_i) = \sum_{n=1}^{\infty} \frac{u_i^n}{n!} e^{-u_i} \cdot \frac{1}{\sqrt{2\pi\sigma_n^2}} \cdot e^{-\frac{1}{2}\frac{(h-n)^2}{\sigma_n^2}} \tag{5.19}$$

with	h	... measured pulse height of the photomultiplier signal
	u_i	... $\langle N_{pe} \rangle$ for particle type i (e,π,K,p)
	$P_{pe}(h, u_i)$	... probability density for getting a signal h out of a Čerenkov system with average photoelectron yield u_i.
	σ_n	... resolution of the n photoelectron peak (only σ_0 and σ_1 have to be known, higher-order terms can be calculated as $\sigma_n \approx \sqrt{n} \cdot \sigma_1$)
	n	... number of the photoelectron peak

The average number of photoelectrons depends on the particle mass and the design of the detector:

$$u_i = N_{pe}(\beta = 1) \cdot \frac{1 - \left(\frac{\beta_t}{\beta_i}\right)^2}{1 - \beta_t^2} \tag{5.20}$$

with $N_{pe}(\beta = 1) = 2.9$ in case of the HERMES Čerenkov detector and

$$\beta_i = \frac{p}{\sqrt{m_i^2 c^2 + p^2}} \tag{5.21}$$

Transition Radiation Detector

The parent distributions for the TRD have been derived from the data directly, defining clean samples of hadrons and positrons by hard cuts on the other three PID detectors. This results in a binned histogram for both parent distributions, instead of the smooth modeling functions used for the other detectors. The parent distributions for the TRD do not currently include any momentum dependence. Also, so far the truncated mean value (pulsTRD) has been used for the 1995 data instead of the single module responses.

5.1.4 Single Detector Contributions to the PID Quantities

It is apparent from figure 5.1 that the contributions of the four PID detectors to the PID quantities like PID3 is of quite different size. This is illustrated easily by the plots of PID_D in figure 5.2 (see equation 5.6). The range of PID_{cal} is about [-19.5,+1.5] and dominates the value of the PID quantities. The contributions of the other three detectors are a lot smaller, with the TRD being the second largest (Čerenkov [-1.5,+3], preshower [-2.5,+2], TRD [-3,+4]).

It can be argued that the range of PID_{cal} is far too large and that the parent distributions should be adjusted accordingly. Let us assume that the calorimeter, perhaps due to a malfunction of a calorimeter block, misidentifies a positron as a hadron and assigns $PID_{cal} = -19$. Even if the other three PID detectors clearly identify this particle as a positron it will be misidentified by PID4 because $-19 + 3 + 2 + 4 = -10 < 0$. This suggests that a far more suitable range of PID_{cal} would be about [-5,+1.5]. This problem should certainly be addressed in the near future. While the inclusive measurements are practically not affected, as this will only result in a negligible decrease in efficiency, it may pose a more serious problem for the semi-inclusive analysis due to positron contamination of the hadron sample.

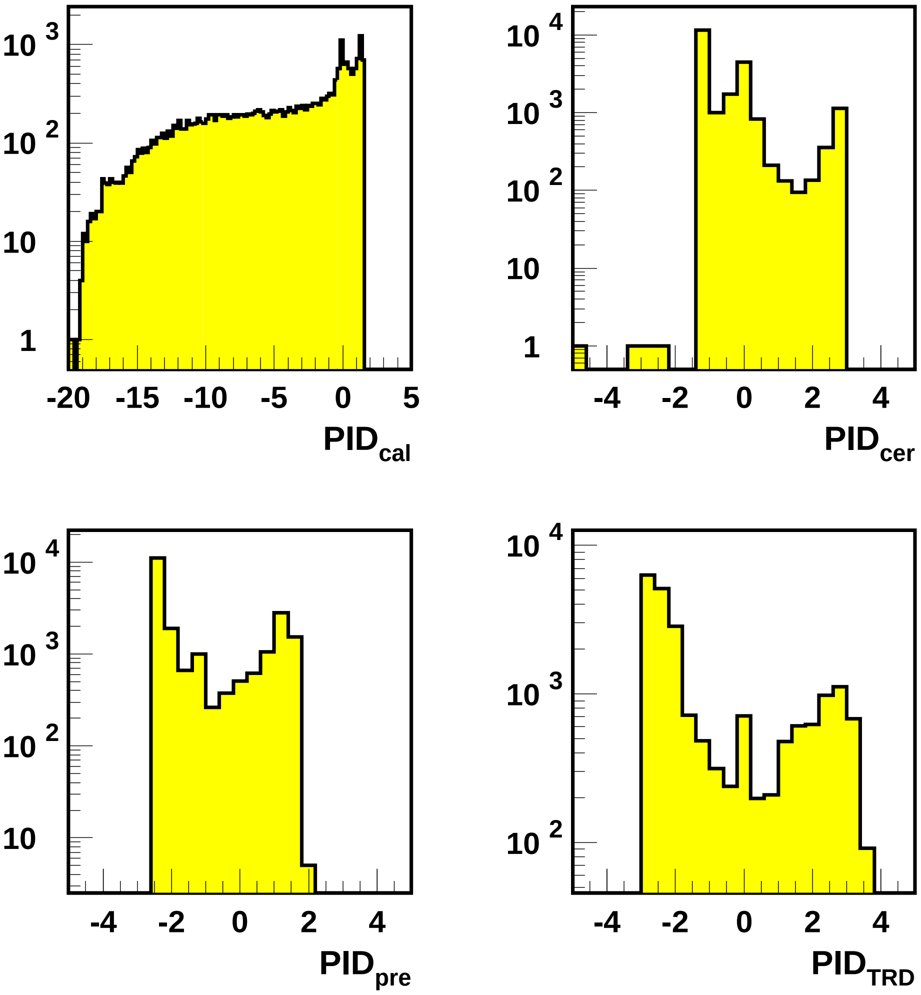

Figure 5.2: Contributions of the PID detectors to the PID quantities.

5.2 Efficiencies, Contaminations, Rejection Factors

5.2.1 Single PID Detector

The operation of a particle identification detector relies on the fact that the detector responds differently to different types of particles. In the simple case of only two kinds of particles the spectrum of the detector response consists of two peaks which can be separated by the application of a single cut. In order to define this cut a second detector or PID quantity is needed which is independent of the one being examined. This detector/quantity can be used to define a clean sample of each particle type and the choice of the cut can be based on these samples.

The true detector responses for the two particle types will be labelled H and P. Without the use of other detectors only their sum $(H + P)$ can be determined. The distributions H and P are divided into the two parts above and below the cut and named H_a, H_b, P_a, P_b (Hadrons above the cut, hadrons below the cut, etc.) By using a second detector or PID quantity to define clean particle samples the measured distributions $H_a^m, H_b^m, P_a^m, P_b^m$ are obtained. As both detectors are independent these distributions will have the same shape as the real distributions, but not necessarily the same relative size. This depends on the cuts applied to the second detector that define the two clean samples.

The measured distributions can be normalised, resulting in the distributions h_a, h_b, p_a, p_b, which can be identified with the conditional probabilities defined in section 5.1.1. The normalisation is defined by $h_a + h_b = p_a + p_b = 1$. These normalised distributions depend only on the detector response, while the real distributions are a product of this response and the incident particle fluxes.

Figure 5.3 shows a schematic drawing of the real, the measured and the normalised distributions. For simplicity the labels of the distributions will also be used synonymously for the numbers of particles in them.

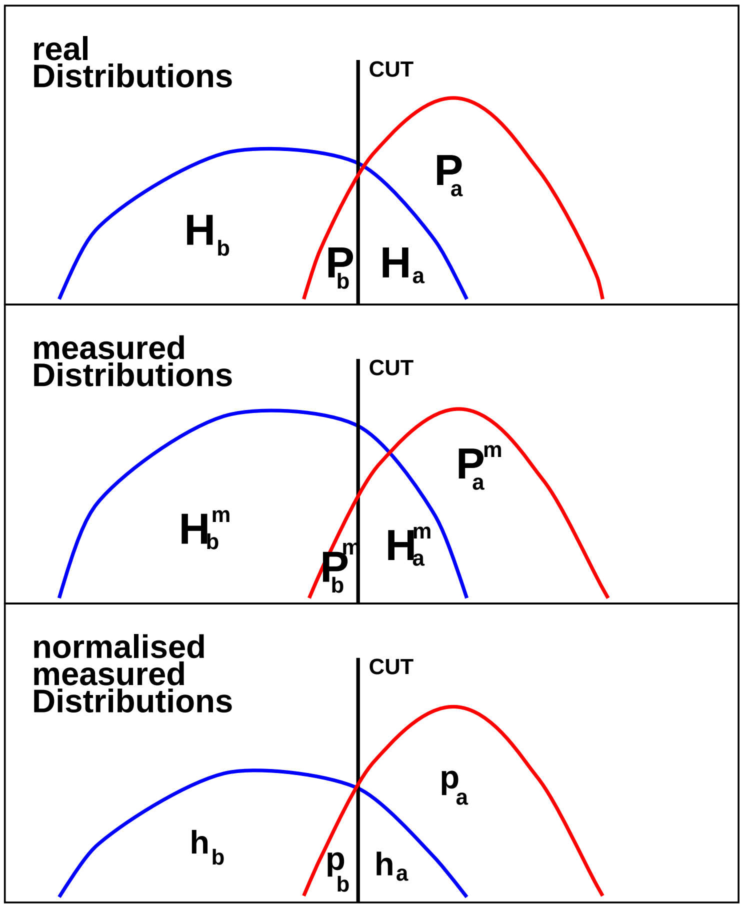

Figure 5.3: Schematic single PID detector response to two types of particles; real, measured and measured/normalised.

The normalised distributions are calculated as follows:

$$h_a = \frac{H_a^m}{H_a^m + H_b^m} \qquad\qquad p_a = \frac{P_a^m}{P_a^m + P_b^m} \tag{5.22}$$

and analogously for h_b, p_b. The ratio between the real and normalised distributions is the flux factor of that particle type:

$$H_a = h_a \cdot \phi_h \qquad\qquad P_a = p_a \cdot \phi_p \tag{5.23}$$

The flux factors cannot be determined exactly from the detector response alone. However, in the case where the separation of the two distributions in the PID detector is good

$$H_a \ll P_a, H_b \qquad P_b \ll H_b, P_a \tag{5.24}$$

the ratio $\Phi = \phi_h/\phi_p$ can be approximated as

$$\Phi = \frac{H_a + H_b}{P_a + P_b} \approx \frac{H_b}{P_a} \approx \frac{H_b + P_b}{P_a + H_a} \tag{5.25}$$

The parameters used for physics analysis such as efficiency (ε), contamination (c) and rejection factor (r) are determined from the normalised measured distributions. For the contamination values the flux factor ratio Φ is needed as well. The positron efficiency ε_p, the hadron rejection factor r_h (also referred to as pion rejection factor) and the hadron contamination of the positron sample c_h can be written as:

$$\varepsilon_p = \frac{P_a}{P_a + P_b} = \frac{p_a\phi_p}{p_a\phi_p + p_b\phi_p} = p_a \tag{5.26}$$

$$r_h = \frac{H_a + H_b}{H_a} = \frac{h_b\phi_h + h_a\phi_h}{h_a\phi_h} = \frac{1}{h_a} \tag{5.27}$$

$$c_h = \frac{H_a}{P_a + H_a} = \frac{h_a\phi_h}{p_a\phi_p + h_a\phi_h} = \frac{\Phi}{\varepsilon_p r_h + \Phi} \tag{5.28}$$

In the same way the hadron efficiency ε_h, the positron rejection factor r_p and the positron contamination of the hadron sample c_p are given as:

$$\varepsilon_h = h_b \tag{5.29}$$

$$r_p = 1/p_b \tag{5.30}$$

$$c_p = \frac{p_b}{\Phi h_b + p_b} = \frac{1}{\varepsilon_h r_p \Phi + 1} \tag{5.31}$$

The contamination at a particular efficiency characterizes the quality of the data, while the rejection factor at a given efficiency measures the performance of the PID detector.

5.2.2 First Order Corrections

The assumption that completely clean particle samples can be created is unfortunately not correct. In practice, there will be contamination of these 'clean' samples. However, given enough redundancy in the particle identification it is possible to quantify the contamination and either correct for it or quote it as part of the systematic uncertainty.

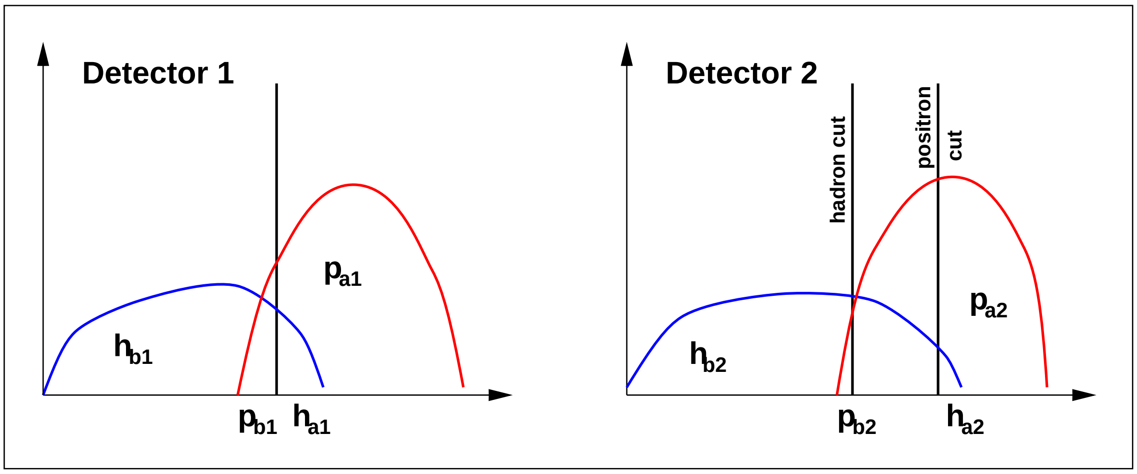

Figure 5.4: Schematic normalised hadron and positron distributions in detector 1 and 2, with the cuts to detector 2 that define the samples for detector 1

Consider the case of two kinds of particles, for example hadrons and positrons (labelled h and p) and two particle identification detectors (labelled 1 and 2). By applying two cuts on the response of detector 2 clean particle particle samples can be created for detector 1 (see figure 5.4). Under the simplifying assumptions that

- the samples in detector 2 are pure, that is they have negligible contamination,
- the numbers of hadrons above (h_a) and positrons below the cut (p_b) in detector 2 are small,
- the normalised distributions of hadrons and positrons in detector 1 (h_1,p_1) reproduce the shape of the real distributions reasonably well,

first order corrections on the normalised measured values in detector 1 can be calculated.

Here the number of hadrons above the cut in detector 1, h_{a1}, will serve as an example. The corrections to h_{b1}, p_{b1} and p_{a1} are calculated in an analogous way. The value including the first order corrections is labelled h'_{a1}. This correction affects the value of the hadron contamination c_h, which is calculated from h_{a1} (see equation 5.28).

Although each distribution h_1, p_1, h_2, p_2 is normalised to 1, the cuts on detector 2 introduce a mismatch in the normalisation. For example, the term (h_{a2} and p_{a2}) comprises the normalised positron sample in detector 1 ($p_{a1} + p_{b1}$), but is itself not necessarily normalised to 1. A term of the form $(p_{a1} + p_{b1})/(h_{a2} + p_{a2})$ is necessary to compensate for this normalisation mismatch.

It is also assumed that the particles that were misidentified by the hard cuts on detector 2 have distributions in detector 1 consistent with their true identity, for example hadrons misidentified as positrons in detector 2 (h_{a2}) nevertheless are distributed as hadrons in detector 1. This is true if the two detectors are independent.

Considering this, there are three contributions to h'_{a1}:

1. Hadrons misidentified as positrons in detector 1 (i.e. that are below the hadron cut in detector 2 and above the cut in detector 1). This is simply the definition of h_{a1}.
2. Hadrons misidentified as positrons in detector 2 (i.e. that are above the positron cut in detector 2 (h_{a2})) and therefore appear as part of the positron sample in detector 1. Assuming that their response in detector 1 is consistent with their true identity as hadrons, the part of them that must be added to h_{a1} is given as $h_{a2} \cdot h'_{a1}/(h'_{a1} + h'_{b1})$. Due to the normalisation mismatch this term has to be multiplied by $(p_{a1} + p_{b1})/(h_{a2} + p_{a2})$.
3. Positrons misidentified as hadrons in detector 2 (i.e. that are below the hadron cut in detector 2 (p_{b2}). Most of these will have to be subtracted from h_{a1}. Again

assuming that their response in detector 1 is consistent with their true identity, in this case as positrons, the term that must be subtracted is $p_{b2} \cdot p'_{a1}/(p'_{a1} + p'_{b1})$. This term must be multiplied by $(h_{a1} + h_{b1})/(h_{b2} + p_{b2})$ to correct for the mismatch in the normalisation.

The combination of the three terms leads to the following expression for $\mathbf{h'_{a1}}$:

$$h'_{a1} = h_{a1} + h_{a2} \cdot \frac{h'_{a1}}{h'_{a1} + h'_{b1}} \cdot \frac{p_{a1} + p_{b1}}{h_{a2} + p_{a2}} - p_{b2} \cdot \frac{p'_{a1}}{p'_{a1} + p'_{b1}} \cdot \frac{h_{a1} + h_{b1}}{h_{b2} + p_{b2}} \tag{5.32}$$

For normalised distributions ($p_{a1} + p_{b1} = h_{a1} + h_{b1} = 1$), this simplifies to:

$$h'_{a1} = h_{a1} + \frac{h'_{a1}}{h'_{a1} + h'_{b1}} \cdot \frac{h_{a2}}{h_{a2} + p_{a2}} - \frac{p'_{a1}}{p'_{a1} + p'_{b1}} \cdot \frac{p_{b2}}{h_{b2} + p_{b2}} \tag{5.33}$$

The second and third terms of equation (5.33) contain the hadron and positron contaminations in detector 2 for a flux ratio of 1. This is to be expected since it shows that the first order corrections to h_{a1} depend on the contamination of the hadron and positron samples defined by detector 2. To simplify the expression the parameters A and B are introduced:

$$\begin{aligned} A &= \frac{h_{a2}}{h_{a2} + p_{a2}} \\ B &= \frac{p_{b2}}{h_{b2} + p_{b2}} \end{aligned} \tag{5.34}$$

A closer look reveals that if the same corrective procedure is applied to h_{b1}, p_{b1}, p_{a1} the normalisation of the distributions in detector 1 is probably no longer correct and they have to be re-normalised so that $p'_{a1} + p'_{b1} = h'_{a1} + h'_{b1} = 1$. This leads to the following expressions:

$$\begin{aligned} h'_{a1} &= \frac{1}{1 + A - B}\left[h_{a1} + Ah'_{a1} - Bp'_{a1}\right] \\ p'_{a1} &= \frac{1}{1 - A + B}\left[p_{a1} - Ah'_{a1} + Bp'_{a1}\right] \\ h'_{b1} &= \frac{1}{1 + A - B}\left[h_{b1} + Ah'_{b1} - Bp'_{b1}\right] \\ p'_{b1} &= \frac{1}{1 - A + B}\left[p_{b1} - Ah'_{b1} + Bp'_{b1}\right] \end{aligned} \tag{5.35}$$

These equations still contain corrected and uncorrected parameters in a mixed fashion. Fortunately the first two equations have the same structure as the last two, so that only a system of two equations with two parameters has to be solved. The final expressions are:

$$\begin{aligned}
h'_{a1} &= \frac{1}{1-A-B}\left[h_{a1} - Ah_{a1} - Bp_{a1}\right] \\
p'_{a1} &= \frac{1}{1-A-B}\left[p_{a1} - Ah_{a1} - Bp_{a1}\right] \\
h'_{b1} &= \frac{1}{1-A-B}\left[h_{b1} - Ah_{b1} - Bp_{b1}\right] \\
p'_{b1} &= \frac{1}{1-A-B}\left[p_{b1} - Ah_{b1} - Bp_{b1}\right]
\end{aligned} \tag{5.36}$$

If, for example, this correction is applied to the hadron rejection factor, the following is obtained:

$$r'_h = \frac{1}{h'_{a1}} = \frac{1-A-B}{h_{a1} - Ah_{a1} - Bp_{a1}} = r_h \cdot \left(\frac{1-A-B}{1-A-B\frac{p_{a1}}{h_{a1}}}\right) \tag{5.37}$$

For $p_{a1} \gg h_{a1}$ and A, B small, which typically is the case, this can be approximated as

$$r'_h \approx r_h \cdot (1 + B\frac{p_{a1}}{h_{a1}}) \tag{5.38}$$

which has two interesting implications: The corrected hadron rejection factor is always larger than the uncorrected one, and the positron contamination of the hadron sample (c_{p2}) has to be small relative to h_{a1} to leave the correction reasonably small. In a similar way it can be seen that the corrected positron efficiency is always larger and the corrected hadron contamination always smaller than the uncorrected one.

Now the sample contaminations c_{h2} and c_{p2} can be used to estimate the systematic errors, or corrected values can be calculated for efficiencies, contaminations and rejection factors in detector 1. To illustrate the effect, here is a numerical example:

$$\begin{array}{llll}
h_{a1} = 0.100 & h_{b1} = 0.900 & p_{a1} = 0.950 & p_{b1} = 0.050 \\
h_{a2} = 0.010 & h_{b2} = 0.700 & p_{a2} = 0.500 & p_{b2} = 0.001
\end{array}$$

Using equations (5.36) the corrected values are

$$h'_{a1} = 0.099 \qquad h'_{b1} = 0.901 \qquad p'_{a1} = 0.967 \qquad p'_{b1} = 0.033$$

In this example the hadron rejection factor of detector 1 is raised from 10 to 10.12 (The approximation (5.38) gives 10.14). Using the contaminations instead for the systematic error, a systematic error of 2% is obtained.

5.2.3 Several PID Detectors

For two or more PID detectors combined efficiencies, contaminations and rejection factors can be determined. If the same straight cuts on the single detector responses are used, this combination is done by multiplying the single detector efficiencies and rejection factors. However, for the combined contamination the flux factor Φ must be taken into account.

$$\begin{aligned}
\mathcal{E}_{h,p} &= \prod_i \varepsilon^i_{h,p} \\
\mathcal{R}_{h,p} &= \prod_i r^i_{h,p} \\
\mathcal{C}_h &= \frac{\Phi}{\mathcal{E}_p \mathcal{R}_h + \Phi} \\
\mathcal{C}_p &= \frac{1}{\mathcal{E}_h \mathcal{R}_p \Phi + 1}
\end{aligned} \tag{5.39}$$

Here $\mathcal{C}_h$ is the total hadron contamination in the positron sample and $\mathcal{C}_p$ is the total positron contamination in the hadron sample.

For the case that the contaminations for each detector are small, $\mathcal{C}$ can be approximated by their product. However, the flux factor Φ can only be used once and therefore has to be divided out (n-1) times (or multiplied in for the case of positron contamination):

$$\begin{aligned}\mathcal{C}'_h &= \frac{1}{\Phi^{n-1}} \prod_i^n c_h^i \lesssim \mathcal{C}_h \\ \mathcal{C}'_p &= \Phi^{n-1} \prod_i^n c_p^i \lesssim \mathcal{C}_p \end{aligned} \tag{5.40}$$

Straight cuts on every PID detector response are the best strategy to minimize the contamination. However, this is not the best way to maximise the efficiency while maintaining a low contamination. In the case of two detectors a linear 'valley cut' in the plane of the two detector responses represents an improvement. It is possible to use the projection onto the axis perpendicular to the cut like a single detector response (see figure 5.5).

The projection along the cut is calculated by a simple coordinate transformation (see figure 5.6). In principle the origin of the coordinate system is moved by (x_0, y_0) and the coordinate system is rotated by an angle α. Therefore the new coordinates x' and y' are given as:

$$\begin{pmatrix} x' \\ y' \end{pmatrix} = \begin{pmatrix} \cos\alpha & \sin\alpha \\ -\sin\alpha & \cos\alpha \end{pmatrix} \begin{pmatrix} x - x_0 \\ y - y_0 \end{pmatrix} \tag{5.41}$$

For the projection only the new x-axis is of interest, so that x_0 can be set to 0. This leads to:

$$x' = \cos\alpha \cdot x + \sin\alpha(y - y_0) \tag{5.42}$$

It is convenient to divide by $\cos\alpha$ to get a parameter X that is also practical for use in the PID3-pulsTRD plane:

$$X = \frac{x'}{\cos\alpha} = x + \tan\alpha \cdot y - \tan\alpha \cdot y_0 \tag{5.43}$$

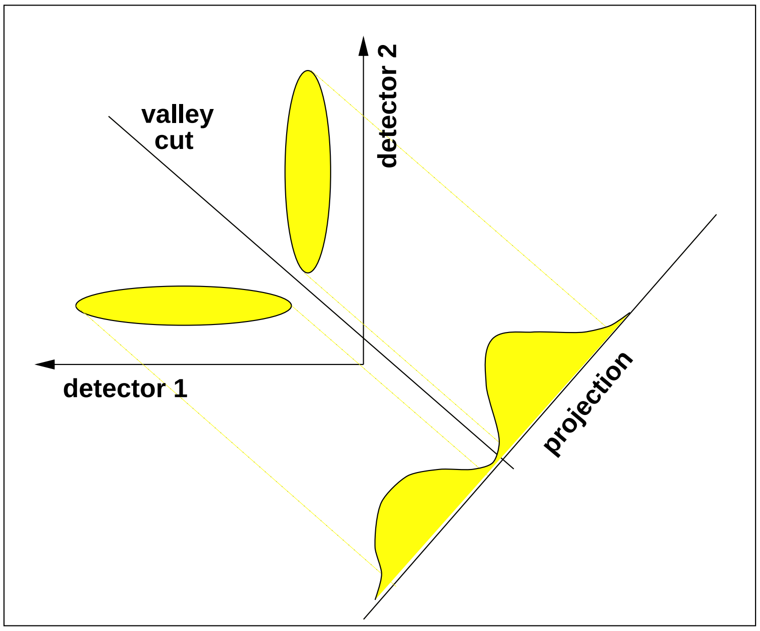

Figure 5.5: Valley cut in the detector 1,2 plane and projection onto the axis perpendicular to the cut.

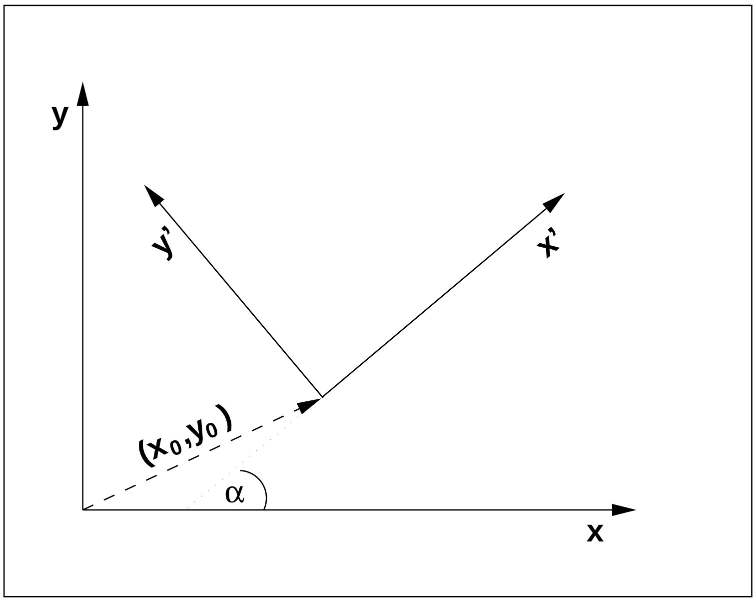

Figure 5.6: Simple 2d coordinate transformation for the valley cut projection.

The cut is by definition at $X = 0$ and the condition for positron identification in the case of PID3 and pulsTRD becomes

$$PID3 + \tan\alpha \cdot \text{pulsTRD} > \tan\alpha \cdot y_0 \tag{5.44}$$

If an additional PID detector is available, efficiency and contamination can be determined as in the single detector case. If on the other hand no additional PID information is available, it is impossible to give exact values for contamination, efficiency and rejection from the data. In this case a Monte Carlo simulation of the detector responses can be used or an estimate can be obtained by using a few simplifying assumptions.

5.2.4 Errors

For a single detector, estimates of the statistical errors on efficiency and rejection factor can be given simply by

$$\begin{aligned} \frac{\delta r_h}{r_h} &= \frac{\delta h_a}{h_a} \sim \frac{1}{\sqrt{H_a^m}} \\ \frac{\delta r_p}{r_p} &= \frac{\delta p_b}{p_b} \sim \frac{1}{\sqrt{P_b^m}} \\ \frac{\delta \varepsilon_h}{\varepsilon_h} &\sim \frac{\delta h_b}{h_b} = \frac{1}{\sqrt{H_b^m}} \\ \frac{\delta \varepsilon_p}{\varepsilon_p} &= \frac{\delta p_a}{p_a} \sim \frac{1}{\sqrt{P_a^m}} \end{aligned} \tag{5.45}$$

which in turn can be used to calculate the error on the contamination:

$$\begin{aligned} \delta c_h &= \frac{1}{(\varepsilon r + \Phi)^2}\sqrt{\varepsilon^2 r^2 \delta^2\Phi + r^2\delta^2\varepsilon + \varepsilon^2\delta^2 r} \\ \delta c_p &= \frac{1}{(\varepsilon r \Phi + 1)^2}\sqrt{\varepsilon^2 r^2 \delta^2\Phi + r^2\Phi^2\delta^2\varepsilon + \varepsilon^2\Phi^2\delta^2 r} \end{aligned} \tag{5.46}$$

For $\Phi = 1$ both expressions become:

$$\delta c_{p,h} = \frac{1}{(\varepsilon r + 1)^2}\sqrt{r^2\delta^2\varepsilon + \varepsilon^2\delta^2 r} \tag{5.47}$$

5.3 HERMES PID Cuts

Cuts on the signals of the single PID detectors or cuts on calculated PID quantities like PID3 can be used for particle identification in HERMES. It is also possible to combine these, treating a PID quantity like the response of a single detector. These possibilities have different advantages.

5.3.1 Single Detector Cuts

The advantage in using single detector cuts is the simplicity of the procedure. It is possible to choose cuts that give the same contamination or efficiency for each detector. Furthermore, very clean samples for detector or PID studies can be produced. Cuts can also be made momentum dependent in such a way that efficiency or contamination are constant for different momenta. Typically both cannot be achieved at the same time.

Generally there are two separate cuts for hadrons and positrons. If not stated otherwise, hard cuts are momentum independent, except in the case of the Čerenkov detector, where the cuts to separate positrons and pions are only applied below the pion threshold of 5.7 GeV. The following table (5.1) lists three different sets of hard cuts, the first one for about 90% efficiency per detector, the second one for about 80% efficiency per detector and the third one defined to give samples as clean as possible while retaining a minimum on statistics. The sets of cuts are listed in table 5.1. In each case the other three detectors using the given cuts have determined the hadron and positron samples for the fourth detector. The contamination of these 'clean' samples is estimated as well and included in the contamination errors. The cuts are based on the data from 250 runs version E 1995, representing about 15% of the 1995 data with all PID detectors working. This size of the data set ensures sufficient statistics.

Contamination values in the following tables (5.2,5.3) are calculated using the formulae developed in the previous section. For the single detectors contamination values are given for $\Phi = 1$, for the total values the flux ratio has been properly taken into account. The average flux ratio Φ is 3.6 for set 1, 3.5 for set 2 and 1.4 for set 3.

These cuts (set 2) have been used to define the hadron and positron samples for the determination of the TRD pion rejection factor (section 4.6).

The hard cut conditions for a hadron are of the form

$$\begin{aligned} & (E_{pre} < C^h_{pre}) \wedge (\frac{E_{cal}}{p} < C^h_{cal}) \\ \wedge\ & (E_{TRD} < C^h_{TRD}) \wedge (E_{cer} < C^h_{cer}) \end{aligned} \tag{5.48}$$

where E_{TRD} is the TRD truncated mean, while the hard cut conditions for a positron are

$$\begin{aligned} & (C^p_{pre} < E_{pre}) \wedge (C^{p1}_{cal} < \frac{E_{cal}}{p} < C^{p2}_{cal}) \\ \wedge\ & (C^p_{TRD} < E_{TRD}) \wedge C^p_{cer} < E_{cer}) \end{aligned} \tag{5.49}$$

Set of Cuts	C^h_{pre} [MeV]	C^p_{pre} [MeV]	C^h_{cal}	C^{p1}_{cal}	C^{p2}_{cal}	C^h_{TRD} [keV]	C^p_{TRD} [keV]	C^h_{cer} [N_{pe}]	C^p_{cer} [N_{pe}]
1	0.007	0.021	0.90	0.90	1.25	15.5	23.0	0.50	1.0
2	0.004	0.025	0.80	0.92	1.10	14.0	26.0	0.20	1.4
3	0.002	0.040	0.50	0.95	1.05	10.0	30.0	0.05	2.0

Table 5.1: Three sets of hard PID detector cuts.

Set 1

Positrons

Detector	Positron Efficiency [%]	Hadron Rejection	Hadron Contamination [%]
Preshower	87.9 ± 0.1	25.6 ± 0.1	4.26 ± 0.09
Calorimeter	92.1 ± 0.1	8.4 ± 0.1	12.75 ± 0.14
TRD	91.2 ± 0.1	128.9 ± 0.9	0.84 ± 0.42
Čerenkov	88.1 ± 0.1	6.1 ± 0.1	15.63 ± 0.22
total	65.1 ± 0.3	$(1.51 \pm 0.04) \times 10^6$	$(9.8 \pm 5.4) \times 10^{-4}$

Hadrons

Detector	Hadron Efficiency [%]	Positron Rejection	Positron Contamination [%]
Preshower	90.3 ± 0.1	85.7 ± 0.9	1.27 ± 0.01
Calorimeter	86.7 ± 0.1	19.4 ± 0.1	5.61 ± 0.03
TRD	87.7 ± 0.1	84.9 ± 0.9	1.33 ± 0.01
Čerenkov	79.2 ± 0.1	17.4 ± 0.1	6.78 ± 0.04
total	54.4 ± 0.2	$(2.45 \pm 0.08) \times 10^6$	$(7.5 \pm 0.2) \times 10^{-5}$

Set 2

Positrons

Detector	Positron Efficiency [%]	Hadron Rejection	Hadron Contamination [%]
Preshower	84.6 ± 0.1	31.1 ± 0.1	3.63 ± 0.14
Calorimeter	83.7 ± 0.1	11.4 ± 0.1	12.74 ± 0.08
TRD	81.4 ± 0.1	341.0 ± 4.3	0.36 ± 0.24
Čerenkov	80.0 ± 0.1	9.4 ± 0.1	11.77 ± 0.12
total	46.1 ± 0.4	$(1.14 \pm 0.02) \times 10^6$	$(2.4 \pm 1.7) \times 10^{-4}$

Hadrons

Detector	Hadron Efficiency [%]	Positron Rejection	Positron Contamination [%]
Preshower	81.7 ± 0.1	366.7 ± 9.3	0.33 ± 0.04
Calorimeter	80.0 ± 0.1	109.7 ± 1.4	1.13 ± 0.14
TRD	77.7 ± 0.1	148.5 ± 2.3	0.86 ± 0.11
Čerenkov	79.4 ± 0.1	26.1 ± 0.1	4.60 ± 0.55
total	40.3 ± 0.3	$(1.56 \pm 0.09) \times 10^8$	$(1.6 \pm 0.8) \times 10^{-6}$

Table 5.2: Hard PID cuts set 1 and set 2

Set 3			
Positrons			
Detector	Positron Efficiency [%]	Hadron Rejection	Hadron Contamination [%]
Preshower	64.2 ± 0.1	62.9 ± 0.7	2.42 ± 0.03
Calorimeter	60.0 ± 0.1	35.3 ± 0.4	8.95 ± 0.02
TRD	61.6 ± 0.1	615 ± 22	0.26 ± 0.01
Čerenkov	67.8 ± 0.2	27.1 ± 0.3	5.16 ± 0.06
total	16.1 ± 0.1	$(3.7 \pm 0.3) \times 10^{7}$	$(5.4 \pm 0.3) \times 10^{-5}$
Hadrons			
Detector	Hadron Efficiency [%]	Positron Rejection	Positron Contamination [%]
Preshower	33.7 ± 0.1	2218 ± 192	0.12 ± 0.01
Calorimeter	62.8 ± 0.1	601 ± 25	0.26 ± 0.26
TRD	43.6 ± 0.1	666 ± 31	0.34 ± 0.34
Čerenkov	74.5 ± 0.1	41.8 ± 0.2	3.11 ± 0.40
total	7.7 ± 0.1	$(3.7 \pm 0.7) \times 10^{10}$	$(1.8 \pm 1.1) \times 10^{-8}$

Table 5.3: Hard PID cuts set 3

5.3.2 PID3-TRD Valley Cut

PID3 and the TRD are used together to achieve a high positron efficiency with low hadron contamination. To this end a linear valley cut in the PID3-TRD plane is used. Figure 5.7 below illustrates the clear separation of hadrons and positrons in the PID3-TRD plane that suggests the use of a valley cut.

The optimal valley cut is assumed to be the one with the smallest number of particles close to it. To determine its position, the projection onto the axis perpendicular to the cut according to equation (5.43) is used:

$$X = PID3 + \tan\alpha \cdot \text{pulsTRD} - \tan\alpha \cdot y_0 \tag{5.50}$$

Here α is the angle of the cut and y_0 is the value of pulsTRD for PID3=0 which together unambiguously determine the cut.

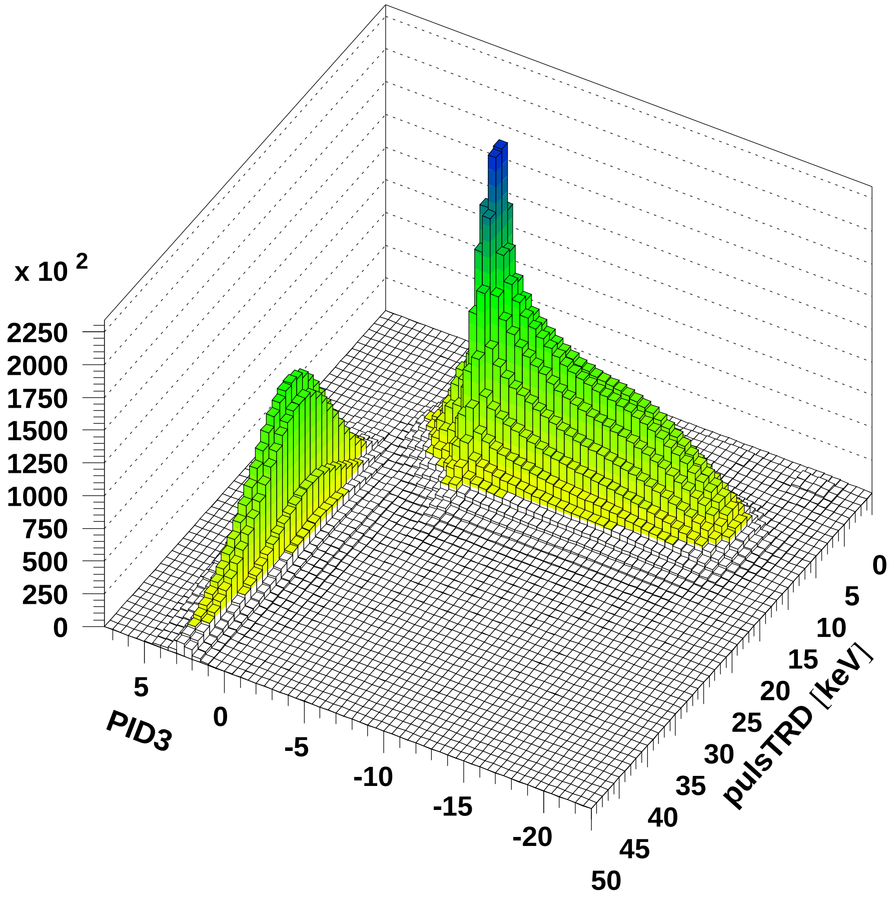

Figure 5.7: 3D representation of the PID3-TRD plane.

The number of particles S in the interval [-1,1] in X was taken as a measure of the number of particles close to the cut and α and y_0 were varied to minimise S. A two-dimensional parameter search was carried out. Figure 5.8 illustrates that this procedure produces reasonable minima in S for α and y_0. The selected values were $\alpha = 0.3$ and $y_0 = 17.7$ keV. For this determination only a subsample of the data was used as soon as version E of the data production was available.

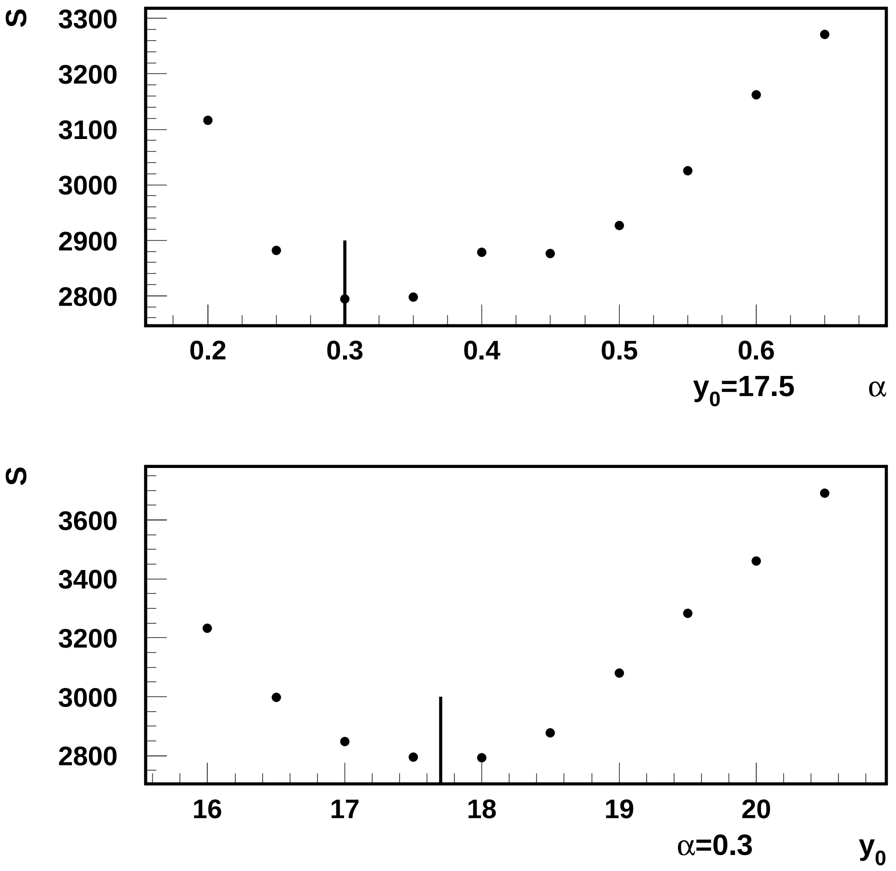

Figure 5.8: Determination of the PID3-TRD valley cut by minimising the number of particles close to the cut. The lines indicate the selected values of α and y_0

The values for the PID2-TRD cut were found in the same way. The resulting cuts are (see equation 5.44):

$$\begin{aligned} PID3 + 0.31 \cdot \text{pulsTRD} &> 5.48 \\ PID2 + 0.51 \cdot \text{pulsTRD} &> 9.0 \end{aligned} \tag{5.51}$$

5.3.3 PID Downshifting

The full complement of PID detectors is not always available for analysis. Some detectors are more sensitive to background; there may be calibration problems for a particular PID detector for a set of runs or there may have been a hardware problem. In this case it is necessary to decide whether the data can be used nevertheless, and which PID scheme must be applied for each subset of the data.

Runs where either the TRD or the Čerenkov are not available can be used for the inclusive analysis of the 1995 HERMES data, but runs where both of them cannot be used should not be included in the physics analysis.

This leads to the following PID downshifting scheme:

- The standard PID cut is the PID3-TRD valley cut.
- If the TRD is not available the cut at PID3=0 is used.
- For runs where the Čerenkov is not available the PID2-TRD valley cut is used.

Cases where the calorimeter or the preshower were not available are already excluded, since both of them are part of the standard physics trigger. Figure 5.9 shows the three cuts and table 5.4 lists the relative percentages for the downshifting scheme.

PID	All Events		Events used for inclusive Analysis	
	Top	Bottom	Top	Bottom
PID3-TRD	89.2 %	84.1 %	97.1 %	98.0 %
PID3	4.6 %	1.9 %	2.9 %	2.0 %
PID2-TRD	6.2 %	14.0 %	0.0 %	0.0 %

Table 5.4: Percentage for the different PID methods in the PID downshifting scheme

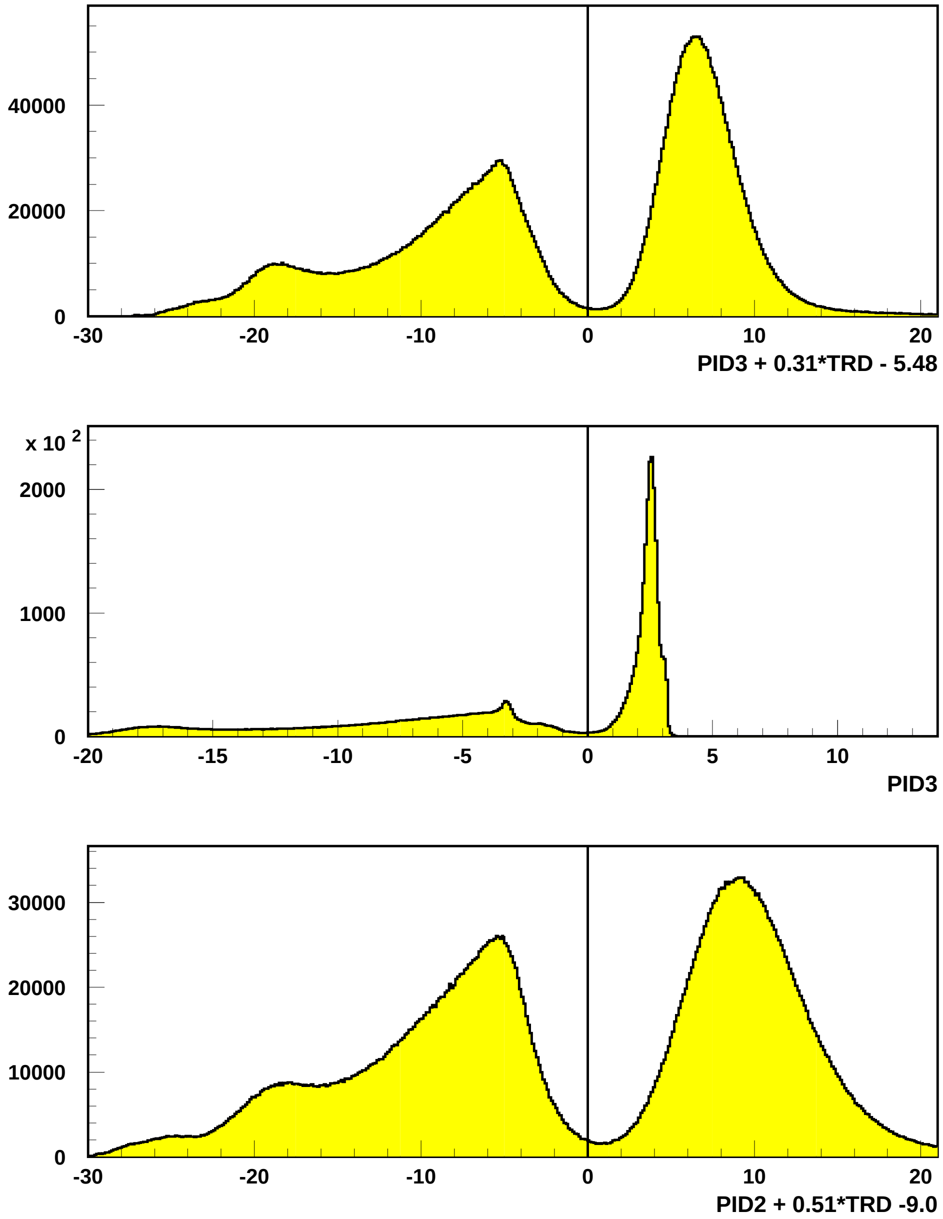

Figure 5.9: Distributions and cuts for the three levels of PID downshifting

5.4 Contamination for the PID3-TRD Valley Cut

It is impossible to calculate the real value of the hadron contamination for the PID3-TRD valley cut, because all four PID detectors are being used and no additional PID information is available to produce clean particle samples. However, there are several ways to estimate the contamination:

1. First Order Estimate of the Contamination.
   Use the contamination in region A calculated from hard cuts (figure 5.10), and additionally make a linear approximation for the hadrons in regions B and C.
2. Fitting the Distributions.
   Fit the projection on the axis perpendicular to the cut with the sum of two Gaussians.
3. Comparison to PID2-TRD Valley Cut.
   Use the Čerenkov detector to create hadron and positron samples.
4. Monte Carlo Simulation.
   Calculate the contamination for a sample of simulated hadrons and positrons where the particle type is a priori known.

Theoretically, the Monte Carlo simulation (HMC) would be the best way to determine the hadron contamination for the PID3-TRD valley cut. Unfortunately the simulation of the responses of the PID detectors in HERMES is not yet good enough for this method to yield precise results. The comparison to a PID2-TRD cut using the Čerenkov detector to create hadron and positron samples is at first compelling. However, it is not possible to create samples that are clean enough for this purpose. This leaves the first two methods to estimate the contamination.

5.4.1 First Order Estimate of the Contamination

The quantity PID3 can be treated as a single detector response. The positron efficiency and hadron contamination can be determined using clean samples defined by the TRD. In turn, clean samples generated by the other detectors can be used to determine efficiency and contamination values for the TRD.

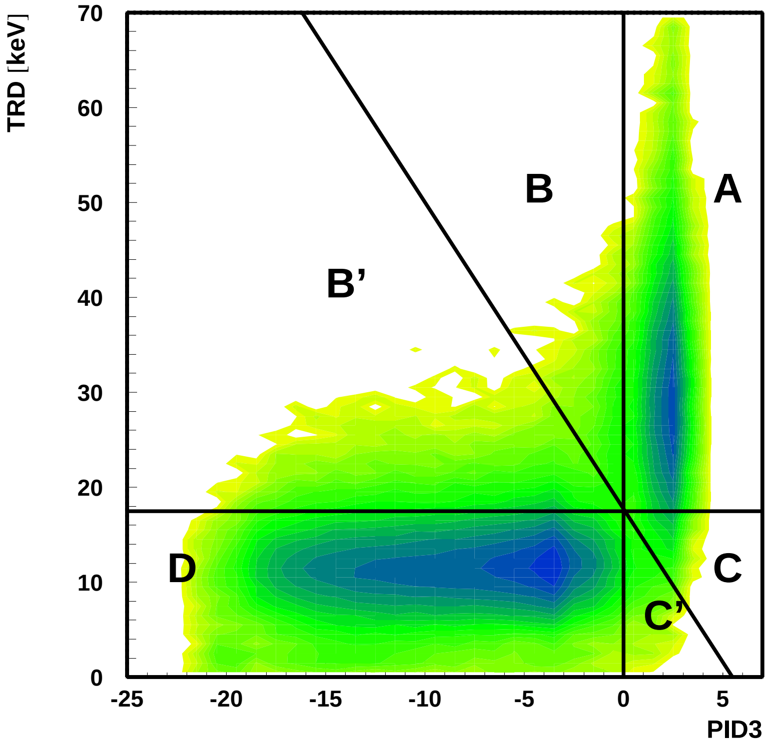

Figure 5.10: The TRD-PID3 plane with straight cuts and valley cut.

The TRD-PID3 plane is shown together with the valley cut and the cuts at PID3=0 and TRD=17.7 keV in figure 5.10. Region A corresponds to the use of both hard cuts to define positrons. The positron efficiency $\mathcal{E}_p(A)$ and hadron contamination $\mathcal{C}_h(A)$ in region A can be calculated from the PID3 and pulsTRD efficiencies and contaminations according to equation (5.39). They in turn can be used to determine approximately the number of hadrons and positrons in the region A that pass both straight cuts. If $N(A)$ is the total number of particles in this region the following is obtained:

$$\begin{aligned} N_h(A) &= N(A) \cdot \mathcal{C}_h \\ N_p(A) &= N(A)(1 - \mathcal{C}_h) \end{aligned} \tag{5.52}$$

and the approximate total number of positrons N_p in the data samples becomes

$$N_p = \frac{N_p(A)}{\mathcal{E}_p} = N(A)\frac{(1 - \mathcal{C}_h)}{\mathcal{E}_p} \tag{5.53}$$

The difference between the valley cut and the two straight cuts is the addition of regions B and C. This increases the positron efficiency but also makes the hadron contamination larger. Estimates of the numbers of hadrons and positrons in both regions are needed. The overall hadron contamination, positron efficiency and hadron rejection can then be calculated as

$$\begin{aligned} \mathcal{E}_p &= \frac{N_p(A) + N_p(B) + N_p(C)}{N_p} \\ \mathcal{R}_h &= \frac{N_h}{\sum_{A,B,C} N_h(i)} \\ \mathcal{C}_h &= \frac{\sum_{A,B,C} N_h(i)}{\sum_{A,B,C} (N_h(i) + N_p(i))} \end{aligned} \tag{5.54}$$

The rejection factor is not of particular interest in this case, as the cut is rather data specific and, as already mentioned, the rejection factor is used to measure detector performance.

The simplest model for two distributions that overlap is the combination of two linear distributions of the same size that add up to a constant value (figure 5.11a). If cut in the middle, the contamination on either side will be 25%, while the efficiency is 75%. The next slightly more elaborate model is to have an overall spectrum of the shape shown in figure 5.11b, with a V-shape on top of a constant contribution. Here it is assumed that 25% of the constant part of the distribution above the cut is the contamination. This is equivalent to describing the distributions as a combination of two linear functions with different slopes above and below the cut.

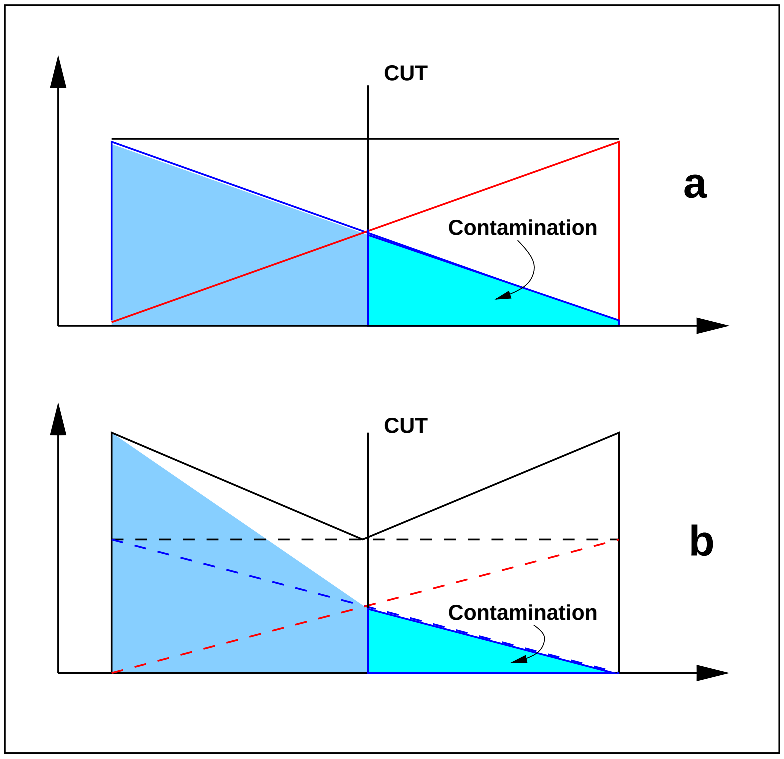

Figure 5.11: Model for a first order estimate of the contamination.

To apply this model to the TRD-PID3 valley cut the regions B,B' and C,C' are projected onto an axis perpendicular to the cut axis. The result is treated as the response of a single detector and the first order estimate model is applied, taking the minimum of the two bins on either side of the cut as the constant value m. The projected histogram of regions B,B' is labelled P_B and $N_h(B)$ and $N_p(B)$ are determined as

$$N_h(B) = \sum_{cut}^{max} \min\left(\frac{\mathrm{m}}{4}, \mathrm{P_B}\right)$$

$$N_p(B) = N(B) - N_h(B) \tag{5.55}$$

$N_h(C)$ and $N_p(C)$ are determined in the same way. The sum to determine $N_h(B)$ runs over all bins between the cut (at zero) and a maximum value that was set to X=4.5. This maximum value was taken from the results of the Gaussian fits in the next section.

Efficiency and contamination can now be calculated using equations (5.54). The output of the PAW[113] macro used for these calculations is shown in figure 5.12. The top plot is the TRD-PID3 plane with the applied cuts. The three other histograms are the projections of the whole plane and regions B,B' and C,C' onto the axis perpendicular to the valley cut. Finally the calculated values for efficiencies and contaminations are given. The projections of B,B' and C,C' illustrate that the simple model used for the contamination estimate works fairly well. The dark areas in the histograms indicates the size (but not the shape) of the estimated hadron contamination.

An estimate of the upper limit on the relative uncertainty of the flux factor $\delta\Phi$ may be expressed:

$$\frac{\delta\Phi}{\Phi} \leq \frac{\sum_{A,B,C} N_h}{\sum_{B',C',D} N(i)} \tag{5.56}$$

For the TRD-PID3 valley cut the relative error on $N_h(B,C)$ is conservatively estimated to be 50% and the contribution $\delta E_{B,C}$ of the regions B and C to the error on the total positron efficiency becomes

$$\delta E_{B,C} = 0.5 \cdot \frac{N_h(B,C)}{\sum_{A,B,C} N_p(i)}. \tag{5.57}$$

In region A the error on the efficiency E_A is calculated using the binomial distribution:

$$\delta E_A = \sqrt{\frac{E_A(1-E_A)}{N(A)}} \tag{5.58}$$

The overall estimate then is the sum of the three errors:

$$\delta E = \delta E_A + \delta E_B + \delta E_C \tag{5.59}$$

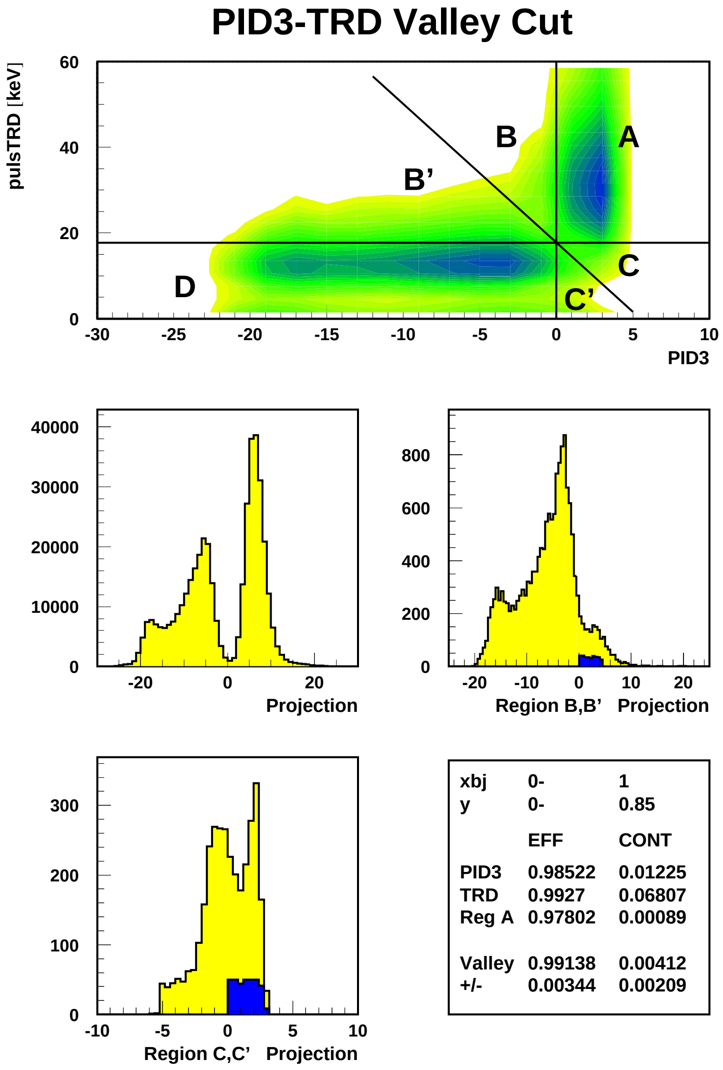

xbj	0-	1
y	0-	0.85
	EFF	CONT
PID3	0.98522	0.01225
TRD	0.9927	0.06807
Reg A	0.97802	0.00089
Valley	0.99138	0.00412
+/-	0.00344	0.00209

Figure 5.12: Output of cont.kumac for DIS particles from 125 runs between 4944 and 5120.

After a rather lengthy calculation and a few approximations the estimated error on the contamination may be written as

$$\frac{\delta C}{C} \approx \frac{\frac{\delta \Phi}{\Phi} N_h(A) + 0.5 \cdot (N_h(B) + N_h(C))}{\sum_{A,B,C} N_h(i)} + \frac{\frac{\delta \Phi}{\Phi}(N_h(A) + N_p(A)) + N_h(B) + N_h(C)}{\sum_{A,B,C}(N_h(i) + N_p(i))} \tag{5.60}$$

5.4.2 Fitting the Distributions

An alternative way to calculate contaminations and efficiencies for the TRD-PID3 valley cut is to fit the projection X onto the axis perpendicular to the cut (see figure 5.5). Suitable functions have to be selected to fit the hadron and positron distributions in the region around the cut. The simplest choice is two Gaussian functions (g_1, g_2), which provides a reasonable description if hadrons and positrons are well separated. The tail of the hadron distribution that overlaps with the positron distribution typically follows a Landau or Poisson distribution; both can be reasonably approximated by a Gaussian. First both slopes are fitted separately at a distance to the cut to establish starting parameters. In the second step the region around zero is fitted with the sum of both functions $(g_1 + g_2)$. This is illustrated in figure 5.13. The output of the PAW macro used for these fits is shown in figure 5.14.

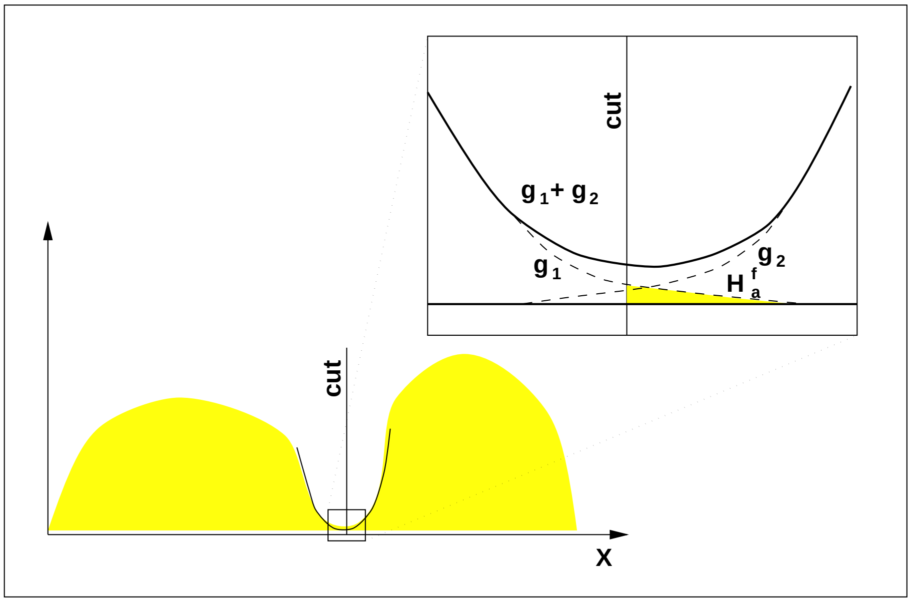

Figure 5.13: Determining the hadron contamination by fitting the distributions.

The number of hadrons above the cut H_a^f is determined by integrating g_1 with the parameters from the $(g_1 + g_2)$-fit:

$$H_a^f = \int_0 g_1 \; dX. \tag{5.61}$$

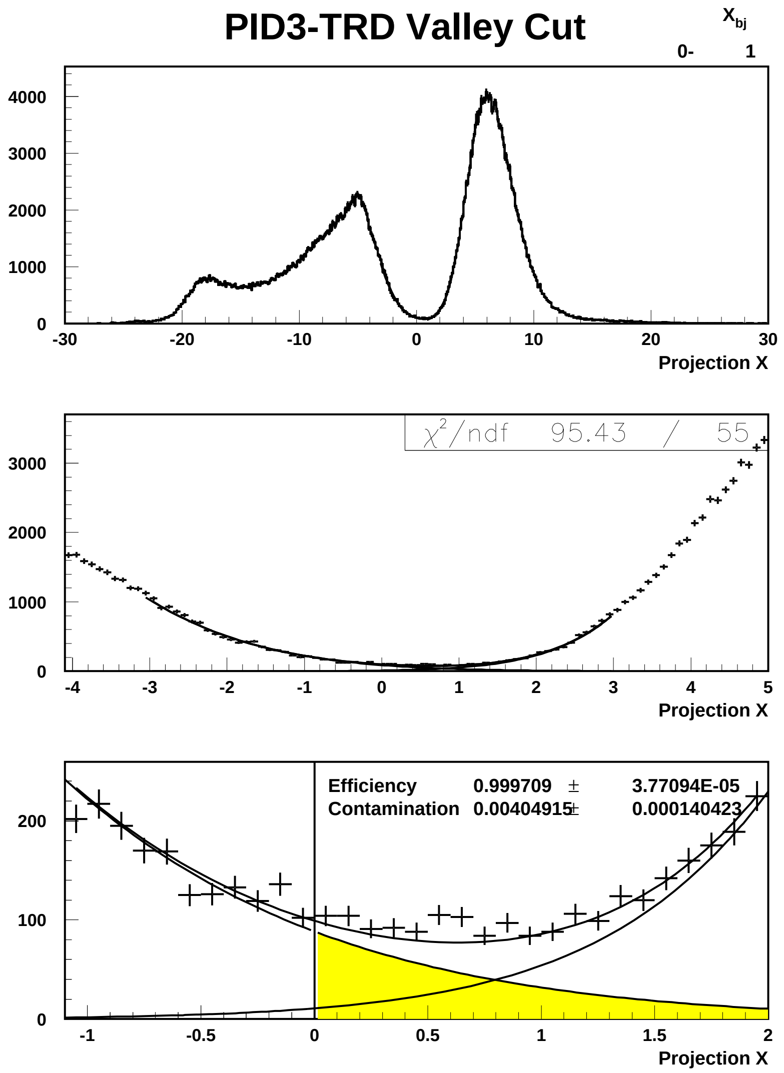

Figure 5.14: Determining the hadron contamination by fitting the distributions. Output of gcont.kumac for DIS particles from 125 runs between 4944 and 5120.

This in turn yields the hadron contamination by dividing by the total number of particles above the cut N_a:

$$\mathcal{C}_h = \frac{H_a^f}{N_a} \tag{5.62}$$

In principle the positron efficiency could be determined from the fit in an analogous way. However, detector inefficiencies cannot be described necessarily by a smooth function and therefore the resulting efficiency values are too large and can only be regarded as an upper limit.

5.5 Details of the Hermes PID

5.5.1 A Closer Look at the Hermes PID

For the data from one run, plots of PID3 vs pulsTRD and for the momentum dependence of both PID3 and pulsTRD show a rather simple structure defined by the two types of particle (hadrons and positrons) and the trigger. If the full available statistics is used for these plots, the Hermes PID presents a more complex picture. A large number of substructures appears in any 3d representation of these data. For example the PID3-P plane is shown in figure 5.15.

A more detailed study of the Hermes particle identification is necessary. This leads to a better understanding of the interplay of the trigger and the PID detectors, to the discovery of problems with the PID and to a few interesting examples of detector physics.

To identify the origin of the observed structures in the PID3-P plane it is divided into a number of different 'zones'. The zones for the PID3-P plane are shown in figure 5.16. The same is done for the PID3-TRD and the TRD-P planes, which display a similar richness in structure. Some zones in one plane are directly related to zones in another plane. In the following sections short descriptions of the different zones will be given as well as more detailed descriptions of selected ones. A complete review can be found in an internal Hermes note[65].

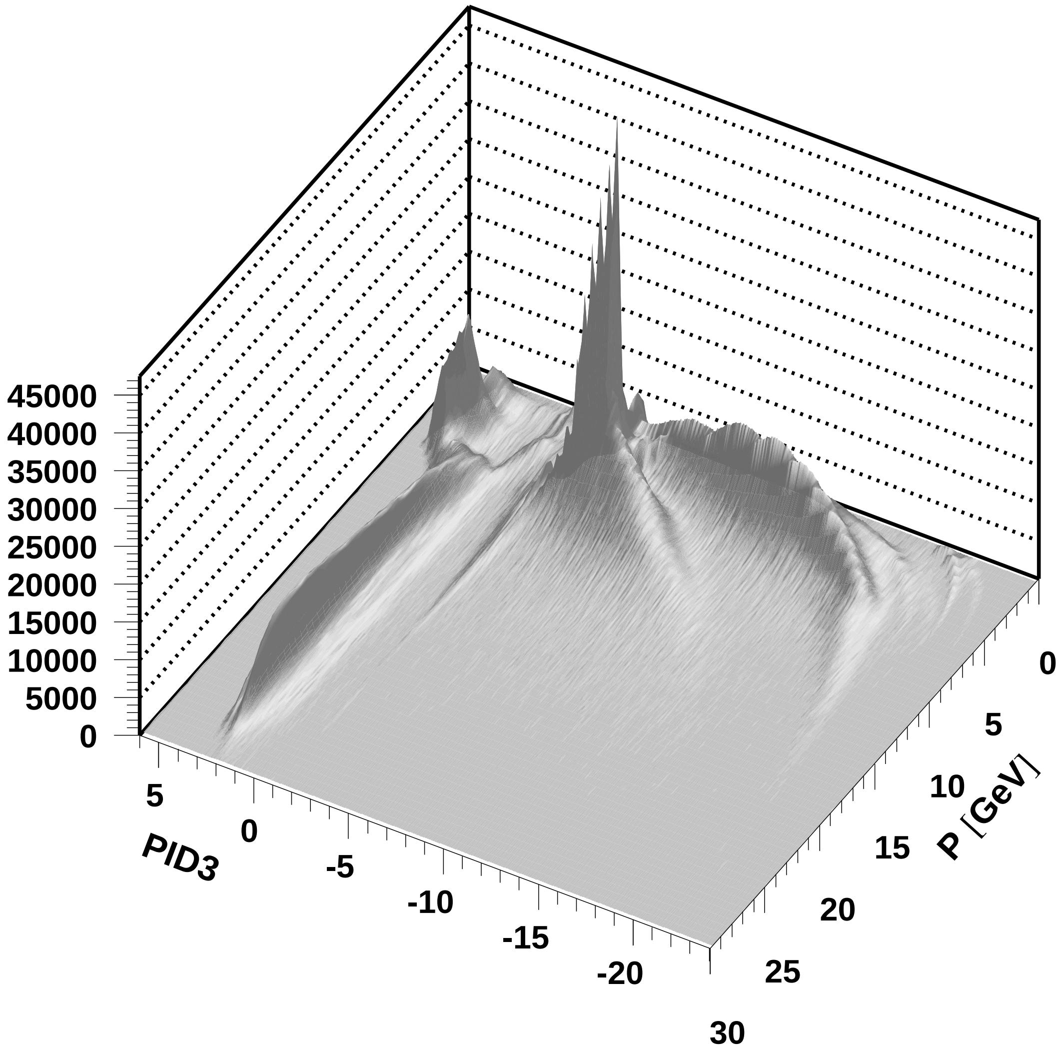

Figure 5.15: 3d picture of the PID3-P plane. The full statistics of the 1995 data has been used.

Several questions have to be answered for every zone:

- What distinguishes the particles in one zone from the ones in another ?
- What leads to the particular shape and the position in a given plane ?
- Is this expected or does it indicate a problem ?

There are a number of parameters that can be used to try to answer these questions. In general this entails the examination of a large number of plots, a subset of which is shown in the following sections. The correlations to study and the plots to make include:

- The signals in the four PID detectors for each zone;
- The xy-distribution at different z, to determine if the particles which belong to a certain zone are localised somewhere in the spectrometer;
- The parent distributions used by the reconstruction program to calculate PID3;
- Kinematics;
- Charge;
- Scattering angles and angles of incidence on particular detectors;
- Particle multiplicity;
- Time of flight;
- Run and burst number, to detect a possible time dependence;
- Correlations to zones in one of the other two planes.

5.5.2 The PID3-P Plane

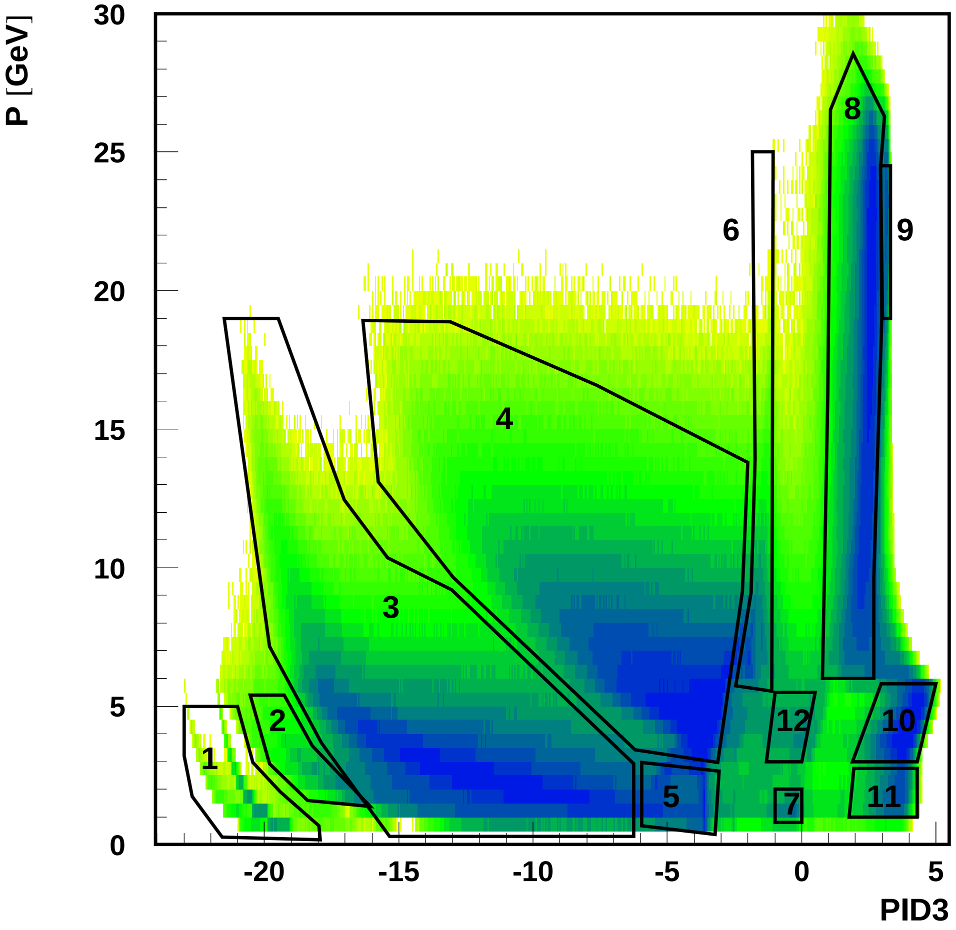

Figure 5.16: The PID3-P plane with zones.

The first plane to be studied is the PID3-P plane. The most basic features are the differences between hadrons and positrons, and between triggering and non-triggering particles. Looking at figure 5.16 these are easily identified. Zones 3 and 4 are clearly hadrons, where zone 4 contains all hadrons that triggered. Zone 8 apparently contains most of the positrons, marked by their positive PID3 value and their large TRD signal. A short description of every zone is given in table 5.5. A more detailed discussion for every zone is given below, illustrated with the relevant plots.

PID3-P Plane	
Zone	Description
1	Hadrons outside of the calorimeter acceptance. Large contribution of protons.
2	Non-triggering hadrons with small calorimeter response.
3	Non-triggering hadrons.
4	Triggering hadrons.
5	Hadrons with $E_{cal}/p \approx 1$.
6	High Momentum Hadrons with $E_{cal}/p = 1$, identified only by the preshower.
7	Low Momentum Positrons that are misidentified by the Čerenkov (Inefficiencies in the photon collection).
8	Positrons above the pion threshold in the Čerenkov.
9	Positrons with large preshower signals due to ADC overflow.
10	Positrons below the pion threshold in the Čerenkov, but above the trigger threshold.
11	Positrons below the pion threshold and the trigger threshold.
12	Positrons above trigger threshold that are misidentified by the Čerenkov or the Preshower

Table 5.5: Overview of the zones in the PID3-P plane.

Zone 1

This zone with very negative values of PID3 contains almost exclusively hadrons with low momentum, with a large contribution of protons. The large negative PID3 value is caused by the calorimeter response. Figure 5.17 shows why the calorimeter signal is zero. The series of plots of the xy-plane for the center of the magnet, the Čerenkov detector and the calorimeter shows that these low momentum hadrons are deflected out of the calorimeter acceptance. The 'gaps' in the upper and lower part of the calorimeter in figure 5.17 are not yet understood.

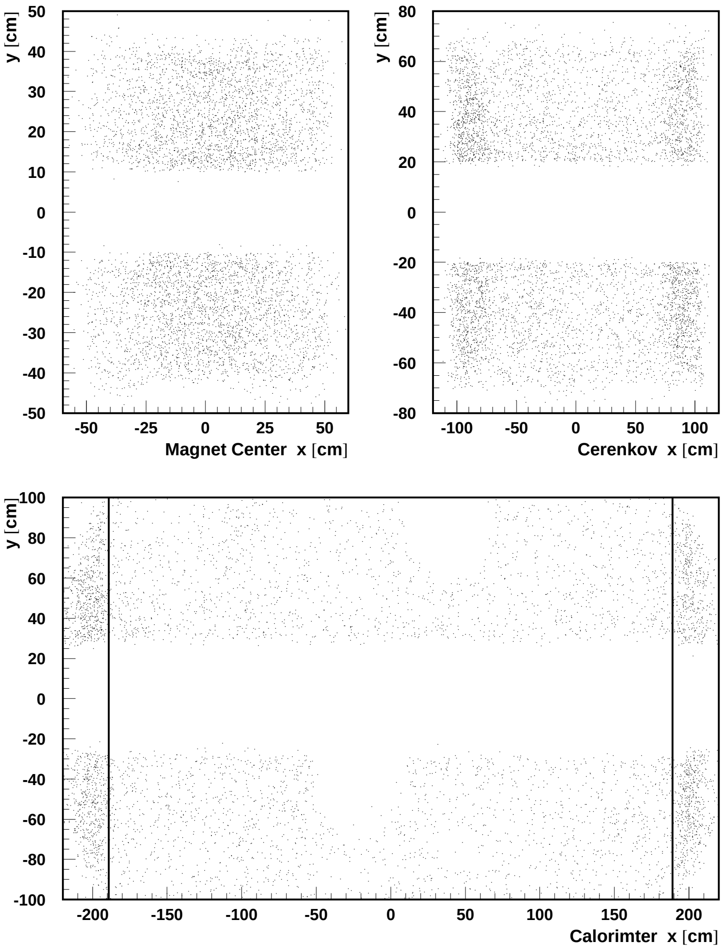

Figure 5.17: XY-Distributions for zone 1 in the PID3-P plane at three different Z: The center of the magnet, the Čerenkov and the calorimeter. The vertical lines indicate the edge of the calorimeter acceptance.

Zone 2

Zone 2 contains hadrons as well, however, these are inside the calorimeter acceptance but they deposit very little energy. While this may happen with a certain probability in any calorimeter block, there appear to be a few blocks that contribute to zone 2 in particular. As in the case of the 'gaps' in zone 1 this may indicate a problem with the pedestal subtraction or the gain of certain calorimeter blocks. Figure 5.18 shows the data from zone 2 in the top part of the calorimeter with one bin per block. Two blocks apparently contribute a large part of this data set.

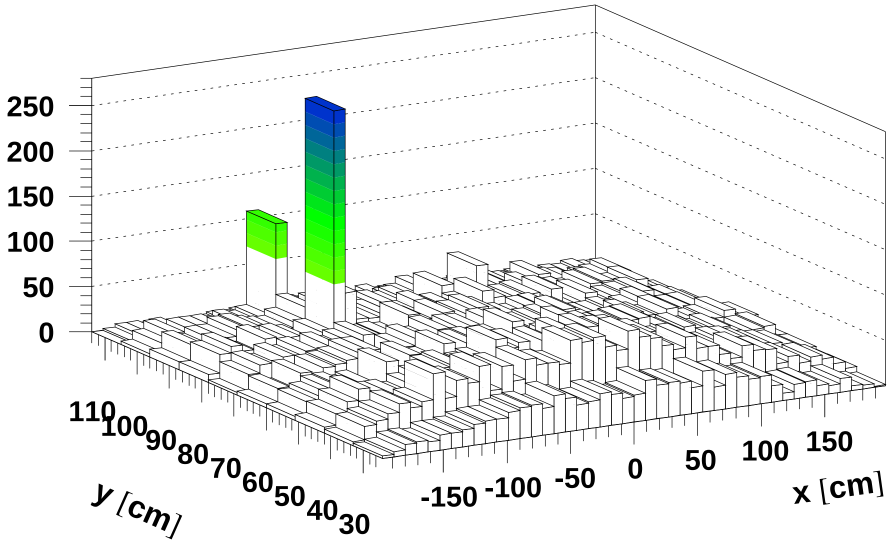

Figure 5.18: XY-distributions for zone 2 PID3-P plane, showing the top part of the calorimeter with one bin per calorimeter block.

Zones 3 and 4

Most of the hadrons are found in zones 3 and 4. The separation between them is an effect of the trigger threshold at 3.5 GeV. While the hadrons in zone 4 are both triggering and non-triggering ones, zone 3 consists of non-triggering hadrons alone. Zone 3 contains low momentum hadrons in coincidence with a DIS positron and most events where a gamma from π^0 decay caused the trigger. This can be deduced from the fact that many of these events remain if a cut on track multiplicity = 1 is made. Without the trigger threshold both zones would merge as well as include zone 5.

Zone 7

Zone 7 is a small positron 'peak' on a rather flat hadronic background. This peak is shown in figure 5.19.

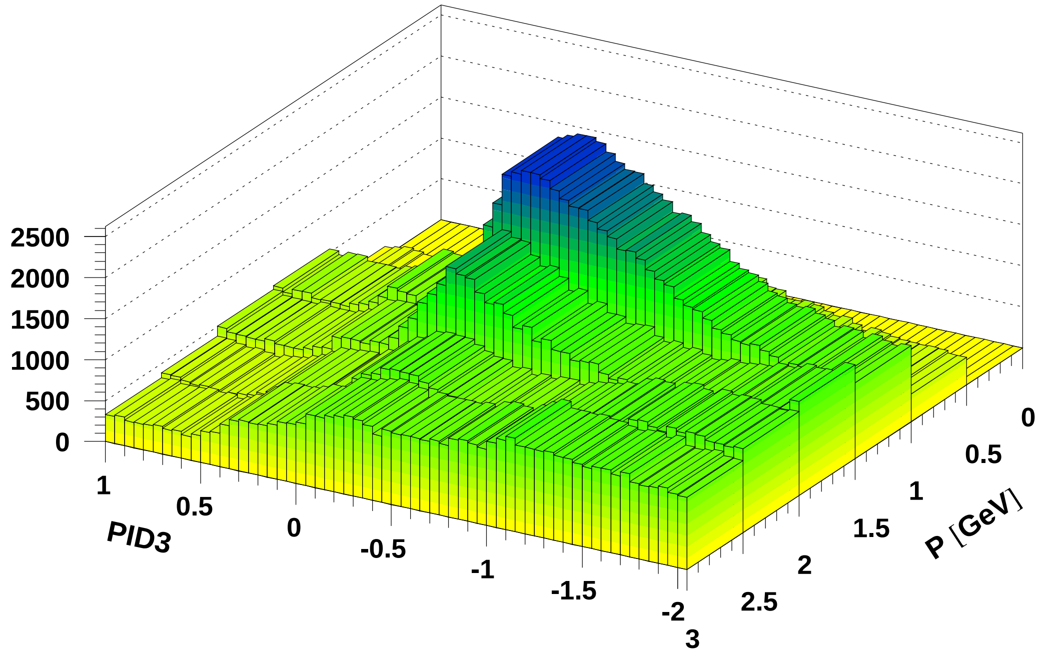

Figure 5.19: Zone 7: Positron peak on hadronic background in the PID3-P plane.

As zone 7 is below PID3=0 the positrons here are misidentified as hadrons by PID3. However, there are no deep inelastic events in this zone, so that it does not have an impact on the (inclusive) physics analysis. An inefficiency in the photon collection of the Čerenkov detector is the cause of this misidentification. It will be shown later (figure 5.22) that this can be traced to the Čerenkov mirrors and Winston cones.

Zone 8

This zone contains the positrons above the Čerenkov pion threshold. Therefore the Čerenkov detector does not contribute to PID3 anymore and the maximum value of PID3 is reduced by about 2. About 40% of the positrons in this zone are deep inelastic and are to be used for the inclusive analysis. Their energy deposition in the calorimeter is above the trigger threshold.

Zone 9

The difference between particles in zone 8 and zone 9 is the unusually high value of E_{pre} for particles in zone 9. This leads to particularly low hadron probabilities according to the preshower parent distributions. If the calorimeter also clearly identifies a particle as a positron a high value of PID3 is assigned. The signals with $E_{pre} > 0.15$ MeV are caused by ADC overflows[70]. The combination of a large energy deposition in the preshower and a higher than average gain of the photomultiplier tube of the preshower paddle can produce such an overflow.

Zones 10 and 11

Zones 10 and zone 11 are related to the Čerenkov detector. Like zones 8 and 9 they contain positrons, but with an energy below the pion threshold where the Čerenkov detector is useful for positron identification. The PID3 value calculated in this case is larger. The onset of Čerenkov radiation for the pions and therefore reduced maximum values of PID3 is seen in the transition from zone 10 to zone 8 (see figure 5.16). The relation of zone 11 to zone 10 is similar to that of zone 3 to zone 4 and is related to the trigger threshold.

5.5.3 The PID3-TRD Plane

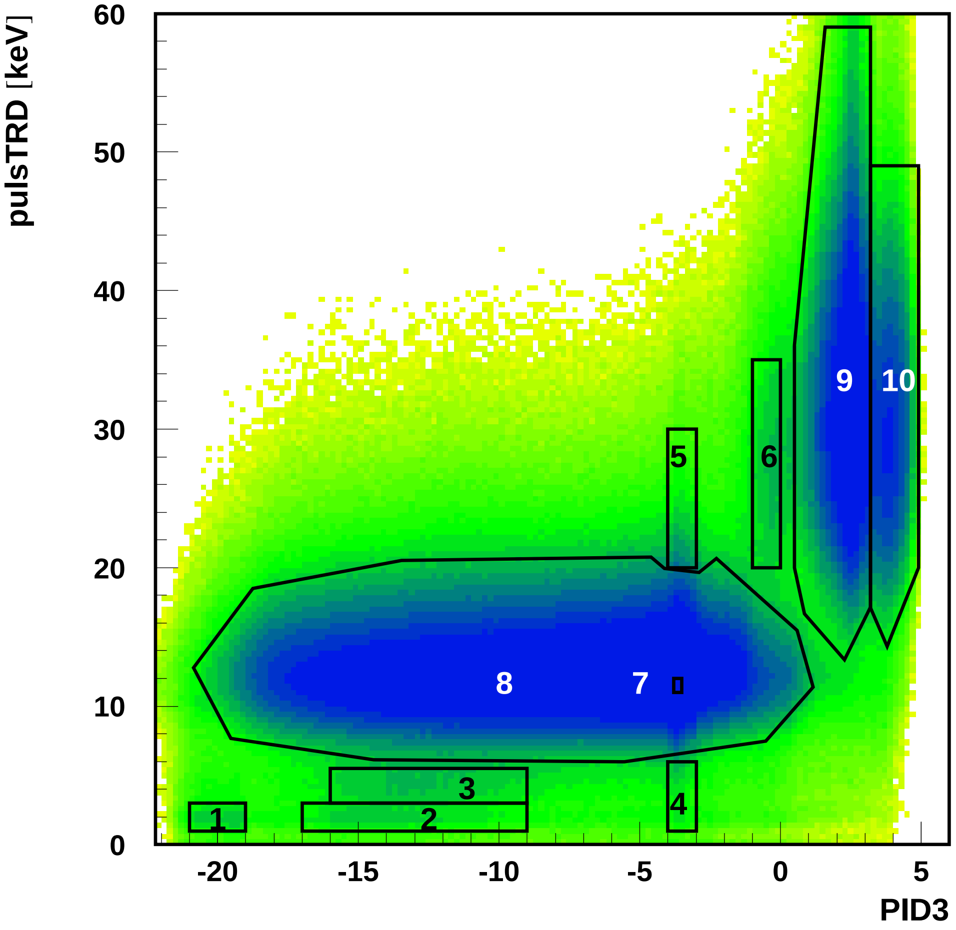

Figure 5.20: The PID3-TRD plane with zones.

This plane is the one used for the PID3-TRD valley cut which is the standard PID cut for the 1995 inclusive data analysis. Therefore it is crucial to understand the features of this plot, particularly the regions close to the valley. While there is no problem identified for the valley cut, a number of interesting details about the particle identification detectors are revealed. The short description of the zones in this plane is again followed by more detailed remarks for selected zones below.

PID3-TRD Plane	
Zone	Description
1	Hadrons that register only in the first two TRD modules and miss the calorimeter.
2	Hadrons that register only in the first two TRD modules.
3	Hadrons that register only in the first three TRD modules.
4	Hadrons with $E_{cal}/p = 1$.
5	Hadrons with $E_{cal}/p = 1$.
6	Low Momentum Positrons with no Čerenkov signal. (Winston cone effect)
7	Peak consisting of hadrons with $E_{cal}/p = 1$ that are clearly identified by preshower, Čerenkov and TRD.
8	Hadrons.
9	Positrons.
10	Positrons with large preshower signal due to ADC overflow.

Table 5.6: Overview of the zones in the PID3-TRD plane.

Zones 1, 2 and 3

The first three zones in this plane have similar origins. Hadrons on the edge of the acceptance of the TRD have to produce a signal in at least the first two TRD modules or the truncated mean value pulsTRD will be zero. The truncated mean response of the TRD for hadrons is about 12 keV, therefore a signal of about 2.4 keV from a hadron that fires the first two and about 4.8 keV from a hadron that fires the first three TRD modules can be expected. These particles can be found in zones 1, 2 and 3 in figure 5.20. Hadrons in zone 1 pass through only the first two TRD modules and then miss the calorimeter. Hadrons in zone 2 also pass through only the first two modules, but leave a signal in the calorimeter, while particles in zone 3 hit the first three TRD modules. It is clear from figure 5.20 that particles which hit the first 4 TRD modules and on average deposit 7.2 keV cannot form a separated substructure.

Zones 4 and 5

Zone 4 and zone 5 in the PID3-TRD plane look unusual. It is particularly important to understand zone 5, because it straddles the valley cut. The origin of these zones turns out to be fairly simple. Figure 5.7 shows that zone 5 results from the tail of a large peak at $PID3 = -3.8$ and pulsTRD $\sim$ 11 keV. Zone 4 is the tail on the low pulsTRD side of the peak.

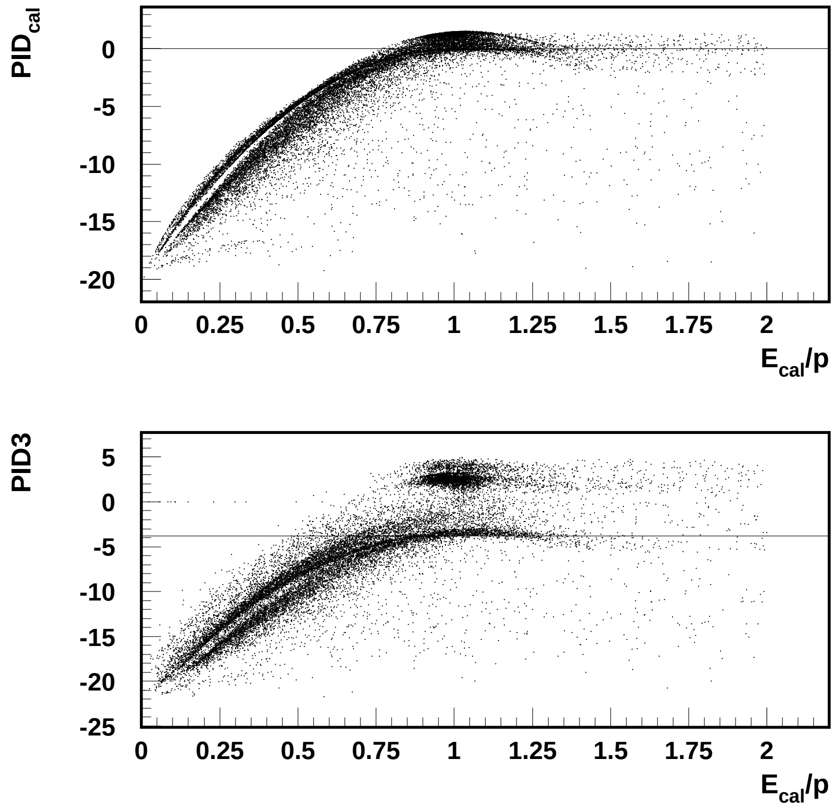

Figure 5.21: Details of the contribution of the calorimeter to PID3. PID_{cal} vs E_{cal}/p (top) and $PID3$ vs E_{cal}/p (bottom). The lines indicate the values $PID_{cal} = 0$ (top) and $PID3 = -3.8$

But what is the origin of the peak at $PID3 = -3.8$? As shown in the top part of figure 5.21, PID_{cal} is small and does not contribute much to PID3 when E_{cal}/p is approximately 1. In fact, PID_{cal} typically has small positive values there and the calorimeter misidentifies these particles as positrons. This is the case for a large fraction of the events in zones 4 and 5. If both the Čerenkov and preshower detectors clearly define a particle as a hadron and $PID_{cal} \approx 0$, it can be seen from figure 5.2 that the resulting PID3 value should be around -4. In fact, it can be seen in the lower part of figure 5.21 that the these events end up around $PID3 = -3.8$.

The shape of the upper plot is a combination of the Gaussian shape of the positron parent distribution around $E_{cal}/p = 1$ and the exponential behaviour of the hadrons for $E_{cal}/p < 1$. On a logarithmic scale this results in a parabola around 1 combined with a linear function at lower values. The double structure observed in the part of this plot with $E_{cal}/p < 1$ is not a trigger effect and can be traced back to the calculation of the calorimeter positron probability.

Zone 6

This zone contains low energy particles with PID3 values between -1 and 0, but which the TRD identifies as positrons. Only few of these events are DIS positrons so the impact on inclusive measurements is small. Nevertheless, a closer look at this zone leads to an interesting result. If the x position of the zone 6 particles is plotted at the z of the Čerenkov mirrors, a regular pattern emerges (see figure 5.22). The vertical lines indicate the position of the mirror edges. It could be assumed that inefficiencies due to gaps between the mirrors are the reason for this effect. But if that were the case, peaks at the position of the edges would be expected, not the asymmetric distributions seen here. Further investigation shows that this effect is due to the Winston cones which are used to collect the Čerenkov light. A Winston cone is a rotational surface of a parabola, followed by a conical section. In the ideal two-dimensional case all incoming photons are collected onto the photocathode after one reflection. In the real three-dimensional case there are some losses due to imperfections and rays with non-normal incidence. This leads to light losses that rise with increasing angle and drop again sharply at the next Winston cone, in principle resulting in a mirror-symmetric saw tooth pattern in x. A convolution of this pattern with the x distribution for positrons and finite resolution effects produce the observed distribution in figure 5.22.

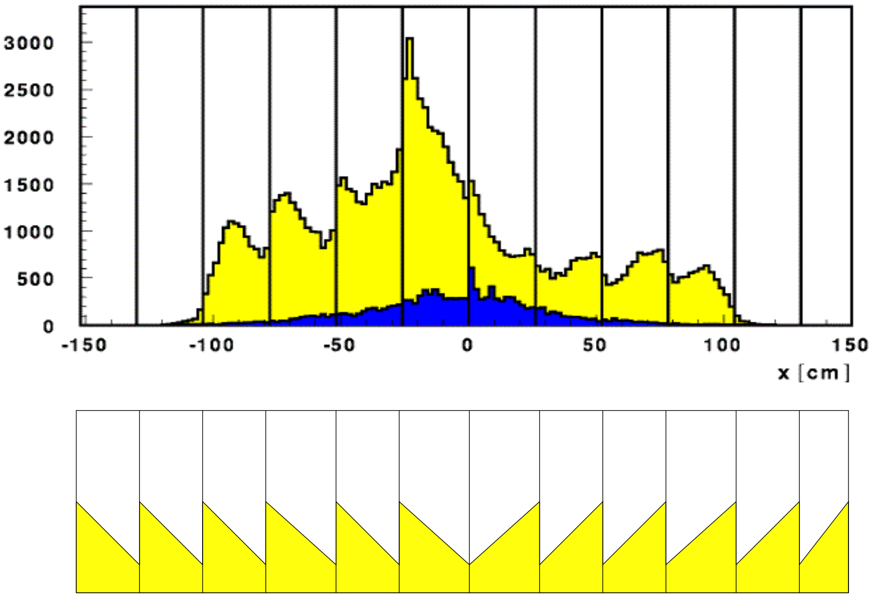

Figure 5.22: Upper part: x distribution of non-DIS (light) and DIS (dark) positrons at the z position of the Čerenkov mirrors. Vertical lines indicate the position of the mirror edges. The lower part schematically shows the distribution that is expected from the effect of the Winston cones.

Zones 8 and 9

Zones 8 and 9 contain most of the particles. Zone 8 consists of hadrons and corresponds to zones 3 and 4 in the PID3-P plane. Zone 9 consists of positrons. It corresponds to zone 8 in the PID3-P plane. Zones 8 and 9 are the only clearly identified particle samples in a 3d-plot of the PID3-TRD plane with linear z scale and relatively large binning (figure 5.7).

5.5.4 The TRD-P Plane

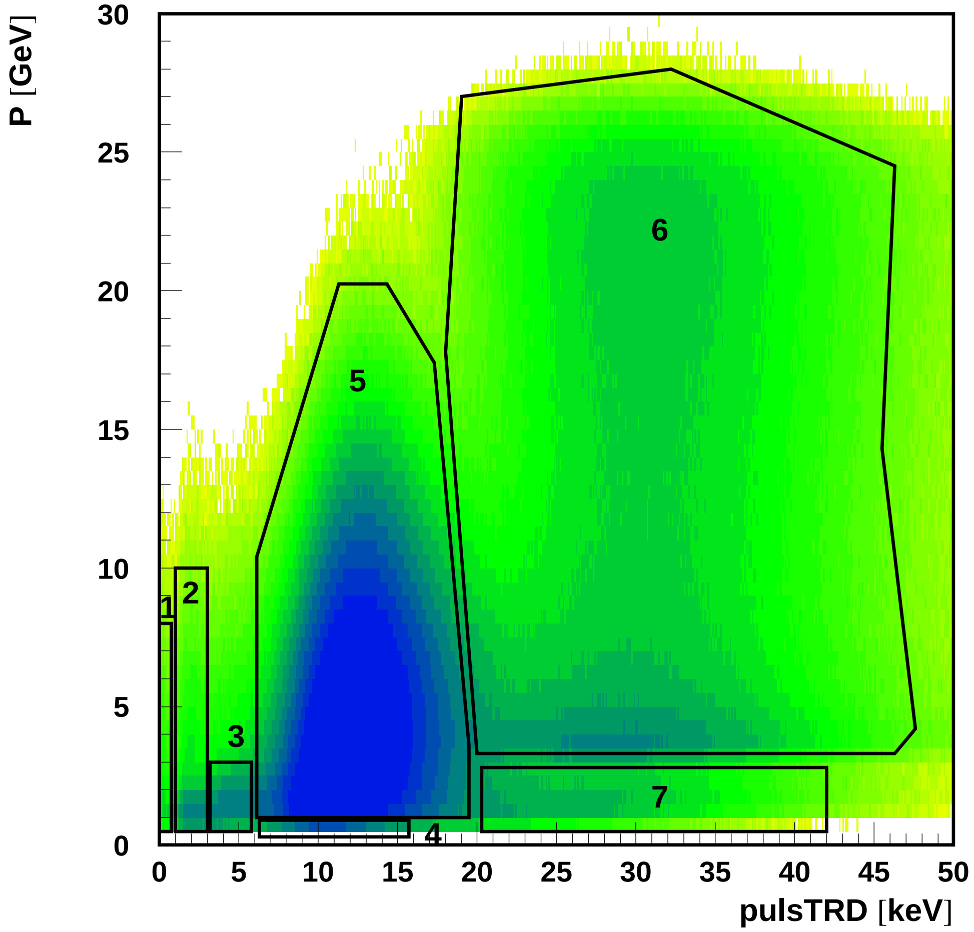

Figure 5.23: The TRD-P Plane with Zones.

This plane is examined for completeness. However, most of the features observed here have been encountered in the two other planes. The two main zones corresponding to hadrons (5) and of positrons (6) are immediately apparent. So is the trigger threshold that causes the separation between zones 6 and 7. This separation appears clearly only for positrons because for them the ration E/p is about 1.

TRD-P Plane	
Zone	Description
1	Hadrons that leave no TRD signal. Typically caused by the MUX setting to 'top or bottom'.
2	Hadrons that register only in the first two TRD modules.
3	Hadrons that register only in the first three TRD modules.
4	Low energy hadrons, including some that miss the last TRD modules.
5	Hadrons.
6	Positrons above the trigger threshold.
7	Positrons below the trigger threshold.

Table 5.7: Overview of the zones in the TRD-P plane.

5.5.5 Correlations between Zones

The zones in each PID plane are related to the zones in the other planes. Many cases of this have been described in the previous sections. The full list of the correlations between the zones is given in tables 5.8-5.10 for completeness. The zones that are described in detail in the text are marked by bold typing.

Zone in TRD-P	Zone in PID3-TRD Plane									
	1	**2**	**3**	**4**	**5**	**6**	7	**8**	**9**	10
1										
2	■	■		■						
3			■	■						
4							■	■		
5							■	■		
6					■	■			■	■
7					■	■			■	■

Table 5.8: Correlations between the zones in the PID3-TRD and the TRD-P plane.

Zone in PID3-P	Zone in PID3-TRD Plane									
	1	**2**	**3**	**4**	**5**	**6**	7	**8**	**9**	10
1	■									
2								■		
3		■	■					■		
4				■	■		■	■		
5				■				■		
6								■		
7						■				
8									■	
9									■	■
10									■	■
11									■	■
12						■				

Table 5.9: Correlations between the zones in the PID3-TRD and the PID3-P plane.

Zone in TRD-P	Zone in PID3-P Plane											
	1	**2**	**3**	**4**	5	6	7	**8**	**9**	**10**	**11**	12
1	■	■	■	■		■	■				■	■
2	■	■	■	■	■	■						
3	■	■	■		■							
4	■				■							
5		■	■	■	■	■	■					
6								■	■	■	■	
7							■					■

Table 5.10: Correlations between the zones in the PID3-P and the TRD-P plane

5.5.6 Improvements in the HERMES PID

There are some improvements to the HERMES PID that will be made in the future. Two of them appear to be particularly important. The parent distributions for the calorimeter and the preshower have to be modelled better and the relative weight of the calorimeter within the overall particle identification has to be reduced. Additionally, the full probability analysis of all detectors should be implemented including flux factors, to achieve optimum values in efficiency and contamination. The probability analysis of the TRD has shown[99] that the HERMES PID can gain here substantially.

5.6 Performance of the HERMES PID

The PID3-TRD valley cut used for the inclusive analysis of the 1995 data yields an average positron efficiency of 99.1 ± 0.3 % and 0.44 ± 0.15 % average hadron contamination.The final values for hadron contamination and positron efficiency for the inclusive 1995 data are shown in figure 5.25. Values for the hadron contamination for each x_{Bj}- and y-bin according to the first order estimate (method 1 section 5.4) are listed in table 5.11.

Hadron Contamination [%]			
x-Bin	y-Bin		
	1	2	3
0.023 - 0.040	0.74±0.38	1.21±0.62	1.36±0.70
0.040 - 0.055	0.34±0.17	0.69±0.35	1.31±0.67
0.055 - 0.075	0.21±0.11	0.35±0.18	1.06±0.54
0.075 - 0.100	0.13±0.07	0.19±0.10	0.76±0.39
0.100 - 0.140	0.13±0.09	0.14±0.07	0.49±0.25
0.140 - 0.200	0.12±0.09	0.11±0.07	0.27±0.14
0.200 - 0.300	0.10±0.10	0.11±0.08	0.18±0.09
0.300 - 0.400	0.10±0.10	0.10±0.10	0.12±0.06
0.400 - 0.600	0.10±0.10	0.10±0.10	0.12±0.06

Table 5.11: Hadron contamination in % from first order estimate (method 2) for every x_{Bj}- and y-bin used for the g_1-analysis.

Both, the first order estimate of the contamination and the Gaussian fit (section 5.4) agree. These results are compiled in table 5.12 for each x_{Bj}-bin. The same values are also shown in figure 5.24. The agreement between both methods is clear. Contaminations smaller than 0.1% cannot be measured in a reliable way by either method.

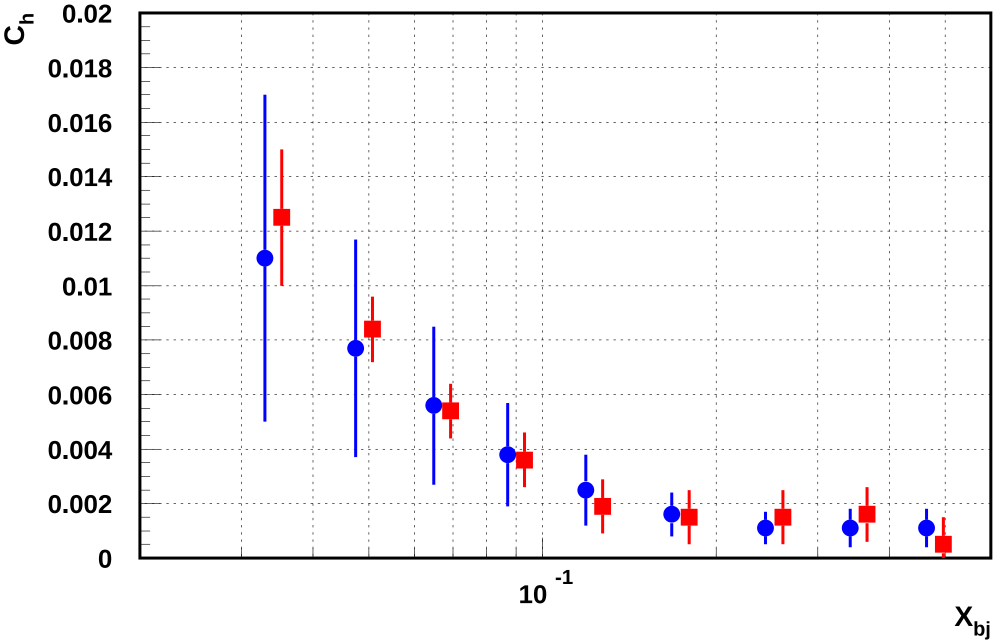

Figure 5.24: Hadron contamination vs x_{Bj} from different methods. Circles: First order estimate, squares: Gaussian fit.

Hadron Contamination [%]			
x_{Bj}-Bin	First Order Estimate	Gaussian Fit	Average
0.023 - 0.040	1.10±0.56	1.25±0.25	1.18±0.43
0.040 - 0.055	0.77±0.39	0.84±0.12	0.81±0.26
0.055 - 0.075	0.56±0.29	0.54±0.10	0.55±0.20
0.075 - 0.100	0.38±0.19	0.36±0.10	0.37±0.15
0.100 - 0.140	0.25±0.13	0.19±0.10	0.22±0.12
0.140 - 0.200	0.16±0.08	0.15±0.10	0.16±0.09
0.200 - 0.300	0.11±0.06	0.15±0.10	0.16±0.06
0.300 - 0.400	0.11±0.07	0.16±0.10	0.16±0.07
0.400 - 0.600	0.11±0.07	0.05±0.10	0.11±0.07

Table 5.12: Hadron contamination in % from first order estimate and from Gaussian fit for every x_{Bj}-bin used for the g_1-analysis.

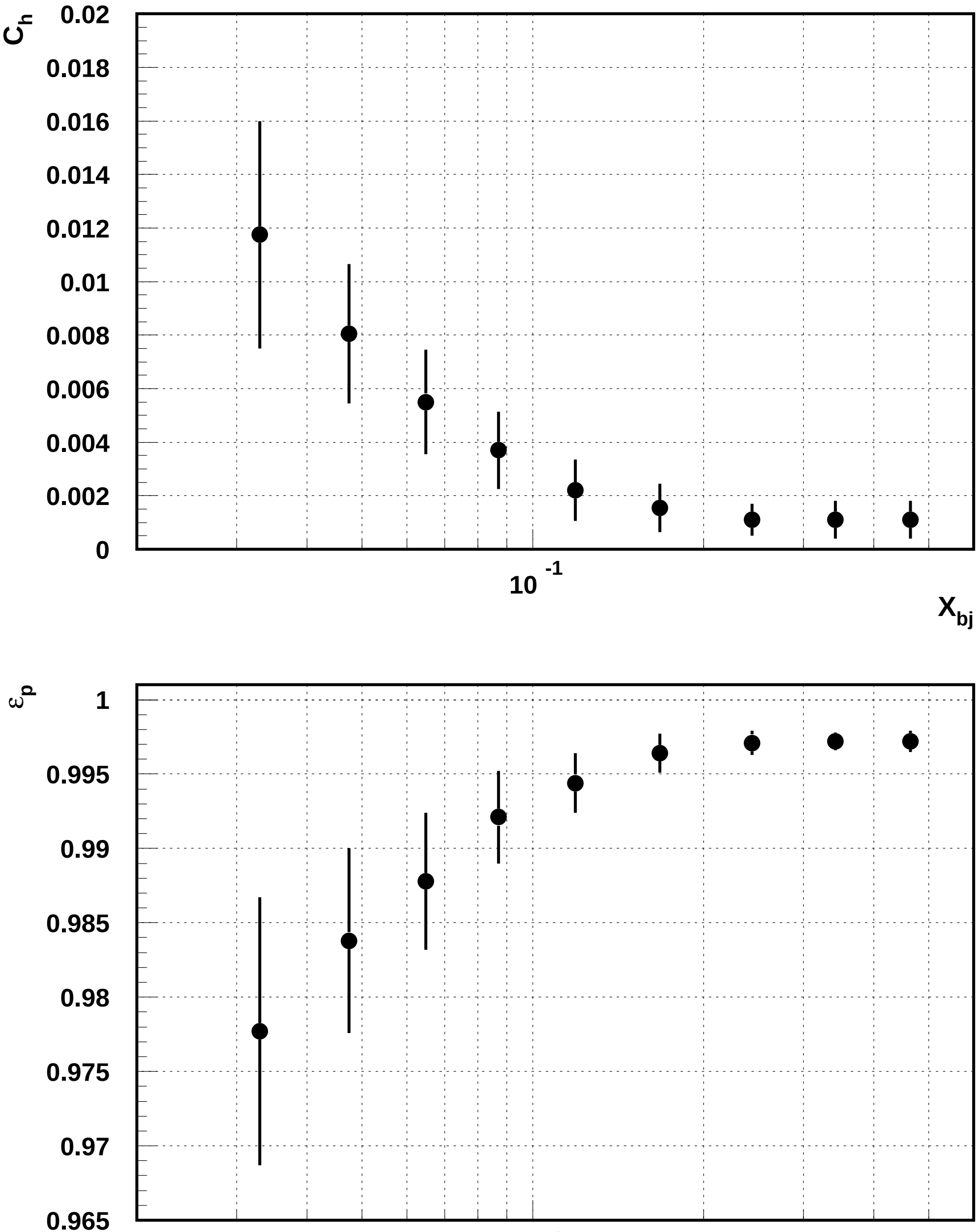

Figure 5.25: Positron efficiency ε_p and hadron contamination c_h vs x_{Bj} for the inclusive 1995 data.

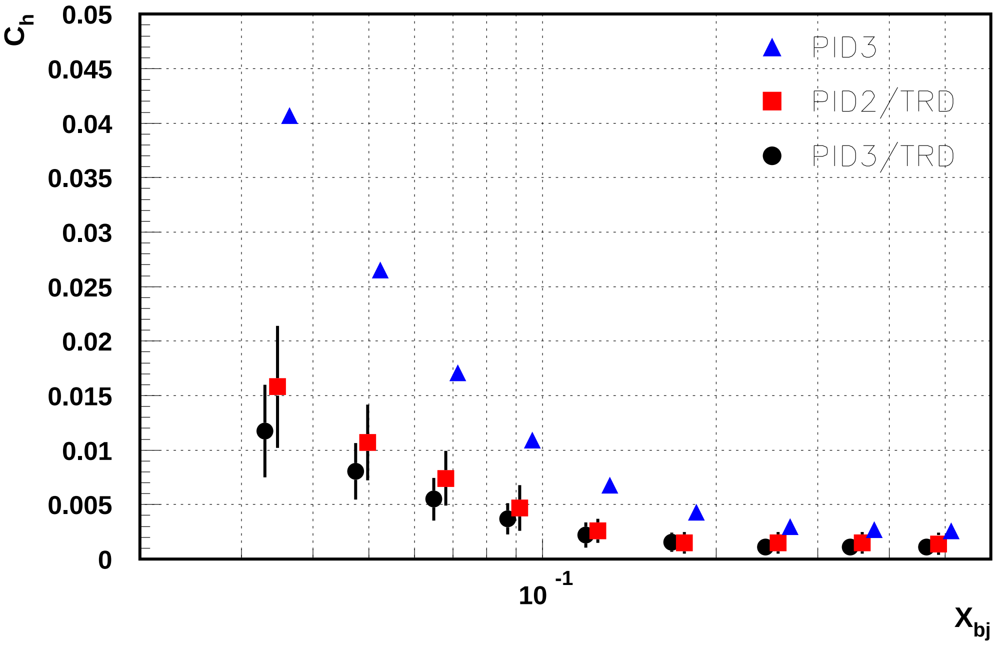

Figure 5.26: Hadron contamination vs x_{Bj} for the PID cuts used in the PID downshifting. The error on the PID3 values is statistical only.

PID Downshifting						
x_{Bj}-Bin	PID3-TRD		PID3		PID2-TRD	
	e^+ eff.	h^+ cont.	e^+ eff.	h^+ cont.	e^+ eff.	h^+ cont.
0.023 - 0.040	97.77	1.18	96.21	4.07	98.55	1.58
0.040 - 0.055	98.38	0.81	97.28	2.65	98.96	1.07
0.055 - 0.075	98.78	0.55	97.93	1.71	99.12	0.74
0.075 - 0.100	99.21	0.37	98.64	1.09	99.47	0.47
0.100 - 0.140	99.44	0.22	99.05	0.68	99.57	0.26
0.140 - 0.200	99.64	0.16	99.33	0.43	99.69	0.15
0.200 - 0.300	99.71	0.16	99.44	0.30	99.74	0.15
0.300 - 0.400	99.72	0.16	99.48	0.27	99.77	0.15
0.400 - 0.600	99.72	0.11	99.48	0.26	99.77	0.14

Table 5.13: Positron efficiency and hadron contamination in % for all three PID methods used in the PID downshifting scheme.

When using the PID downshifting technique (section 5.3.3) the question arises as to how much of the data is analysed in each PID scheme. This information is given in table 5.4. For the 1995 inclusive analysis the PID3-TRD valley cut has been used for about 97.5% of the events. Quoting the valley cut efficiencies and contaminations for the inclusive analysis is thus justified. The positron efficiency and hadron contamination for all three PID methods used in the PID downshifting scheme was given in table 5.13. The contaminations are also plotted in figure 5.26.

The advantage of the two valley cuts is apparent. While the overall contamination value (for all x_{Bj}) with the PID3=0 cut is still good (about 1.3%), the additional use of the TRD improves this value by a factor of almost 4 for the lowest x_{Bj}-bin.

Chapter 6

The Measurement of g_1^n

6.1 Data Analysis Software

The HERMES data analysis software chain begins with the raw data and produces sorted and organized sets of data in ADAMO format for the physics analysis. ADAMO[75] is a relational database used throughout the HERMES experiment. The raw data fall into two categories: the detector output in EPIO[108] format which is written onto tape by the data acquisition system (DAQ) and the slow control data from the various detectors. The HERMES data are organized in several levels that are characterised by different time scales:

- **fill**, defined by one fill of the HERA positron ring, typically about 8 hours;
- **run**, about 10 minutes of data, chosen to fit 2 runs onto each computer tape in the central computing tape silo;
- **burst**, 10 seconds long, defined by the scaler readout; the smallest timescale on which slow control data are available.

The detector data are organized in runs, while the slow control data are collected in fillfiles.

The Hermes decoder Hdc processes the raw data from the electronics (for example ADC values) into physical quantities and performs a first calibration of the data. The output of Hdc is in the form of Adamo structures. This output is piped into the Hermes reconstruction program Hrc[64], which finds and reconstructs the tracks, provides particle identification and performs further calibrations. Both, the decoder and the reconstruction program access the necessary calibration and geometry information from Dad[78] servers. The slow control data (for example high voltage values) are also fed to several Dad servers, from which they are collected by the taping client. These data are combined with the non-spectrometer data from the target and the beam polarimeter by a merger program and stored in fillwise slow control files. These files are in Adamo format as well. The slow control data in the servers are used for online monitoring purposes as well (see section 3.4.2).

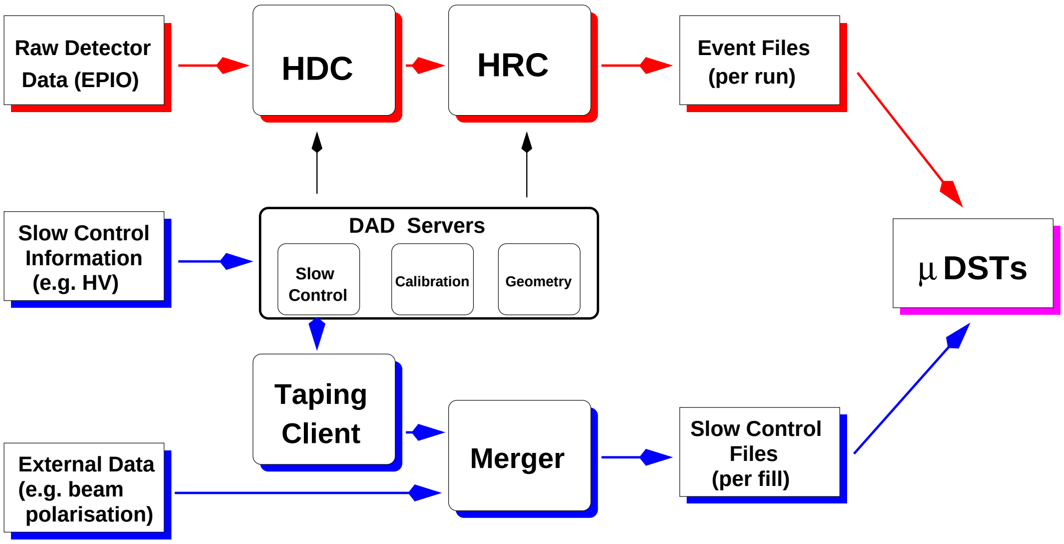

Figure 6.1: Schematics of the Hermes analysis chain.

For the physics analysis both data streams are synchronised, preselected and processed into the so-called 'micro-DSTs' (historical acronym for 'data summary tape') that contain all necessary information from one run for the physics analysis. At the moment there are two sets of DSTs, g1DSTs for the inclusive analysis and smDSTs for the semi-inclusive analysis. While the amount of raw data from the 1995 running period is about 2 TeraBytes, the size of the g1DST files for the 1995 inclusive analysis is only about 4 GByte. The sets of DSTs from different data production runs are labelled according to the version of the event file production (A-E) and the DST production (1-5). The data used in the present analysis are generally from the last 1995 data production (E5). Some systematic studies were done with the previous version E4 and did not need to be repeated with E5, because the differences between the versions were small for most physics quantities.

A simple schematic of the HERMES analysis chain is shown in figure 6.1. There are several other programs and important programming packages, such as the ACE program (Alignment, Calibration, Efficiency) which calculates the tracking chamber efficiencies. They have been left out in this overview because they do not affect the basic structure of the analysis chain.

The g1DSTs were analysed with a FORTRAN program that uses the standard burst quality (which is discussed below) and performs all calculations to produce a single PAW ntuple file[113] from the 1995 data. This ntuple file contains fill wise values for all necessary quantities for the g_1 analysis. The small size of the ntuple file (several MByte) allows the storage of multiple versions of the fill-wise data for systematic studies. The FORTRAN program uses the HAT[110] scheme based on a PERL script that produces FORTRAN HBOOK[109] code from simple definition files. The output ntuple was finally analysed with PAW[113] and FORTRAN subroutines.

6.2 Data Quality Selection

The year 1995 was the first year of data taking for the HERMES experiment and experience with both the detector and the data analysis had to be acquired. The necessary software tools for the detector monitoring and for the data analysis were largely developed while data were already being taken. For some time periods, parts of the experiment were unstable, and hence not all recorded data can be used for the analysis. Also the slowcontrol data were only partly stored for the first part of the year. For these reasons a large part of the collected raw data are not suitable for a precision analysis as is necessary for the measurement of g_1^n and a major part of the analysis effort was the determination of the data quality. Data quality was assigned on three levels: run, burst and track. Basically the runlevel quality weeds out unusable data, the burst level quality takes care of wire chamber trips etc., and the track level cuts (mostly PID and kinematics) determine the DIS positrons that are to be used for the physics analysis. While the track level cuts are necessarily determined specifically for the inclusive analysis, run and burst level cuts also apply to the semi-inclusive analysis of the 1995 data.

6.2.1 Run Selection

The full data set consists of 4011 runs that were taken in 1995. The run selection reduces this to 2183 runs which are collected in the runlist that is used for the g1DST production. The first source of information is the HERMES logbook together with the run summaries compiled by the shift crews. The logbook identified about 3/4 of the runs as potentially usable for the analysis. The rest was discarded because of bad running conditions or unpolarised gas in the target and because some data were taken for detector studies or alignment purposes. The beam and target polarisation values are obviously needed for the g_1^n-measurement. Hence, runs where the beam polarimeter and target groups do not believe that this information is reliable have also been removed. Finally 3 runs could not be synchronised successfully with the slow control information, so that 2180 runs are used for the g1DST production (see table 6.1).

A second criterion for the run selection involves the particle identification detectors. In principle, the calorimeter and the preshower detector are always on when data are taken, as they are both part of the trigger. However, the entire detector may not always be available.

Information from the gain monitoring system (GMS) is available on the run level for the calorimeter and the preshower detector. This is not possible on the burst level

Criterion	runs cut	remaining runs
all runs 1995		4011
logbook	965	3046
beam polarisation	720	2326
target	143	2183
no slow control info	3	2180
runs on μDSTs		2180

Table 6.1: Run Quality Selection

since not enough statistics can be collected in this time to assign a GMS quality to a photomultiplier tube. GMS information is not used to discard runs, but rather is included in the DST files to keep the analysis more flexible.

The same is true for the TRD and the Čerenkov detector. The data quality can be assigned only on a run-by-run basis, because statistics prohibit a smaller timescale. The 'quality-bits' for both detectors and for the top and the bottom detectors separately are also included in the DSTs. Since a run is discarded if neither the TRD nor the Čerenkov were working properly, the number of good runs is reduced to 2132. For a large part of the running period insufficient slow control information was stored and it was necessary to define the run quality for the TRD and the Čerenkov on the basis of the detector data alone. This is likely to remain an idiosyncracy of the 1995 analysis, because towards the end of the running period the slow control and online monitoring system became fully operational and has performed well throughout 1996.

Čerenkov Quality

Two criteria were used for the quality of the Čerenkov data: the detector efficiency and the mean number of photoelectrons for high momentum positrons. The detector efficiency $\varepsilon_{\mathrm{cer}}$ was calculated as the percentage of positrons that were recognized by the Čerenkov. The data sample was defined by the calorimeter and the preshower alone to be independent of the TRD quality. The average number of photoelectrons $\langle N_{pe} \rangle$ for positrons above 6 GeV should be about 3. Therefore the following conditions were imposed (separately for top and bottom detector):

$$\begin{aligned} 2.5 < & \ \langle N_{pe} \rangle & < 3.5 \\ 0.925 < & \ \varepsilon_{\rm cer} & < 0.999 \end{aligned} \tag{6.1}$$

Both cuts are relatively loose and only remove runs with clearly bad detector quality. The cuts are illustrated in figures 6.2 A-D.

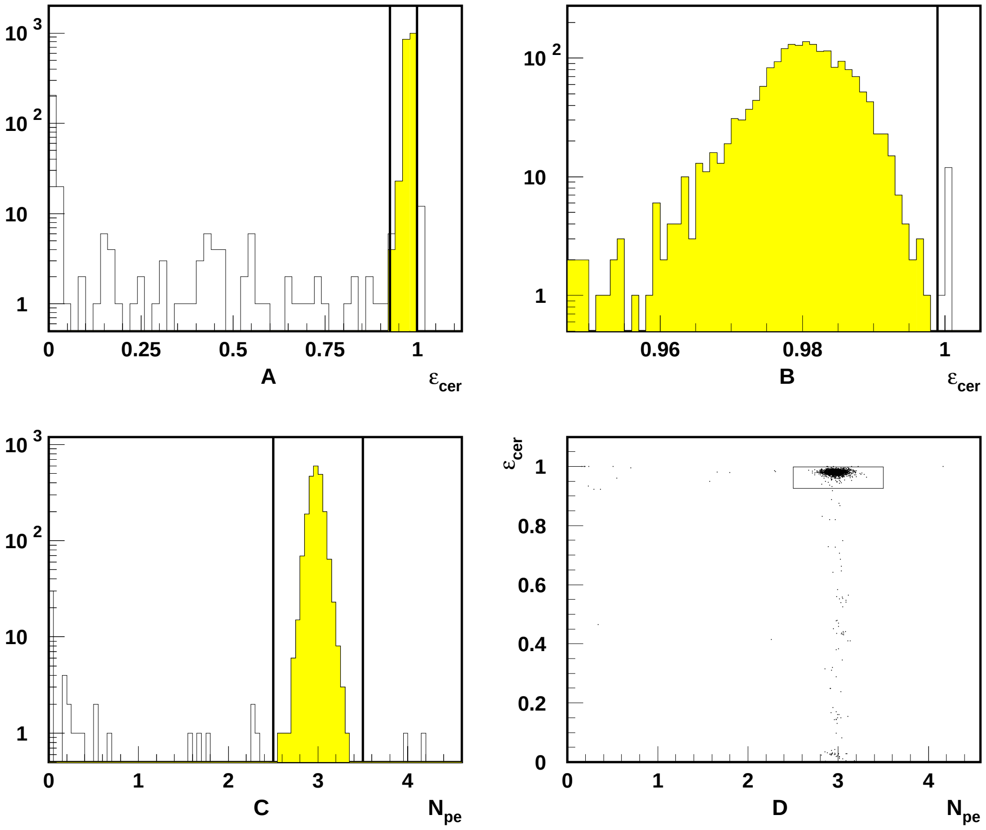

Figure 6.2: Čerenkov Quality Cuts: (A) low efficiencies, (B) unphysical efficiencies, (C) average number of photoelectrons, (D) the same cuts in the $\varepsilon_{cer} - \langle N_{pe} \rangle$ plane. All plots for the top detector.

TRD Quality

The TRD quality was originally defined using the truncated mean (pulsTRD) data from analysis version C. For each run the positron and pion data at 5 GeV (as defined by the calorimeter and the preshower) were analysed for the top and the bottom detectors separately. The distributions were fitted with Gaussians to determine their mean m and standard deviation σ. The number of tracks in top and bottom TRD and the percentages of tracks without a TRD signal (tnull and bnull) were determined, and mean M and rms of the histograms themselves were recorded as well. The series of cuts that were imposed on the TRD was chosen to detect trips, check the linearity of the detector and determine whether the data were calibrated properly. The criteria are listed in table 6.2.

<table>
<tr><th>Criterion</th><th>Top TRD</th><th>Bottom TRD</th></tr>
<tr><td>operating</td><td colspan="2">$N(\text{tracks}) > 2000$</td></tr>
<tr><td>calibrated</td><td colspan="2">$10 \text{ keV} < m(\pi) < 13.4 \text{ keV}$
$1.75 \text{ keV} < \sigma(\pi) < 3.2 \text{ keV}$</td></tr>
<tr><td>linear</td><td>$2.4 < m(\text{e})/m(\pi) < 2.75$</td><td>$2.3 < m(\text{e})/m(\pi) < 2.7$</td></tr>
<tr><td rowspan="2">trip detection</td><td colspan="2">$m(\pi)/M(\pi) < 1.01$</td></tr>
<tr><td>$0.2 < \text{tnull} < 0.34$
or $\text{tnull} < 0.1$</td><td>$0.2 < \text{bnull} < 0.28$
or $\text{bnull} < 0.1$</td></tr>
</table>

Table 6.2: TRD Run Quality Criteria

As soon as the single module TRD responses were available (data version D) they were used for the calibration and also for the determination of run quality. Runs whose calibration results looked suspicious (25 runs) were individually analysed and a single run (3382) was additionally assigned bad TRD quality, because a TRD chamber clearly had tripped. Like the Čerenkov quality the TRD quality is defined separately for the top and bottom detectors.

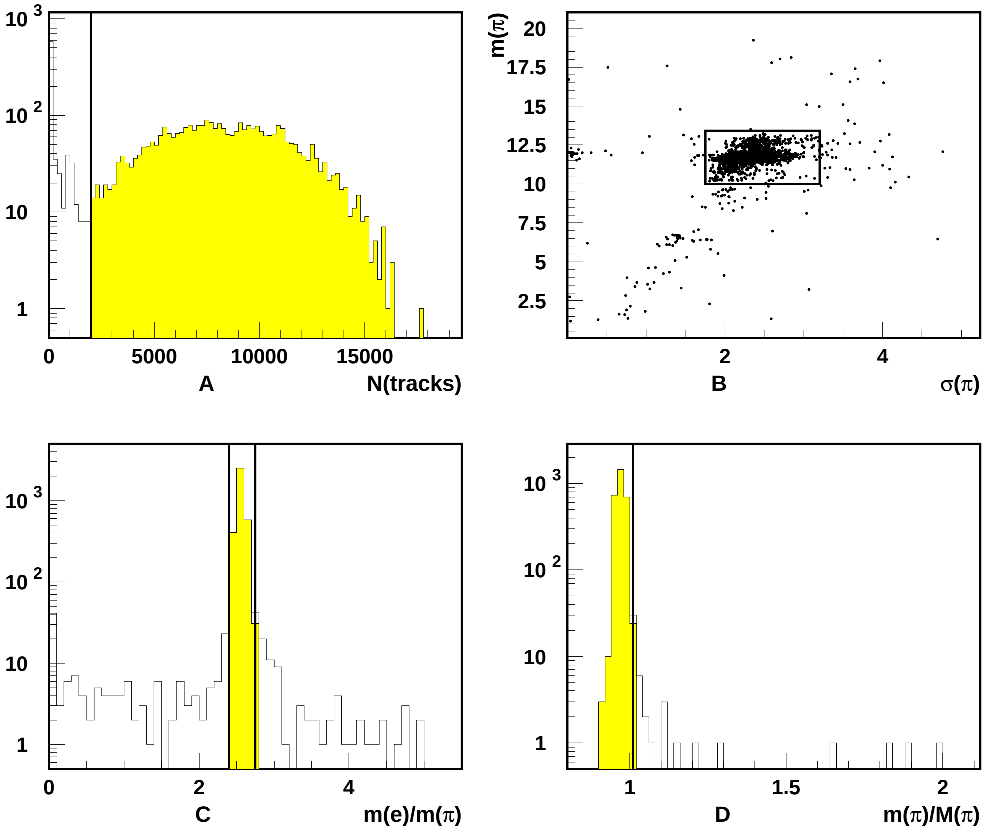

Figure 6.3: TRD Quality Cuts: (A) operating, sufficient number of tracks, (B) calibrated, (C) linear, (D) trip detection.

Figure 6.3 illustrates the TRD run quality cuts:

A. The number of tracks per run is used to determine if the TRD was operating over the entire run.

B. Mean and sigma of the Gaussian fit to the pion peak detect if the TRD is properly calibrated.

C. The ratio of the positron and pion peak positions indicates the linearity of the TRD.

D. The ratio of the fitted mean of the pion distribution to the simple mean of the pion histogram can be used to detect trips. Usually the fitted mean will be lower than the simple mean, due to the Landau-tail of the pion distribution. If a trip occurs during the run their ratio will become larger than 1.

The plots were made for the top half of the TRD, but they are not significantly different for the bottom half. The last cut from table 6.2 is illustrated in figure 6.4 for the top TRD. Plotted is the percentage tnull of tracks in the zero-bin versus the run number after the other TRD run quality cuts already were applied. Periods with a different multiplexer setting can be clearly distinguished, because tnull is either about 0.25 or around 0.03. Runs with values that have tnull values that are significantly larger than these values probably contain a high voltage trip and are therefore cut. The detailed effect of these run quality criteria on the number of runs is listed in table 6.3 below.

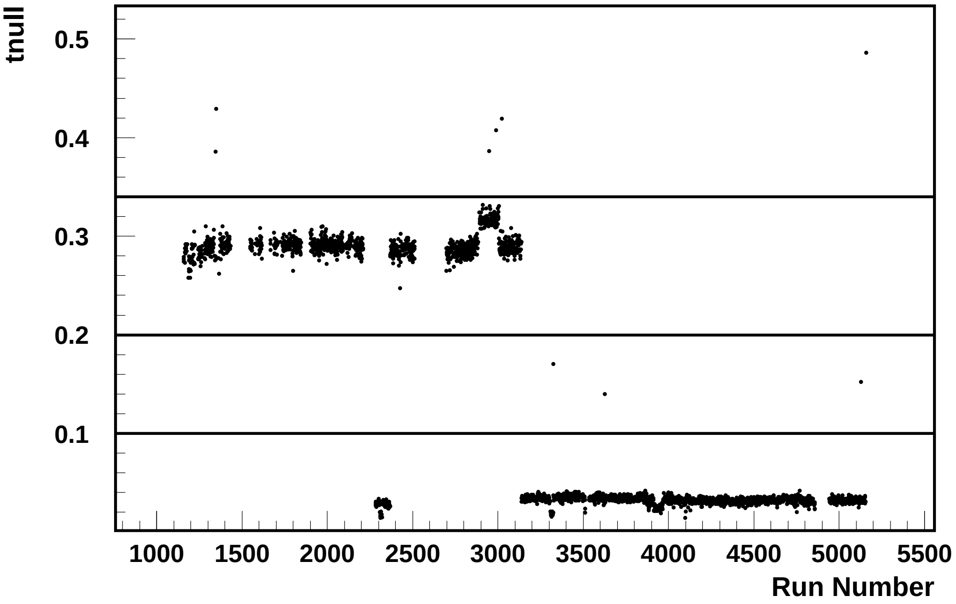

Figure 6.4: TRD zero bin percentage vs run number.

As a result of these cuts, the largest useful runlist for the analysis contains 2132 runs. In this case the PID downshifting scheme (section 5.3.3) is used for particle identification. The optimal PID (PID3-TRD valley cut) is available for the entire

Criterion	runs cut	remaining runs
runs on μDSTs		2180
both detectors bad (t&b)	48	2132
bad Čerenkov (t)	264	1868
bad Čerenkov (b)	289	1843
bad TRD (t)	113	1755
bad TRD (b)	56	1787
both detectors good (t&b)		1725

Table 6.3: Run Quality Selection for Čerenkov and TRD

detector for 1725 runs. The first list is used to extract $g_1^n(x)$ with the largest possible statistics, which for the 1995 data is 2.8 million DIS positrons. The shorter list with optimal PID for top and bottom represents the largest data sample that can be used for systematic studies that involve the particle identification.

6.2.2 Burst Selection

The burst level quality cuts are applied separately for the top and the bottom detectors at the time of the DST production and are stored in the form of bit patterns in a so called 'badbits file'. In this analysis these badbits have been used as the burstlevel quality, no particular subselection has taken place. Burst level cuts have been applied to all important parameters, starting with the target and beam polarisation. The target polarisation was limited to the range [30%-60%] and the beam polarisation to [40%-70%]. The lower boundaries were set to exclude data from the rise of the beam polarisation and after the flip of the target polarisation. Either of these would contribute little to the asymmetry. The upper boundaries mark the maximum measured values. Beam and target polarisation as well as the related instrumentation are described in chapter 3. The burst level cuts on beam and target polarisation are illustrated in figure 6.6 below.

The DAQ had periods where the deadtime was very large and where the burst length was longer (or shorter) than 10 seconds. For this reason cuts were applied to both the live time and the burst length.

Due to the relatively long time between target polarisation reversals (10 minutes) the luminosity rate is of great importance for the asymmetry measurement. The luminosity rate is cross checked with the product of beam current and target density and cuts on these parameters ensure that the luminosity values are reasonable.

The program ACE (Alignment, Calibration, Efficiencies) calculates among other things the tracking efficiencies for all front and back chamber planes. Unfortunately for most of the 1995 data this provides the only way to identify high voltage trips of the tracking chambers since the high voltage values were not in the slow control data stream yet. The cuts are again applied separately for the top and bottom halves of the detector. To ensure that in the case of a trip the entire time period that is affected is rejected, the burst preceding a burst that fails the ACE cuts is rejected as well. The cut on the efficiency ε_{front} of the front chambers is illustrated in the third row of figure 6.6 for top and bottom. A trip of the front chambers that was detected by the cut on their efficiency is shown in figure 6.5 below.

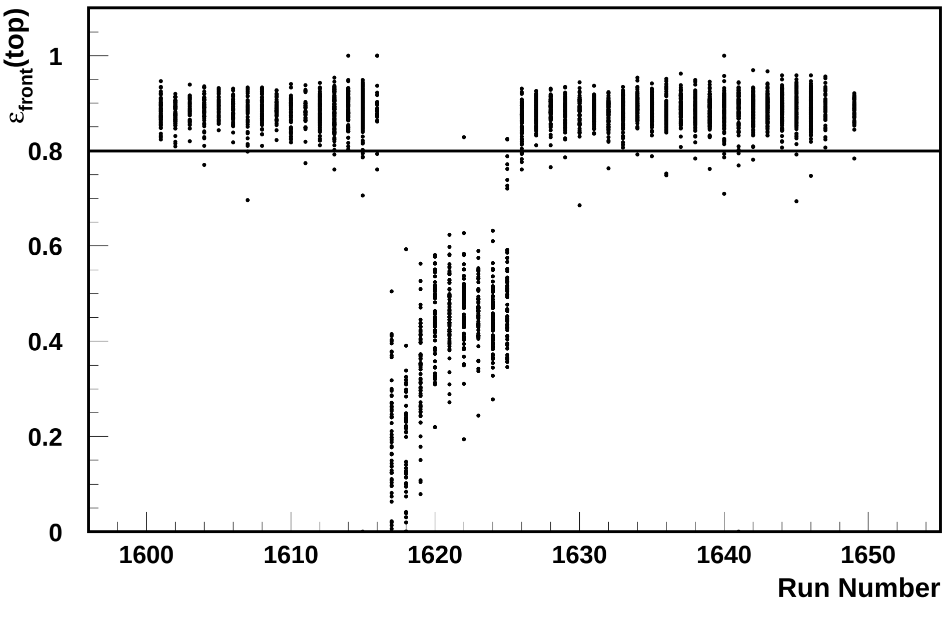

Figure 6.5: The cut on the front chamber efficiency $\varepsilon_{front} > 0.8$ detects a high voltage trip in runs 1617-1625

The gain monitoring system provides the numbers of sub-standard photomultiplier channels in the preshower and the calorimeter on a run-by-run basis. To better specify when a run has to be rejected due to problems detected by the GMS, both detectors are divided into an inner and an outer region. The inner region requires the stricter cuts, as most of the DIS positrons are detected there.

After the burst quality has been assigned, the runs and fills are examined again, to determine whether enough good data are left to declare them as usable. A run with a particularly large number of high voltage trips or very few good bursts should probably not be used in the analysis. The same is valid on the fill level, where at least enough data in both spin states have to be left to be able to calculate an asymmetry. This leads to two requirements on the run level on the maximum fraction of allowed gaps and the minimum required fraction of good bursts. A gap is defined as the change of burstquality from good to bad. The requirements are that on average not more than one gap may occur every ten bursts, and that more than 40% of all bursts in a run have to pass all other burst cuts. On the fill level it is required that at least 100 bursts with good quality are left in each target state, so that an asymmetry value can be calculated.

The burst level cuts remove about 40 % of the data that pass the run level cuts. The most significant cuts are the ones on the beam polarisation (9.7 %), tracking efficiency (11.6 %) and the gap/bad burst cut (25.2 %). However, these cuts largely overlap, and therefore only 4.6 % of the data are removed by the gap/bad burst cut after the application of the other cuts. 60 fills for the top detector and 63 fills for the bottom detector remain in the 1995 data sample after the application of the fill level 'good bursts' criteria.

The numerical values for all burst level cuts are listed in table 6.4 and some of them are illustrated in figure 6.6.

Parameter	**Burst Quality Criterion**
Target	
well defined state	Target Bit = {3,5}
target polarisation p_t	$30\% < p_t < 60\%$
target density n [nucleons/cm^2]	$0.85 \cdot 10^{15} < n < 1.4 \cdot 10^{15}$
Beam	
beam polarisation p_b	$40\% < p_b < 70\%$
beam current I	8 mA $< I <$ 32 mA
DAQ	
cleanup	reject first 3 and last burst
live time T_{live}	$50\% < T_{live} < 100\%$
burst length T_{burst}	$9\ s \leq T_{burst} \leq 11\ s$
Lumi	
luminosity rate $\dot{N}_{lumi}$	40 Hz $< \dot{N}_{lumi} <$ 210 Hz
$\dot{N}_{lumi}/(I \cdot n)$	$5 \cdot 10^{-15} < \frac{\dot{N}_{lumi}}{I \cdot n} < 7.2 \cdot 10^{-15}$
ACE	
Front tracking efficiency ε_{front}	$\varepsilon_{front} > 80\%$
Back tracking efficiency ε_{back}	$\varepsilon_{back} > 94\%$
	also reject previous burst
GMS	maximal allowed bad channels
top inner calorimeter	3
bottom inner calorimeter	4
outer calorimeter	8
inner preshower	1
outer preshower	5
Scaler Counts	maximal allowed bad channels
top H1	1
bottom H1	0
top preshower	0
bottom preshower	0
'Swiss Cheese'	
maximum fraction of gaps per run	$n_{gaps}/n_{bursts} < 0.1$
minimum fraction of good bursts per run	$n_{goodbursts}/n_{bursts} > 0.4$
minimum number of good bursts per fill	$n^{\pm}_{goodbursts} \geq 100$

Table 6.4: Burst Level Cuts

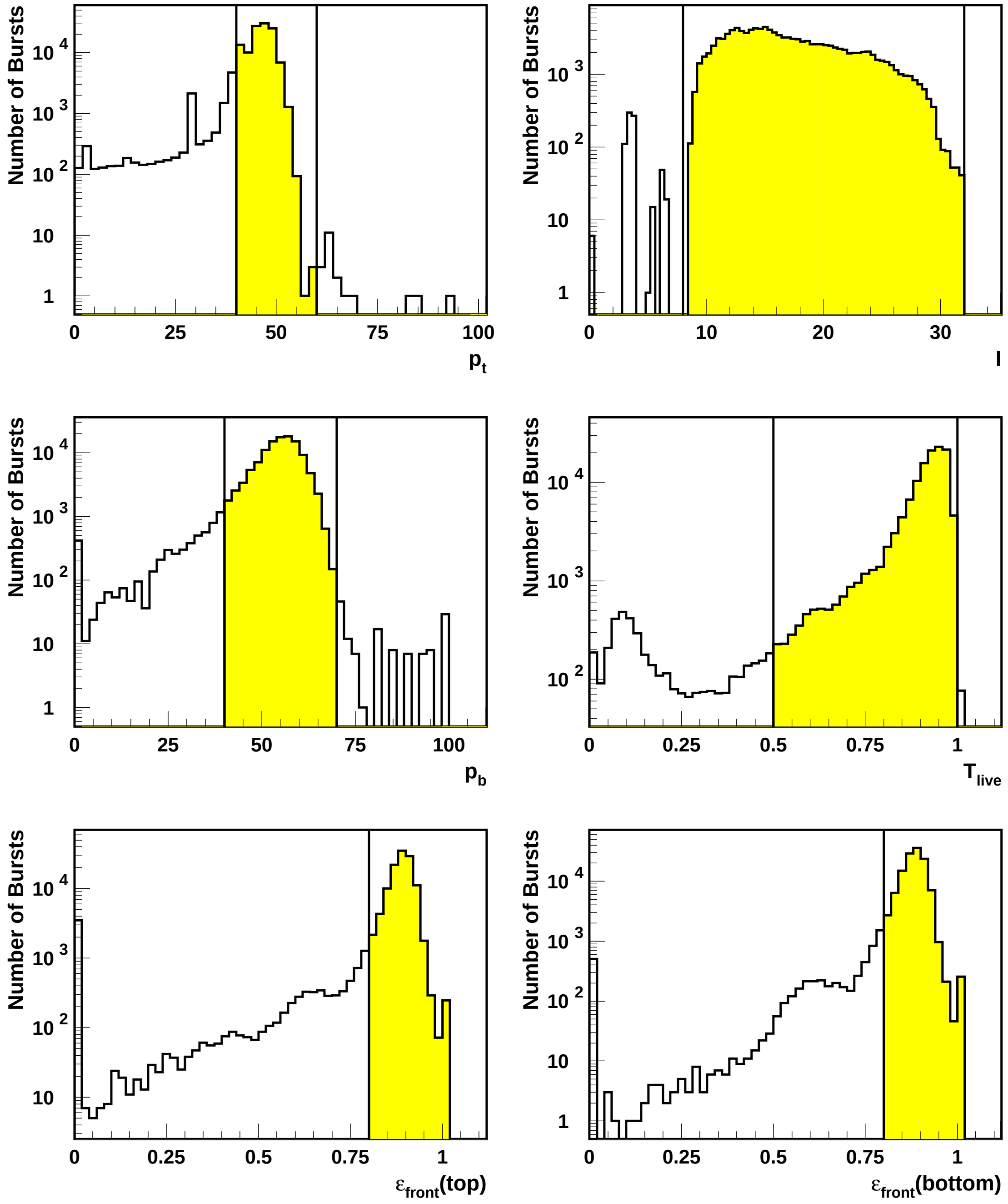

Figure 6.6: Illustration of the burst level cuts on beam polarisation p_b, beam current I, target polarisation p_t, DAQ live time T_{live}, front chamber efficiency ε_{front} for top and bottom detector.

6.2.3 Track Selection

The track selection defines which track from a given event is kept in the data sample used for the inclusive analysis. While the run and burst level cuts described above also apply to any other physics analysis based on the 1995 data, the track selection is necessarily specific to a particular analysis such as the inclusive analysis in this case. There are three sets of track selection cuts: Geometry cuts, kinematic cuts, and particle identification cuts.

Parameter	**Track Selection Criterion**
Geometry	
interaction point inside target	$-30 < z_{vertex} < 30$ cm
transverse vertex offset r_{vertex}	$r_{vertex} < 0.75$ cm
horizontal fiducial cut	$\|x\| < 175$ cm at calorimeter
vertical fiducial cut	$\|y\| > 30$ cm at calorimeter
septum plate	$\|\theta_y\| > 40$ mrad
Kinematics	
scaling region	$Q^2 > 1$ GeV
non-resonance region	$W^2 > 4$ GeV
small radiative corrections	$y < 0.85$
Particle Identification	
positive charge	charge $= +1$
PID3-TRD valley cut	$PID3 + 0.31 * pulsTRD > 5.48$
downshifting: no TRD	$PID3 > 0$
downshifting: no Čerenkov	$PID2 + 0.51 * pulsTRD > 9.0$

Table 6.5: Track Level Cuts

The geometry cuts ensure that the selected track originates from the target and was reconstructed successfully all the way through the detector up to the calorimeter (see the target density profile in figure 3.6). The kinematic cuts select the deep inelastic particles by rejecting events with small momentum transfer and events from resonance production and by removing events with large radiative corrections.

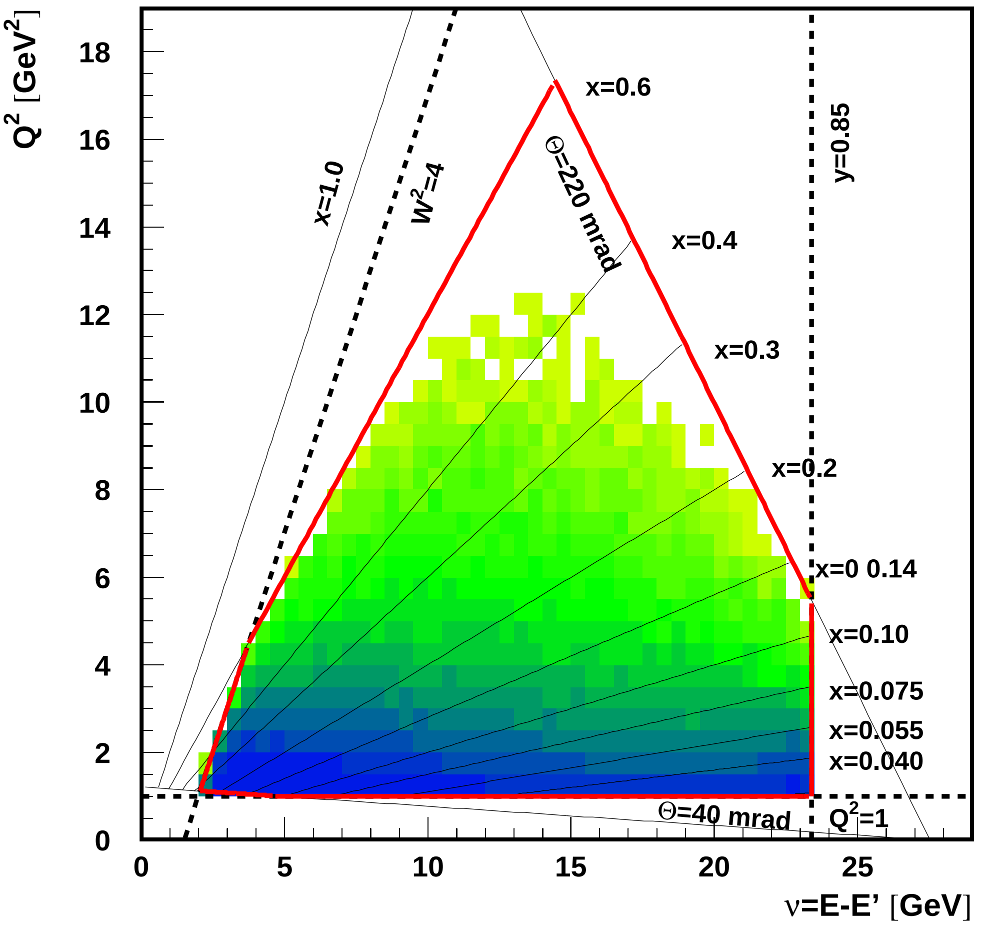

Figure 6.7: Kinematic plane for the Hermes experiment at a beam energy of 27.52 GeV. The lines indicate the kinematic and geometric cuts as well as the x-bins used for the inclusive analysis.

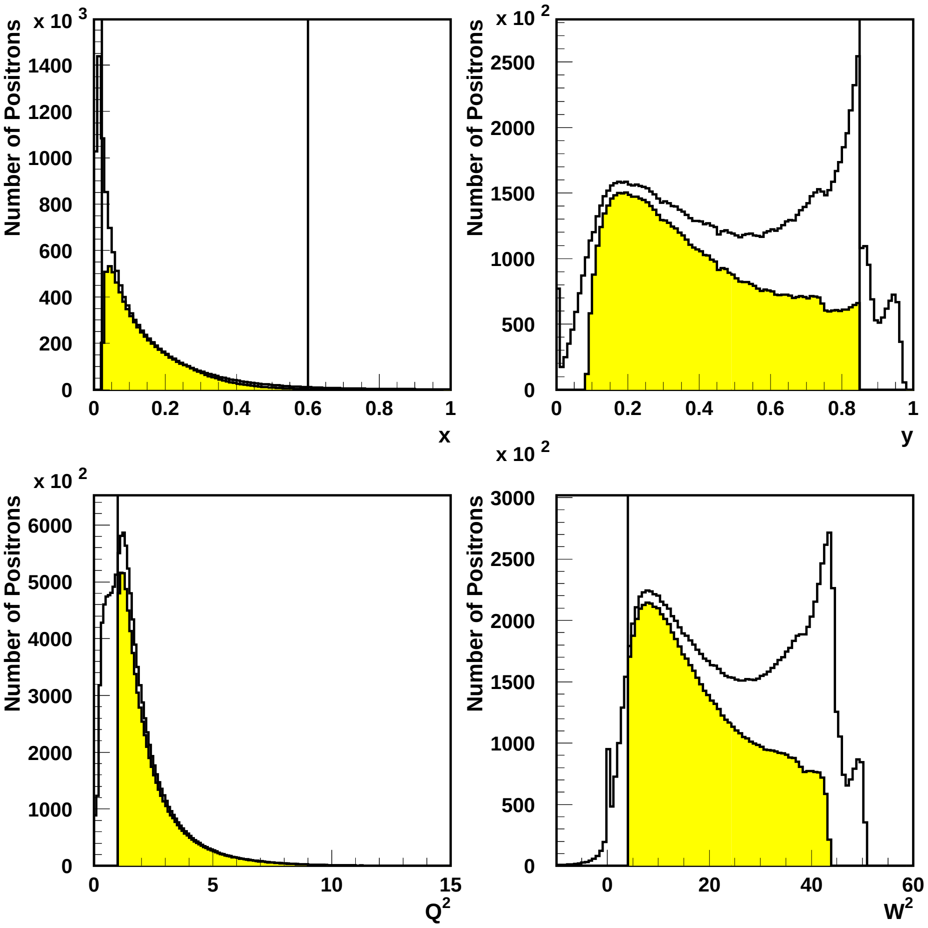

Figure 6.8: Distributions of the kinematic variables x, y, Q^2 and W^2 before (light) and after the application of the kinematic cuts

The particle identification cuts select the positrons from each of the remaining events. The best possible PID is applied, which for the 1995 data means either the PID3-TRD valley cut (section 5.3.2) or the PID downshifting scheme (section 5.3.3). The specific properties of the HERMES particle identification are discussed in chapter 5; for hadron contaminations and positron efficiencies see section 5.6.

The kinematic variables are calculated from the particle momenta and the scattering angles. The value used for the beam energy is 27.52 GeV and the proton mass is taken to be 0.93827 GeV/c^2. The track selection parameters and cuts are listed in table 6.5. The kinematic plane in Q^2 and ν for the HERMES experiment is shown in figure 6.7 along with the geometric and kinematic cuts and the distribution of the DIS positrons. The accepted region is limited by the spectrometer acceptance ($\theta \in [40\,\mathrm{mrad}, 220\,\mathrm{mrad}]$), the Q^2, W^2 and y cuts and the upper boundary of the highest x-bin (0.6). The nine x-bins used for the inclusive HERMES analysis are indicated as well.

The effect of the kinematic cuts on x, y, Q^2 and W^2 is illustrated in figure 6.8 which shows the distribution of positrons in the smDSTs before and after the application of the kinematic cuts. The data in the g1DSTs is not appropriate for this illustration, because cuts at $Q^2 = 0.8$ and $y = 0.85$ were already applied in the production of the g1DSTs. For single track events a cut at $y = 0.85$ was applied in the smDST production as well.

6.3 Extraction of the Asymmetry $A_1^{^3\mathrm{He}}$

6.3.1 Extraction of $A_1^{^3\mathrm{He}}$

After the data quality has been determined the asymmetry $A_1^{^3\mathrm{He}}$ can be calculated as the first step towards the extraction of g_1^n. The count rates N^+ and N^- for the two spin states are given by:

$$N^+ = \int_+ \mathcal{A}(t,x,Q^2)\mathcal{E}(t,x,Q^2)\sigma^{(unpol)}(x,Q^2) \times \Big(\mathcal{L}(t) - A_1^{^3\mathrm{He}}(x,Q^2)\mathcal{L}(t)D(x,Q^2)p_b(t)p_t(t)\Big)\,dt \quad (6.2)$$

$$N^- = \int_- \mathcal{A}(t,x,Q^2)\mathcal{E}(t,x,Q^2)\sigma^{(unpol)}(x,Q^2) \times \Big(\mathcal{L}(t) + A_1^{^3\mathrm{He}}(x,Q^2)\mathcal{L}(t)D(x,Q^2)p_b(t)p_t(t)\Big)\,dt \quad (6.3)$$

where (+) and (−) denote the positive and negative spin states, $\mathcal{A}$ is the acceptance and $\mathcal{E}$ the efficiency of the detector; $\mathcal{L}$ is the luminosity, p_b and p_t are beam and target polarisation, and D is the depolarisation factor.

Assuming that the acceptance $\mathcal{A}$ and the detector efficiency $\mathcal{E}$ are constant over the time period of the measurement and assuming that the data are binned in x and y, the two count rates can be written as

$$\begin{aligned} N^+ = & \ \mathcal{A}\mathcal{E}\sigma^{(unpol)}\left(\int_+ \mathcal{L}(t)dt - A_1^{^3\mathrm{He}}(x,y)\langle D\rangle \int_+ \mathcal{L}(t)p_b(t)p_t(t)dt\right) \\ N^- = & \ \mathcal{A}\mathcal{E}\sigma^{(unpol)}\left(\int_- \mathcal{L}(t)dt + A_1^{^3\mathrm{He}}(x,y)\langle D\rangle \int_- \mathcal{L}(t)p_b(t)p_t(t)dt\right) \end{aligned} \quad (6.4)$$

where $\langle D\rangle$ is the average depolarisation factor for each (x,y)-bin.

Over the short time of a burst (10 s) the beam and target polarisation can be assumed to be constant and the number of events n_i in a burst with positive (negative) polarisation can be expressed as

$$n_i^{\pm} = \mathcal{A}\mathcal{E}\sigma^{(unpol)}\left(L_i - (\pm)A_1^{^3\mathrm{He}}(x,y)\langle D\rangle L_i p_{bi} p_{ti}\right) \quad (6.5)$$

where L_i is the integrated luminosity per burst. The notation

$$\begin{aligned} N^{\pm} &= \sum_{i\pm} n_i \\ L^{\pm} &= \sum_{i\pm} L_i \\ P^{\pm} &= \sum_{i\pm} |L_i p_{bi} p_{ti}| \end{aligned} \quad (6.6)$$

will be used, where the summations run over all positive and negative polarisation bursts. The luminosity values are corrected for the DAQ live time T_{live}:

$$L_i = L_i(\text{measured}) \cdot T_{live}. \quad (6.7)$$

The asymmetry $A_1^{^3\mathrm{He}}(x,y)$ can now be extracted as

$$A_1^{^3\mathrm{He}}(x,y) = \frac{1}{\langle D\rangle}\frac{N^-L^+ - N^+L^-}{N^-P^+ + N^+P^-} \quad (6.8)$$

If the simplifying assumptions are made that the beam and target polarisations are identical for both spin states, equation (6.8) reduces to

$$A_1^{^3\mathrm{He}}(x,y) = \frac{1}{\langle D\rangle\langle p_b\rangle\langle p_t\rangle}\frac{N^-/L^- - N^+/L^+}{N^-/L^- + N^+/L^+}. \tag{6.9}$$

which is familiar as equation (2.28) with $A_{||}$ as defined in equation (2.22).

The statistical error on $A_1^{^3\mathrm{He}}(x,y)$ can be calculated using

$$\delta A_1^{^3\mathrm{He}} = \frac{1}{\langle D\rangle}\frac{L^+P^- + L^-P^+}{(N^-P^+ + N^+P^-)^2}\sqrt{(N^-)^2N^+ + (N^+)^2N^-} \tag{6.10}$$

$A_{||}^{^3\mathrm{He}}(x,y)$ is simply defined as

$$A_{||}^{^3\mathrm{He}}(x,y) = \langle D\rangle \cdot A_1^{^3\mathrm{He}}(x,y) \tag{6.11}$$

so that

$$A_{||}^{^3\mathrm{He}}(x,y) = \frac{N^-L^+ - N^+L^-}{N^-P^+ + N^+P^-}. \tag{6.12}$$

6.3.2 Kinematic Binning and the Depolarisation Factor

To determine the structure function g_1^n as a function of x, bins in x are introduced. The lowest useful x value for the 1995 data set is 0.023. For large values of x the number of events drops rapidly and there are relatively few events above $x = 0.6$. These two values are taken as the lowest and the highest x-bin boundaries and the region between them was divided into 9 bins such that the number of events in each bin is approximately the same. The x-distribution of the DIS positrons is shown in figure 6.9; the bin boundaries are indicated.

The depolarisation factor D (see eq.2.23) is defined as

$$D = \frac{y(2-y)}{y^2 + 2(1-y)(1+R)} \tag{6.13}$$

where R is taken from the parametrisation by Whitlow et al.[111]. It would be best to weigh every event with its correct depolarisation factor, or to be exact with the

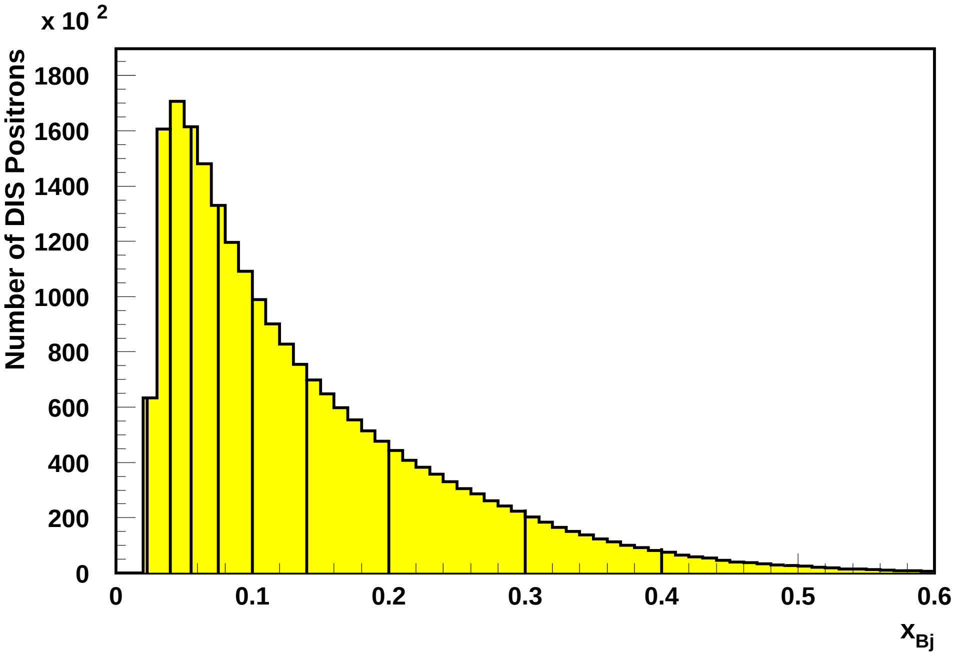

Figure 6.9: x_{Bj}-distribution of the DIS positrons

product of depolarisation factor and the beam and target polarisations. However, the use of a few bins in y appears to be sufficient for this correction. To satisfy the demands of statistics only three bins in y are chosen. This leads to 27 (x,y) bins in total. Their boundaries are defined in table 6.6.

x-bin	$\langle x \rangle$	**y-bin 1**	**y-bin 2**	**y-bin 3**
0.023 - 0.040	0.033	0.073 - 0.68	0.68 - 0.78	0.78 - 0.85
0.040 - 0.055	0.047	0.073 - 0.53	0.53 - 0.67	0.67 - 0.85
0.055 - 0.075	0.065	0.073 - 0.42	0.42 - 0.58	0.58 - 0.85
0.075 - 0.100	0.087	0.073 - 0.34	0.34 - 0.49	0.49 - 0.85
0.100 - 0.140	0.119	0.073 - 0.27	0.27 - 0.42	0.42 - 0.85
0.140 - 0.200	0.168	0.073 - 0.22	0.22 - 0.34	0.34 - 0.85
0.200 - 0.300	0.244	0.073 - 0.17	0.17 - 0.26	0.26 - 0.85
0.300 - 0.400	0.342	0.073 - 0.14	0.14 - 0.23	0.23 - 0.85
0.400 - 0.600	0.464	0.073 - 0.15	0.15 - 0.22	0.22 - 0.85

Table 6.6: Definition of x- and y-bins.

6.3.3 Background Correction

There are two background processes for which the measured asymmetry $A_{||m}^{^3\mathrm{He}}$ must be corrected: Hadron contamination and charge symmetric background.

While the HERMES particle identification is excellent, small amounts of hadron contamination cannot be avoided. Assuming that the absolute values of the beam and target polarisations are the same for both orientations ($P^+ = P^-$), the measured asymmetry $A_{||m}^{^3\mathrm{He}}$ may be expressed as

$$A_{||m}^{^3\mathrm{He}} = (1 - c_h) \cdot A_{||}^{^3\mathrm{He}} + c_h A_{h^+}^{^3\mathrm{He}} \tag{6.14}$$

where

$$c_h = \frac{N_{h^+}}{N_{h^+} + N_{e^+}} \tag{6.15}$$

as discussed in section 5.2 and $A_{h^+}^{^3\mathrm{He}}$ denotes the hadron asymmetry calculated in an analogous way to $A_{||}^{^3\mathrm{He}}$. From this follows

$$A_{||}^{^3\mathrm{He}} = \frac{A_{||m}^{^3\mathrm{He}}}{(1 - c_h)} - \frac{c_h A_{h^+}^{^3\mathrm{He}}}{(1 - c_h)} \tag{6.16}$$

where in the case of small contaminations c_h and small hadron asymmetries the second term can be neglected. This correction has to be applied for every x-bin or preferably for every (x,y)-bin. If the statistics do not allow for this, the same contamination value can be taken for the three y bins corresponding to one x-bin. In the present analysis the (x,y)-bins from table 5.11 in chapter 5.6 have been used.

Charge symmetric background results from pair production processes with the positrons detected as DIS positrons. The best way to account for them is to accept all identified DIS positrons, not only the leading positron in each event. The data can then be corrected for the charge symmetric background by measuring the number of electrons in each (x,y) bin. This is correct under the assumption that the acceptance of the detector is the same for electrons and positrons. The charge symmetric background can be described in the same way as the hadronic background:

$$A_{||m}^{^3\mathrm{He}} = (1 - c_s) \cdot A_{||}^{^3\mathrm{He}} + c_s A_{e^-}^{^3\mathrm{He}} \tag{6.17}$$

with

$$c_s = \frac{N_{e^-}}{N_{e^-} + N_{e^+}}. \tag{6.18}$$

The asymmetry of electrons from pair production is expected to be zero. This is verified within the statistical uncertainties. It therefore can be neglected and the charge symmetric background correction combined with the hadron correction now gives the background corrected asymmetry $A_{||}^{^3\mathrm{He}}$:

$$A_{||}^{^3\mathrm{He}} = \frac{A_{||m}^{^3\mathrm{He}}}{(1 - c_h)(1 - c_s)}. \tag{6.19}$$

The charge symmetric background has been determined in (x,y)-bins as well; the measured values for c_s are listed in table 6.7. The contribution due to charge symmetric processes is larger than the hadronic background, particularly in the high y-bins.

Charge Symmetric Contamination c_s			
x-bin	y-bin 1	y-bin 2	y-bin 3
1	0.0124	0.0489	0.1273
2	0.0021	0.0105	0.0755
3	$5.7 \cdot 10^{-4}$	0.0030	0.0419
4	$3.0 \cdot 10^{-4}$	0.0011	0.0210
5	$1.1 \cdot 10^{-4}$	$3.9 \cdot 10^{-4}$	0.0080
6	$1.4 \cdot 10^{-4}$	$1.2 \cdot 10^{-4}$	0.0021
7	$2.2 \cdot 10^{-5}$	$3.8 \cdot 10^{-5}$	$5.8 \cdot 10^{-4}$
8	$1.0 \cdot 10^{-4}$	$1.1 \cdot 10^{-4}$	$2.2 \cdot 10^{-4}$
9	$1.0 \cdot 10^{-4}$	$4.2 \cdot 10^{-5}$	$3.6 \cdot 10^{-5}$

Table 6.7: Charge Symmetric Background

6.3.4 Fill Averaged Asymmetries

For the derivation of the formula to calculate $A_{||}^{^3\mathrm{He}}$ (6.12) it was assumed that detector efficiency and acceptance are identical for the two spin states. Unfortunately in the HERMES experiment both parameters fluctuate over time and the data for the two spin states are taken sequentially, so that this assumption is not strictly true. Particularly the beam conditions such as beam current, polarisation, beam position and slope at the interaction point and beam induced backgrounds change over time. Therefore the asymmetry should only be calculated for a relatively short time period and then averaged. These fluctuations are illustrated best by the DIS positron yield Y_{DIS} per fill which is defined as the ratio of the number of DIS positrons per fill to the dead time corrected luminosity L integrated over the fill:

$$Y_{DIS} = \frac{N(DIS\ \mathrm{e}^+)}{L}. \tag{6.20}$$

The positron yield per fill for the 1995 data is shown in figure 6.10.

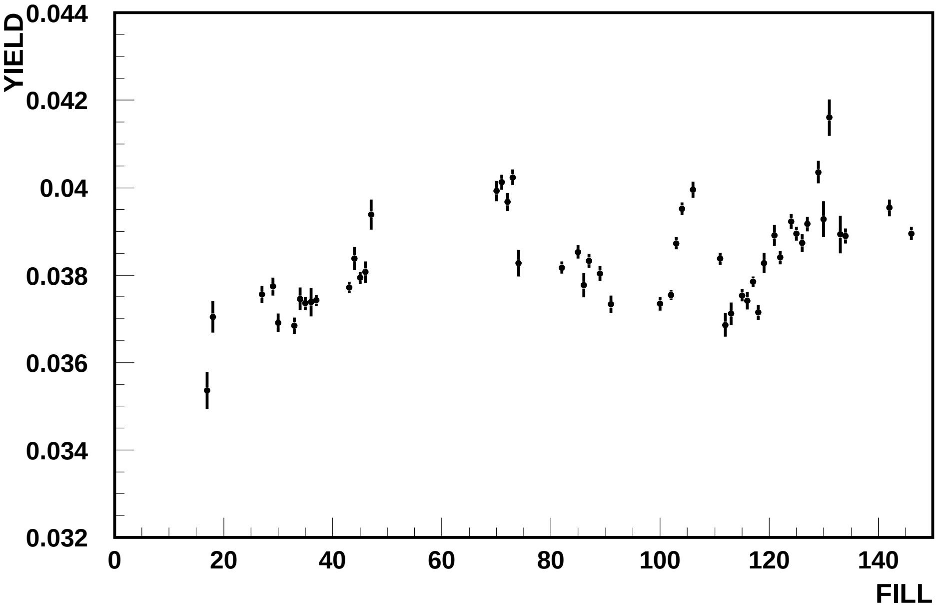

Figure 6.10: Fill averaged DIS positron yields for the 1995 data

The target polarisation is reversed only every ten minutes, and at least two time periods are needed to be able to calculate an asymmetry; about one or two orders of magnitude more to get a reasonably stable result. The fill boundaries are therefore the natural divisions for the data. The beam conditions tend to be stable within one fill; the same is true for the spectrometer. At the same time a fill will contain on average about 50 target polarisation reversals so that a reasonable result for the asymmetry can be obtained.

For these reasons the asymmetry $A_1^{3\mathrm{He}}$ was extracted on a fill-by-fill basis and then averaged to the final result. The asymmetry per fill was calculated for each x and y bin separately, corrected for hadronic and charge symmetric backgrounds and then combined to the final $A_1^{3\mathrm{He}}$ in x-bins.

First the asymmetries for the three y-bins are combined and the depolarisation factor D is applied:

$$\left(A_1^{3\mathrm{He}}(x)\right)^i = \frac{\sum\limits_{y-bins\ j} \frac{1}{\langle D(y)\rangle} \frac{(A_{||}^{3\mathrm{He}}(x,y))^j}{\sigma_j^2}}{\sum\limits_{y-bins\ j} 1/\sigma_j^2} \tag{6.21}$$

The statistical uncertainty is combined as well, according to

$$\sigma_i(x) = \sqrt{\frac{1}{\sum_{j=1}^{3} 1/\sigma_j^2}} \tag{6.22}$$

A weighted average of the asymmetry for all fills i is the calculated:

$$A_1^{3\mathrm{He}}(x) = \frac{\sum\limits_{fills\ i} \frac{(A_1^{3\mathrm{He}}(x))^i}{\sigma_i^2}}{\sum\limits_{fills\ i} 1/\sigma_i^2}, \tag{6.23}$$

with the following total uncertainty:

$$\delta A_1^{3\mathrm{He}}(x) = \sqrt{\frac{1}{\sum_i 1/\sigma_i^2(x)}} \tag{6.24}$$

To obtain $A_{||}^{3\mathrm{He}}(x)$ the depolarisation factor is simply left out. $A_{||}^{3\mathrm{He}}$ is useful to compare data from different analyses that might calculate the depolarisation factor differently. All x-bins per fill might be combined to study the time dependence of the asymmetry. The asymmetries $A_{||}^{3\mathrm{He}}(x)$ and $A_1^{3\mathrm{He}}(x)$ that were calculated in this way for the 1995 data are shown in figure 6.11.

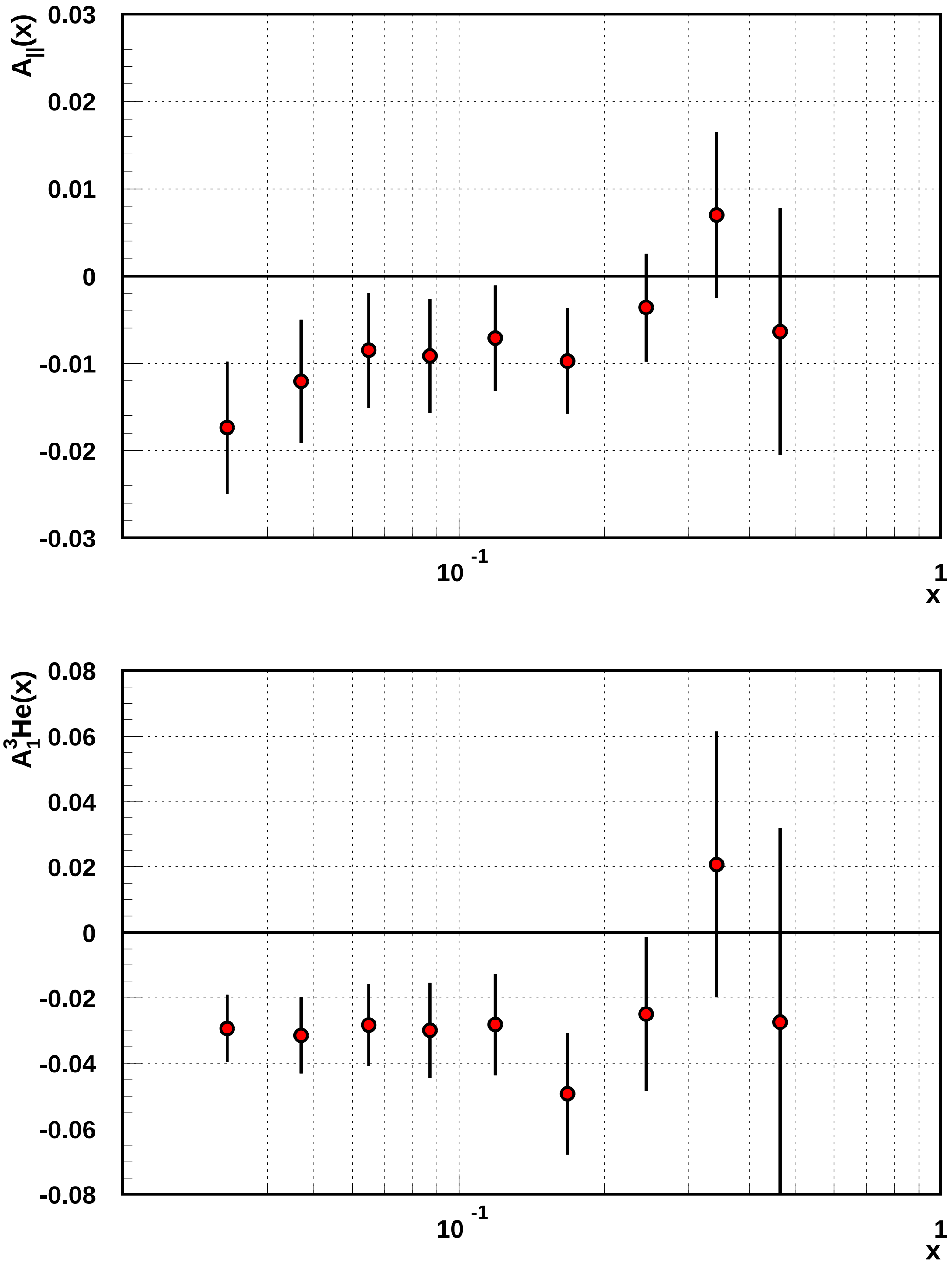

Figure 6.11: Fill averaged asymmetries $A_{||}^{^3\mathrm{He}}(x)$ and $A_1^{^3\mathrm{He}}(x)$

6.4 Extraction of A_1^n and g_1^n

To proceed from the ^{3}He asymmetry to the neutron asymmetry and finally to the structure function g_1^n requires two additional corrections due to the fact that the single photon treatment of deep inelastic scattering is an approximation and that the target is a neutron inside a ^{3}He nucleus and not a free polarised neutron.

6.4.1 Radiative Corrections

As mentioned in section 2.1 the treatment of deep inelastic scattering as one photon exchange is an approximation, although a good one for the kinematics at Hermes. In general higher QED terms have to be taken into account such as vertex corrections, Z-γ interference and multi-photon exchange. Some of these, for example the multi-photon exchange, can be entirely neglected under the experimental conditions at Hermes. Of importance however are initial and final state bremsstrahlung processes that change the kinematics at the interaction point and virtual photon contributions. The external radiative corrections that are important in the case of solid targets are not as large for the much thinner Hermes target. The Feynman diagrams for the simplest and most important radiative corrections are shown in figure 6.12.

The largest contributions to the radiative corrections result from initial and final state bremsstrahlung. They lead to different kinematics at the interaction point and move events from lower values of transferred energy to higher, but incorrect, detected values. For this reason events that result from elastic, quasi-elastic or non-DIS inelastic scattering can be recorded as DIS events. The inclusion of radiative corrections takes this into account. The total cross section can be expressed as the sum of DIS plus 'tails' of the inelastic, elastic, and quasi-elastic cross sections, and additional virtual photon terms (figure 6.12 d-f) such as vacuum polarisation and vertex corrections:

$$\sigma = \sigma_{\rm DIS} + \sigma_{\rm non-DIS\ in} + \sigma_{\rm el} + \sigma_{\rm q} + \sigma_{\rm v} \tag{6.25}$$

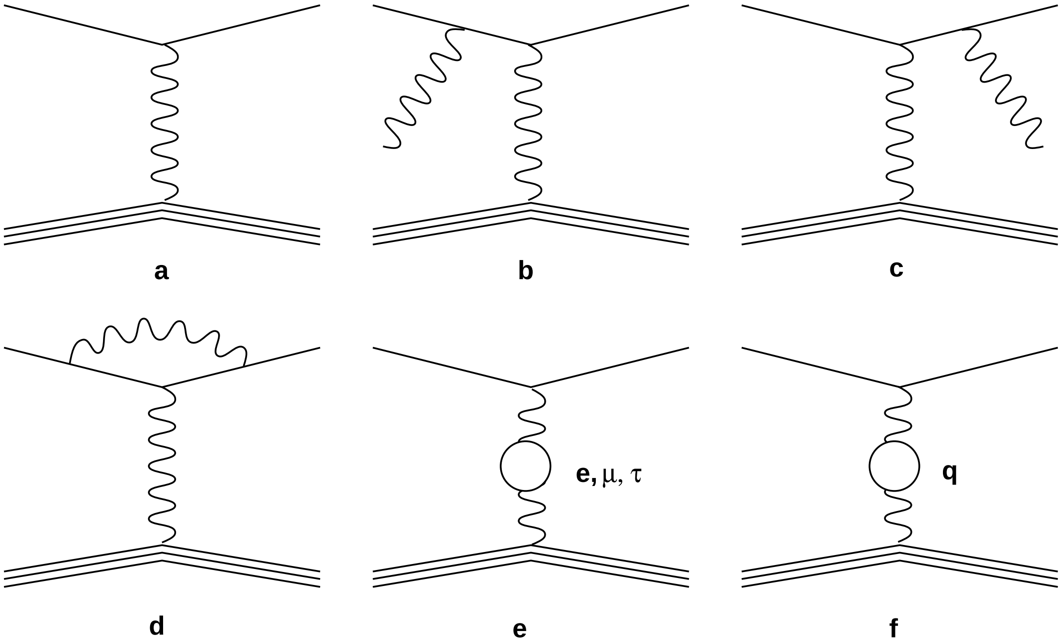

Figure 6.12: Feynman diagrams for radiative corrections: (a) Born term, (b) initial state bremsstrahlung, (c) final state bremsstrahlung, (d) vertex correction, (e),(f) vacuum polarisation

A Fortran code based on Polrad[114][115] is used to calculate radiative corrections for the Hermes analysis. The different contributions from the various tails are calculated and the radiative corrections to $A_1^{^3\mathrm{He}}(x)$ are determined iteratively by the program. The data points are fitted with functions as suggested by Schäfer[112] from which the radiative corrections Δ_{RC} are calculated which leads to a new, corrected A_1. The kth iteration is then given as:

$$A_1^k = A_{1m} - \Delta_{RC}(A_1^{k-1}) \tag{6.26}$$

where A_{1m} is the fit to the measured $A_1^{^3\mathrm{He}}(x)$ values. The procedure usually converges after 4-5 iterations. The values for Δ_{RC} used in this analysis are listed in table 6.8.

As already mentioned, the largest part of the radiative corrections originates in the infrared corrections to the inelastic cross section. However, for large values of y the contributions of elastic and quasi-elastic tails become large. This leads to the track level cut at y=0.85 (table 6.5) that keeps the radiative corrections from becoming too large.

6.4.2 Nuclear Corrections

If the ^{3}He wave function were in a pure S state, the Pauli principle would force the two protons to have opposite spin and the remaining neutron would indeed carry the entire ^{3}He spin. However, theoretical calculations and measurements have shown that there are non-negligible contributions from S' and D waves to the ^{3}He wave function[116–119] which leads to a proton contribution to the ^{3}He spin.

The size of this contribution can be calculated from the probabilities $P^{\pm}_{p(n)}$ to have a proton (neutron) with spin parallel (+) or antiparallel (−) to the ^{3}He spin. For a pure S wave the following would result:

$$P_n^+ = 1 \qquad P_n^- = 0 \qquad P_p^+ = P_p^- = \frac{1}{2}$$

while for a realistic model of the ^{3}He wavefunction the following is derived[14]:

$$\begin{aligned} P_n^+ &= \ 1-\Delta \\ P_n^- &= \quad \Delta \\ P_p^+ &= \ \tfrac{1}{2}-\Delta' \\ P_p^- &= \ \tfrac{1}{2}+\Delta' \end{aligned} \tag{6.27}$$

where $\Delta = 0.07 \pm 0.01$ and $\Delta' = 0.014 \pm 0.002$ are determined by the S' and D wave contributions[14].

The effective nucleon polarisations are therefore

$$\begin{aligned} p_n = &\ P_n^+ - P_n^- = \ 0.86 \pm 0.02 \\ p_p = &\ P_p^+ - P_p^- = \ -0.028 \pm 0.004 \end{aligned} \tag{6.28}$$

and following Ciofi degli Atti et al.[120] $A_1^{^3\mathrm{He}}$ can be expressed in terms of the neutron and proton asymmetries:

$$A_1^{^3\mathrm{He}} = 2 f_p p_p A_1^p + f_n p_n A_1^n \tag{6.29}$$

where

$$f_p = \frac{F_2^p}{2F_2^p + F_2^n}$$
$$f_n = \frac{F_2^n}{2F_2^p + F_2^n} \tag{6.30}$$

are the proton and neutron dilution factors.

This in principle allows A_1^n to be deduced from $A_1^{^3\mathrm{He}}$. However, there are no direct measurements for F_2^n and F_2^d must be used instead. F_2^d is given by:

$$F_2^d = \frac{1}{2}(F_2^p + F_2^n) \tag{6.31}$$

Equations (6.29),(6.30) and (6.31) can be combined into the prescription used for the nuclear corrections in the HERMES g_1^n analysis:

$$A_1^n = \frac{(2F_2^d + F_2^p)}{p_n(2F_2^d - F_2^p)} \cdot A_1^{^3\mathrm{He}} - \frac{p_p \cdot 2F_2^p}{p_n(2F_2^d - F_2^p)} \cdot A_1^p \tag{6.32}$$

For F_2^d and F_2^p a parametrisation of the NMC data[122] was used, while A_1^p was taken from the result of the SLAC experiment E143[9].

The neutron asymmetry $A_1^n(x)$ is shown in figure 6.13 with a logarithmic x-scale to better separate the different bins.

6.4.3 Extraction of g_1^n

The neutron spin structure function $g_1^n(x)$ finally is extracted from $A_1^n(x)$ for the nine x-bins defined in table 6.6 assuming that both $A_2^n(x)$ and $g_2^n(x)$ are negligible (see section 2.1.3):

$$g_1^n(x) = \frac{A_1^n(x) \cdot F_2^n(x, Q^2)}{2x(1 + R(x, Q^2))} \tag{6.33}$$

where the values for R, F_2^d and F_2^p were taken from the NMC and SLAC parametrisations[111, 122] for the average x and Q^2 values of the HERMES data. The values used for both the A_1^n and the g_1^n extraction are listed in table 6.8. The results for $A_{||}^{^3\mathrm{He}}(x)$, $A_1^{^3\mathrm{He}}(x)$, $A_1^n(x)$ and $g_1^n(x)$ are listed in table 6.9 below.

Figure 6.13 shows $xg_1^n(x)$ at the measured Q^2 values. The advantage of plotting xg_1 with a logarithmic scale lies in the fact that the area under the function is conserved,

$$\int xg_1(x)d(\ln x) = \int xg_1(x)\frac{d(\ln x)}{dx}dx = \int xg_1(x)\frac{1}{x}dx = \int g_1(x)dx \qquad (6.34)$$

while a better separation of the data points can be achieved. For completeness the final $g_1^n(x)$ for the 1995 data is also shown with a linear x-scale in figure 6.14.

x-bin	Δ_{RC}	A_1^p	F_2^p	F_2^d	R
1	0.0059	0.0718	0.3241	0.3096	0.3761
2	0.0051	0.1015	0.3360	0.3193	0.3573
3	0.0048	0.1360	0.3449	0.3251	0.3316
4	0.0044	0.1784	0.3514	0.3271	0.2999
5	0.0042	0.2354	0.3549	0.3239	0.2639
6	0.0040	0.3154	0.3515	0.3112	0.2248
7	0.0040	0.4237	0.3278	0.2788	0.1885
8	0.0040	0.5379	0.2693	0.2195	0.1556
9	0.0039	0.6493	0.1771	0.1370	0.1184

Table 6.8: Factors for the A_1^n and g_1^n extraction.

x-bin	$A_{\|\|}^{^3\mathrm{He}}(x)$	$A_1^{^3\mathrm{He}}(x)$	$A_1^n(x)$	$g_1^n(x)$
1	-0.0174 ± 0.0076	-0.0293 ± 0.0103	-0.1037 ± 0.0383	-0.3370 ± 0.1246
2	-0.0121 ± 0.0071	-0.0315 ± 0.0116	-0.1108 ± 0.0435	-0.2626 ± 0.1032
3	-0.0085 ± 0.0066	-0.0283 ± 0.0125	-0.0973 ± 0.0474	-0.1717 ± 0.0836
4	-0.0092 ± 0.0066	-0.0299 ± 0.0144	-0.1017 ± 0.0558	-0.1363 ± 0.0747
5	-0.0071 ± 0.0060	-0.0281 ± 0.0155	-0.0933 ± 0.0616	-0.0909 ± 0.0600
6	-0.0097 ± 0.0060	-0.0492 ± 0.0185	-0.1793 ± 0.0775	-0.1180 ± 0.0510
7	-0.0036 ± 0.0062	-0.0249 ± 0.0236	-0.0727 ± 0.1055	-0.0289 ± 0.0418
8	+0.0070 ± 0.0095	+0.0208 ± 0.0406	+0.1565 ± 0.1973	+0.0336 ± 0.0423
9	-0.0064 ± 0.0141	-0.0274 ± 0.0594	-0.0711 ± 0.3218	-0.0067 ± 0.0300

Table 6.9: Results of the A_1^n and g_1^n extraction.

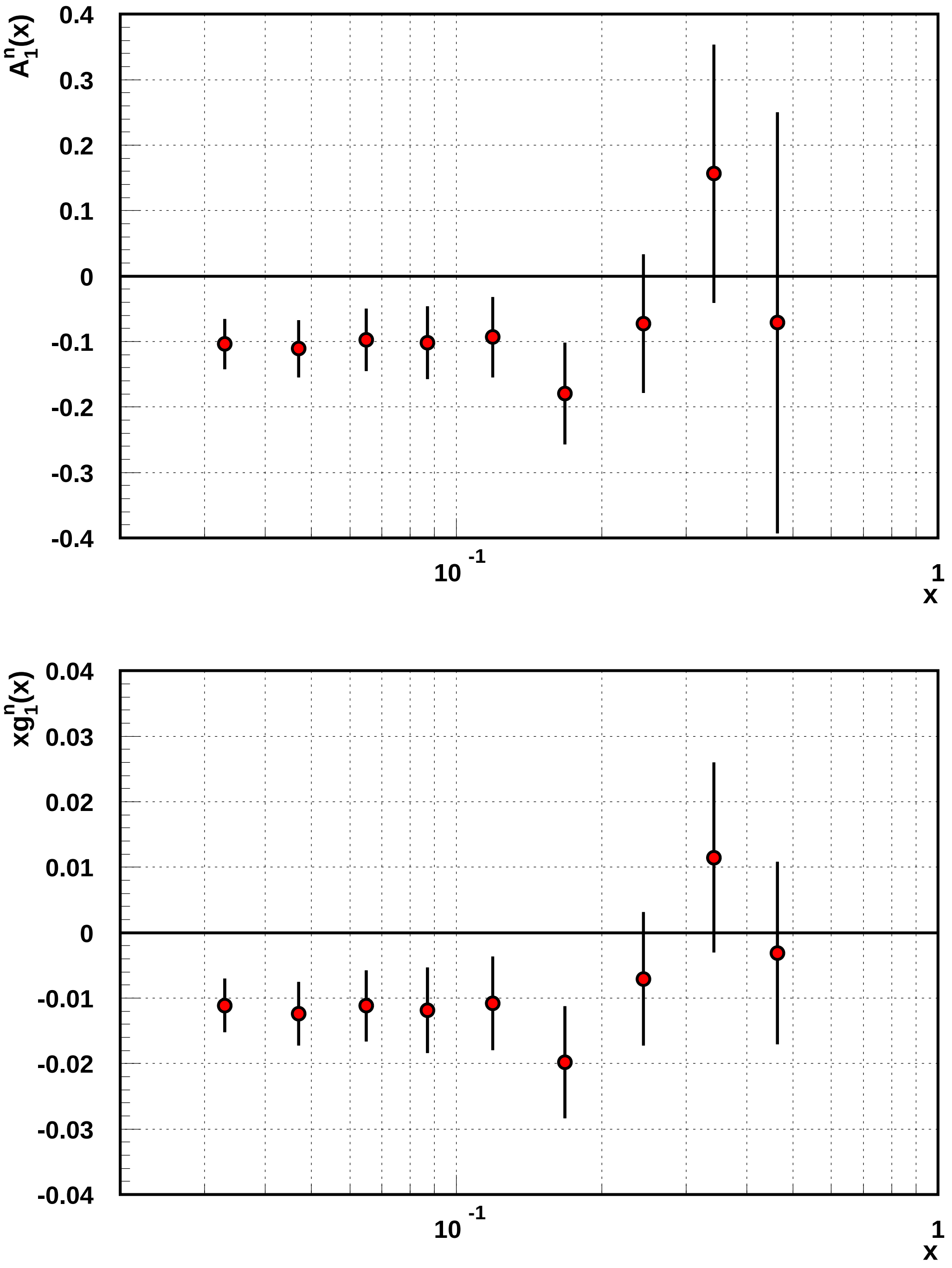

Figure 6.13: $A_1^n(x)$ and $xg_1^n(x)$ at the measured Q^2 values

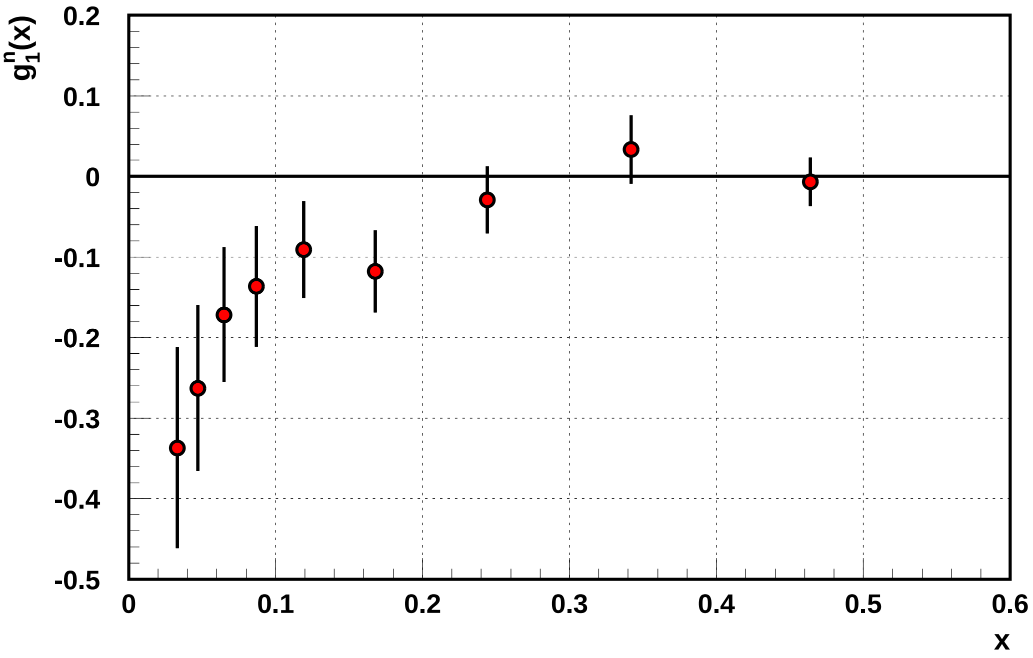

Figure 6.14: $g_1^n(x)$ at the measured Q^2 values

6.5 Systematic Studies

6.5.1 Different Subsets of the Data

To further investigate the quality of the data a large number of systematic studies have been performed. The data were split up into two subsets of about the same size depending on a series of different criteria[121]:

- top and bottom half of the detector
- right and left half of the detector
- large and small values of the beam polarisation (cut at $p_b = 55\%$)
- up- and downstream half of the target cell (cut at $z_{vertex} = 0$)
- low and high luminosity (cut at $L = 100$ Hz)

- first and second half of the year

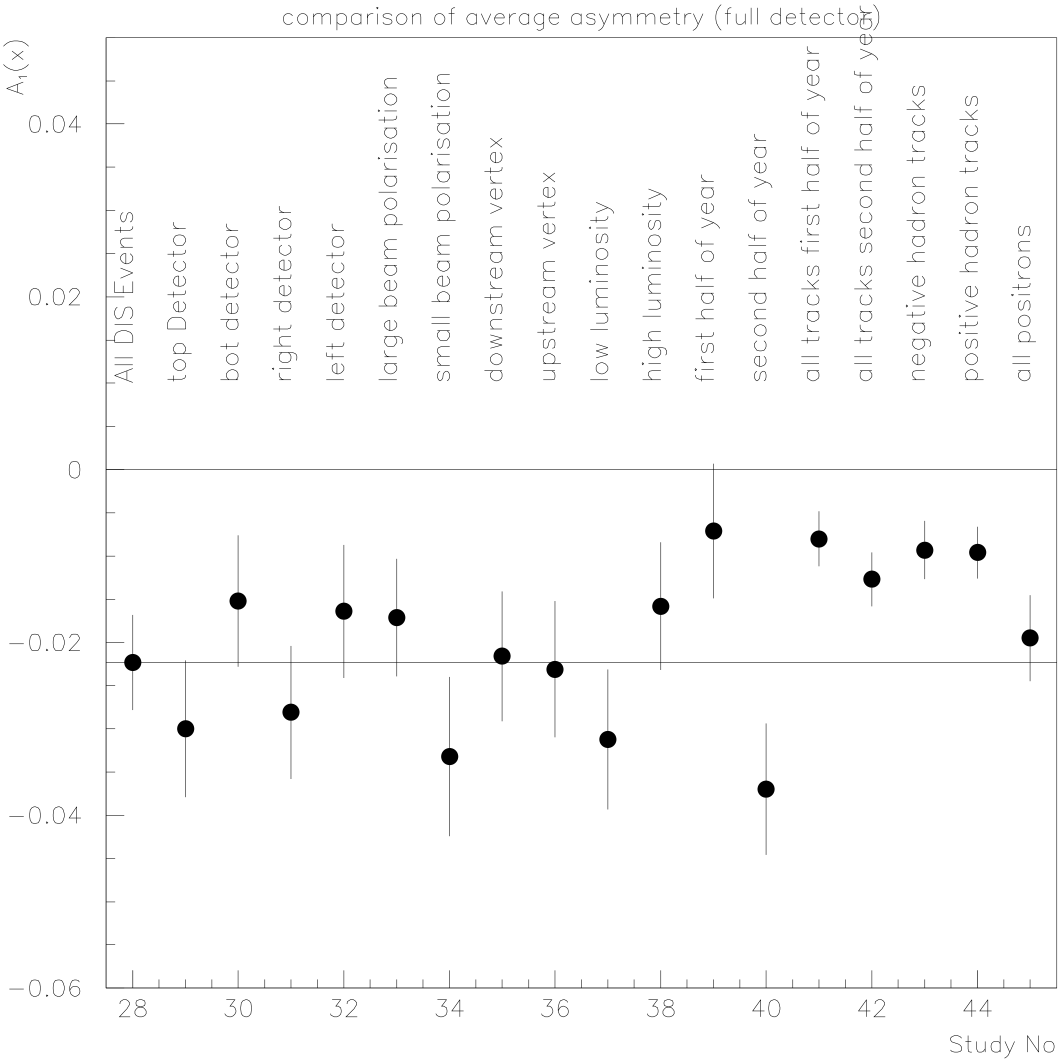

Figure 6.15: Average $A_1^{^3\mathrm{He}}$ for different subsets of the data

Additionally asymmetries were calculated for the following:

- all tracks for the first and second half of the year
- all positive and negative hadrons
- all positrons (including non-DIS)

The results of these studies for $A_1^{^3\mathrm{He}}$ are shown in figure 6.15[121]. They display a significant difference between both samples in only one case: the early-late division of the data. None of the other studies either suggested a more detailed investigation or the assignment of an additional systematic error.

6.5.2 Time Dependence

The observed difference in the asymmetry between the first and second halves of the 1995 data set has been of some concern. For this reason the time dependence of the asymmetry was examined to determine whether this effect is consistent with a statistical fluctuation or whether it is an indication of a deeper problem with the data[121].

For this study version E4 of the data together with the E4 badbits has been used. All standard cuts on the track level were applied and additionally only the bursts with top and bottom badbit equal to zero were used. This left 52 fills for the analysis. To avoid the introduction of any additional ambiguities, $A_{||}^{^3\mathrm{He}}$ without background corrections was examined. The asymmetry $A_{||}^{^3\mathrm{He}}$ per fill is plotted in figure 6.16.

The difference B between two subsets of the data, e.g. the first ($A_{||}^1 \pm \sigma_1$) and the second half ($A_{||}^2 \pm \sigma_2$), can be expressed best in units of σ:

$$B = \frac{A_{||}^1 - A_{||}^2}{\sqrt{\sigma_1^2 + \sigma_2^2}} \quad [\sigma]. \tag{6.35}$$

The cut between the first and second half has been made usually at fill 95, based on equal statistics in both subsets. The question arises as to how much this rather arbitrary choice influences the observed value of B. To examine this, a running cut between the first and second parts of the data set was introduced and the difference B was plotted as a function of the cut position (figure 6.17). If the data are distributed in a purely statistical way, this plot should be flat with fluctuations above and below zero which are larger near the edges of the plot and smaller (between -1 and 1) near the center, in the limit of a large number of data points.

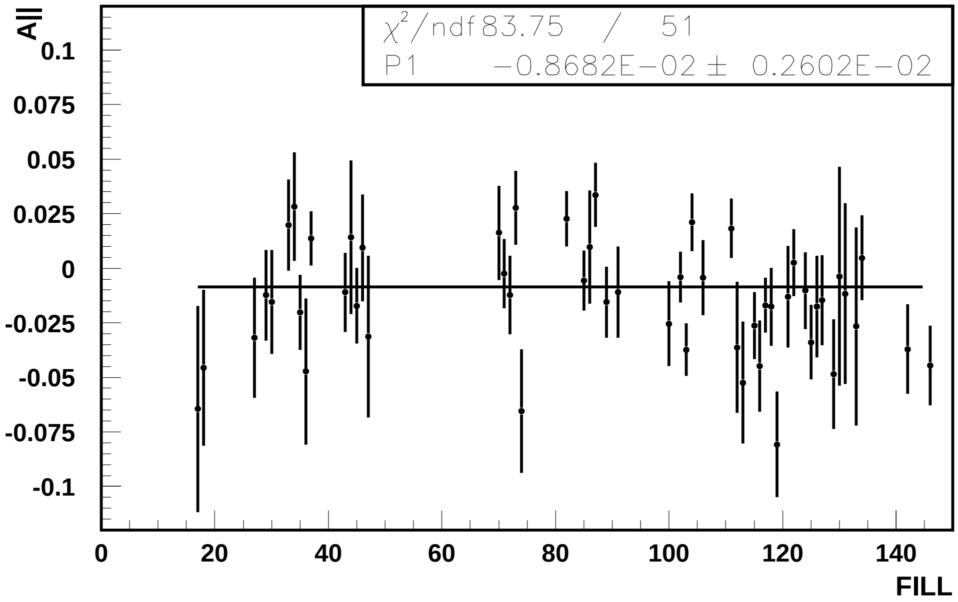

Figure 6.16: $A_{||}^{3He}$ per fill

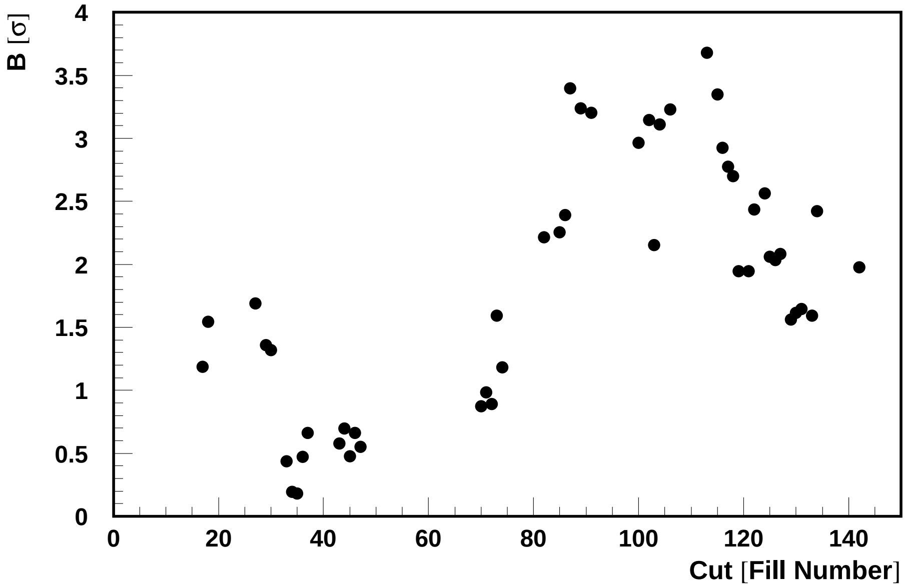

Figure 6.17: Difference between both parts of the data depending on the cut position.

On the other hand, when dealing with two parts of the data set that have a systematic difference in their values of $A_{||}$, but good χ^2 values for each subset, a steady rise in |B| is expected up to the boundary between the subsets and then a steady decline. Instead a steep rise and decline was observed with a plateau between approximately fill 80 to 120. Also the χ^2 values of the subsets are better than the overall χ^2, but not as much as would be expected from a systematic effect (1.35 and 1.59 compared to 1.64). This hints that either a few isolated fills strongly influence the behaviour of the early and late subsets or that there is a systematic problem with the fills in the plateau.

The next step was to look for bad fills and to observe what happens if they are removed from the sample. Fills were removed in a systematic way using the difference d between the average asymmetry and the asymmetry of the particular fill in terms of σ as the cut parameter:

$$d = \frac{A_{||}(\text{fill}) - A_{||}(\text{average})}{\sigma_{A_{||}}(\text{fill})} \quad [\sigma]. \tag{6.36}$$

The remaining fills were divided into two equally large subsets and the value of B is calculated. The cut position stayed between fills 90 and 100. After only the four fills with the largest d values were removed, the situation had improved dramatically. The value of B decreased from 3.2 σ to 1.4 σ and the d-distribution of all fills showed an improvement from an RMS of 1.26 to an RMS of 1.08 (figure 6.18). It is not possible to tell, given the limited number of data points, whether removing four fills makes the distribution any more or less Gaussian. The χ^2 of the average of the entire data set dropped from 1.64 to 1.17. The reason for this becomes apparent if the removed fills are marked. (figure 6.19).

As it happens the two fills with the largest positive $A_{||}$ are to be found just before the set boundary and the two fills with the largest negative values are found just after it. It is this particular grouping that enlarges the value of B. The four fills in question are 82, 87, 103, and 119. This is consistent with the observation of the plateau in figure 6.17 but goes against the hypothesis that there is a general problem with all fills in this region.

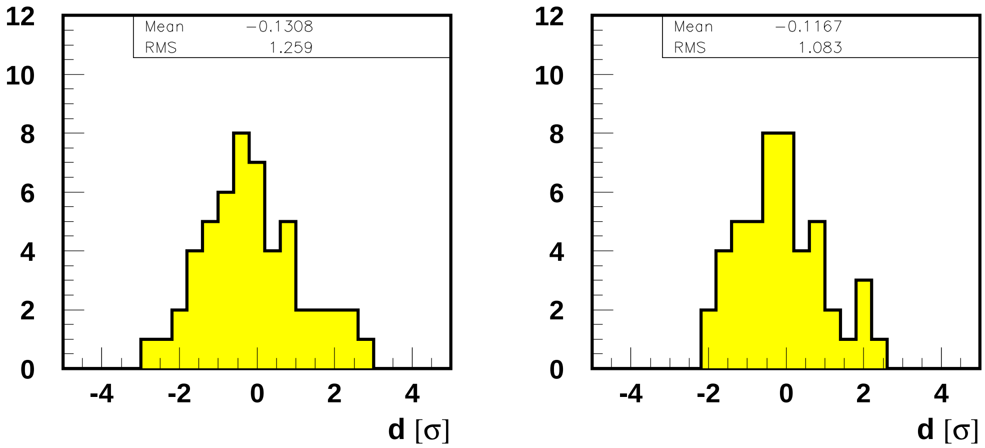

Figure 6.18: Distribution of d per fill for all fills (left) and for all but four (right).

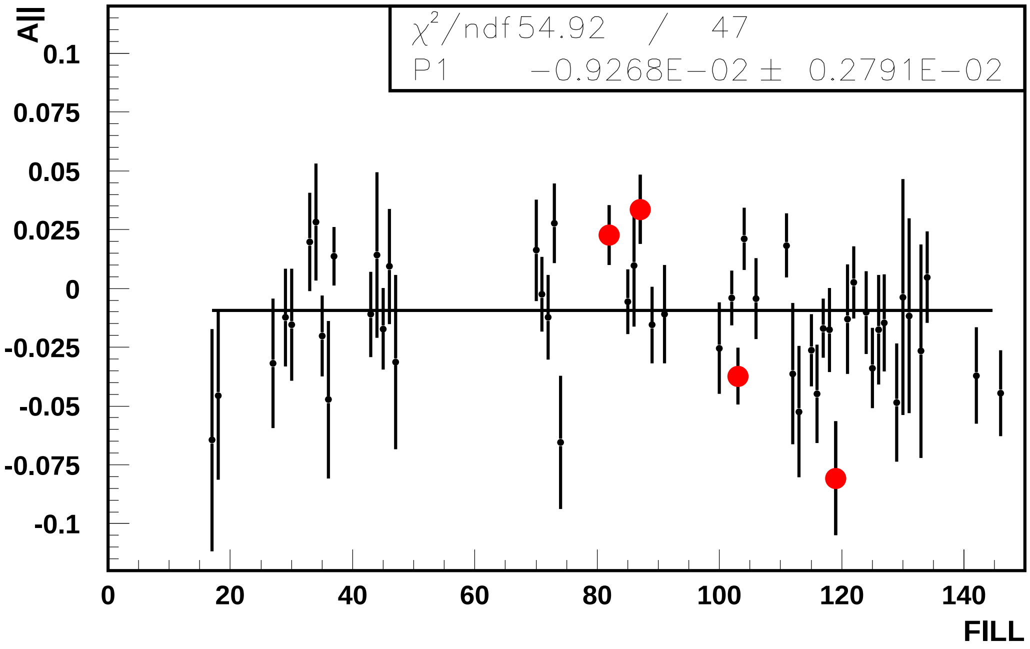

Figure 6.19: $A_{||}^{3He}$ per fill, marking the four fills with the largest d.

If the fills are removed one after the other by making a cut on the distance d to the average value of $A_{||}$, a quick drop from the initial value of B=3.2 to about 1.6 is observed, followed by a rough plateau and a further drop after the removal of 25% of the data (figure 6.20). This is a strong indication of one of two possibilities. Either there is a problem with the first 2-3 fills removed in this process or they are part of a statistical fluctuation.

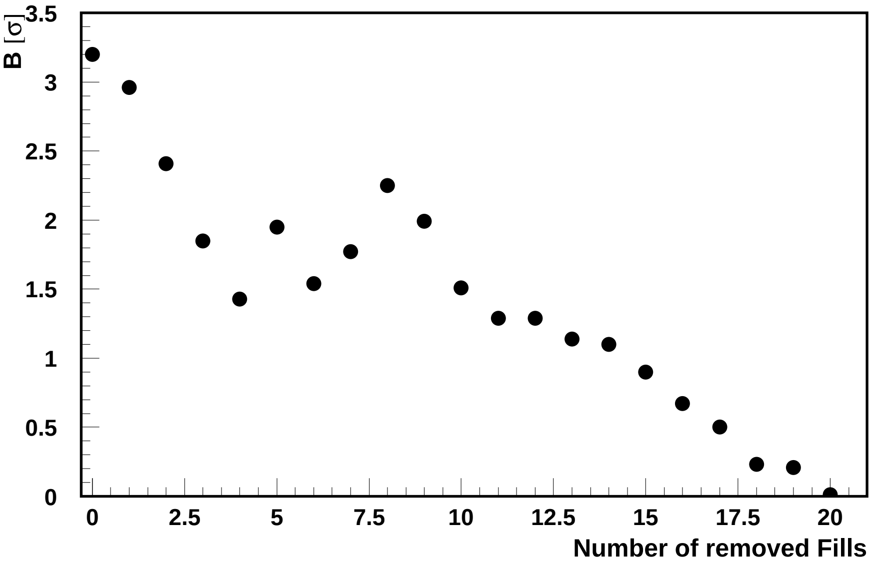

Figure 6.20: Difference between $A_{||}$ for the early and late subsets vs number of fills removed.

Fills can certainly not be removed from the data set because of their inconvenience. However, the 1995 logbook mentions certain problems with the fills in question:

- Fill 82: beam polarisation measurement
- Fill 87: oscillating target temperature
- Fill 103: target temperature measurement, Čerenkov channel 19 intermittent
- Fill 119: bad beam tune, hot wires in the FCs, beam polarisation measurement, relatively short fill

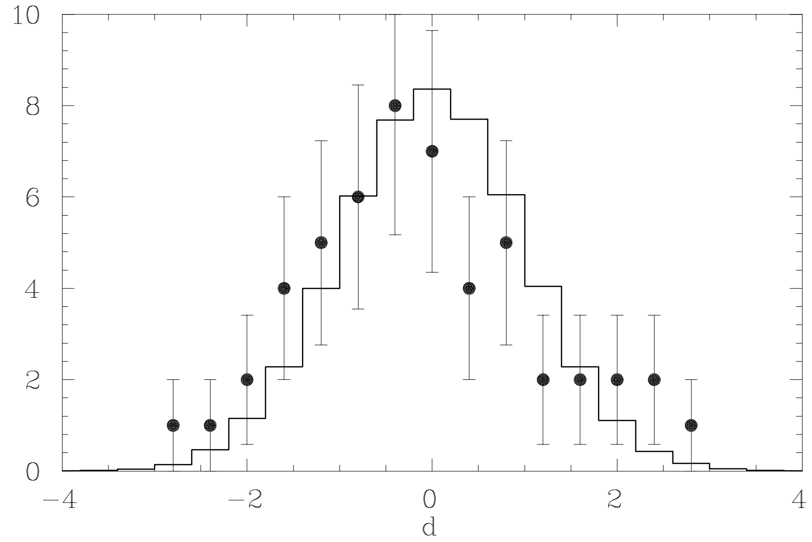

Figure 6.21: Histogram of d (equation 6.36) averaged over 1000 Monte Carlo runs compared to data points for the distribution from the HERMES data set.

An inspection of the beam and target polarisation values for these four fills does not lead to any reason to exclude them from the data set. Only for fill 119 can an argument for removal be made on the basis of generally bad running conditions.

As a test of the expected size of statistical fluctuations, a simple Monte Carlo procedure was written that simulates the 1995 measurement of a constant asymmetry. Specifically, for each simulation, 52 counting asymmetries with a magnitude of -0.008 are formed with statistical precision defined by the statistical uncertainty of each of the 52 fills from the 1995 data set.

As an estimate of the size of typical fluctuations within a Monte Carlo run, the deviation is calculated with respect to the weighted average asymmetry of that run (see equation 6.36). For a large number of fills this distribution must approach a Gaussian, but it is clear that for 52 measurements the Gaussian nature may not be immediately apparent. The Monte Carlo was run 1000 times for 52 fill values each and the Gaussian result for the distribution of d agrees within the errors with the data (see figure 6.21).

The sensitivity of the statistical analysis to a relatively small number of fills (4 of 52) makes it unlikely that there is a widespread systematic problem with the 1995 data. However, no 'smoking gun' was found to justify excluding these fills from the data set except possibly for fill #119. No additional systematic error needs to be assigned to $A_{||}^{^3\mathrm{He}}$ for the early-late discrepancy based on this analysis. A series of other time dependence analyses[121] comes to the same conclusion.

6.5.3 Influence of the Particle Identification

So far the official Hermes run and burst selection has been used. When studying the impact of the chosen particle identification scheme on g_1^n, the data sample has to be restricted to the 1725 runs where the TRD and the Čerenkov quality are good for the entire detector and only bursts with good quality for top and bottom are used. The number of events is reduced significantly (by 21%) from 2.8 million DIS positrons to 2.2 million positrons. The asymmetry $A_{||}^{^3\mathrm{He}}$ has been selected as the parameter to study the impact of the different PID schemes instead of $A_1^{^3\mathrm{He}}$ as in most other systematic studies (see figure 6.15). The reason for this is to study the result assuming all particles identified as DIS positrons are in fact positrons. Therefore no background corrections have been made.

The first comparison is the one between the previously derived $A_{||}$ from the full data set and the result that is obtained from the reduced 'good PID' dataset with 1725 runs. For convenience, to better distinguish between the x-bins a logarithmic x-scale is adopted (see figure 6.22). The differences that are observed between both data samples are of the same order of magnitude as observed in the previous systematic studies (see figure 6.15).

The asymmetry $A_{||}$ has been extracted from the reduced 'good PID' data set for eight different PID schemes defining the DIS positrons. All include the same standard kinematic track level cuts, the difference is solely in the particle identification. These cuts are the standard PID3-TRD valley cut, PID4 which basically uses the same

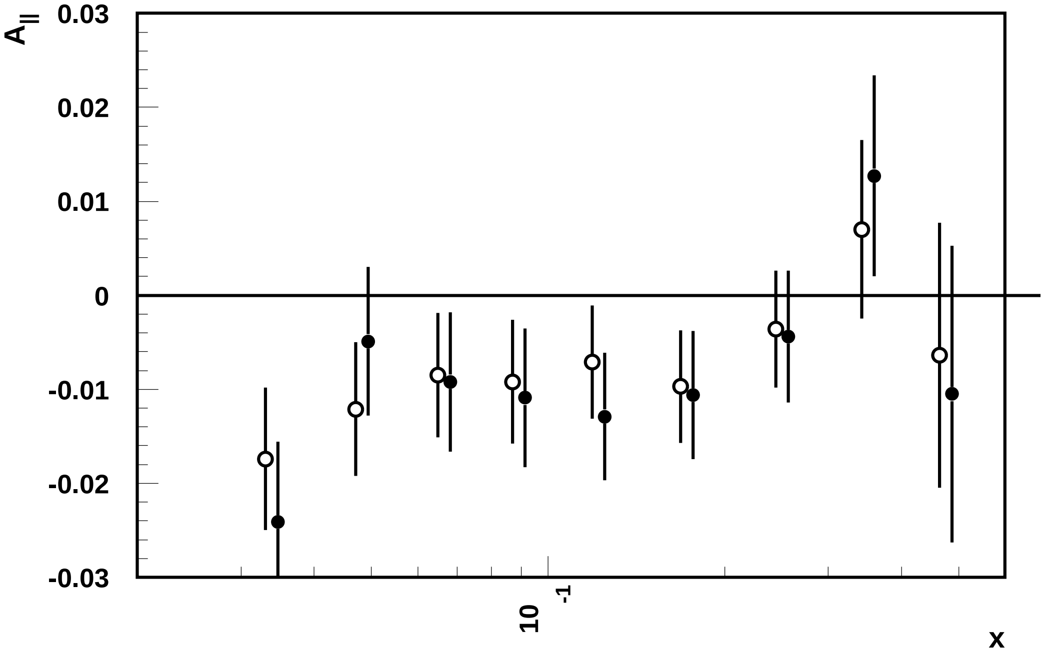

Figure 6.22: Comparison between $A_{||}$ with PID downshifting and full dataset (empty circles) and reduced 'good PID' dataset with PID3-TRD valley cut only. (solid circles)

information, PID3 and PID2 with less PID information, a combination of straight cuts on PID3 and the TRD response (region A), the TRD alone, a set of hard PID cuts on all four detectors and finally no PID cut at all. The results are shown in figures 6.23; for clarity the results have been divided into two figures, where both contain the PID3-TRD valley scheme as a reference. The numbers of identified DIS 'positrons' and the average asymmetry are listed together with the requirements for each PID scheme in table 6.10 below. The average asymmetries are also shown in figure 6.24.

The comparison shows that the results for the valley cut and for PID4 are practically indistinguishable as expected. The PID3 result is extremely close and even when using PID2 the data hardly changes. The difference in the number of identified DIS positrons between these four methods is of the order of 0.3%. This also means that the differences in the lowest two x-bins in figure 6.22 are the result of the difference in the data samples, not a hadron contamination effect.

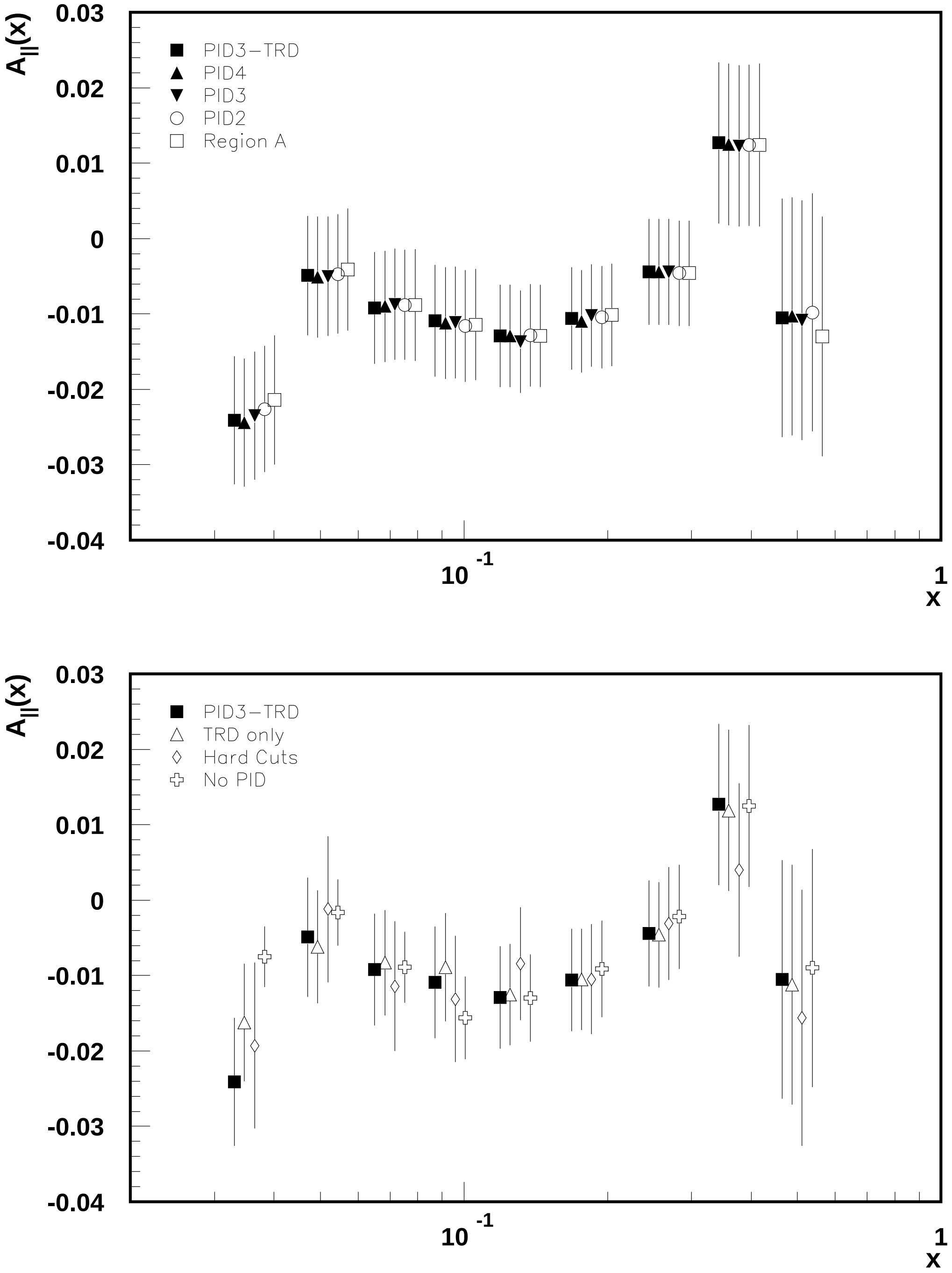

Figure 6.23: Comparison of $A_{||}(x)$ for different PID schemes.

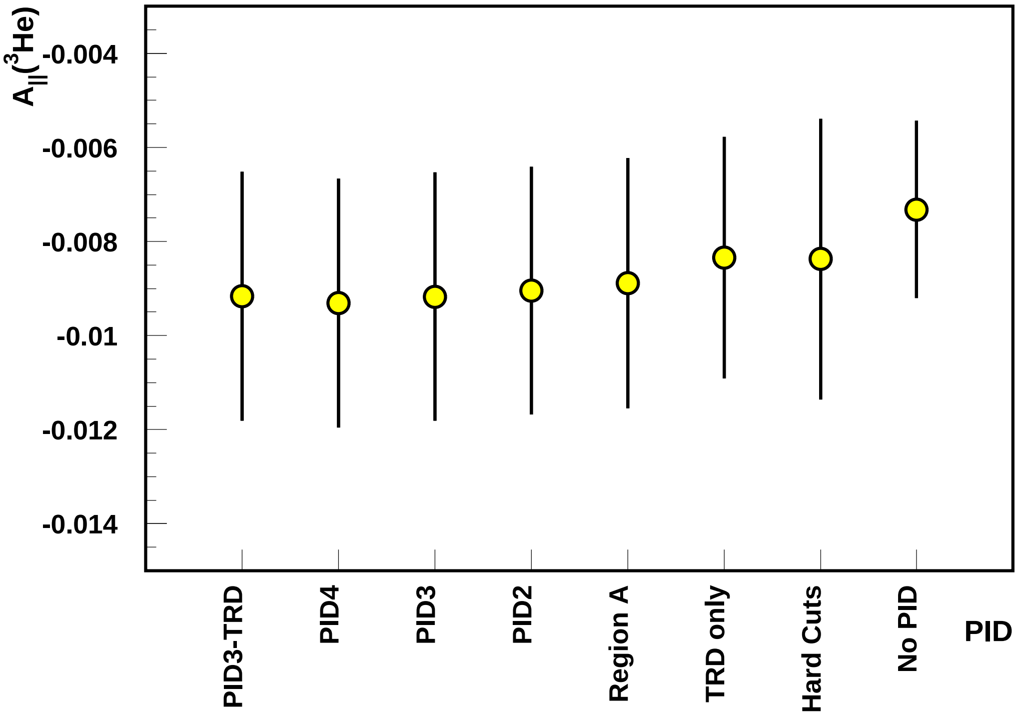

Figure 6.24: Comparison of $A_{||}$ for different PID schemes.

PID Cut	Cut Condition	Number of DIS Positrons	$A_{\|\|}$
PID3-TRD	$PID3 + 0.31 * pulsTRD > 5.48$	$2.237 \cdot 10^6$	-0.0092 ± 0.0027
PID4	$PID4 > 0$	$2.232 \cdot 10^6$	-0.0093 ± 0.0027
PID3	$PID3 > 0$	$2.237 \cdot 10^6$	-0.0092 ± 0.0027
PID2	$PID2 > 0$	$2.244 \cdot 10^6$	-0.0091 ± 0.0027
Region A	$PID3 > 0 \wedge pulsTRD > 17.7$keV	$2.200 \cdot 10^6$	-0.0089 ± 0.0027
TRD only	$pulsTRD > 17.7$keV	$2.355 \cdot 10^6$	-0.0084 ± 0.0026
Hard Cuts	Set 1 (see table 5.1)	$1.746 \cdot 10^6$	-0.0084 ± 0.0030
No PID	charge > 0, DIS track cuts	$4.367 \cdot 10^6$	-0.0073 ± 0.0019

Table 6.10: $A_{||}$ for different PID cuts.

The more restrictive combination of straight cuts ('region A') represents a subset of the valley cut DIS positrons and the difference in the first and last x-bin are likely statistical fluctuations. The asymmetry resulting from the use of only the TRD for particle identification is different from the valley cut result only in the lowest x-bin.

The hadron contamination for this cut in this x-bin is about 17%. The comparison of the valley cut result with the asymmetry without positron PID is interesting. The absolute value of the asymmetry in the lowest two x-bins is significantly higher, indicating that the hadron asymmetry is small and that particle identification is crucial for the lowest x-bins.

The use of hard cuts for all four PID detectors greatly reduces the statistics and illustrates the advantages of the particle identification being based on the PID quantities derived from a probability analysis.

In light of the fact that the asymmetry does not change in response to the different choices of particle identification, as long as all available information is used in an efficient way, no additional systematic error due to the particle identification has to be assigned.

6.5.4 Estimates of the Systematic Uncertainties

A possibly serious source of uncertainty for the 1995 HERMES data lies in the rather large yield fluctuations (see figure 6.10). The fluctuations are larger for the data from the top detector, where they exceed 10%. Most of the yield fluctuations happen between fills, so the uncertainty arising from these fluctuations is already greatly reduced by calculating asymmetries for each fill. The cause of these yield fluctuations is not entirely clear. Between fills a number of things may change. In particular the position and slope of the HERA beam and the beam related background varied significantly from fill to fill.

The size of the uncertainty from yield fluctuations was estimated using two different methods[121]. The first one is to calculate the integrated asymmetry $A_1^{^3\mathrm{He}}$ from the data with randomised target spin in each burst. This procedure was done 3000 times and the resulting distribution is in fact Gaussian around zero. By subtracting the statistically expected standard deviation $\delta A_1^{\mathrm{stat}}$ of the distribution from the measured standard deviation σ in quadrature, the contribution from the yield fluctuations is obtained:

$$\delta A_1^{\text{yield}} = \sqrt{\sigma^2 - (\delta A_1^{\text{stat}})^2} \tag{6.37}$$

The value of $\delta A_1^{\text{yield}}$ is 46% of the statistical error.

The second method used to study yield fluctuations is based on the fact that for a purely statistical error a $1/\sqrt{n}$ behaviour is expected as the number of bursts n combined to form the asymmetry is increased. The deviation from this behaviour can be taken as a measure for the systematic uncertainty due to yield fluctuations[121]. This study also clearly shows that the formation of fill-wise asymmetries already removes most of the problem. The estimate of the uncertainty on the asymmetry from the second method is estimated to be 50% of the statistical error.

It can be argued that for a longer data taking period the fill level yield fluctuations would eventually cancel. For this reason the uncertainty from the yield fluctuations was added to the statistical uncertainty. The statistical errors on g_1^n were increased by a factor of $\sqrt{1.0^2 + 0.5^2} = 1.12$ for the final result at $Q^2 = 2.5$ (see table 6.13).

Apart from the yield fluctuations there are three different sources of systematic uncertainties: Systematic errors on target and beam polarisation measurements, the radiative corrections and the external data used for the extraction of g_1. The systematic errors on both the beam and the target polarisation, 5.5% and 5% respectively, are the largest sources of systematic uncertainty. This is already present at the level of the raw asymmetry $A_{||}^{^3\text{He}}$ and has to be propagated from there. The second source of systematic uncertainties lies in the procedure used for the radiative corrections. The input here is the asymmetry $A_1^{^3\text{He}}$. The systematic error of the radiative corrections has been derived by D.Ryckbosch et al. in an internal HERMES note[115] (see table 6.11).

Finally there are systematic errors that have been assigned to the data from other experiments or from theory. These systematic uncertainties are the following:

- $\mathbf{A_1^p}$: The uncertainty was assigned as 10% of the value[9].
- $\mathbf{p_n}, \mathbf{p_p}$: The errors are 0.02 and 0.04 absolute, respectively (see equation 6.28).
- $\mathbf{F_2^n/F_2^p}$: The relative error was set to 2%[122].
- $\mathbf{F_2^n}$: The errors were taken from the NMC parametrisation of the upper and lower error bounds and the absolute error on F_2^n was set to half the difference between the extremes.
- **R**: The error on R was calculated with the routine R1990 by L.W. Whitlow[111].
- $\mathbf{A_2^n}$: The uncertainty was taken from the E143 measurements of A_2^p and A_2^d. The errors from both measurements were added and in the highest x-bin the theoretical bound $\sqrt{R}$ was used.

The resulting systematic uncertainties on g_1, both for measured Q^2 and evolved to $Q^2 = 2.5$ are compiled in two tables below (6.11,6.12). The largest reduction of the total systematic uncertainty could be achieved by improving the accuracy of the beam and target polarisation measurements and by better constraints on the shape of $A_1^{^3\mathrm{He}}$ at low x, which would reduce the systematic uncertainty of the radiative corrections.

Parameter	**x-bin**									**Integral**
	1	2	3	4	5	6	7	8	9	
P_b	0.0216	0.0153	0.0091	0.0096	0.0073	0.0057	0.0014	0.0014	0.0006	0.0021
P_t	0.0196	0.0140	0.0083	0.0087	0.0067	0.0052	0.0012	0.0013	0.0006	0.0019
Δ_{Rc}	0.0351	0.0120	0.0044	0.0012	0.0025	0.0028	0.0025	0.0019	0.0010	0.0018
A_1^p	0.0018	0.0018	0.0018	0.0017	0.0017	0.0016	0.0014	0.0011	0.0007	0.0007
p_n	0.0127	0.0069	0.0052	0.0050	0.0036	0.0041	0.0015	0.0011	0.0006	0.0013
p_p	0.0026	0.0025	0.0025	0.0025	0.0024	0.0023	0.0021	0.0016	0.0010	0.0010
F_2^n/F_2^p	0.0073	0.0039	0.0028	0.0027	0.0020	0.0023	0.0010	0.0007	0.0003	0.0008
F_2^n	0.0053	0.0044	0.0034	0.0025	0.0017	0.0019	0.0005	0.0005	0.0004	0.0006
R	0.0131	0.0072	0.0038	0.0025	0.0019	0.0012	0.0005	0.0004	0.0002	0.0008
A_2^n	0.0052	0.0041	0.0034	0.0027	0.0021	0.0015	0.0015	0.0021	0.0017	0.0012
total	0.0520	0.0278	0.0162	0.0155	0.0122	0.0104	0.0048	0.0046	0.0027	0.0046

Table 6.11: Contributions to the systematic error on g_1^n at the measured values of Q^2.

Parameter	**x-bin**									**Integral**
	1	2	3	4	5	6	7	8	9	
P_b	0.0248	0.0169	0.0097	0.0097	0.0073	0.0057	0.0014	0.0016	0.0008	0.0022
P_t	0.0226	0.0154	0.0089	0.0088	0.0067	0.0052	0.0013	0.0015	0.0008	0.0020
Δ_{Rc}	0.0404	0.0130	0.0046	0.0012	0.0025	0.0029	0.0026	0.0021	0.0013	0.0020
A_1^p	0.0021	0.0019	0.0018	0.0018	0.0017	0.0016	0.0015	0.0012	0.0009	0.0008
p_n	0.0146	0.0075	0.0054	0.0049	0.0036	0.0041	0.0016	0.0012	0.0008	0.0014
p_p	0.0030	0.0027	0.0026	0.0025	0.0024	0.0023	0.0021	0.0017	0.0012	0.0011
F_2^n/F_2^p	0.0084	0.0042	0.0030	0.0026	0.0020	0.0023	0.0010	0.0009	0.0004	0.0008
F_2^n	0.0093	0.0058	0.0037	0.0025	0.0017	0.0019	0.0005	0.0007	0.0008	0.0008
R	0.0150	0.0079	0.0039	0.0026	0.0019	0.0012	0.0005	0.0004	0.0003	0.0008
A_2^n	0.0060	0.0044	0.0035	0.0028	0.0021	0.0015	0.0016	0.0023	0.0021	0.0013
total	0.0605	0.0307	0.0172	0.0156	0.0121	0.0104	0.0050	0.0051	0.0036	0.0051

Table 6.12: Contributions to the systematic error on g_1^n at $Q^2 = 2.5$ (GeV/c)^2.

6.6 Evaluation of the Integral of g_1^n

6.6.1 Evolution to constant Q^2

It is necessary to evolve the data to a fixed value of Q^2 to evaluate the integral $\int_o^1 g_1^n(x)\ dx$ in a consistent way, because of the Q^2 dependence of g_1^n. The measured values of g_1^n for the nine x-bins were evolved to a common Q^2 of 2.5 (GeV/c)^2 which is close to the average Q^2 value of the HERMES experiment. The asymmetry A_1^n is assumed to be independent of Q^2. In this case g_1^n evolves with F_2^n and R (see equation 6.33) and can be calculated from either A_1^n or from g_1^n at the measured Q^2 values according to

$$g_1^n(x, Q^2 = 2.5) = g_1^n(x, \langle Q^2 \rangle) \cdot \frac{F_2^n(x, Q^2 = 2.5)}{F_2^n(x, \langle Q^2 \rangle)} \frac{(1 + R(x, \langle Q^2 \rangle))}{(1 + R(x, Q^2 = 2.5))}. \tag{6.38}$$

The visible effect of the Q^2 evolution is a shift of the data in the lowest x-bins to more negative values, thus increasing the integral (see figure 6.25). The values used for F_2^n and R as well as the values of g_1^n at $Q^2 = 2.5$ are listed in table 6.13. From these values the integral of g_1^n for $Q^2 = 2.5$ (GeV/c)^2 over the measured range of x is evaluated as

$$\Gamma_1^{\mathbf{n}}(\text{measured}) = \int_{\mathbf{0.023}}^{\mathbf{0.6}} \mathbf{g_1^n(x)\ dx} = \mathbf{-0.030 \pm 0.012}(\text{stat.}) \pm \mathbf{0.005}(\text{syst.}). \tag{6.39}$$

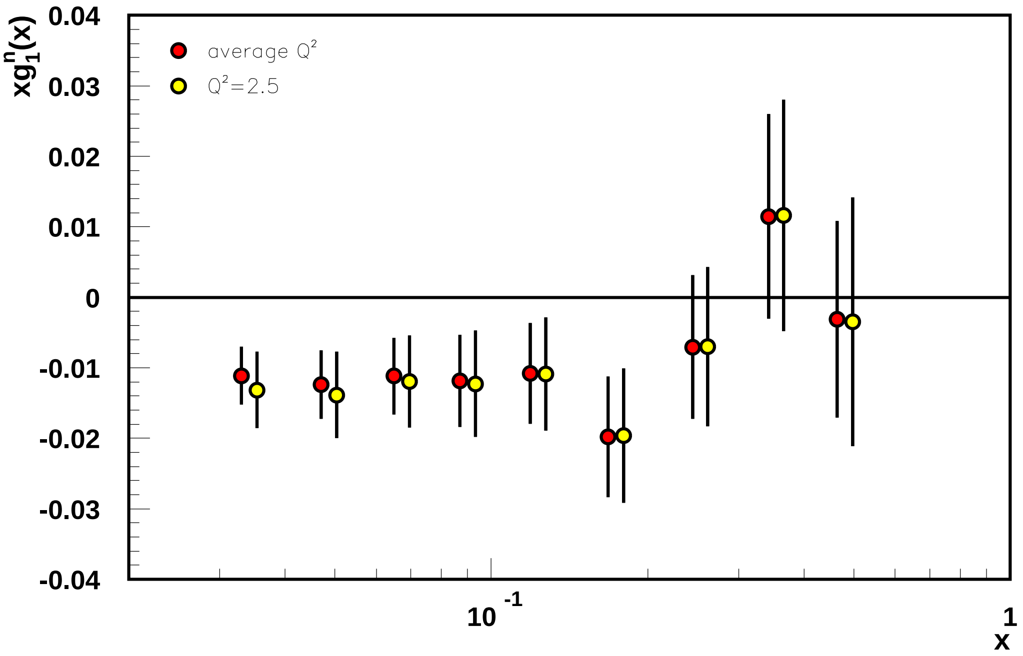

Figure 6.25: xg_1^n for measured Q^2 and for $Q^2 = 2.5$ (GeV/c)^2.

x-bin	$F_2^n(x, Q^2 = 2.5)$	$R(x, Q^2 = 2.5)$	$g_1^n(x, Q^2 = 2.5)$
1	0.3326	0.3115	-0.3985 ± 0.1650
2	0.3259	0.3036	-0.2945 ± 0.1297
3	0.3180	0.2924	-0.1842 ± 0.1005
4	0.3079	0.2775	-0.1410 ± 0.0866
5	0.2936	0.2585	-0.0915 ± 0.0676
6	0.2708	0.2363	-0.1168 ± 0.0566
7	0.2326	0.2168	-0.0286 ± 0.0463
8	0.1792	0.2050	0.0340 ± 0.0480
9	0.1175	0.1984	-0.0075 ± 0.0381

Table 6.13: Factors and results for the Q^2 evolution; the error on g_1^n includes the factor of 1.1 due to yield fluctuations.

6.6.2 Extrapolation

To obtain the integral Γ_1^n over the whole range of x it is necessary to extrapolate the measured data for the low and the high x-values not reached by the experiment. The total integral is then given as the sum of the integral over the measured region and the two extrapolations:

$$\Gamma_1^n = \Gamma_1^n(x < 0.023) + \Gamma_1^n(\text{measured}) + \Gamma_1^n(x > 0.6) \tag{6.40}$$

The high x region is straight forward. There is a QCD based prediction by Brodsky et al.[123] that for $x \to 1$ the structure function is expected to behave like

$$g_1^2 \sim C\ (1-x)^3 \tag{6.41}$$

where C is an arbitrary constant that can be used as fit parameter. The result for the high x region is then given as

$$\Gamma_1^n(x > 0.6) = \int_{x_{max}}^{1} C\ (1-x)^3\ dx = \frac{1}{4}C(1-x_{max})^4 \tag{6.42}$$

which for $x_{max} = 0.6$ becomes $0.0064 \cdot C$. If the last two x-bins are used for the extrapolation to higher x the result is

$$\Gamma_1^n(x > 0.6) = 0.0004 \tag{6.43}$$

while if only the highest bin is used as input to the fit the result becomes

$$\Gamma_1^n(x > 0.6) = -0.0003 \tag{6.44}$$

The conclusion is that the high x contribution is compatible with zero and negligible.

The low x region requires a more sophisticated treatment. The most conventional low-x extrapolation is based on the assumption of Regge-like behaviour, that is $g_1 \sim x^\alpha$ for $x \to 0$ with $\alpha \in [0, 0.5]$. Usually $\alpha = 0$ is selected which means that g_1 is fitted with a constant for small x values. The number of points used in the fit has been varied between one and four, reaching up to $x = 0.1$, which is the region in which

Regge theory is supposed to be valid. The calculated contributions to the integral vary between -0.005 and -0.009.

However, the Regge fit does not seem to describe the data well. More recently, a logarithmic functional behaviour has been suggested[124]. Two logarithmic fit functions based on this model have been used to calculate $\Gamma_1^n(x > 0.6)$ as well, together with a third logarithmic function that is purely empirical, but describes the data very well. These functions are:

$$g_1^n \sim A \ln x \tag{6.45}$$

$$g_1^n \sim A(1 + 2 \ln x) \tag{6.46}$$

$$g_1^n \sim A \ln x + B \tag{6.47}$$

These fits use the four lowest x-bins and result in larger contributions to the integral with values between -0.009 and -0.028. The large value of the empirical fit that describes the data the best indicates the importance of further measurements at small x to determine Γ_1^n more exactly.

Finally, the third method used to extrapolate to low x is a linear extrapolation of the running integral of g_1^n, $\int_x^1 g_1^n(x)\ dx$. The number of x-bins taken into account for this fit was varied between two and four. The results are shown together with the running integral itself in figure 6.26. All numerical results of the extrapolation for low x are collected in table 6.14 below.

The resulting estimate for the low x contribution to the total Γ_1^n is

$$\Gamma_1^n(x < 0.023) = -0.007 \pm 0.007 \tag{6.48}$$

which is the average value for the four different Regge fits and also the result of the linear extrapolation of the running integral of g_1^n for the lowest four x-bins. It is in agreement with the lowest result of the logarithmic extrapolations. While the result of the empirical fit is significantly higher than all other values and does not appear to be likely, the value of -0.016 for the running integral extrapolation does not seem impossible. Due to the speculative nature of the extrapolation an uncertainty of 100% is assigned to the result.

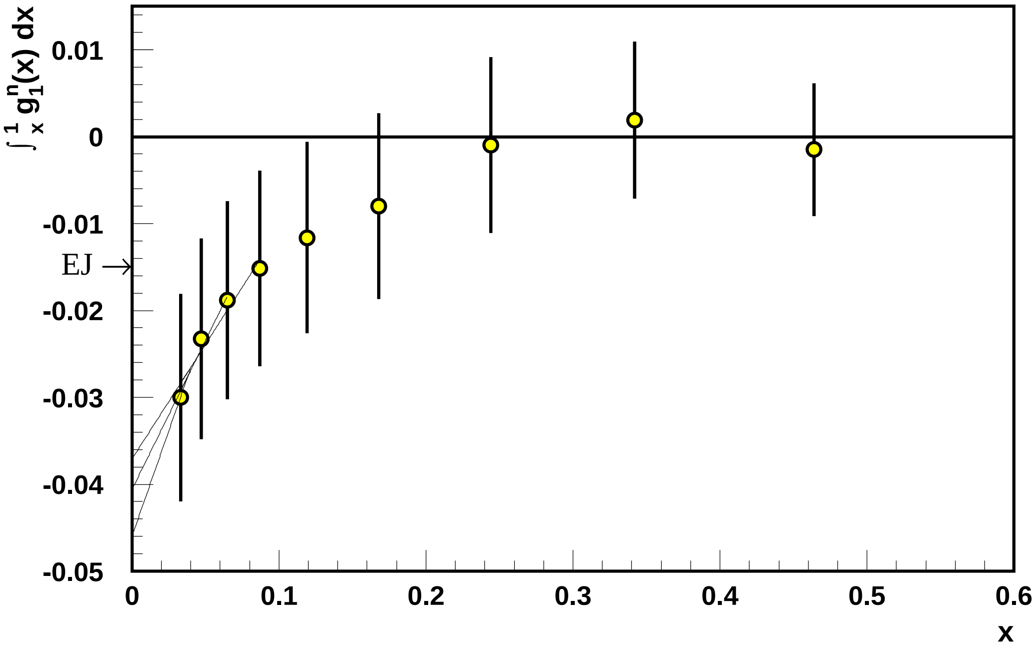

Figure 6.26: $\int_x^1 g_1^n(x)\ dx$ with linear extrapolation for $x \to 0$

Extrapolation Method	$\Gamma_1^n(x < 0.023)$
Regge	
1 x bin	-0.0092
2 x bins	-0.0077
3 x bins	-0.0059
4 x bins	-0.0048
Logarithmic Fit	
$A \ln x$	-0.0087
$A(1 + 2\ln x)$	-0.0095
$A \ln x + B$	-0.0287
$\int_x^1 \mathbf{g_1^n(x)\ dx}$	
2 x bins	-0.0160
3 x bins	-0.0106
4 x bins	-0.0070

Table 6.14: Different methods of low x extrapolation.

6.7 Interpretation of the Results

The final value of the Ellis-Jaffe integral extracted from the 1995 HERMES data is

$$\boxed{\boldsymbol{\Gamma_1^n = -0.037 \pm 0.012}(\text{stat.}) \pm \mathbf{0.005}(\text{syst.}) \pm \mathbf{0.007}(\text{extrapol.})} \tag{6.49}$$

This value is roughly one sigma larger than the quark parton model expectation value of

$$\Gamma_1^n = -0.024 \tag{6.50}$$

and even further removed from the theoretical value including QCD corrections of

$$\Gamma_1^n(\text{theory}) = -0.015 \pm 0.005 \tag{6.51}$$

which indicates that the Ellis-Jaffe sum rule is violated. This theoretical value has been calculated for $Q^2 = 2.5$ (GeV/c)^2 according to equation (2.52) using[55]:

$$\alpha_s(Q^2 = 2.5\ (\text{GeV/c})^2) = 0.27 \pm 0.02 \tag{6.52}$$

In the framework of the quark parton model and under the assumption that the Bjorken sum rule holds, values for the total quark contribution to the neutron spin $\Delta\Sigma$ as well as the individual quark contributions Δu, Δd, Δs can be derived. The statistic and systematic uncertainties on Γ_1^n were added in quadrature for this purpose. The resulting total uncertainty is ±0.015. The results for both the simple quark parton model, derived according to equations (2.51), and the QCD corrected quark parton model, using equations (2.57) are listed in table 6.15 below. For comparison the recently published results of the SLAC experiment E142[24] are listed as well.

The SLAC experiment is the only experiment besides HERMES that has published g_1^n measured with a ^{3}He-target and it is therefore natural to compare the HERMES results with theirs. The comparison of both the x-dependence and the integral of g_1^n shows that HERMES and E142 are in good agreement within the uncertainties. The SLAC experiment quotes an Ellis-Jaffe integral of

$$\Gamma_1^n = -0.031 \pm 0.006(\text{stat.}) \pm 0.009(\text{syst.}) \tag{6.53}$$

Parameter	**Hermes** QPM $Q^2 = 2.5$ (GeV/c)^2	**Hermes** QPM & QCD $Q^2 = 2.5$ (GeV/c)^2	**E142** QPM & QCD $Q^2 = 2.0$ (GeV/c)^2
Δu	$+0.88 \pm 0.05$	$+0.85 \pm 0.06$	$+0.86 \pm 0.04$
Δd	-0.38 ± 0.05	-0.41 ± 0.05	-0.40 ± 0.04
Δs	-0.04 ± 0.06	-0.07 ± 0.06	-0.06 ± 0.06
$\Delta\Sigma$	$+0.46 \pm 0.16$	$+0.37 \pm 0.16$	$+0.39 \pm 0.11$

Table 6.15: Quark contributions to the neutron spin from the quark parton model without and with QCD correction

which agrees well with the HERMES result. The structure function xg_1^n evolved to common Q^2 from both experiments is shown for comparison in figure 6.27; both results are plotted with statistical errors only. The functional form of g_1^n agrees within these errors. The results for the quark contributions to the neutron spin from both experiments are in excellent agreement if QCD corrections are included.

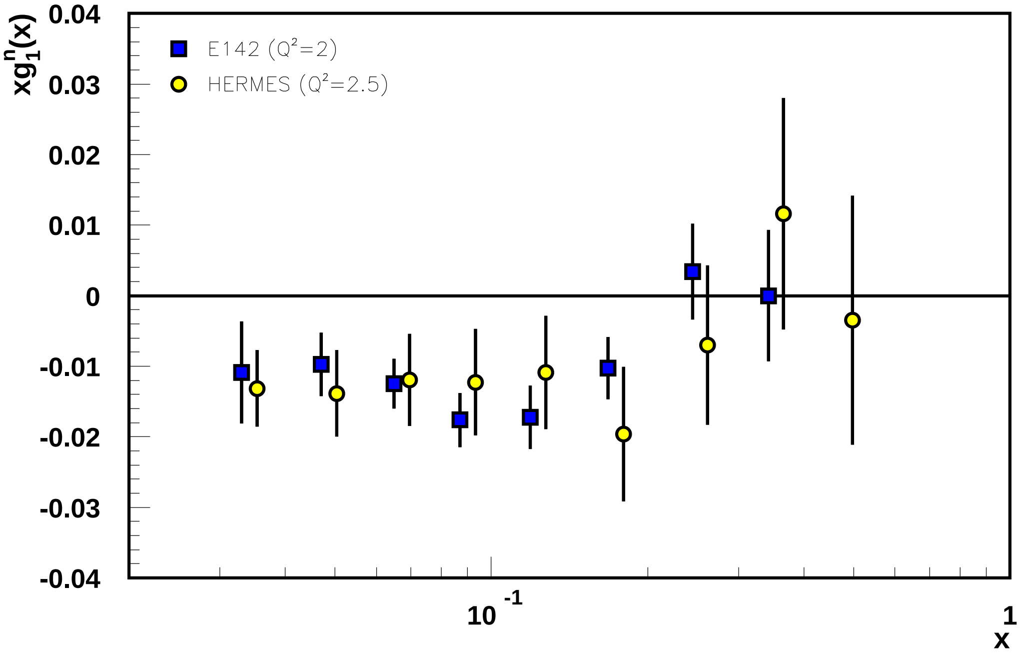

Figure 6.27: xg_1^n for common Q^2 from HERMES and E142

The result of the 1995 HERMES measurement of g_1^n shows that the Ellis-Jaffe sum rule is violated. The interpretation in the framework of the quark parton model indicates that less than half of the spin of the neutron is carried by the quarks, leaving more than half to gluons and orbital angular momentum. This result agrees qualitatively with the predictions by Ji and Balitsky based on the evolution of the gauge invariant spin sum rule. The HERMES result also indicates a small degree of polarisation for the strange sea, in agreement with the available world data.

Chapter 7

Conclusion

The HERMES experiment started to take data in 1995 with a polarised ^{3}He target after a short commissioning phase.

The HERMES transition radiation detector (TRD) was commissioned together with the rest of the HERMES apparatus and proved to be an essential part of the HERMES particle identification. As one of the largest TRDs in existence it is also among the best performing ones. It has completely met all expectations and exceeded some of them. The design value for the TRD was a pion rejection factor (PRF) of 100 at 5 GeV and 90% positron efficiency. For these conditions and using the truncated mean algorithm a PRF of 130 was achieved. The average PRF for all momenta is 150 for the truncated mean algorithm and 1460 for the full probability analysis.

The HERMES particle identification system includes the TRD as well as a Čerenkov detector, a calorimeter and a preshower detector. The combination of these four detectors allowed the identification of positrons for the analysis of the inclusive 1995 data with an efficiency of 99% and an average hadron contamination of less than 0.5%.

About 2.8 million positrons with good data quality were identified in the 1995 data and the neutron spin structure function g_1^n was extracted successfully.

The resulting integral $\Gamma_1^n = \int_0^1 g_1^n(x)\, dx$ was measured to be

$$-0.037 \pm 0.012(\text{stat.}) \pm 0.005(\text{syst.}) \pm 0.007(\text{extrapol.})$$

at $Q^2 = 2.5(\text{GeV/c})^2$. The difference between this result and the theoretical prediction of the Ellis-Jaffe sum rule of -0.015 ± 0.005 is 1.4 standard deviations. Taken in combination with other experiments which have measured g_1^n, g_1^p and g_1^d, this result indicates a likely violation of the Ellis-Jaffe sum rule. In the framework of the quark parton model with QCD corrections the results described in this thesis correspond to a contribution of the quarks to the spin of the neutron of 37% ± 16% and to a small negative polarisation of the strange sea ($\Delta s = -0.07 \pm 0.06$). This value confirms previous measurements at SLAC[8]. It also agrees well with the results for the quark contribution to the spin of the nucleon from the data of the other CERN and SLAC experiments. Ellis and Karliner quote a combined value from the world data of $\Delta\Sigma = 0.27 \pm 0.04$ at $Q^2 = 3$ (GeV/c)^2[40].

The existing measurements do not completely answer the question of the origin of the nucleon spin and more data will be needed.

There are basically four main routes that are being followed:

- Improved statistics,
- Semi-inclusive Measurements,
- Low x,
- Gluon Polarisation.

The experiments E154 and E155 at SLAC[125] have already taken data on the spin structure functions of the proton, the neutron and the deuteron. It can be expected that they will improve the accuracy of the present measurements of g_1 and provide first results on g_2. The HERMES experiment has already taken data successfully with a polarised hydrogen target in 1996 and will continue to do so in 1997. Over the course of the next years, data with improved statistics can be expected from HERMES as well.

The semi-inclusive measurement program of HERMES will allow the separation of the sea and valence quark contributions to the nucleon spin. The impending upgrade of the HERMES particle identification system by replacing the existing threshold Čerenkov detector with an aerogel RICH detector will significantly improve the hadron identification capabilities of HERMES. As a result the strange sea will become accessible through the measurement of kaon asymmetries.

The largest uncertainty in the first moments of g_1^p and g_1^n lies in the low x behaviour of g_1. Measurements of the spin structure functions at lower x will therefore determine the integral of g_1 more exactly. Plans are in progress to polarise the proton beam in HERA[126] which would allow the extension of the low x range by about two orders of magnitude.

Experimental data relevant to the gluon contribution to the nucleon spin would allow important insights into the role of the axial anomaly. A measurement of ΔG could decide about the size of $\Delta\Sigma$ without the term arising from the axial anomaly and would be decisive about the relative contributions of quarks, gluons and orbital angular momentum to the spin of the nucleon. This clearly makes it the most interesting of the four routes that are being followed. This is also indicated by the number of planned experiments at different laboratories. Projects to measure ΔG are on their way at the COMPASS experiment at CERN, in the spin program at RHIC[127, 128] and with real photons in photon-gluon fusion at SLAC[125] and at the recently proposed APOLLON experiment at HERA. The HERMES Charm Upgrade[130] is also directed at a measurement of ΔG.

The next ten years will be an exciting time in high energy spin physics and will likely see the nucleon spin puzzle solved at last. It can be expected that in the coming years HERMES will contribute prominently to this exploration.

Bibliography

[1] E. Rutherford, Phil. Mag. 21 (1911), 669

[2] F.Abe, *et al.* Phys.Rev.Let. 74 (1995), 2626

[3] S.Abachi, *et al.* Phys.Rev.Let. 74 (1995), 2632

[4] R.P.Feynman, *Photon-Hadron Interactions*, Addison-Wesley, 1972

[5] V.W.Hughes, *Spin Physics - A personal recollection*, in: Prospects of Spin Physics at HERA, eds. J.Blümlein, W.D.Nowak, DESY 95-200, 1995

[6] M.J.Alguard *et al.*, Phys.Rev.Let. 37 (1976), 1258

[7] G.Baum *et al.*, Phys.Rev.Let. 51 (1983), 1135

[8] P.L.Anthony *et al., Determination of the Neutron Spin Structure Function*, Phys.Rev.Let. Vol.71, No.7 (1993) 959-962

[9] K.Abe *et al., Precision Measurement of the Proton Spin Structure Function* g_1^p, Phys.Rev.Let. Vol.74, No.3 (1995) 346-350

[10] J.Ashman *et al., An Investigation of the Spin Structure of the Proton in Deep Inelastic Scattering of Polarised Muons on Polarised Protons*, Nucl.Phys. B328 (1989) 1-35

[11] B.Adeva *et al.*, Phys.Let. B302 (1993), 553

[12] HERMES Collaboration, *Proposal*, DESY-PRC 90-01, 1990

[13] D.Barber, *et al., High Spin Polarization at the* HERA *Electron Storage Ring*, Nucl.Inst.Meth. A338 (1994), 166-184

[14] J.L.Friar *et al., Neutron Polarization in polarized* ^3He *Targets*, Phys.Rev.C Vol.42, (1990) 2310

[15] The HERMES Collaboration, *Measurement of the Neutron Spin Structure Function* g_1^n *with a Polarized 3He Target*, HERMES Internal Report 97-08, to be published in Physics Letters

[16] F.Halzen, A.D.Martin, *Quarks and Leptons*, J.Wiley & Sons, 1984

[17] W.Greiner,A.Schäfer, *Quantum Chromodynamics*, Springer, 1994

[18] R.G.Roberts, *The structure of the proton*, Cambridge University Press, 1990

[19] M.Anselmino, A.Efremov, E.Leader, *The Theory and Phenomenology of Polarized Deep Inelastic Scattering*, CERN-TH/7216/94, Phys.Rept.261 (1995) 1-124.

[20] R.Jaffe, *Spin, Twist and Hadron Structure in Deep Inelastic Processes*, International School of Nucleon Structure, Erice, August 1995, MIT-CTP-2506, 1996

[21] R.Jaffe, *The Context of High Energy QCD Spin Physics*, Talk presented at the Adriatico Research Conference Trends in Collider Spin Physics, ICTP, Trieste, December 1995, MIT-CTP-2518, 1996

[22] A.V.Manohar, *An Introduction to Spin Dependent Deep Inelastic Scattering*, Proc. of the 7th Lake Louise Winter Institute, World Scientific, 1992

[23] M.G.Doncel, E. de Rafael, Nuovo Cim. 4A, 363 (1971)

[24] P.L.Anthony *et al., Deep inelastic scattering of polarized electrons by polarised* ^3He *and the study of the neutron spin structure*, Phys.Rev.D 54 (1996) 6620

[25] J.D.Bjorken, *Applications of the Chiral* $U(6) \otimes U(6)$ *Algebra of Current Densities* Phys.Rev. Vol.148, No.4 (1966) 1467

[26] R.L.Jaffe, A.V.Manohar, Nucl.Phys. B337 (1990) 509

[27] F.E.Close, R.G.Roberts, Phys.Let. B316 (1993) 165

[28] J.Ellis, M.Karliner, Phys.Let. B341 (1995) 397

[29] D.Gross, F.Wilczek, Phys.Rev. D9 (1974) 980

[30] M.Gell-Mann, Phys.Let. 8 (1964) 214

[31] G.Zweig, internal CERN report, CERN-TH-412, 1964

[32] J.D.Bjorken, Phys.Rev. 179 (1969) 1547

[33] J.Ellis, R.Jaffe, *Sum Rule for Deep Inelastic Electroproduction from Polarised Protons*, Phys.Rev.D, Vol.9, No.5 (1974) 1444

[34] S.A.Larin, Phys.Let. B334 (1994) 192

[35] K.Heller, *Spin Effects at High Energies*, Proceedings of the Seventh Lake Louise Winter Institute, eds. B.A. Campbell et al., World Scientific, 1992

[36] M.Birkel, H.Fritzsch, *Nucleon Spin and the Mixing of Axial Vector Mesons*, MPI-PhT/95-112, hep-ph/9511424v3, June 1996

[37] S.L.Adler, Phys.Rev. 177 (1969) 2426

[38] J.S.Bell, R.Jackiw, Nuovo Cim. 60A (1969) 47

[39] J.F.Donoghue, E.Golowich, B.R.Holstein, *Dynamics of the Standard Model*, Cambridge Monographs on Particle Physics, Nuclear Physics and Cosmology 2, 1992

[40] J.Ellis, M.Karliner, *The Strange Spin of the Nucleon*, Invited lectures at the Int. School of Nucleon Spin Structure, Erice, August 1995, CERN-TH/95-334, hep-ph/9601280, 1996

[41] E.Witten, Nucl.Phys. B160, 57 (1979)

[42] A.Schäfer, *The Nucleon Spin Structure in the Skyrme Model and other Effective Models*, Proceeding of the Workshop on the Prospects of Spin Physics at HERA, eds. J.Blümlein, W.D.Nowak, DESY 95-200, 1995

[43] X.Ji, *Hunting for the Remaining Spin of the Nucleon*, Plenary talk at the 12th Int.Symposium on High-Energy Spin Physics, Amsterdam, Sept. 1996, hep-ph/9610369

[44] I.Balitsky, X.Ji, *How much of the Nucleon Spin is Carried by Glue?*, JLAB-THY-97-05, hep-ph/9702277, 1997

[45] HERMES Collaboration, *Technical Design Report*, DESY-PRC 93-06, MPIH-V20 1993, 1993

[46] A.A.Sokolov, I.M.Ternov, *On Polarisation and Spin Effects in the Theory of Synchrotron Radiation*, Soviet Physics, DOKLADY, Vol.8.No.12 (1964), 1203-1205

[47] D.Barber, *et al., The First Achievement of Longitudinal Spin Polarisation in a High Energy Electron Storage Ring*, Phys.Lett. B343 (1995) 436

[48] D.Barber, *Theory and Observation of Electron Polarisation in High Energy Electron Storage Rings*, Proc. of the 10th Int.Symposium of High Energy Spin Physics, Nagoya, 1992, eds. T.Hasegawa et al. (Univ. Acad. Press, Tokyo, 1993)

[49] J.Buon, K.Steffen, HERA *Variable Energy 'Mini' Spin Rotator and head-on ep Collision Scheme with Choice of Electron Helicity*, Nucl.Inst.Meth. A245 (1986) 248

[50] D.Barber, *et al., The* HERA *Polarimeter and the First Observation of Electron Spin Polarization in* HERA, Nucl.Inst.Meth. A329 (1993), 79-111

[51] U.Fano, J.Op.Soc.Am. 39 (1949) 859

[52] R.Kaiser, *The Calorimeter of the* HERA *Polarimeter: Installation, Calibration, First Measurements*, DESY F35D-92-02, Diplom Thesis, University of Münster, 1992

[53] J.E.Belz, *Beam Polarization Smoothing for Analysis of 1995 Data*, HERMES Internal Note 96-051, 1996

[54] J.E.Belz, private communication

[55] Particle Data Group, *Review of Particle Physics*, Phys.Rev.D54 (1996)

[56] HERMES Collaboration, *The* HERMES *internal Target*, DESY-HERMES 97-11, (1997), to be published

[57] K.Lee *et al., A laser optically pumped polarised* ^{3}He *target for storage rings*, Nucl.Inst.Meth. A333 (1993) 294

[58] S.F.Pate *et al., Cryogenic Polarized Internal* ^{3}He *Gas Target for* HERMES, Proc. of the Int. Workshop on Polarized Beams and Polarized Gas Targets, Cologne, Germany, June 6-9, 1995, eds. H.Paetz gen. Schieck and L. Sydow (World Scientific, Singapore, 1996) p. 413

[59] M.Pitt *et al., TOM: A Target Optical Monitor of Polarisation and Luminosity for Polarised Internal Gas Targets*, Proc. of the Int. Workshop on Polarized Beams and Polarized Gas Targets, Cologne, Germany, June 6-9, 1995, eds. H.Paetz gen. Schieck and L. Sydow (World Scientific, Singapore, 1996) p. 39

[60] M.Düren, *The* HERMES *Experiment: From the Design to the First Results*, Habilitation Thesis, University of Erlangen, 1995, DESY HERMES-95-02

[61] HERMES Collaboration, *The* HERMES *Spectrometer*, DESY HERMES 97-10, (1997), to be published

[62] G.Roeper, *Messung der Feldverteilung des HERMES-Spektrometer-Magneten*, Diplom thesis, University of Hamburg, DESY HERMES 95-073, 1995

[63] S.Bernreuther *et al., Design and Performance of the large* HERMES *drift chambers*, Nucl.Inst.Meth. A 367 (1995) 96-99

[64] W.Wander, *Rekonstruktion hochenergetischer Streuereignisse im HERMES Experiment*, PhD Thesis, University of Erlangen, April 1996

[65] R.Kaiser, *Particle Identification at* HERMES, HERMES Internal Report 1997

[66] S.Potashov, *Offline Calibration of the* HERMES *Luminosity Monitor: Procedure and Software*, DESY HERMES 96-013, 1996

[67] C.W.Fabjan, *Calorimetry in High Energy Physics*, in: T.Ferbel, Experimental Techniques in High Energy Physics, Addison-Wesley, 1987

[68] A.Fantoni, *et al., The HERMES Electromagnetic Calorimeter*, Proc. of CALOR 96 (VI International Conference on Calorimetry in High Energy Physics), Frascati, June 1996

[69] A.Fantoni, *Costruzione del calorimetro a contatori di vetro al piombo dell'esperimento HERMES per la misura delle funzioni di struttura di spin dei nucleoni*, PhD Thesis, Università degli Studi della Calabria, March 1996, HERMES Internal Note 96-015

[70] Bruce Bray, private communication

[71] H.Avakian, *et al., Performance of F101 Radiation Resistant Lead Glass Shower Counters*, to be published in Nucl.Inst.Meth.

[72] O.Hansen, private communication

[73] H.E.Jackson *et al., Proposal for a Dual Radiator RICH for* HERMES, HERMES Internal Note 97-03, January 1997

[74] R.Kaiser *et al., Online Monitoring at* HERMES, Proc. of CHEP 97, Berlin, 1997

[75] ADAMO-*Entity Relationship Programming System, Version 3.3*, Programming Techniques Group, ECP Division, CERN, Geneva, 1994

[76] K.Ackerstaff and M.-A.Funk, PinK*: A* Tcl/Tk *based Database Interface to* Adamo *and* Dad, Proc. of CHEP 95, Rio de Janeiro, 1995

[77] J.K.Ousterhout, *Tcl and the Tk Toolkit*, Addison-Wesley, 1994

[78] W.Wander, Dad-*Distributed* Adamo *Database System at* Hermes, Proc. of CHEP 95, Rio de Janeiro, 1995

[79] V.L.Ginzburg, I.M.Frank, Soviet Phys. JETP 16 (1946) 15

[80] G.M.Garibian, Zh.Eksp.Teor.Fiz. 33 (1957) 1043 [Soviet Phys. JETP 6 (1958) 1079] Zh.Eksp.Teor.Fiz. 37 (1959) 527 [Soviet Phys. JETP 10 (1960) 372]

[81] F.Harris *et al*, Nucl.Inst.Meth. 107 (1973) 413
M.L.Cherry *et al*, Nucl.Inst.Meth. 115 (1974) 141

[82] X.Artru, G.B. Yodh, G.Mennessier, *Practical Theory of the Multilayered Transition Radiation Detector*, Phys.Rev.D, Vol.12, No.5 (1975) 1289-1306

[83] B.Dolgoshein, *Transition Radiation Detectors*, Nucl.Inst.Meth. A326 (1993) 434-469

[84] B.Dolgoshein, *Transition Radiation Detectors and Particle Identification*, Nucl.Inst.Meth. A252 (1986) 137-144

[85] W.R.Leo, *Techniques for Nuclear and Particle Physics Experiments*, Springer, 1987

[86] F.Sauli, *Principles of Operation of Multiwire Proportional and Drift Chambers*, in: T.Ferbel, Experimental Techniques in High Energy Physics, Addison-Wesley, 1987, and CERN 77-09, May 1977

[87] G.Charpak *et al*, Nucl.Inst.Meth. 62 (1968) 235

[88] C.A.Miller, private communication

[89] J.Emerson, *Modeling of the HERMES Transition Radiation Detector*, MSc Thesis, Simon Fraser University, August 1995

[90] C.W.Fabjan *et al., Practical Prototype of a Cluster-Counting Transition Radiation Detector*, Nucl.Inst.Meth. 185 (1981) 119-124

[91] E.Barbarito *et al., A Large Area Transition Radiation Detector to measure the Energy of Muons in the Gran Sasso Underground Laboratory*, Nucl.Inst.Meth. A365 (1995) 214-223

[92] T.Åkeson *et al., Particle Identification Performance of a Straw Transition Radiation Tracker Prototype*, Nucl.Inst.Meth A372 (1996) 70-84

[93] A.Trudel, private communication

[94] A.Büngener *et al., Electron Identification beyond 1 GeV by Means of Transition Radiation*, Nucl.Inst.Meth. A214 (1983) 261-268

[95] R.Openshaw, private communication

[96] D.Thiessen, *The Gas System for the HERMES Transition Radiation Detector*, MSc Thesis, Simon Fraser University, March 1996

[97] H.Coombes, private communication

[98] M.Vetterli, private communication

[99] Felix Menden, private communication

[100] Gordon Greeniaus, private communication

[101] R.Ansari *et al., Design and Rejection Studies for a Cylindrical Transition Radiation Detector for the UA2 Upgrade*, Nucl.Inst.Meth. A263 (1988) 51-57

[102] J.F.Detoeuf *et al., The D0 Transition Radiation Detector*, Nucl.Inst.Meth. A265 (1988) 157-166

[103] N.Terunuma *et al., Initial Performance of the* VENUS *Transition Radiation Detector*, Nucl.Inst.Meth. A323 (1992) 471-476

[104] H.Grässler *et al., Simultaneous Track Reconstruction and Electron Identification in the H1 Radial Drift Chambers*, Nucl.Inst.Meth. A283 (1989) 622-627

[105] E.O'Brien *et al., Electron Identification in the* PHENIX *Experiment using a Tracking TRD*, Nuclear Physics A566 (1994) 615c-618c

[106] ZEUS TRD Group, *The Transition Radiation Detector for* ZEUS, Nucl.Inst.Meth. A323 (1986) 135-139

[107] G.D.Barr *et al., A large Area Transition Radiation Detector*, Nucl.Inst.Meth. A294 (1990) 465-472

[108] Experimental Physics Input Output Package, CERN Program Library Long Writeup I101, CERN 1993

[109] HBOOK - Statistical Analysis and Histogramming, CERN Program Library entry Y250, CERN 1994

[110] Arthur Mateos, Dirk de Schepper, *HAT (Histogram and Test Package)*, private communications

[111] L.W.Whitlow, *et al., A precise extraction of* $R = \sigma_L/\sigma_T$ *from a global analysis of the SLAC deep inelastic e-p and e-d scattering cross sections*, Phys.Let.B Vol.250, No.1,2, 1990

[112] Andreas Schäfer, *Spin-Dependent Structure Functions for the Proton and the Neutron*, Phys.Let.B Vol.208, No.2, 1988

[113] *PAW -Physics Analysis Workstation*, CERN Program Library entry Q121

[114] I.V.Akushevich, N.M.Shumeiko, *Radiative effects in deep inelastic scattering of polarized leptons by polarized light nuclei*, J.Phys.G 20(1994) 513-531

[115] D.Ryckbosch, M.Tytgat, I.Akushevich, *Systematic error from the radiative correction procedure* Hermes Internal Note 96-046, 1996

[116] M.Vetterli, *The* $^1H(\vec{d},\gamma)^3He$ *Reaction and D-State Effects in* ^3He, Ph.D. Thesis, McMaster University, 1985

[117] I.R.Afnan, N.D.Birrell, *Comparison of the unitary pole and Adhikari-Sloan expansion in the three nucleon system*, Phys.Rev.C Vol.16, No.2, (1977) 823

[118] R.M.Woloshyn, *Polarized Lepton Deep-Inelastic Scattering from Few-Nucleon Targets*, Nuclear Physics A496 (1989) 749-769

[119] B.Blankleider, R.M.Woloshyn *Quasi-Elastic Scattering of Polarized Electrons on Polarized* ^3He, Phys.Rev.C Vol.29, No.2, (1984) 538

[120] C.Ciofi degli Atti *et al., Nuclear Effects in deep inelastic scattering of polarized electrons off polarised* ^3He *and the neutron spin structure functions*, Phys.Rev.C Vol.48, No.3, (1993) R968

[121] HERMES g_1^n-Group, *Determination of the 1995 Data Quality and the Extraction of the Spin Structure Function of the Neutron*, HERMES Internal Report 97-07

[122] M.Arneodo *et al., Measurement of the proton and deuteron structure functions,* F_2^p *and* F_2^d, Phys.Let. B364 (1995) 107-115

[123] S.J.Brodsky, M.Burkardt, I.Schmidt, *QCD constraints on the shape of polarized quark and gluon distributions*, Nucl.Phys. B441 (1995) 197-214

[124] F.E.Close, R.G.Roberts, Phys.Let. B336 (1994) 257

[125] S.Rock, *Future Spin Experiments at SLAC*, in: Prospects of Spin Physics at HERA, eds. J.Blümlein, W.D.Nowak, DESY 95-200, 1995

[126] D.P.Barber, *Possibilities for polarized protons in* HERA, in: Prospects of Spin Physics at HERA, eds. J.Blümlein, W.D.Nowak, DESY 95-200, 1995

[127] J.Soffer, O.V.Teryaev, *Gluon polarisation in transversely polarised nucleons and jet spin asymmetries at RHIC*, hep-ph/9702352, February 1997

[128] N.E.Tyurin, *Some Aspects of Spin Physics at RHIC*, hep-ph/9512235, Talk presented at the PHENIX project meeting, Vladimir, Russia, 1995

[129] COMPASS Proposal, CERN/SPSLC 96-14, 1996

[130] M.Amarian *et al., The HERMES Charm Upgrade Program: A Measurement of the Double Spin Asymmetry in Charm Leptoproduction*, Hermes Internal Note 97-004